Bridge aerodynamics in skew winds:
Generalized buffeting load modelling and response analysis

by

Bernardo Morais da Costa

Thesis submitted in
partial fulfilment of the
requirements for the degree of
Doctor of Philosophy

Faculty of Science and Technology
Department of Mechanical and Structural Engineering and Materials Science
2022

University of Stavanger
NO-4036 Stavanger
Norway

ISBN: 978-82-8439-133-5
ISSN: 1890-1387
UiS PhD Thesis No. 674

Title: Bridge aerodynamics in skew winds: Generalized buffeting load modelling and response analysis
Author: Bernardo Morais da Costa
Date: September 2022

Abstract

This thesis deals with the modelling of wind loads on bridges. When turbulent wind blows past a bridge deck, the deck experiences fluctuating loads, i.e., buffeting loads. Most buffeting theories concern straight bridge decks subjected to normal wind action, i.e., winds perpendicular to the bridge deck. This thesis initially reproduces the normal wind buffeting theory in a format that can be easily generalized to skew winds (i.e., non-perpendicular). The thesis then revises the state-of-the-art of the skew wind buffeting theory and proposes novel corrections, significant simplifications, and generalizations to that theory. Since the preferred skew wind load formulation requires the estimation of yaw- and inclination-angle-dependent aerodynamic coefficients, the thesis also provides a generalization and improvements to the traditional approach using only inclination-angle-dependent aerodynamic coefficients.

Multiple challenges arise when putting into practice the skew wind buffeting theory. An ongoing floating bridge project, whose details are described in the thesis, is considered an ideal case for this application. The long, curved, continuous and flexible structure is planned to span a record 5000 m wide section of the Bjørnafjord in Norway, where it will be subjected to strong winds from multiple directions.

Wind tunnel experiments were conducted by a third party, where a sectional model of the bridge girder was tested under skew winds for a large domain of yaw angles. Six aerodynamic coefficients are estimated for 30 combinations of yaw and inclination angles. Four different approaches to fit and extrapolate the coefficients are compared and discussed, enabling a 360-degree assessment of the skew wind buffeting response of the bridge. The proposed approach uses continuous and differentiable piecewise constrained bivariate polynomial functions covering the spherical domain of possible wind directions while respecting symmetries and imposing physical principles at certain angles.

A simplified numerical model of the bridge is developed, whose properties, assembling process, modal analysis and sensitivity results are presented in the thesis. The numerical model is then used to assess the novel and the traditional buffeting load formulations. The bridge displacement response is compared for different fits of the aerodynamic coefficients and for different buffeting and quasi-steady motion-dependent force formulations. Both frequency- and time-domain analyses are performed to increase confidence in the results. Methods that neglect the three-dimensionality of the wind-structure interaction and only consider the two-dimensional normal-plane projection of the wind are shown to underestimate the bridge response under skew winds.

The exceptionally long span of the case study makes it an equally good candidate for examining the wind field homogeneity assumption and its implications. A full long-term response analysis is performed considering all strong wind events in a 20-year-long wind field simulation period. Inhomogeneous (i.e., space-varying) wind speeds and directions were provided by a high-resolution Weather Research and Forecasting (WRF) model. Inhomogeneous wind turbulence intensities are estimated using a hybrid method combining formulations given in a European standard with an artificial neural network, trained with five years of relevant measurement data. An analogous database of equivalent homogeneous wind fields is created to compare the associated bridge responses. The long-term response is analysed, demonstrating a varying accuracy of the homogeneity assumption. On average, the bridge response under inhomogeneous winds is larger than that under homogeneous winds, but to a different extent for different response components. Large underestimations and overestimations of the response are obtained for particular wind events.

The use of a state-of-the-art skew wind formulation in combination with comprehensive wind tunnel tests and careful long-term inhomogeneous wind buffeting analyses is encouraged in the design of wind-sensitive bridges subjected to strong skew winds.

Acknowledgements

I want first to thank my main supervisor Prof. Jasna Bogunović Jakobsen and my internal supervisor Prof. Jungao Wang.

Jasna, thank you for giving me a first and clearly motivating introduction to the fields of wind engineering and bridge aerodynamics. Thank you for then enabling this PhD programme, for your simultaneously delegative and attentive supervision, and your kind support throughout all stages of the programme.

Jungao, you managed to be a motivating, challenging and tireless supervisor, as well as a friend, all at once. From the big decisions to the small technical details, you brought knowledge, meaning and joy to this journey.

To my co-supervisors, Prof. Jónas Þór Snæbjörnsson and Prof. Ole Andre Øiseth, I am grateful for your countless contributions. Thank you for always finding the time for our many productive discussions and your precious revisions.

I want to thank the Norwegian Public Roads Administration and the Research Council of Norway for approving this project and providing financial support.

Finally, I thank Madalena, my dear family and friends for their love and support.

Preface

This thesis is submitted in partial fulfilment of the requirements for the degree of *Philosophiae Doctor* (PhD) at the University of Stavanger (UiS), Norway. The research has been carried out at the Faculty of Science and Technology, Department of Mechanical and Structural Engineering and Materials Science, and at the Norwegian Public Roads Administration (NPRA). The compulsory PhD courses were offered at the UiS. This doctoral project was funded by the NPRA and the Research Council of Norway as a Public Sector PhD under the project number 299727. It was carried out in the period from September 2019 to September 2022.

Professor Jasna Bogunović Jakobsen, Professor Jungao Wang, Professor Jónas Þór Snæbjörnsson and Professor Ole Andre Øiseth have supervised the research work.

The thesis is based on journal and conference papers, either published or submitted, which comply with the peer-review process.

Bernardo Morais da Costa

Stavanger, Norway
September 2022

Publications

This dissertation is based on the following published or submitted works in International Scientific Indexing (ISI) journals and peer-reviewed proceedings of conferences:

Paper 1

Costa, B.M., Wang, J., Jakobsen, J.B., Øiseth, O.A., Snæbjörnsson, J.Þ., 2022a. Bridge buffeting by skew winds: A revised theory. Journal of Wind Engineering and Industrial Aerodynamics 220, 104806.
https://doi.org/10.1016/j.jweia.2021.104806

Paper 2

Costa, B.M., Wang, J., Jakobsen, J.B., Øiseth, O.A., Snæbjörnsson, J.Þ., 2022b. Bridge buffeting by skew winds: A quasi-steady case study. Journal of Wind Engineering and Industrial Aerodynamics 227, 105068.
https://doi.org/10.1016/j.jweia.2022.105068

Paper 3

Costa, B.M., Snæbjörnsson, J.Þ., Øiseth, O.A., Wang, J., Jakobsen, J.B., 2021. Data-driven prediction of mean wind turbulence from topographic data, IOP Conference Series: Materials Science and Engineering. IOP Publishing, p. 012005.
https://doi.org/10.1088/1757-899X/1201/1/012005

Paper 4

Costa, B.M., Wang, J., Jakobsen, J.B., Snæbjörnsson, J.Þ., Øiseth, O.A., 2022c. Long-term response of a floating bridge to inhomogeneous wind fields. Manuscript submitted for publication.

Contents

Nomenclature

Variables:

β	Local mean yaw angle
$\tilde{\beta}$	Local instantaneous yaw angle (turbulence dependent)
$\tilde{\tilde{\beta}}$	Local instantaneous relative yaw angle (turbulence and motion dependent)
β^*	Smallest angle between the $\boldsymbol{xy}$-projection of $\boldsymbol{X_u}$ and the $\boldsymbol{y}$ axis
$\beta_{Cardinal}$	Mean yaw angle, with respect to the cardinal directions the wind blows from (0° = N, 90° = E, 180° = S, 270° = W)
β_G	Global mean yaw angle, in homogeneous wind conditions, with respect to the Gs coordinate system
β_i	Mean yaw angle, either local or global, with respect to the generic coordinate system i
$\beta_{rx=0}$	β, before rotating the model test by rx
γ	A generic angle
$\boldsymbol{\Delta}, \dot{\boldsymbol{\Delta}}, \ddot{\boldsymbol{\Delta}}$	Vectors of displacements, velocities, accelerations (for each element)
$\boldsymbol{\Delta^G}, \dot{\boldsymbol{\Delta}}^{\boldsymbol{G}}, \ddot{\boldsymbol{\Delta}}^{\boldsymbol{G}}$	Global vectors of displacements, velocities, accelerations (for all nodes)
$\widetilde{\Delta\beta}$, $\widetilde{\widetilde{\Delta\beta}}$	Change in β due to: turbulence $\left(\widetilde{\Delta\beta}\right)$, turbulence and structural motions $\left(\widetilde{\widetilde{\Delta\beta}}\right)$
$\widetilde{\Delta\theta}$, $\widetilde{\widetilde{\Delta\theta}}$	Change in θ due to: turbulence $\left(\widetilde{\Delta\theta}\right)$, turbulence and structural motions $\left(\widetilde{\widetilde{\Delta\theta}}\right)$
$\widetilde{\Delta\theta}_{yz}$, $\widetilde{\widetilde{\Delta\theta}}_{\widetilde{yz}}$	Change in θ_{yz} due to: turbulence $\left(\widetilde{\Delta\theta}_{yz}\right)$, turbulence and structural motions $\left(\widetilde{\widetilde{\Delta\theta}}_{\widetilde{yz}}\right)$
ΔX, ΔY, ΔZ	Distance between two reference points, along the axes $\boldsymbol{X}$, $\boldsymbol{Y}$, $\boldsymbol{Z}$

ΔX_u, ΔY_v, ΔZ_w	Distance between two reference points, along the axes $\boldsymbol{X_u}$, $\boldsymbol{Y_v}$, $\boldsymbol{Z_w}$
$\Delta\overline{x_u}$, $\Delta\overline{y_v}$, $\Delta\overline{z_w}$	Distance between two reference points, along the averaged wind axes $\overline{\boldsymbol{x_u}}$, $\overline{\boldsymbol{y_v}}$, $\overline{\boldsymbol{z_w}}$
θ	Local mean inclination angle
$\tilde{\theta}$	Local instantaneous inclination angle (turbulence dependent)
$\tilde{\tilde{\theta}}$	Local instantaneous relative inclination angle (turbulence and motion dependent)
θ_{yz}, $\tilde{\theta}_{yz}$, $\tilde{\tilde{\theta}}_{yz}$	$\boldsymbol{yz}$-plane projection counterparts of θ, $\tilde{\theta}$, $\tilde{\tilde{\theta}}$
θ_G	Global mean inclination angle, with respect to the Gs coordinate system
θ_i	Mean inclination angle, either local or global, with respect to the generic coordinate system i
ρ	Air density
σ_i	Standard deviation of the displacements in the i axis
$\boldsymbol{\sigma_\Delta}$	Global vector of standard deviations of displacements (for all nodes)
$\boldsymbol{\Phi}$	Matrix of mode shapes
$\chi_{i,j}$	Cross-sectional admittance function, associated with C_i and turbulence component j
ω	Angular frequency (radians per second)
a_i, $\boldsymbol{a_i}$	a_i is the wind turbulence component in the i-axis (e.g. a_x). $\boldsymbol{a_i}$ is the wind turbulence vector in the i-system (e.g. $\boldsymbol{a_{Gw}} = [u, v, w]^T$)
$\tilde{\tilde{a}}_D$, $\tilde{\tilde{a}}_A$, $\tilde{\tilde{a}}_L$	Counterparts of $\tilde{\tilde{u}}$, $\tilde{\tilde{v}}$, $\tilde{\tilde{w}}$ in the Lnw-system
$\boldsymbol{A}$	Matrix dependent on tested β and θ angles such that $\boldsymbol{Ax}$ returns polynomials
$\boldsymbol{A_b}$	Buffeting force coefficient matrix (turbulence dependent)
A_i	Non-dimensional parameter to regulate the frequency distribution of $i = u, v, w$
A_i^*	Quasi-static flutter derivatives for self-excited moment ($i = 1, 2 \ldots 6$)
$\boldsymbol{A_\Delta}$	Motion-dependent force coefficient matrix of structural displacements
$\boldsymbol{A_{\dot{\Delta}}}$	Motion-dependent force coefficient matrix of structural velocities
$\boldsymbol{A_{i,axial}}$	Separate axial force contribution to $\boldsymbol{A_i}$, for $\boldsymbol{i} = \boldsymbol{\Delta}, \dot{\boldsymbol{\Delta}}, b$
$\boldsymbol{A_{Scanlan,\Delta}}$	Alternative formulation of $\boldsymbol{A_\Delta}$, using Scanlan's flutter derivatives

$\boldsymbol{A_{Scanlan,\dot{\Delta}}}$	Alternative formulation of $\boldsymbol{A_{\dot{\Delta}}}$, using Scanlan's flutter derivatives
$\boldsymbol{b}$	Vector of tested aerodynamic coefficients
B	Cross-section width
$\boldsymbol{B}$	Diagonal matrix: $diag(B, B, B, B^2, B^2 B^2)$
$\boldsymbol{B_{Lnw}}$	Diagonal matrix: $diag(H, 0, B, 0, B^2, 0)$ (where the drag is normalized by H)
c_i	Polynomial coefficients
C, $\boldsymbol{C}$	Aerodynamic coefficient C. Vector of aerodynamic coefficients $\boldsymbol{C}$. C_i is in the i-axis (e.g. C_{X_u}). $\boldsymbol{C_i}$ is in the i-system (e.g. $\boldsymbol{C_{Gw}}$). $\tilde{C}$ and $\widetilde{\boldsymbol{C}}$ depend on, e.g. $(\tilde{\beta}, \tilde{\theta})$. $\tilde{\tilde{C}}$ and $\widetilde{\widetilde{\boldsymbol{C}}}$ depend on, e.g. $\left(\tilde{\tilde{\beta}}, \tilde{\tilde{\theta}}\right)$
C', $\boldsymbol{C'}$	Derivative of C or $\boldsymbol{C}$ with respect to θ_{yz}
C'^{β}, $\boldsymbol{C'^{\beta}}$	Partial derivative of C or $\boldsymbol{C}$ with respect to β
C'^{θ}, $\boldsymbol{C'^{\theta}}$	Partial derivative of C or $\boldsymbol{C}$ with respect to θ
$\widehat{\boldsymbol{C}}$	Modal damping matrix
$\boldsymbol{C^G}$	Global damping matrix (for all nodes)
$\boldsymbol{C_{AE}}$	Aerodynamic damping matrix (for each element)
$\boldsymbol{C_{AE}^G}$	Global aerodynamic damping matrix (for all nodes)
$\boldsymbol{C_S^G}$	Global structural damping matrix (for all nodes)
f	Frequency, in Hertz
$\tilde{\boldsymbol{f}}_{\boldsymbol{ad}}$	Aerodynamic forces per unit length (due to $\boldsymbol{f_{mean}}$ and $\tilde{\boldsymbol{f}}_{\boldsymbol{b}}$)
$\tilde{\tilde{\boldsymbol{f}}}_{\boldsymbol{ad}}$	Aerodynamic forces per unit length (due to $\boldsymbol{f_{mean}}$ and $\tilde{\tilde{\boldsymbol{f}}}_{\boldsymbol{b}}$)
$\tilde{\boldsymbol{f}}_{\boldsymbol{b}}$	Buffeting forces per unit length (due to turbulence)
$\tilde{\tilde{\boldsymbol{f}}}_{\boldsymbol{b}}$	Buffeting forces per unit length (due to turbulence and structural motions)
$\boldsymbol{f_{i,axial}}$	Separate axial force contribution to $\boldsymbol{f_i}$, for $\boldsymbol{i} = ad, b, mean$
$\boldsymbol{f_{mean}}$	Mean wind forces per unit length
$\widetilde{\boldsymbol{F}}_{\boldsymbol{ad}}$	Aerodynamic forces $\left(\widetilde{\boldsymbol{F}}_{\boldsymbol{ad}} = L\tilde{\boldsymbol{f}}_{\boldsymbol{ad}}\right)$
$\boldsymbol{F_b^G}$	Global buffeting force vector (for all nodes)
H	Cross-section height
H_i^*	Quasi-static flutter derivatives for self-excited lift $(i = 1, 2 \dots 6)$
$\widehat{\boldsymbol{H}}$	Modal frequency response function matrix
I_i	Turbulence intensity of i

k	Reduced frequency ($k = B\omega/U$)
$\widehat{\boldsymbol{K}}$	Modal stiffness matrix
$\boldsymbol{K^G}$	Global stiffness matrix (for all nodes)
$\boldsymbol{K_{AE}}$	Aerodynamic stiffness matrix (for each element)
$\boldsymbol{K_{AE}^G}$	Global aerodynamic stiffness matrix (for all nodes)
$\boldsymbol{K_S^G}$	Global structural stiffness matrix (for all nodes)
$K_{i,j}$	Non-dimensional decay coefficient of the turbulence component i, to decrease coherence along the direction j
L	Element length
L_{i,X_u}	Characteristic length scale of i in the direction of $\boldsymbol{X_u}$
$\boldsymbol{M^G}$	Global mass matrix (for all nodes)
$\widehat{\boldsymbol{M}}$	Modal mass matrix
N_M	Number of modes
N_N	Number of nodes
P	Polynomial function
$\boldsymbol{P_b}$	Coefficient matrix of buffeting forces (for each element)
$\boldsymbol{P_b^G}$	Global coefficient matrix of buffeting forces (for all nodes)
$\boldsymbol{P_b^{G^*}}$	Complex conjugate of $\boldsymbol{P_b^G}$
P_i^*	Quasi-static flutter derivatives for self-excited drag ($i = 1, 2, \dots 6$)
q	Air velocity pressure
$\boldsymbol{R_i}(\gamma)$	Rotation matrix around a generic i-axis, by a generic angle γ
$S, \tilde{S}, \tilde{\tilde{S}}$	Sign functions: $sgn(\cos\beta)$, $sgn(\cos\tilde{\beta})$, $sgn\left(\cos\tilde{\tilde{\beta}}\right)$
$\boldsymbol{S_\Delta}$	Auto-spectral density matrix of the nodal displacement response
$\boldsymbol{S_{\Delta\Delta}}$	Cross-spectral density matrix of the nodal displacement response
$\boldsymbol{S_{\hat{\eta}\hat{\eta}}}$	Cross-spectral density matrix of the modal displacement response
$\boldsymbol{S_{aa}}$	Cross-spectral density matrix of the fluctuating wind components
$\boldsymbol{S_{\hat{F}\hat{F}}}$	Cross-spectral density matrix of the modal buffeting loads
S_i (or $S_{i,n}$)	One-point spectral density matrix entry of turbulence component i (at node n)
S_{ii}, $S_{i_1 i_2}$ (or $S_{i_1 n_1 i_2 n_2}$)	Two-point cross-spectral density matrix entry of two equal (ii) or two generic ($i_1 i_2$) turbulence components (associated with two nodes n_1 and n_2)

t	Time (position in time)
$\boldsymbol{T_{ji}}$	Transformation matrix from the coordinate system i to the coordinate system j
$\boldsymbol{T_{sym}}$	Transformation matrix to impose symmetry properties
u	Turbulence component along the mean wind
$\tilde{\tilde{u}}$	Relative velocity between u and the moving bridge
U, U_i, $\boldsymbol{U_i}$	Mean wind speed U; mean wind projection in the i-axis or i-plane U_i; mean wind vector in the i-system $\boldsymbol{U_i}$
$\widetilde{U}$, $\widetilde{U}_i$, $\widetilde{\boldsymbol{U}}_{\boldsymbol{i}}$	Local instantaneous wind speed $\widetilde{U}$ (turbulence dependent); local instantaneous wind projection in the i-axis or i-plane $\widetilde{U}_i$, or vector in the i-system $\widetilde{\boldsymbol{U}}_{\boldsymbol{i}}$
$\widetilde{\widetilde{U}}$, $\widetilde{\widetilde{U}}_i$, $\widetilde{\widetilde{\boldsymbol{U}}}_{\boldsymbol{i}}$	Local instantaneous relative wind speed $\widetilde{\widetilde{U}}$ (turbulence and motion dependent); local instantaneous relative wind projection in the i-axis or i-plane $\widetilde{\widetilde{U}}_i$, or vector in the i-system $\widetilde{\widetilde{\boldsymbol{U}}}_{\boldsymbol{i}}$
$\boldsymbol{U}_{rx=0}$	Mean wind vector, before rotating the model test by rx
v	Horizontal turbulence component across the mean wind direction
$\tilde{\tilde{v}}$	Relative velocity between v and the moving bridge
v_i	A generic vector in the coordinate system i
w	Upward turbulence component, perpendicular to u and v
$\widetilde{\widetilde{w}}$	Relative velocity between w and the moving bridge
$\boldsymbol{x}$	Vector of polynomial coefficients

Accents / superscripts / styles:

$\bar{}$	Quantity averaged from a pair of reference points
$\sim$	Time-varying quantity due to turbulence
$\approx$	Time-varying quantity due to turbulence (if applicable) and structural motions
$\dot{}$	First-time derivative
$\ddot{}$	Second-time derivative
$\widehat{}$	Modal quantity
^{G}	Global quantity, relative to all nodes/elements and all DOF (omitted when there is no ambiguity between nodal/elemental and global quantities (e.g. $\boldsymbol{S_{\Delta\Delta}}$))
^{H}	Quantity estimated in homogeneous wind conditions

^{I}	Quantity estimated in inhomogeneous wind conditions
^{Q}	Quantity related to the quadratic wind speed U^2
boldface	Variables in **bold** represent vectors and matrices

Acronyms:

1D, 2D or 3D	1-, 2-, or 3-dimensional (in space)
AAF	Aerodynamic admittance function(s)
AGL	Above ground level
ANN	Artificial neural network(s)
CFD	Computational fluid dynamics
DOF	Degree(s) of freedom
FEM	Finite element method
NPRA	Norwegian Public Roads Administration
PSD	Power spectral density
QS	Quasi-steady
TLP	Tension-leg platform
WRF	Weather research and forecasting (model)

Coordinate systems and respective axes:

Lnw $(\boldsymbol{D}, \boldsymbol{A}, \boldsymbol{L})$	Local mean normal wind $(\boldsymbol{D}, \boldsymbol{A}, \boldsymbol{L}, \boldsymbol{rD}, \boldsymbol{M}, \boldsymbol{rL})$
$\widetilde{Lnw}$ $(\tilde{\boldsymbol{D}}, \tilde{\boldsymbol{A}}, \tilde{\boldsymbol{L}})$	Local instantaneous normal wind $\left(\tilde{\boldsymbol{D}}, \tilde{\boldsymbol{A}}, \tilde{\boldsymbol{L}}, \widetilde{\boldsymbol{rD}}, \tilde{\boldsymbol{M}}, \widetilde{\boldsymbol{rL}}\right)$
$\widetilde{\widetilde{Lnw}}$ $(\tilde{\tilde{\boldsymbol{D}}}, \tilde{\tilde{\boldsymbol{A}}}, \tilde{\tilde{\boldsymbol{L}}})$	Local instantaneous relative normal wind $\left(\tilde{\tilde{\boldsymbol{D}}}, \tilde{\tilde{\boldsymbol{A}}}, \tilde{\tilde{\boldsymbol{L}}}, \widetilde{\widetilde{\boldsymbol{rD}}}, \tilde{\tilde{\boldsymbol{M}}}, \widetilde{\widetilde{\boldsymbol{rL}}}\right)$
Ls $(\boldsymbol{x}, \boldsymbol{y}, \boldsymbol{z})$	Local (static) structural $(\boldsymbol{x}, \boldsymbol{y}, \boldsymbol{z}, \boldsymbol{rx}, \boldsymbol{ry}, \boldsymbol{rz})$
$\widetilde{Ls}$ $(\tilde{\boldsymbol{x}}, \tilde{\boldsymbol{y}}, \tilde{\boldsymbol{z}})$	Local dynamic structural $\left(\tilde{\boldsymbol{x}}, \tilde{\boldsymbol{y}}, \tilde{\boldsymbol{z}}, \widetilde{\boldsymbol{rx}}, \widetilde{\boldsymbol{ry}}, \widetilde{\boldsymbol{rz}}\right)$
Lw $(\boldsymbol{x_u}, \boldsymbol{y_v}, \boldsymbol{z_w})$.	Local (inhomogeneous) mean wind, $(\boldsymbol{x_u}, \boldsymbol{y_v}, \boldsymbol{z_w}, \boldsymbol{rx_u}, \boldsymbol{ry_v}, \boldsymbol{rz_w})$
$\widetilde{Lw}$ $(\boldsymbol{X}_{\tilde{U}}, \boldsymbol{Y}_{\tilde{U}}, \boldsymbol{Z}_{\tilde{U}})$	Local instantaneous wind $(\boldsymbol{X}_{\tilde{U}}, \boldsymbol{Y}_{\tilde{U}}, \boldsymbol{Z}_{\tilde{U}}, \boldsymbol{rX}_{\tilde{U}}, \boldsymbol{rY}_{\tilde{U}}, \boldsymbol{rZ}_{\tilde{U}})$
$\widetilde{\widetilde{Lw}}$ $\left(\boldsymbol{X}_{\tilde{\tilde{U}}}, \boldsymbol{Y}_{\tilde{\tilde{U}}}, \boldsymbol{Z}_{\tilde{\tilde{U}}}\right)$	Local instantaneous relative wind $\left(\boldsymbol{X}_{\tilde{\tilde{U}}}, \boldsymbol{Y}_{\tilde{\tilde{U}}}, \boldsymbol{Z}_{\tilde{\tilde{U}}}, \boldsymbol{rX}_{\tilde{\tilde{U}}}, \boldsymbol{rY}_{\tilde{\tilde{U}}}, \boldsymbol{rZ}_{\tilde{\tilde{U}}}\right)$
Gs $(\boldsymbol{X}, \boldsymbol{Y}, \boldsymbol{Z})$	Global structural $(\boldsymbol{X}, \boldsymbol{Y}, \boldsymbol{Z}, \boldsymbol{rX}, \boldsymbol{rY}, \boldsymbol{rZ})$
Gw $(\boldsymbol{X_u}, \boldsymbol{Y_v}, \boldsymbol{Z_w})$	Global (homogeneous) mean wind $(\boldsymbol{X_u}, \boldsymbol{Y_v}, \boldsymbol{Z_w}, \boldsymbol{rX_u}, \boldsymbol{rY_v}, \boldsymbol{rZ_w})$

1. Introduction

1.1. Research context

Norway, with its complex topography and deeply indented coastline, faces important challenges regarding its transport infrastructure. To overcome them, innovative solutions, including ground-breaking bridge projects, have been developed. This presents unique opportunities to advance the state-of-the-art of bridge engineering.

A transport corridor in the Western Region of Norway, connecting the cities of Stavanger, Bergen and Ålesund, up to the city of Trondheim, is vital for the energy, maritime, fish and other industries. This region is home to 26% of the Norwegian population (Statistisk Sentralbyrå, 2022) and is responsible for 41% of Norwegian exports (Basso et al., 2021). In the National Transport Plan 2022-2033 (Samferdselsdepartementet, 2021a), the improvement of this corridor is prioritized, of which the Coastal Highway Route E39 project is part. Replacing existing ferry crossings with fixed links is a key part of the project, as it can reduce travel time, improve transport predictability and even reduce greenhouse gas emissions (Askeland et al., 2022; Samferdselsdepartementet, 2021b).

A driving distance of 210 km currently separates Stavanger and Bergen, which includes two ferry crossings. Flight traffic represents a large share of the personal transportation between these two cities due to long travel time (Samferdselsdepartementet, 2021a). The Coastal Highway Route E39 project aims to reduce the travel time between these two cities from around 4.5 hours to around 2 hours (Samferdselsdepartementet, 2021b). This includes the construction of a 27 km long undersea road tunnel, a 1.7 km long suspension bridge and a 5 km long floating bridge. This research is motivated by the challenges that arise with a record-long wind-sensitive bridge such as the aforementioned floating bridge, which is planned to cross the 500 m deep Bjørnafjord.

To comply with the relevant standards and requirements, bridges must have: (1) sufficient capacity to resist the expected stress levels in their ultimate limit state; (2) satisfactory operability in their serviceability limit state; (3) acceptable risk, structural integrity and recovery costs in their accidental limit state; and 4) a sufficient predicted lifetime in their fatigue limit state. The wind spectrum is most energetic at low frequencies, and as the bridge span and slenderness increase, the wind loads can increasingly affect these limit states and dominate the bridge design. These loads must then be predicted with adequate accuracy and reliability for the success of long-span bridge projects and a safe and cost-effective design.

The present thesis deals with some of the challenges of accurately estimating wind loads on long-span bridges and how these affect the bridge response predictions, using the Bjørnafjord floating bridge as a case study.

1.2. Research questions

In connection with the case study of the 5 km long floating bridge, many novel challenges arise related to, for instance: metocean studies, hydrodynamics, aerodynamics, ship collision assessments, non-linear stability phenomena, the establishment of physical and numerical models, risk and vulnerability analysis, management, fabrication and construction processes, marine operations, bridge operability, maintenance, impact on the environment, society, economy and even politics. This particular research project investigates several of the challenges related to the aerodynamics, metocean studies and physical and numerical modelling of the bridge.

Buffeting loads are one of the critical aspects of a wind-resistant design of flexible structures. Buffeting loads are caused by fluctuating wind speeds, i.e., turbulence in the incoming flow. Additionally, self-excited forces, also denoted motion-dependent forces, arise when the relative velocities and the relative angles between the wind turbulence and the vibrating bridge are considered in the load model.

The goal of this research is to:

1. Review and further develop the buffeting theory applicable to a general orientation of the bridge deck relative to the wind.
2. Apply established and newly developed wind load models on a curved floating bridge.

3. Study the bridge response for all wind directions and for different load models.
4. Assess the effects of the wind inhomogeneity on the bridge response.
5. Find and develop relevant machine learning applications for the project.

The Bjørnafjord floating bridge is used as a case study addressing the above questions 2), 3) and 4). More specifically, this research aims to answer the following questions:

1. How accurate is the traditional bridge buffeting theory, which was developed for mean winds perpendicular to a straight bridge, when this theory is applied to a long and curved bridge, for any generic mean wind direction, i.e., for skew winds?
2. Can the current quasi-steady bridge buffeting theory for skew winds be improved?
3. How can this theory be applied to the case of the Bjørnafjord floating bridge, combining a numerical model and limited data from a physical bridge model subjected to skew winds in a wind tunnel?
4. In which way are skew wind effects important for the response of the Bjørnafjord floating bridge?
5. How can long-term wind conditions be predicted across a wide fjord, where no wind measurements are available?
6. For strong wind events, do the mean wind properties vary significantly across the fjord over a long-term period, and how does that wind inhomogeneity affect the floating bridge response to skew winds?

1.3. Thesis outline

The thesis is written as a collection of four papers, as listed in the Publications section. The natural progression of these papers allowed this thesis to be organized into a structured series of chapters. Chapter 3, Chapter 5 and Appendix B are reproduced from published papers. Chapter 6 corresponds to a submitted manuscript. Further details are given in the respective preface sections 3.1, 5.1 and B.1. The main sections of the thesis are briefly summarized below, and an outline sketch follows in Fig. 1.

Chapter 1. Introduction:

General context, goals and outline of the thesis.

Chapter 2. Normal wind buffeting theory:

Description of the traditional bridge buffeting theory, dealing with the case of mean wind normal (perpendicular) to a straight bridge girder. The theory is presented in a format that can be easily generalized into three-dimensional and generically oriented mean winds (skew winds). General non-linear expressions and their linearized forms are included.

Chapter 3. Skew wind buffeting theory:

This chapter revises, simplifies and generalizes the current bridge buffeting theory for skew winds. The proposed theory is divided into two parts: 1) when yaw- and inclination-angle-dependent aerodynamic coefficients are available, and 2) when only inclination-angle-dependent aerodynamic coefficients are available.

Chapter 4. The Bjørnafjord Bridge:

Description of the floating bridge solution studied and the respective wind site properties. The history of the Bjørnafjord crossing project, leading to the case study, is included in Appendix A. The simplified numerical model of the bridge that was developed during this research is introduced, including a description of all relevant properties, such as its local mass, damping and stiffness matrices and their assembling process into a global finite element model.

Chapter 5. Skew wind buffeting application:

This chapter uses the numerical model from Chapter 4 to apply the bridge buffeting theories previously available and those introduced in Chapter 3. Wind tunnel experiments, under skew winds, are presented. Challenges related to the data collection, application and extrapolation are carefully discussed, and solutions are proposed. The bridge buffeting response is estimated in the frequency- and time-domain. The response is assessed for different buffeting load models, different extrapolation methods, different components of the aerodynamic coefficients considered and different models of the quasi-steady self-excited forces.

Chapter 6. Long-term response to inhomogeneous skew wind:

The skew wind buffeting theory and application developed in chapters 3 and 5 is expanded to consider the inhomogeneity in the mean wind field, i.e., a wind field with mean properties varying across the fjord. The load models are updated to consider these space-varying properties. Synthetic long-term wind data is used to describe the mean wind conditions in the Bjørnafjord from the year 2000 to 2020. Estimation of the turbulence intensity across the fjord, for each mean wind direction, follows the data-driven procedure developed in Appendix B. The bridge static and buffeting response is estimated for 670 relevant strong wind events in the 20-year period and compared with response estimates based on the traditional wind homogeneity assumption.

Chapter 7. Conclusions:

The contributions of this research work are summarized, the conclusions presented, and suggestions for further work are provided.

Appendix A: History of the Bjørnafjord crossing project:

A summary of the development of the Bjørnafjord crossing project is provided and the various crossing solutions proposed throughout the project are described.

Appendix B: Inhomogeneous mean wind turbulence predictions:

This appendix describes the development and application of artificial neural networks to predict wind turbulence intensities at locations where wind data is unavailable, given only a previous training dataset of wind data and topography elsewhere, and the topography of the target location. A comparison with predictions based on available Eurocode formulations is included.

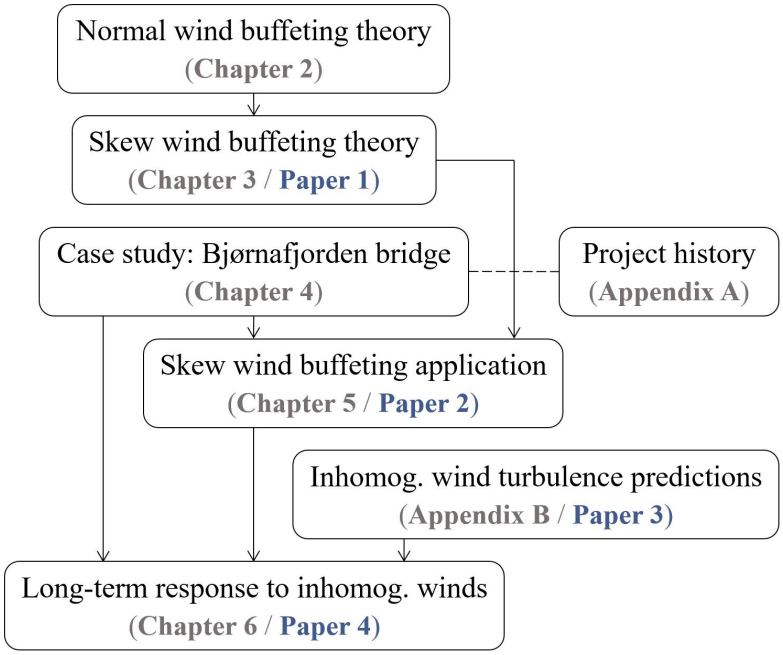

Fig. 1 – A sketch outlining the contents of the thesis.

2. Normal wind buffeting theory

2.1. Context

In the context of bridge aerodynamics and skew winds, normal wind denotes a mean wind that is perpendicular to the bridge girder (Zhu, 2002). In other words, the mean wind vector $\boldsymbol{U}$ lies in the $\boldsymbol{yz}$-plane that is normal to the local bridge girder element. In contrast, skew wind refers to wind with a mean vector $\boldsymbol{U}$ in a plane that is yawed relative to the $\boldsymbol{yz}$-plane by an angle β. Both normal and skew mean wind vectors are parallel to the local $\boldsymbol{xy}$-plane only if the mean inclination angle θ is zero. Topographic effects and sloping bridge girders can lead to non-zero mean inclination angles θ. These definitions are illustrated in Fig. 2. The terms normal and perpendicular are used here interchangeably, as well as the terms skew and yaw.

The traditional bridge buffeting theory, for normal winds, was pioneered by A.G. Davenport (Davenport, 1961a, 1962). In the following decades, numerous progresses were made. An extensive literature review can be found in Chapter 2 of the PhD thesis by L.D. Zhu (Zhu, 2002).

Relative to other references of the buffeting theory for normal winds, e.g. (Dyrbye and Hansen, 1997; Strømmen, 2010), the theory presented in this section opts to give a higher emphasis on the definition of coordinate systems, on maintaining vector representations of most wind-related variables, and on performing coordinate system transformations to arrive at the desired wind loads. On the one hand, this approach leads to a rather cumbersome notation system, but on the other hand, it enables a consistent and smooth transition from the normal wind theory to the skew wind buffeting theory presented in Chapter 3.

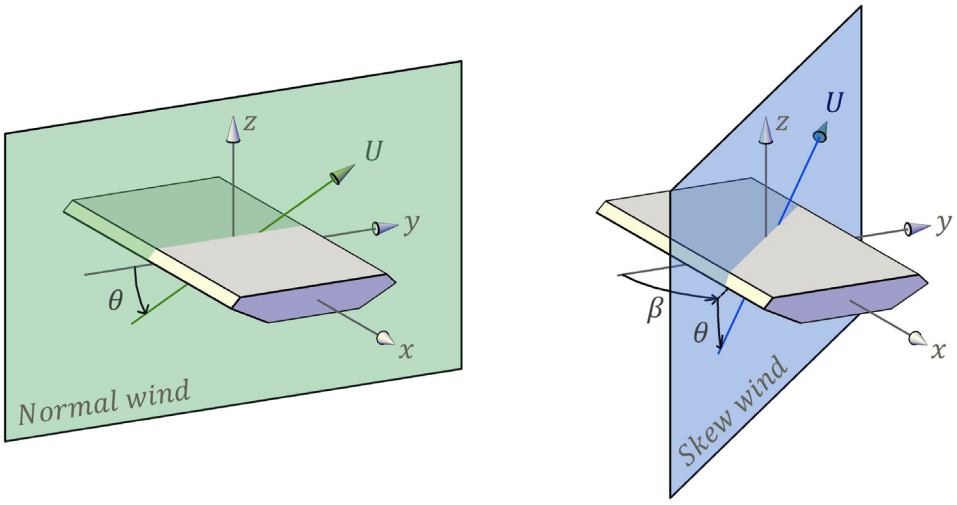

Normal wind		Skew wind	
Perpendicular & Horizontal	Perpendicular & Inclined	Yawed & Horizontal	Yawed & Inclined
$\beta = 0$ $\theta = 0$	$\beta = 0$ $\theta \neq 0$	$\beta \neq 0$ $\theta = 0$	$\beta \neq 0$ $\theta \neq 0$

Fig. 2 – Defining mean normal wind, skew wind, yaw angle β and inclination angle θ.

2.2. Mean wind forces acting on a bridge deck

In incompressible fluid dynamics, according to Bernoulli's equation, the dynamic pressure, q, given in eq. (1), is the total fluid pressure minus its static pressure, where ρ is the fluid density and U is the mean flow speed. This equation can also be deduced by imposing the conservation of fluid momentum in a steady flow and the conservation of mass of an incompressible fluid.

$$q = \frac{1}{2}\rho U^2 \tag{1}$$

In order to obtain the mean force F_{mean} exerted by the wind on a given structural element, this equation can be complemented with a force coefficient C that depends on the structural element shape, and a reference area A_{ref}. The area is often taken as the projected area of the object onto a plane that is normal to the wind. This leads to eq. (2).

$$F_{mean} = \frac{1}{2}\rho U^2 A_{ref} C \tag{2}$$

The force coefficient C changes if the relative angle between the wind and the object changes unless the object is cylindrical or spherical. In the context of normal wind ($\beta = 0$), the coefficient $C(\theta)$, also known as the aerodynamic coefficient, depends on the inclination angle θ, also denoted angle-of-attack.

Wind forces generated on a structural element are often not aligned with the wind direction or the structural axes. The wind force vector is then usually divided into its orthogonal components. The wind-aligned force component (often horizontal) is called drag, and the upward orthogonal component (often vertical) is called lift. Aerofoils, for instance, are designed to produce large lift forces. Besides these translational forces, the wind can also impose a rotational force, i.e., a moment, on the structure, if the point of action does not coincide with the centre of stiffness. These forces and moments can be represented by a vector, for convenience. For better consistency with the skew wind theory presented in Chapter 3, vectors are kept here with six degrees of freedom (DOF), where the first three DOF concern the three orthogonal axes in 3D space, e.g. representing translational forces, and the remaining three DOF concern rotational quantities around those same axes, e.g. representing moments. The letter r (for rotation) is used to distinguish the first three DOF (e.g. $\boldsymbol{x}$, $\boldsymbol{y}$, $\boldsymbol{z}$) from the last three DOF (e.g. $\boldsymbol{rx}$, $\boldsymbol{ry}$, $\boldsymbol{rz}$). All axes follow the right-hand rule.

First, the mean wind force vector $\boldsymbol{F_{mean,Ls}}$, represented in the local structural coordinate system Ls, is introduced in eq. (3). In order to obtain a convenient and fixed value for A_{ref}, the preferred convention in this thesis is to multiply the bridge girder length L by the girder cross-section width B, regardless of the force component. For the moments, L can be multiplied by B^2. This is expressed by the matrix $\boldsymbol{B}$. There are only three relevant response components when performing a typical normal wind analysis, namely the two DOF along the $\boldsymbol{y}$- and $\boldsymbol{z}$-axis, and the rotational DOF around the $\boldsymbol{x}$-axis, denoted $\boldsymbol{rx}$. The $\boldsymbol{x}$, $\boldsymbol{ry}$ and $\boldsymbol{rz}$ components are usually neglected. Vectors (and axes) and matrices are represented in bold.

$$\boldsymbol{F_{mean,Ls}} = L\frac{1}{2}\rho U^2 \boldsymbol{B C_{Ls}}(\theta) = L\frac{1}{2}\rho U^2 \begin{bmatrix} 0 & 0 & 0 & 0 & 0 & 0 \\ 0 & B & 0 & 0 & 0 & 0 \\ 0 & 0 & B & 0 & 0 & 0 \\ 0 & 0 & 0 & B^2 & 0 & 0 \\ 0 & 0 & 0 & 0 & 0 & 0 \\ 0 & 0 & 0 & 0 & 0 & 0 \end{bmatrix} \begin{bmatrix} 0 \\ C_y(\theta) \\ C_z(\theta) \\ C_{rx}(\theta) \\ 0 \\ 0 \end{bmatrix} \tag{3}$$

The aerodynamic coefficients, represented by the vector $\boldsymbol{C}$, are non-dimensional and are generally obtained in a wind tunnel facility by measuring the mean wind forces, $\boldsymbol{F_{mean}}$, on a reduced-scale model of the bridge girder. They can also be estimated using computational fluid dynamics (CFD), usually performed on a 2D cross-section of the bridge girder under normal wind.

Despite the convenient representation shown in eq. (3), it is more common to represent these forces in a mean wind coordinate system, i.e., a system whose first axis is aligned with the mean wind direction. Since, in this chapter, the wind is assumed homogeneous and normal to a straight bridge girder, this system can be denoted as either global mean wind Gw or local normal mean wind Lnw (both coordinate systems are described and later used in Chapter 3 for different purposes). The mean wind system denoted by Lnw is adopted here.

It is common to normalize the drag forces by the cross-section height H, since H contributes more directly to the drag than B, when θ is small. One disadvantage is that this leads to an inconsistent normalization across coefficients and force components which is often overlooked and may lead to mistakes (e.g. if these coefficients with different normalizations are assembled into a vector and linearly transformed to another coordinate system).

For a conventional Lnw representation of the wind forces, the wind-oriented coefficients $\boldsymbol{C_{Lnw}}(\theta)$ are used instead. These coefficients can be obtained from eq. (4). Since, by definition, these coefficients produce forces that are aligned with the axes of the Lnw system, a transformation matrix $\boldsymbol{T_{LnwLs}}$ is introduced to relate these to the forces in the Ls coordinate system.

$$\boldsymbol{T_{LnwLs}}\boldsymbol{F_{mean,Ls}} = \boldsymbol{F_{mean,Lnw}} = L\frac{1}{2}\rho U^2 \boldsymbol{B_{Lnw}}\boldsymbol{C_{Lnw}}(\theta) \tag{4}$$

Here, the $\boldsymbol{B}$ normalization is replaced by $\boldsymbol{B_{Lnw}} = diag(H, 0, B, 0, B^2, 0)$, assuming the drag is normalized by H, the lift by B and the moment by B^2. In the case of normal wind, $\boldsymbol{C_{Lnw}}(\theta) = [C_D(\theta) \quad 0 \quad C_L(\theta) \quad 0 \quad C_M(\theta) \quad 0]^T$, where D, L and M stand for drag, lift and moment, respectively. Since this system follows the right-hand rule, the moment M is positive when it forces the girder's windward edge up. The transformation matrix from the Ls system to the Lnw system, $\boldsymbol{T_{LnwLs}}$, can be deduced from intuitive chained rotations, given three elemental rotation matrices, $\boldsymbol{R_x}$, $\boldsymbol{R_y}$ and $\boldsymbol{R_z}$. This is described in more detail in Section 3.4. $\boldsymbol{T_{LnwLs}}$ can then be expressed from eqs. (5) to (7). It should be noted that $\boldsymbol{T_{LnwLs}} = \boldsymbol{T_{LsLnw}}^{-1} = \boldsymbol{T_{LsLnw}}^{T}$.

$$\boldsymbol{T}_{\boldsymbol{LnwLs}}^{(6\times6)} = \begin{bmatrix} \boldsymbol{T}_{\boldsymbol{LnwLs}}^{(3\times3)} & \mathbf{0} \\ \mathbf{0} & \boldsymbol{T}_{\boldsymbol{LnwLs}}^{(3\times3)} \end{bmatrix} \tag{5}$$

$$\mathbf{0} = \begin{bmatrix} 0 & 0 & 0 \\ 0 & 0 & 0 \\ 0 & 0 & 0 \end{bmatrix} \tag{6}$$

$$\boldsymbol{T}_{\boldsymbol{LnwLs}}^{(3\times3)} = \left(\boldsymbol{R}_{\boldsymbol{z}}(\pi/2)\, \boldsymbol{R}_{\boldsymbol{y}}(-\theta)\right)^{\boldsymbol{T}} = \begin{bmatrix} 0 & \cos\theta & \sin\theta \\ -1 & 0 & 0 \\ 0 & -\sin\theta & \cos\theta \end{bmatrix} \tag{7}$$

In Fig. 3, the $\boldsymbol{D}$ and $\boldsymbol{L}$ axes of the Lnw system are illustrated together with the mean inclination angle θ and the mean wind speed vector $\boldsymbol{U}$ that is, by definition, parallel to the D axis.

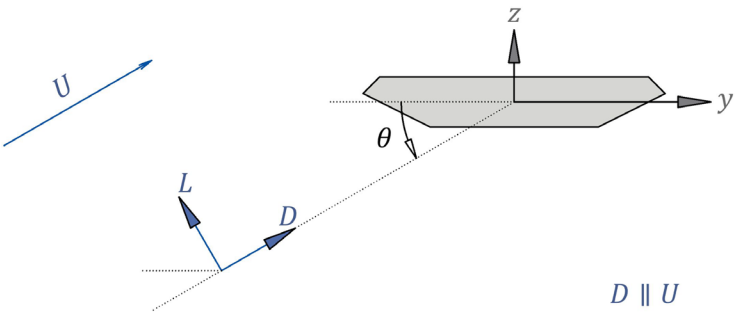

Fig. 3 – Representation of the mean drag ($\boldsymbol{D}$) and lift ($\boldsymbol{L}$) axes of the Lnw system, the mean inclination angle θ and the mean wind speed vector $\boldsymbol{U}$ ($\boldsymbol{D}$ is parallel to $\boldsymbol{U}$).

2.3. Fluctuating wind forces due to turbulence

2.3.1. General formulation

In wind engineering, the wind velocity is typically separated into a time-invariant part, i.e., the mean, and a zero-mean fluctuating part, i.e., turbulence. Near the Earth's surface (i.e., in the planetary boundary layer), the wind is turbulent. Structures are thus subjected to fluctuating wind velocities that can greatly surpass the mean wind speed. The term "aerodynamic loads" is used here to denote loads that are caused by the instantaneous turbulent wind velocity $\widetilde{U}$. The single tilde accent is used here to denote "instantaneous" quantities dependent on turbulence, which is time dependent.

In the normal wind case, using the Lnw coordinate system, the instantaneous wind speed vector $\widetilde{\boldsymbol{U}}$ can be defined from its mean component U, its along-wind turbulence component u and its orthogonal and upward turbulence component w, according to eq. (8). The instantaneous wind speed $\widetilde{U}$ is obtained in eq. (9), adopting the traditional assumption that the remaining orthogonal horizontal turbulence component, v, (parallel to the bridge axis) can be neglected in normal wind buffeting analyses.

$$\widetilde{\boldsymbol{U}}_{\boldsymbol{Lnw}} = \begin{bmatrix} \widetilde{U}_D \\ 0 \\ \widetilde{U}_L \end{bmatrix} = \begin{bmatrix} U+u \\ 0 \\ w \end{bmatrix} \tag{8}$$

$$\widetilde{U} = \left\|\widetilde{\boldsymbol{U}}\right\| = \sqrt{(U+u)^2 + w^2} \tag{9}$$

By adapting eq. (3) to the turbulent instantaneous wind speed $\widetilde{U}$, the aerodynamic forces $\widetilde{\boldsymbol{F}}_{\boldsymbol{ad}}$, expressed in the Ls coordinate system, can be simply obtained by eq. (10).

$$\widetilde{\boldsymbol{F}}_{\boldsymbol{ad,Ls}} = L\frac{1}{2}\rho\widetilde{U}^2\boldsymbol{B}\widetilde{\boldsymbol{C}}_{\boldsymbol{Ls}}(\tilde{\theta}) \tag{10}$$

Here, the vector $\widetilde{\boldsymbol{C}}_{\boldsymbol{Ls}}(\tilde{\theta})$ is obtained just like $\boldsymbol{C}_{\boldsymbol{Ls}}(\theta)$, but the mean inclination angle θ is replaced by the instantaneous inclination angle $\tilde{\theta}$, which is varying in time due to turbulence, according to eq. (11).

$$\tilde{\theta} = \arcsin\left(\widetilde{U}_z/\widetilde{U}\right) \tag{11}$$

$\widetilde{U}_z$ is the projection of the instantaneous wind vector $\widetilde{U}$ onto the $\boldsymbol{z}$-axis and can be extracted from eq. (12), where the instantaneous wind is expressed as a vector, both in the Ls and in the Lnw coordinate systems. Transformation matrices, $\boldsymbol{T}^{(6\times6)}$ and $\boldsymbol{T}^{(3\times3)}$, for 6 and 3 DOF formats, are used according to their context, and the superscripts $^{(3\times3)}$ and $^{(6\times6)}$ are omitted hereafter for simplicity.

$$\widetilde{\boldsymbol{U}}_{\boldsymbol{Ls}} = \begin{bmatrix} 0 \\ \widetilde{U}_y \\ \widetilde{U}_z \end{bmatrix} = \boldsymbol{T}_{\boldsymbol{LsLnw}}\widetilde{\boldsymbol{U}}_{\boldsymbol{Lnw}} = \boldsymbol{T}_{\boldsymbol{LnwLs}}^{\boldsymbol{T}}\widetilde{\boldsymbol{U}}_{\boldsymbol{Lnw}} = \begin{bmatrix} 0 & -1 & 0 \\ \cos\theta & 0 & -\sin\theta \\ \sin\theta & 0 & \cos\theta \end{bmatrix}\begin{bmatrix} U+u \\ 0 \\ w \end{bmatrix} \tag{12}$$

Again, however, it is common to represent the wind loads as a function of aerodynamic coefficients previously estimated in a coordinate system that is solidary with the wind. For this, the previously presented aerodynamic coefficients that were aligned with the mean wind, $\boldsymbol{C}_{\boldsymbol{Lnw}}$, should now be used again, but as a

function of the instantaneous inclination angle, $\tilde{\theta}$, instead of the mean inclination angle θ. These aerodynamic coefficients are represented as $\widetilde{\boldsymbol{C}}_{\widetilde{Lnw}}(\tilde{\theta}) = \left[\tilde{C}_{\tilde{D}}(\tilde{\theta}) \quad 0 \quad \tilde{C}_{\tilde{L}}(\tilde{\theta}) \quad 0 \quad \tilde{C}_{\tilde{M}}(\tilde{\theta}) \quad 0\right]^T$. Then, the instantaneous-wind-aligned forces associated with these coefficients will be associated with a new coordinate system whose first axis is aligned with the turbulent wind vector, $\widetilde{\boldsymbol{U}}$, instead of $\boldsymbol{U}$. The new coordinate system, denoted $\widetilde{Lnw}$, is introduced, where the instantaneous drag axis $\widetilde{\boldsymbol{D}}$ is parallel to $\widetilde{\boldsymbol{U}}$ and where the instantaneous lift axis $\widetilde{\boldsymbol{L}}$ is orthogonal to it. These quantities are illustrated in Fig. 4.

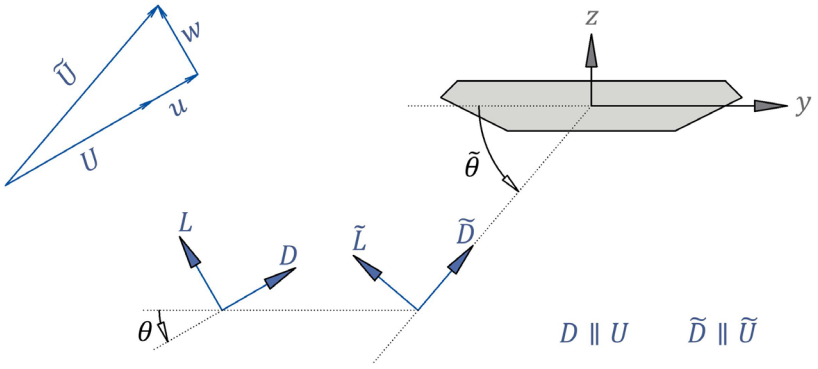

Fig. 4 – Introduction of the instantaneous drag ($\widetilde{\boldsymbol{D}}$) and lift ($\widetilde{\boldsymbol{L}}$) axes of the $\widetilde{Lnw}$ system, instantaneous inclination angle $\tilde{\theta}$ and instantaneous wind speed vector $\widetilde{\boldsymbol{U}}$ ($\widetilde{\boldsymbol{D}}$ is parallel to $\widetilde{\boldsymbol{U}}$).

Since the $\widetilde{Lnw}$ system changes with turbulence, which varies with each time step, it is then necessary to express the resulting aerodynamic forces in a time-invariant coordinate system instead, such as the Lnw or the Ls systems. The Ls system is used again to represent these forces in eq. (13), but as a function of $\widetilde{\boldsymbol{C}}_{\widetilde{Lnw}}(\tilde{\theta})$. For this, the new transformation matrix, $\boldsymbol{T}_{\boldsymbol{Lnw}\widetilde{\boldsymbol{Lnw}}}$, from the $\widetilde{Lnw}$ to the Lnw system, is introduced in eqs. (14) to (16), in a 3 DOF format for compactness.

$$\widetilde{\boldsymbol{F}}_{\boldsymbol{ad,Ls}} = \boldsymbol{T}_{\boldsymbol{Ls}\widetilde{\boldsymbol{Lnw}}}\, L\frac{1}{2}\rho\tilde{U}^2\boldsymbol{B}_{\boldsymbol{Lnw}}\widetilde{\boldsymbol{C}}_{\widetilde{\boldsymbol{Lnw}}}(\tilde{\theta}) \tag{13}$$

$$\boldsymbol{T}_{\boldsymbol{Ls}\widetilde{\boldsymbol{Lnw}}} = \boldsymbol{T}_{\boldsymbol{LsLnw}}\boldsymbol{T}_{\boldsymbol{Lnw}\widetilde{\boldsymbol{Lnw}}} \tag{14}$$

$$\boldsymbol{T}_{\boldsymbol{Lnw}\widetilde{\boldsymbol{Lnw}}} = \left(\boldsymbol{R}_{\boldsymbol{y}}(\tilde{\theta})\,\boldsymbol{R}_{\boldsymbol{y}}(-\theta)\right)^{\boldsymbol{T}} = \begin{bmatrix} \cos\widetilde{\Delta\theta} & 0 & -\sin\widetilde{\Delta\theta} \\ 0 & 1 & 0 \\ \sin\widetilde{\Delta\theta} & 0 & \cos\widetilde{\Delta\theta} \end{bmatrix} \tag{15}$$

$$\widetilde{\Delta\theta} = \tilde{\theta} - \theta \tag{16}$$

The term "buffeting loads" can also be used when focusing on the turbulence effects only, without the mean wind effects. If only the buffeting forces $\widetilde{\boldsymbol{F}}_{\boldsymbol{b}}$ are of interest, the mean wind forces $\boldsymbol{F}_{\boldsymbol{mean}}$ can be simply subtracted from the aerodynamic forces $\widetilde{\boldsymbol{F}}_{\boldsymbol{ad}}$, in a consistent coordinate system (e.g. the Ls system), following eq. (17).

$$\widetilde{\boldsymbol{F}}_{\boldsymbol{b,Ls}} = \widetilde{\boldsymbol{F}}_{\boldsymbol{ad,Ls}} - \boldsymbol{F}_{\boldsymbol{mean,Ls}} \tag{17}$$

It is here assumed that the instantaneous aerodynamic coefficients, concerning each single time instant in a turbulent flow, are equivalent to the mean aerodynamic coefficients in a smooth (or turbulent) flow with an equivalent constant (or mean) inclination angle. This assumption and buffeting formulation neglect: a) the effects of reducing a cross-section to a discrete point in space and considering only the instantaneous wind at that point, b) the changes in spanwise flow coherence due to the effect of the bridge on the surrounding flow, c) the effects from vortex shedding, and d) the effects from changes in Reynolds number. To improve this so-called quasi-steady assumption and to address some of these effects, aerodynamic admittance functions, described in Section 2.3.3, can be introduced.

2.3.2. Linear formulation

In this section, all relevant quantities that are dependent on turbulence are linearized. A first-order Taylor expansion is performed on these quantities, with respect to u and w, which are assumed small compared to U. These linearizations facilitate linear analyses of the bridge buffeting response (e.g. typical frequency-domain analyses). These linearized quantities are shown in eqs. (18) to (20). The instantaneous aerodynamic coefficients $\widetilde{\boldsymbol{C}}_{\widetilde{\boldsymbol{Lnw}}}(\tilde{\theta})$ can also be linearized at θ, with respect to the small angle variation $\widetilde{\Delta\theta}$, according to eq. (21), where $\boldsymbol{C}' = \partial\boldsymbol{C}(\theta)/\partial\theta$. The linearized vector of the buffeting forces follows in eq. (22), where $\chi_{i,j}$ represents an aerodynamic admittance function, associated with the aerodynamic coefficient i and the turbulence component j, which is further described in Section 2.3.3 and is often used in the frequency-domain. The C_D, C_L and C_M are still dependent on θ, but θ is omitted in eq. (22) for compactness.

$$\widetilde{U}^2 = U^2 + 2Uu + u^2 + w^2 \approx U^2 + 2Uu \tag{18}$$

$$\widetilde{\Delta\theta} \approx w/U \tag{19}$$

$$\boldsymbol{T}_{\boldsymbol{Lnw}\widetilde{\boldsymbol{Lnw}}} \approx \begin{bmatrix} 1 & 0 & -w/U \\ 0 & 1 & 0 \\ w/U & 0 & 1 \end{bmatrix} \tag{20}$$

$$\widetilde{\boldsymbol{C}_{\widetilde{\boldsymbol{Lnw}}}}(\tilde{\theta}) \approx \boldsymbol{C_{Lnw}}(\theta) + \boldsymbol{C'_{Lnw}}(\theta)\,\widetilde{\Delta\theta} \tag{21}$$

$$\widetilde{\boldsymbol{F}}_{\boldsymbol{b,Ls}} = \boldsymbol{T_{LsLnw}}\,\widetilde{\boldsymbol{F}}_{\boldsymbol{b,Lnw}} \approx \boldsymbol{T_{LsLnw}}\,L\frac{1}{2}\rho U \begin{bmatrix} 2HC_D\,\chi_{D,u} & (HC'_D - BC_L)\chi_{D,w} \\ 0 & 0 \\ 2BC_L\,\chi_{L,u} & (BC'_L + HC_D)\chi_{L,w} \\ 0 & 0 \\ 2B^2C_M\,\chi_{M,u} & B^2C'_M\,\chi_{M,w} \\ 0 & 0 \end{bmatrix} \begin{bmatrix} u \\ w \end{bmatrix} \tag{22}$$

2.3.3. Aerodynamic admittance functions

The expressions for the fluctuating wind forces due to turbulence depend on aerodynamic coefficients that are typically obtained from time-averaged forces, measured in a wind tunnel. However, time-averaged coefficients, alone, may not be sufficient to accurately estimate instantaneous turbulent wind forces.

A Fourier decomposition of the wind turbulence reveals significant energy across many different frequencies. Assuming the superposition principle, different frequency components of the wind turbulence, with different wavelengths, may have different effects on the pressures around a cross-section of the bridge. In particular, frequency components with (finite) wavelengths that are similar or smaller than the dimensions of the cross-section are, by definition, not uniform in space. This lack of instantaneous wind speed correlation along the perimeter of the cross-section, estimated without the presence of the bridge girder, affects the resulting buffeting forces. For example, very short wavelengths often produce localized pressures that are negatively correlated and cancel each other to some extent when integrated along the perimeter of the cross-section at each timestep, thus reducing the total cross-sectional buffeting forces.

When the presence of the bridge girder is considered, the complex fluid-structure interaction, both in the normal plane and in the spanwise direction, introduces changes and non-linearities in the fluid. The commonly assumed strip theory considers that each strip, i.e., each cross-section of the bridge girder, can be considered separately in the buffeting load model. This assumes that the presence of the bridge girder does not affect the coherence of the incoming flow. So-called signature turbulence, induced by the bridge, may then lead to inaccuracies in the quasi-steady buffeting response predictions (Cheynet et al., 2019; Zhu et al., 2009; Zhu and Xu, 2014). In fact, studies have shown that buffeting forces can have a significantly higher spanwise correlation than the associated wind turbulence in undisturbed flow, e.g. (Daniotti, 2022; Haan Jr et al., 2016; Jakobsen, 1997; Larose, 1997).

In order to consider these aspects and to improve the quasi-steady buffeting load model, aerodynamic admittance functions (AAF), $\chi_{i,j}$, associated with the DOF i and the turbulence component j, as shown in eq. (22), can be introduced. These functions can be obtained in different ways. Theoretical functions for a thin airfoil can be found in (Sears, 1941). Alternative approximate expressions have been suggested in, e.g. (Liepmann, 1952). Four experimental methods to obtain these functions were explored in (Jakobsen, 1995), which require a Fourier transform on both sides of eq. (22), together with one of the following:

a) A comparison of the measured power spectral densities (PSD) of the local forces, concerning a single cross-section of the girder, with the expected force PSD obtained from the buffeting theory, using the turbulence PSD. The difference is then assumed to be explained by the AAF.

b) A comparison of the measured PSD of the global forces, concerning the entire girder section model, with those expected from the buffeting theory, using the PSD of the turbulence and the spanwise correlation of the undisturbed turbulence.

c) Same as b), but where the spanwise correlation of the forces is measured and used instead.

d) Same as b), but where the global forces are estimated from the buffeting response of a dynamic model where motion-dependent forces are naturally included.

Pressure tap measurements are required around one cross-section in method a), and around multiple cross-sections in method c). Methods b) and d) require simultaneous anemometric measurements to estimate the spanwise correlation of the incoming wind turbulence. A lower aerodynamic admittance is obtained with methods a) and c), which should then be used together with a consistent buffeting model that includes the bridge-induced increase in turbulence coherence, as also proposed in, e.g. (Larose and Mann, 1998).

For convenience, one common assumption is that AAF that concern the same DOF are equally valued (e.g. $\chi_{D,u} = \chi_{D,w}$) (Daniotti, 2022; Larose, 1997; Zhu and Xu, 2014). Li et al. (Li et al., 2018) give a revision of other methods of estimating AAF, resulting in a distinction between three different types of AAF. They further describe the need for consistency between the adopted buffeting load model and AAF. The identification of six-component AAF and a verification with an aeroelastic model can be found in (Zhu et al., 2018).

2.4. Fluctuating wind forces due to turbulence and structural motions

2.4.1. General formulation

The wind loading is affected by the structural motion, as the airflow has to adapt to the bridge deck as a moving obstacle. The wind load is governed by the relative velocity between the wind and the vibrating girder, and by the relative angle between the girder and the wind, which affects the aerodynamic coefficients.

The girder motions are divided into two types, displacements, $\boldsymbol{\Delta}$, and velocities, $\dot{\boldsymbol{\Delta}}$. These can be represented in the Ls system or, more conveniently, in the Lnw system:

a) Displacements:

- $\boldsymbol{\Delta_{Ls}} = \left[\Delta_x, \Delta_y, \Delta_z, \Delta_{rx}, \Delta_{ry}, \Delta_{rz}\right]^T$
- $\boldsymbol{\Delta_{Lnw}} = [\Delta_D, \Delta_A, \Delta_L, \Delta_{rD}, \Delta_M, \Delta_{rL}]^T = \boldsymbol{T_{LnwLs}}\, \boldsymbol{\Delta_{Ls}}$

b) Velocities:

- $\dot{\boldsymbol{\Delta}}_{\boldsymbol{Ls}} = \left[\dot{\Delta}_x, \dot{\Delta}_y, \dot{\Delta}_z, \dot{\Delta}_{rx}, \dot{\Delta}_{ry}, \dot{\Delta}_{rz}\right]^T$
- $\dot{\boldsymbol{\Delta}}_{\boldsymbol{Lnw}} = \left[\dot{\Delta}_D, \dot{\Delta}_A, \dot{\Delta}_L, \dot{\Delta}_{rD}, \dot{\Delta}_M, \dot{\Delta}_{rL}\right]^T = \boldsymbol{T_{LnwLs}}\, \dot{\boldsymbol{\Delta}}_{\boldsymbol{Ls}}$

However, in a normal wind analysis, only one rotational component of the displacements and two translational velocity components are of interest, namely Δ_{rx}, $\dot{\Delta}_y$ and $\dot{\Delta}_z$, or, alternatively, Δ_M, $\dot{\Delta}_D$ and $\dot{\Delta}_L$.

First, the relative (motion-dependent) wind speed $\widetilde{\widetilde{U}}$, and the relative turbulence components $\tilde{\tilde{u}}$ and $\widetilde{\widetilde{w}}$ are introduced in eqs. (23) to (25). The double-tilde accent is used to indicate a dependence on the structural motions, in addition to the dependence on turbulence (if applicable).

$$\widetilde{\widetilde{U}} = \sqrt{\left(U + \tilde{\tilde{u}}\right)^2 + \widetilde{\widetilde{w}}^2} \tag{23}$$

$$\tilde{\tilde{u}} = u - \dot{\Delta}_D \tag{24}$$

$$\widetilde{\widetilde{w}} = w - \dot{\Delta}_L \tag{25}$$

The relative inclination angle $\tilde{\tilde{\theta}}$, and the relative wind speed vector $\tilde{\tilde{\boldsymbol{U}}}$ are given in eqs. (26) to (29), where a new local dynamic structural coordinate system, solidary with the rotating girder, is introduced as $\widetilde{\widetilde{Ls}}\ \left(\tilde{\tilde{\boldsymbol{x}}}, \tilde{\tilde{\boldsymbol{y}}}, \tilde{\tilde{\boldsymbol{z}}}, \tilde{\tilde{\boldsymbol{rx}}}, \tilde{\tilde{\boldsymbol{ry}}}, \tilde{\tilde{\boldsymbol{rz}}}\right)$, for convenience.

$$\tilde{\tilde{\theta}} = \arcsin\left(\tilde{\tilde{U}}_{\tilde{\tilde{z}}}/\tilde{\tilde{U}}\right) \tag{26}$$

$$\tilde{\tilde{\boldsymbol{U}}}_{\widetilde{\widetilde{Ls}}} = \begin{bmatrix} 0 \\ \tilde{\tilde{U}}_{\tilde{\tilde{y}}} \\ \tilde{\tilde{U}}_{\tilde{\tilde{z}}} \end{bmatrix} = \boldsymbol{T}_{\widetilde{\widetilde{Ls}}\boldsymbol{Ls}}\boldsymbol{T}_{\boldsymbol{LsLnw}}\tilde{\tilde{\boldsymbol{U}}}_{\boldsymbol{Lnw}} = \boldsymbol{T}_{\widetilde{\widetilde{Ls}}\boldsymbol{Ls}}\boldsymbol{T}_{\boldsymbol{LsLnw}}\begin{bmatrix} U+\tilde{\tilde{u}} \\ 0 \\ \tilde{\tilde{w}} \end{bmatrix} \tag{27}$$

$$\boldsymbol{T}_{\widetilde{\widetilde{Ls}}\boldsymbol{Ls}} = \left(\boldsymbol{R}_{\boldsymbol{x}}(\Delta_{rx})\right)^{\boldsymbol{T}} = \begin{bmatrix} 1 & 0 & 0 \\ 0 & \cos\Delta_{rx} & \sin\Delta_{rx} \\ 0 & -\sin\Delta_{rx} & \cos\Delta_{rx} \end{bmatrix} \tag{28}$$

$$\Delta_{rx} = -\Delta_M \tag{29}$$

With a similar reasoning to that in the introduction of the $\widetilde{Lnw}$ system, a new local instantaneous normal and relative wind coordinate system $\widetilde{\widetilde{Lnw}}$ is introduced, where the first axis, $\tilde{\tilde{\boldsymbol{D}}}$, is aligned with $\tilde{\tilde{\boldsymbol{U}}}$. This is the new system in which the wind-aligned aerodynamic coefficients are automatically represented when the inclination angle that they depend on, θ (or $\tilde{\theta}$), is replaced with its relative counterpart $\tilde{\tilde{\theta}}$. The aerodynamic coefficients in the $\widetilde{\widetilde{Lnw}}$ system are $\tilde{\tilde{\boldsymbol{C}}}_{\widetilde{\widetilde{\boldsymbol{Lnw}}}}\left(\tilde{\tilde{\theta}}\right) = \left[\tilde{\tilde{C}}_{\tilde{\tilde{D}}}\left(\tilde{\tilde{\theta}}\right) \quad 0 \quad \tilde{\tilde{C}}_{\tilde{\tilde{L}}}\left(\tilde{\tilde{\theta}}\right) \quad 0 \quad \tilde{\tilde{C}}_{\tilde{\tilde{M}}}\left(\tilde{\tilde{\theta}}\right) \quad 0\right]^{T}$. The $\tilde{\tilde{\boldsymbol{D}}}$ and $\tilde{\tilde{\boldsymbol{L}}}$ axes of the $\widetilde{\widetilde{Lnw}}$ system, the $\tilde{\tilde{\theta}}$ angle and the relevant girder motions are illustrated in Fig. 5.

By adapting eq. (13), the aerodynamic forces due to both turbulence and bridge motions, $\tilde{\tilde{\boldsymbol{F}}}_{\boldsymbol{ad}}$, are expressed in the time-invariant Ls coordinate system as a function of the instantaneous-relative-wind-aligned aerodynamic coefficients, and can be obtained according to eqs. (30) to (32).

$$\tilde{\tilde{\boldsymbol{F}}}_{\boldsymbol{ad,Ls}} = \boldsymbol{T}_{\boldsymbol{Ls}\widetilde{\widetilde{\boldsymbol{Lnw}}}}\, L\frac{1}{2}\rho\tilde{\tilde{U}}^2\boldsymbol{B}_{\boldsymbol{Lnw}}\tilde{\tilde{\boldsymbol{C}}}_{\widetilde{\widetilde{\boldsymbol{Lnw}}}}\left(\tilde{\tilde{\theta}}\right) \tag{30}$$

$$\boldsymbol{T}_{\boldsymbol{Ls}\widetilde{\widetilde{\boldsymbol{Lnw}}}} = \boldsymbol{T}_{\boldsymbol{Ls}\widetilde{\widetilde{\boldsymbol{Ls}}}}\boldsymbol{T}_{\widetilde{\widetilde{\boldsymbol{Ls}}}\widetilde{\widetilde{\boldsymbol{Lnw}}}} = \boldsymbol{T}_{\widetilde{\widetilde{\boldsymbol{Ls}}}\boldsymbol{Ls}}^{\ \boldsymbol{T}}\boldsymbol{T}_{\widetilde{\widetilde{\boldsymbol{Ls}}}\widetilde{\widetilde{\boldsymbol{Lnw}}}} \tag{31}$$

$$\boldsymbol{T}_{\widetilde{\widetilde{\boldsymbol{Ls}}}\widetilde{\widetilde{\boldsymbol{Lnw}}}} = \left(\boldsymbol{R}_{\boldsymbol{y}}\left(\tilde{\tilde{\theta}}\right)\boldsymbol{R}_{\boldsymbol{z}}(-\pi/2)\right)^{\boldsymbol{T}} = \begin{bmatrix} 0 & -1 & 0 \\ \cos\tilde{\tilde{\theta}} & 0 & -\sin\tilde{\tilde{\theta}} \\ \sin\tilde{\tilde{\theta}} & 0 & \cos\tilde{\tilde{\theta}} \end{bmatrix} \tag{32}$$

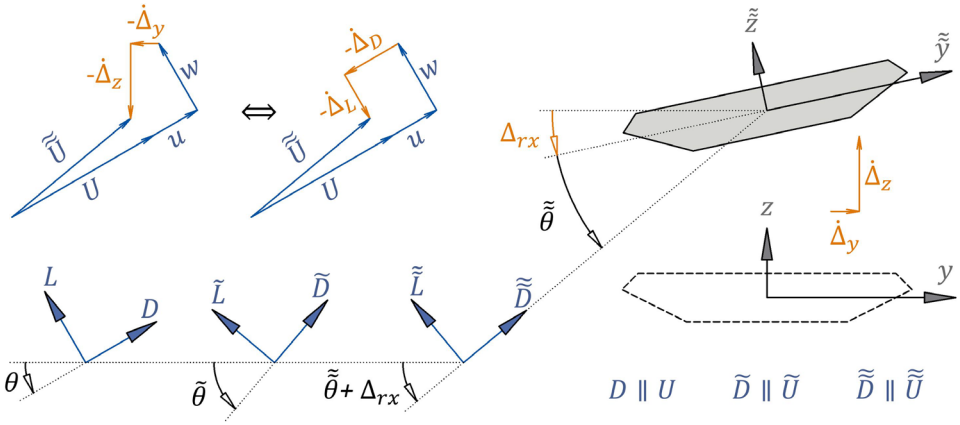

Fig. 5 – Introduction of the local instantaneous relative drag ($\tilde{\tilde{\boldsymbol{D}}}$) and lift ($\tilde{\tilde{\boldsymbol{L}}}$) of the $\widetilde{\widetilde{Lnw}}$ system, the local instantaneous relative inclination angle $\tilde{\tilde{\theta}}$ and the local instantaneous relative wind speed vector $\tilde{\tilde{\boldsymbol{U}}}$ ($\tilde{\tilde{\boldsymbol{D}}}$ is parallel to $\tilde{\tilde{\boldsymbol{U}}}$).

The turbulence- and motion-dependent buffeting forces $\tilde{\tilde{\boldsymbol{F}}}_{\boldsymbol{b}}$ can be obtained by subtracting the mean wind forces $\boldsymbol{F}_{\boldsymbol{mean}}$ from the aerodynamic forces $\tilde{\tilde{\boldsymbol{F}}}_{\boldsymbol{ad}}$, following eq. (33).

$$\tilde{\tilde{\boldsymbol{F}}}_{\boldsymbol{b,Ls}} = \tilde{\tilde{\boldsymbol{F}}}_{\boldsymbol{ad,Ls}} - \boldsymbol{F}_{\boldsymbol{mean,Ls}} \tag{33}$$

The quasi-steady assumption described in Section 2.3 is also adopted here. Additionally, it assumes that measuring the instantaneous relative aerodynamic forces on a vibrating girder, at each time instant, is equivalent to measuring the mean aerodynamic forces on a static girder under an equivalent and constant wind speed and inclination angle (and equivalent to measuring time-averaged forces on a static girder under a turbulent wind with equivalent mean wind speed and inclination angle). Aerodynamic derivatives, described in Section 2.4.3, can be used to deal with known frequency dependencies of these aerodynamic forces.

2.4.2. Linear formulation

The linearizations presented in Section 2.3.2, with respect to u and w, can be expanded in this section to also include the structural motions. In the Lnw system, the rotational displacement Δ_M can be assumed to follow the small angle approximation. The two girder velocity components $\dot{\Delta}_D$ and $\dot{\Delta}_L$ can be assumed small compared to U. The resulting first-order Taylor expansions of the relevant turbulence- and motion-dependent quantities are presented in eqs. (34) to (39).

$$\widetilde{\widetilde{U}}^2 = U^2 + 2U\tilde{u} + \tilde{u}^2 + \widetilde{\widetilde{w}}^2 \approx U^2 + 2U\tilde{u} \tag{34}$$

$$\tilde{\theta} = \theta + \widetilde{\widetilde{\Delta\theta}} \approx \theta + \frac{\widetilde{\widetilde{w}}}{U} + \Delta_M \tag{35}$$

$$\boldsymbol{T}_{\boldsymbol{Ls}\widetilde{\widetilde{\boldsymbol{Lnw}}}} = \boldsymbol{T}_{\boldsymbol{LsLnw}}\boldsymbol{T}_{\boldsymbol{Lnw}\widetilde{\widetilde{\boldsymbol{Lnw}}}} = \boldsymbol{T}_{\boldsymbol{LsLnw}}\begin{bmatrix} 1 & 0 & -\widetilde{\widetilde{w}}/U \\ 0 & 1 & 0 \\ \widetilde{\widetilde{w}}/U & 0 & 1 \end{bmatrix} \tag{36}$$

$$\widetilde{\widetilde{\boldsymbol{C}}}_{\widetilde{\widetilde{\boldsymbol{Lnw}}}}\left(\tilde{\theta}\right) \approx \boldsymbol{C}_{\boldsymbol{Lnw}}(\theta) + \boldsymbol{C}'_{\boldsymbol{Lnw}}(\theta)\,\widetilde{\widetilde{\Delta\theta}} \tag{37}$$

$$\widetilde{\widetilde{\boldsymbol{F}}}_{\boldsymbol{b,Ls}} = \boldsymbol{T}_{\boldsymbol{LsLnw}}\,\widetilde{\widetilde{\boldsymbol{F}}}_{\boldsymbol{b,Lnw}} \tag{38}$$

$$\widetilde{\widetilde{\boldsymbol{F}}}_{\boldsymbol{b,Lnw}} \approx \widetilde{\boldsymbol{F}}_{\boldsymbol{b,Lnw}} + L\frac{1}{2}\rho U^2\begin{bmatrix} HC'_D \\ 0 \\ BC'_L \\ 0 \\ B^2C'_M \\ 0 \end{bmatrix}\Delta_M - L\frac{1}{2}\rho U\begin{bmatrix} 2HC_D & HC'_D - BC_L \\ 0 & 0 \\ 2BC_L & BC'_L + HC_D \\ 0 & 0 \\ 2B^2C_M & B^2C'_M \\ 0 & 0 \end{bmatrix}\begin{bmatrix} \dot{\Delta}_D \\ \dot{\Delta}_L \end{bmatrix} \tag{39}$$

2.4.3. Aerodynamic derivatives

With the flutter-induced collapse of the original Tacoma Narrows Bridge in 1940, the aeroelastic instability of bridges became a serious study field. Aerodynamic effects from the interaction between a turbulent wind flow and a motionless bridge deck were covered in Section 2.3.3 using aerodynamic admittance functions. However, additional fluid-structure interaction effects arise when the bridge deck is set in motion, which are relevant for the bridge response predictions. Aerodynamic derivatives are introduced in the buffeting theory to deal with these additional effects. Analogous to the aerodynamic admittance functions that are dependent on the frequencies of the incoming wind turbulence, aerodynamic derivatives can also be made dependent on the frequencies of the bridge motions.

Quasi-steady frequency-independent aerodynamic derivatives were introduced in eq. (39), where three motion-dependent forces (obtained from $\widetilde{\widetilde{\boldsymbol{F}}}_{\boldsymbol{b,Lnw}} - \widetilde{\boldsymbol{F}}_{\boldsymbol{b,Lnw}}$) are presented as functions of Δ_M, $\dot{\Delta}_D$ and $\dot{\Delta}_L$. On the left side of the equation of motion of a mass-spring-damper system (shown in eq. (170)), the structural stiffness ($\boldsymbol{K_S}$) and damping ($\boldsymbol{C_S}$) matrices are also multiplied by these motions ($\boldsymbol{\Delta}$ and $\dot{\boldsymbol{\Delta}}$). It is then common to gather the motion-dependent forces on the same left side of the equation, in the form of aerodynamic stiffness ($\boldsymbol{K_{AE}}$) and aerodynamic damping ($\boldsymbol{C_{AE}}$), which can then be added to the respective structural matrices (eqs. (171)

and (172)). Scanlan and Tomko's (Scanlan and Tomko, 1971) formulation of these self-excited (motion-dependent) forces is widely used in bridge engineering. This is presented in an equivalent but alternative format in Chapter 3, eqs. (104) to (108), in the context of skew winds and for 6 DOF.

Unsteady frequency-dependent aerodynamic derivatives are mainly used in the study of unstable motions at high wind speeds (Strømmen, 2010), where the quasi-steady theory is known to greatly underestimate the flutter stability since no aerodynamic torsional damping is introduced in the model (Øiseth, 2011). However, for buffeting analyses, the quasi-steady theory can be used in cases where the reduced wind velocity, $U/(fB)$, is high, e.g. larger than 10 (Zhu, 2002). Reduced wind velocity above 10 is associated with a relatively low frequency of the deck motion and insignificant non-linear effects of the aerodynamic forces (Xu, 2013). In other cases, unsteady aerodynamic derivatives should be estimated.

Unsteady aerodynamic derivatives can be obtained by the following methods:

a) Free vibration tests. Typically, an initially displaced model is released into free motion under different mean wind speeds. The motion-dependent forces can be estimated from changes in the resonance frequency (related to the aerodynamic stiffness) and from the decay of the response amplitude (related to the aerodynamic damping). The transient response can be analysed for one or more DOF at a time. Alternatively, statistical and mathematical models from the system identification theory can be used to extract aeroelastic properties under different ambient vibration conditions, either in reduced or full-scale, provided sufficient knowledge of the loading process and its signature in the response data. E.g. (Bartoli et al., 2009; Gu et al., 2000; Iwamoto and Fujino, 1995; Jakobsen and Hjorth-Hansen, 1995; Nikitas et al., 2011; Xu and Zhang, 2017).

b) Forced vibration tests. With the installation of a forced vibration rig in a wind tunnel, it is possible to actively impose prescribed motions on a sectional bridge model, under different mean wind speeds, while measuring the total forces. These can either be sinusoidal or random motions. In order to distinguish the motion-dependent forces from the other forces, the static and inertial forces can be estimated at zero wind speed, the buffeting forces can be minimized by having smooth flow conditions with negligible turbulence, and the static aerodynamic forces can be associated with the mean force values. E.g. (Chen et al., 2005; Diana et al., 2004; Helgedagsrud et al., 2019; Li, 1995; Siedziako et al., 2017).

3. Skew wind buffeting theory

3.1. Preface

This chapter is reproduced from a published article (Costa et al., 2022a). The formatting has been adapted to the thesis, but the content remains essentially unchanged. The full reference of the paper is:

Costa, B.M., Wang, J., Jakobsen, J.B., Øiseth, O.A., Snæbjörnsson, J.Þ., 2022a. Bridge buffeting by skew winds: A revised theory. Journal of Wind Engineering and Industrial Aerodynamics 220, 104806.
https://doi.org/10.1016/j.jweia.2021.104806

3.2. Abstract

An improved bridge buffeting theory is established with an emphasis on skew wind directions, for both turbulence- and motion-dependent forces. It provides simplifications and generalizations of previously established methods. The formulation starts with a preferred 3D approach, which is suitable when aerodynamic coefficients for different yaw and inclination angles are readily available. The 3D approach includes a new convenient choice of coordinate systems and an intuitive derivation of transformation matrices, supporting clear and compact wind load expressions as well as a more accurate formulation of the quasi-steady motion-dependent forces. When the aerodynamic coefficients have only been obtained for wind normal to the bridge girder, an alternative 2D approach is provided. The 2D approach, where only the normal projection of the wind is considered, is further expanded to include mean wind directions that are both yawed and inclined, axial forces in the longitudinal direction (1D) in an optional 2D + 1D format, and forces due to all in-plane and out-of-plane motions. All expressions are first presented in a compact non-linear format and then linearized

through numerous multivariate Taylor series approximations. A general, more straightforward and more accurate framework is thus established for both time- and frequency-domain analyses of the buffeting response.

3.3. Introduction

Advances in economy and technology lead to increasingly innovative structures. In the field of bridge engineering, the planned bridge for Bjørnafjorden, in Norway, illustrated in Fig. 6a, is a notable example of a long, flexible and complex wind-exposed floating structure which drives the need for more accurate wind and aerodynamic prediction models.

Classical buffeting analyses of straight bridges, first introduced by (Davenport, 1961a), deal with wind normal (perpendicular) to the bridge girder, which is often assumed to be the governing load case. Relevant aerodynamic parameters (e.g. aerodynamic coefficients and flutter derivatives) are usually obtained experimentally, in wind tunnel facilities, on a section of the bridge girder positioned perpendicularly to the mean wind direction.

When skew winds are considered, i.e., winds whose mean direction is not normal to the bridge longitudinal axis, the analyses are typically simplified to different extent. One common simplification is to decompose the wind into its normal and longitudinal components, discarding the latter one and proceeding with a 2D interaction problem in the normal plane. This is also referred to as the cosine rule, cosine law or decomposition method, which follow the so-called independence principle or cross-flow principle.

This principle was first observed in circular wires under a subcritical flow regime (see e.g. (Jones, 1947) illustrating the original experimental results from (Relf and Powell, 1917)). Approximate laminar boundary layer equations for yawed infinite cylinders (Sears, 1948) and yawed swept-back wings (Wild, 1949) further supported this principle. On the other hand, worse agreements were found for yawed cylinders near and above critical flow regimes (Bursnall and Loftin Jr, 1951), at high yaw angles ((Sumer, 2006) and (Ersdal and Faltinsen, 2006)), with respect to vortex-induced vibrations (Van Atta, 1968), using CFD simulations to look at the flow structure (Wang et al., 2019), and in the recommended practice by (Veritas, 2010) which only supports this principle for yaw angles up to 45°.

The same principle was then also applied to bridges, with inconsistent outcomes. A simplified buffeting theory for turbulence using the cosine rule is proposed in (Xie

et al., 1991) with reasonable agreement with experimental results. In (Tanaka and Davenport, 1982), the cosine rule underestimated the response of taut strip models in boundary layer turbulence, under highly turbulent wind. In (Zhu, 2002), the Tsing Ma suspension bridge experiences its maximum lateral buffeting response when the mean wind has a yaw angle β of $+5°$ and an inclination angle $\theta = -2.5°$. This response is practically constant within a β range of $\pm 15°$, which diverges from the cosine rule estimation. The maximum vertical response was observed at $\beta = \pm 12°$ and $\theta = 4°$. In (Wang et al., 2011), a numerical cosine rule analysis, when compared with the measured response of the Runyang suspension bridge, showed somewhat underestimated torsional and vertical responses, but several other uncertainty sources were also present. In (Huang et al., 2012), sectional model tests were compared with numerical analyses of two girders with rectangular cross-sections with B/H (width to height) ratios of 5 and 10. Significant underestimations of the response when using the cosine rule were observed, especially for the $B/H = 10$ case, where, also, the minimum flutter speed was observed for $\beta = 20°$. For bridges under construction, where the girder has one or both ends free and exposed to the wind, additional flow asymmetries are expected. For such cases, significant differences were observed by (Kimura and Tanaka, 1992), even when complementing the cosine rule with a sine rule. (Li et al., 2016) saw larger wind loads for β between $10°$ and $30°$, (Jian et al., 2020) for β between $0°$ and $30°$, whereas (Scanlan, 1993) reported a reasonable match between calculated and measured responses when carefully assessing several aerodynamic and structural parameters.

It can be concluded that previous literature, despite some inconsistencies, has shown that the maximum wind response can occur under skew winds and that a simplified cosine rule analysis can underestimate the response. These findings, which only concern straight bridges, raise further questions for a curved line-like structure such as the planned bridge for Bjørnafjorden in Fig. 6a, where its curved design creates a natural variation of the mean yaw angle β along the bridge, as exemplified in Fig. 6b. Additionally, its grade (slope) adds a variation of the mean inclination angle θ, for any given global mean wind direction.

Fig. 6a – A planned floating bridge solution for Bjørnafjorden, Norway. Fig. 6b – Plan view sketch. Example of β variation for one mean wind direction.

Complex bridge geometries, such as the one illustrated, also draw the need to reformulate previous buffeting theories, which have been mainly developed for straight bridges. A careful and comprehensive use of coordinate systems, consistent for all mean wind directions, when possible, can lead to simpler and clearer expressions. An intuitive and systematic use of transformation matrices ensures that all DOF (degrees of freedom) and motion dependencies are handled correctly.

The present skew wind buffeting theory consists of a partial revision and a complement to the pioneering doctoral thesis by Prof. Le-Dong Zhu (Zhu, 2002) where the present work was based. The theory by Zhu is also summarized in (Xu and Zhu, 2005; Zhu and Xu, 2005) and in (Xu, 2013). The main changes introduced in this revised version are summarized at the end of Section 3.8, in Table 1.

The present theory addresses the 3D load effects of the wind turbulence as well as the motion-dependent forces that arise from the interaction between the turbulent wind and the moving structure, for an arbitrary mean wind direction. A quasi-steady (frequency-independent) motion-dependent force formulation, considering all six DOF, is presented first. This formulation should only be used whenever the preferred unsteady (frequency-dependent) estimates are unavailable for the different skew angles. An alternative quasi-steady formulation using only the three typical DOF in Scanlan's flutter derivatives (Scanlan and Tomko, 1971) is also provided, which can then be readily adapted to an unsteady format.

Despite the criticism, there are no general and well-established alternatives to the cosine rule whenever the yaw-dependency of the aerodynamic coefficients is unknown. To facilitate simplified preliminary studies, as well as for comparison

purposes, the present theory also includes a 2D approach as a more rigorous generalization of the cosine rule. Whereas the cosine rule assumes the bridge and the wind to be both horizontal and ignores motions outside the normal plane, the 2D approach presented allows for any mean yaw angle and mean inclination angle, for both buffeting and motion-dependent forces, including motions in all degrees of freedom.

Linearized forms of the relevant forces and variables for both 3D and 2D approaches are achieved through numerous multivariate Taylor series approximations and extensive mathematical simplifications. The general non-linear and linearized forms are presented separately to facilitate typical time-domain and frequency-domain analyses of the bridge buffeting response. Wind loads are presented as functions of the turbulence in global wind coordinates (i.e., as a function of u, v and w) to also facilitate wind field simulations in the time domain and allow the use of available spectral and three-dimensional coherence models of the wind turbulence.

The computer algebra systems SymPy (v1.6.2) (a Python library for symbolic mathematics) and Wolfram Mathematica (v12.1) were both used to help deduce, linearize, simplify and verify the present theory.

3.4. Background concepts, conventions and terms

To represent a general case of arbitrary wind and bridge orientations, it is convenient to establish a set of right-handed Cartesian coordinate systems that can be chosen freely by the user, as well as the associated transformation matrices.

First, a global wind $(\boldsymbol{X_u}, \boldsymbol{Y_v}, \boldsymbol{Z_w})$ coordinate system is introduced in Fig. 7 and Fig. 8, hereby denoted Gw. The axis $\boldsymbol{X_u}$ describes the direction of the mean wind, with a mean velocity U, and the along-wind turbulence, with velocity u. $\boldsymbol{Y_v}$ describes the direction of the across-wind horizontal turbulence v and $\boldsymbol{Z_w}$ describes the direction of the turbulence component w, such that $\boldsymbol{Z_w} = \boldsymbol{X_u} \times \boldsymbol{Y_v}$ (cross-product). The global structural Gs $(\boldsymbol{X}, \boldsymbol{Y}, \boldsymbol{Z})$ coordinate system adopted is also illustrated in Fig. 7.

The local structural Ls $(\boldsymbol{x}, \boldsymbol{y}, \boldsymbol{z})$ coordinate system adopted (for each element) is illustrated in Fig. 8, along with the main angles in the context of skew winds, β and θ, hereby defined as follows:

- β, the yaw angle, is defined as the angle between the local $\boldsymbol{y}$-axis and the mean wind vector $\boldsymbol{X_u}$ projection onto the $\boldsymbol{xy}$-plane, in the half-open interval $]-180°, 180°]$, with a positive sign if the projection of $\boldsymbol{X_u}$ on the $\boldsymbol{x}$-axis has opposite direction to $\boldsymbol{x}$.
- θ, the inclination angle, is defined as the angle between the bridge local $\boldsymbol{xy}$-plane and the $\boldsymbol{X_u}$, in the open interval $]-90°, 90°[$, with a positive sign if the projection of $\boldsymbol{X_u}$ on the $\boldsymbol{z}$-axis has the same direction as $\boldsymbol{z}$.

The same angles, when measured with respect to the global Gs coordinate system, are called β_G and θ_G, and can be directly related to the wind cardinal directions.

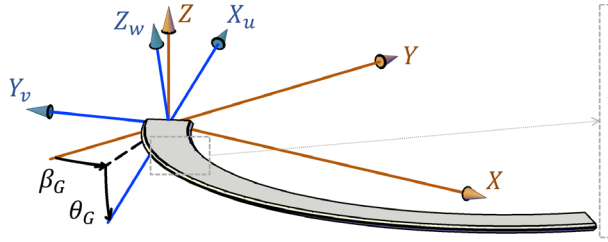

Fig. 7 – Global wind – Gw – $(\boldsymbol{X_u}, \boldsymbol{Y_v}, \boldsymbol{Z_w})$ and global structural – Gs – $(\boldsymbol{X}, \boldsymbol{Y}, \boldsymbol{Z})$ coordinate systems; global mean yaw angle β_G and global mean inclination angle θ_G.

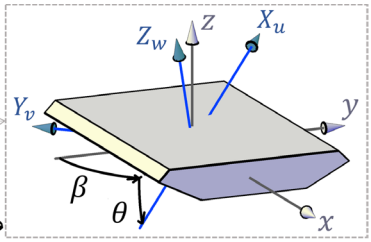

Fig. 8 – Global wind – Gw – $(\boldsymbol{X_u}, \boldsymbol{Y_v}, \boldsymbol{Z_w})$ and local structural – Ls – $(\boldsymbol{x}, \boldsymbol{y}, \boldsymbol{z})$ coordinate systems; local mean yaw angle β and local mean inclination angle θ.

Analogous to Earth's longitude and latitude, respectively, β and θ describe all possible wind directions, provided that the two singularities at $\theta = \pm 90°$ can be ignored. The aerodynamic coefficients, $\boldsymbol{C}(\beta, \theta)$, necessary to estimate the wind loads, can then be described at each bridge element as functions of both these angles. In the Gw system, for instance, when all 6 DOF are considered, $\boldsymbol{C_{Gw}}(\beta, \theta) = \left[C_{X_u}, C_{Y_v}, C_{Z_w}, C_{rX_u}, C_{rY_v}, C_{rZ_w}\right]^T$.

Any coordinate system can now be conveniently expressed through transformations or rotations of the previously defined systems. A transformation matrix is the transpose, and also the inverse, of a rotation matrix, as both are orthogonal.

To transform any column vector $\boldsymbol{v_{XYZ}}$, represented in a coordinate system $(\boldsymbol{X}, \boldsymbol{Y}, \boldsymbol{Z})$, into the same vector $\boldsymbol{v_{xyz}}$, represented in another coordinate system $(\boldsymbol{x}, \boldsymbol{y}, \boldsymbol{z})$ with the same origin, eqs. (40) to (42) can be used. $\boldsymbol{T_{xyzXYZ}}$ is a generic transformation matrix. γ_{ij} is the angle between two vectors $\boldsymbol{i}$ and $\boldsymbol{j}$.

$$\boldsymbol{v}_{xyz} = \boldsymbol{T}_{xyzXYZ}\, \boldsymbol{v}_{XYZ} \tag{40}$$

$$\boldsymbol{T}_{xyzXYZ} = \begin{bmatrix} \cos(\gamma_{xX}) & \cos(\gamma_{xY}) & \cos(\gamma_{xZ}) \\ \cos(\gamma_{yX}) & \cos(\gamma_{yY}) & \cos(\gamma_{yZ}) \\ \cos(\gamma_{zX}) & \cos(\gamma_{zY}) & \cos(\gamma_{zZ}) \end{bmatrix} = \boldsymbol{T}_{XYZxyz}{}^{T} \tag{41}$$

$$\cos(\gamma_{ij}) = \frac{\boldsymbol{i} \cdot \boldsymbol{j}}{\|\boldsymbol{i}\| \cdot \|\boldsymbol{j}\|} \tag{42}$$

In the 6 DOF format mentioned henceforth, e.g. $(\boldsymbol{x}, \boldsymbol{y}, \boldsymbol{z}, \boldsymbol{rx}, \boldsymbol{ry}, \boldsymbol{rz})$, each of the three additional r-axes represents a rotation around the axis its second letter refers to. To expand to this format, the vectors in eq. (40) can be replaced by their 6 DOF counterparts, such that the 6×6 transformation matrix follows eq. (43). All 6 DOF can then be included, even though only the first 3 are usually mentioned, for the sake of simplicity.

$$\boldsymbol{T}^{(6\times6)}_{xyzXYZ} = \begin{bmatrix} \boldsymbol{T}^{(3\times3)}_{xyzXYZ} & \boldsymbol{0} \\ \boldsymbol{0} & \boldsymbol{T}^{(3\times3)}_{xyzXYZ} \end{bmatrix}, \text{ with } \boldsymbol{0} = \begin{bmatrix} 0 & 0 & 0 \\ 0 & 0 & 0 \\ 0 & 0 & 0 \end{bmatrix} \tag{43}$$

Transformation matrices also have the properties presented in eqs. (44) and (45), where the subscripts $_{S1}$, $_{S2}$ and $_{S3}$ are used to denote three different coordinate systems and where for instance $\boldsymbol{T}_{\boldsymbol{S3S1}}$ denotes a transformation from $_{S1}$ to $_{S3}$.

$$\boldsymbol{T}_{\boldsymbol{S2S1}} = \boldsymbol{T}_{\boldsymbol{S1S2}}{}^{-1} = \boldsymbol{T}_{\boldsymbol{S1S2}}{}^{T} \tag{44}$$

$$\boldsymbol{T}_{\boldsymbol{S3S1}} = \boldsymbol{T}_{\boldsymbol{S3S2}}\, \boldsymbol{T}_{\boldsymbol{S2S1}} \tag{45}$$

A transformation matrix can also be obtained through meaningful rotations from one known system to another. Three elemental rotation matrices are presented in eqs. (46) to (48). Each one represents a rotation around an axis, by a generic angle γ, following the right-hand rule.

$$\boldsymbol{R}_{\boldsymbol{X}}(\gamma) = \begin{bmatrix} 1 & 0 & 0 \\ 0 & \cos(\gamma) & -\sin(\gamma) \\ 0 & \sin(\gamma) & \cos(\gamma) \end{bmatrix} = \boldsymbol{T}_{\boldsymbol{X}}(\gamma)^{T} \tag{46}$$

$$\boldsymbol{R}_{\boldsymbol{Y}}(\gamma) = \begin{bmatrix} \cos(\gamma) & 0 & \sin(\gamma) \\ 0 & 1 & 0 \\ -\sin(\gamma) & 0 & \cos(\gamma) \end{bmatrix} = \boldsymbol{T}_{\boldsymbol{Y}}(\gamma)^{T} \tag{47}$$

$$\boldsymbol{R}_{\boldsymbol{Z}}(\gamma) = \begin{bmatrix} \cos(\gamma) & -\sin(\gamma) & 0 \\ \sin(\gamma) & \cos(\gamma) & 0 \\ 0 & 0 & 1 \end{bmatrix} = \boldsymbol{T}_{\boldsymbol{Z}}(\gamma)^{T} \tag{48}$$

Chained rotations are then composed of two or more of these elemental rotations. They can be extrinsic (rotations around the original coordinate system axes, which remain fixed during all rotations, when each rotation matrix is pre-multiplied by the next rotation matrix), or intrinsic (rotations around the axes that are solidary to the rotating object, which change for each rotation, when each rotation matrix is post-multiplied by the next rotation matrix). To conveniently obtain the necessary transformation matrices, intrinsic chained rotations are adopted.

Based on Fig. 7, the fixed Gw system can be obtained from given values of β_G and θ_G, by first rotating the Gs system around the $\boldsymbol{Z}$-axis by the angle $\pi/2 + \beta_G$, and then around the newly obtained axis $\boldsymbol{Y_v}$ by the negative angle θ_G, as shown in eq. (49).

$$\begin{aligned} \boldsymbol{T_{GwGs}} &= (\boldsymbol{R_Z}(\pi/2 + \beta_G)\, \boldsymbol{R_Y}(-\theta_G))^T \\ &= \begin{bmatrix} -\cos(\theta_G)\sin(\beta_G) & \cos(\theta_G)\cos(\beta_G) & \sin(\theta_G) \\ -\cos(\beta_G) & -\sin(\beta_G) & 0 \\ \sin(\theta_G)\sin(\beta_G) & -\sin(\theta_G)\cos(\beta_G) & \cos(\theta_G) \end{bmatrix} \end{aligned} \tag{49}$$

To obtain the transformation matrices $\boldsymbol{T_{LsGs}}$, between the global structural and the local structural coordinate systems (one $\boldsymbol{T_{LsGs}}$ for each finite element), the generic eqs. (41) and (42) can be used, after defining all local $\boldsymbol{x}$, $\boldsymbol{y}$ and $\boldsymbol{z}$ axes. When a static analysis precedes the buffeting analysis, the axes of the Ls systems and relevant transformation matrices should be updated accordingly. It should be noted that the deck rotation due to the static wind may play an important role.

The "for each element" and "for each node" representations used throughout the text are not strict. They are often interchangeable, provided that the principles of finite element modelling are followed (e.g. (Bathe, 2006; Hutton, 2004)).

The mean wind speed U, mean yaw angle β and mean inclination angle θ have their time-varying counterparts $\tilde{U}$, $\tilde{\beta}$ and $\tilde{\theta}$ which consider the instantaneous wind turbulence components u, v and w at each time instant. The turbulence-dependent quantities are denoted "instantaneous" and represented by a single tilde accent. Subscripts are used to indicate the coordinate systems (e.g. Ls, Gw) in which these quantities are represented as vectors, or the axes (e.g. $\boldsymbol{x}$, $\boldsymbol{y}$, $\boldsymbol{z}$) or plane (e.g. $\boldsymbol{xy}$) they are projected onto. These quantities can be obtained through eqs. (50) to (59), for each element.

Mean quantities:		Instantaneous quantities:	
$\boldsymbol{U_{Gw}} = [U, 0, 0]^T$	(50)	$\widetilde{\boldsymbol{U}}_{\boldsymbol{Gw}} = [U + u, v, w]^T$	(51)
$\boldsymbol{U_{Ls}} = \left[U_x, U_y, U_z\right]^T = \boldsymbol{T_{LsGw}}\, \boldsymbol{U_{Gw}}$	(52)	$\widetilde{\boldsymbol{U}}_{\boldsymbol{Ls}} = \left[\widetilde{U}_x, \widetilde{U}_y, \widetilde{U}_z\right]^T = \boldsymbol{T_{LsGw}}\, \widetilde{\boldsymbol{U}}_{\boldsymbol{Gw}}$	(53)
$U_{xy} = \sqrt{{U_x}^2 + {U_y}^2}$	(54)	$\widetilde{U}_{xy} = \sqrt{{\widetilde{U}_x}^2 + {\widetilde{U}_y}^2}$	(55)
$\beta = -\arccos\left(U_y/U_{xy}\right) sgn(U_x)$	(56)	$\tilde{\beta} = -\arccos\left(\widetilde{U}_y/\widetilde{U}_{xy}\right) sgn(\widetilde{U}_x)$	(57)
$\theta = \arcsin\left(U_z/U\right)$	(58)	$\tilde{\theta} = \arcsin\left(\widetilde{U}_z/\widetilde{U}\right)$	(59)

Where $\boldsymbol{T_{LsGw}} = \boldsymbol{T_{LsGs}}\boldsymbol{T_{GsGw}} = \boldsymbol{T_{LsGs}}\boldsymbol{T_{GwGs}}^T$ and sgn is the sign function. Alternatively, $\beta = atan2(-U_x, U_y)$ and $\tilde{\beta} = atan2(-\widetilde{U}_x, \widetilde{U}_y)$ can be used, where $atan2$ is the "2-argument arctangent" function. The instantaneous wind speed $\widetilde{U}$ is obtained by eq. (60).

$$\widetilde{U} = \left\|\widetilde{\boldsymbol{U}}_{\boldsymbol{Ls}}\right\| = \left\|\widetilde{\boldsymbol{U}}_{\boldsymbol{Gw}}\right\| = \sqrt{(U+u)^2 + v^2 + w^2} \tag{60}$$

Next, motion-dependent (or simply "relative") variables are introduced which, in addition to the effects of turbulence (when applicable), also consider the effects of the structure in motion and are represented by a double tilde accent. The turbulence components u, v and w, when accounting for the relative velocity between the wind and the moving structure are denoted $\widetilde{\tilde{u}}$, $\widetilde{\tilde{v}}$ and $\widetilde{\tilde{w}}$ and are defined in eqs. (61) to (63). $\boldsymbol{\Delta}$ is the structural displacement vector (e.g. at the centre of a given element) and its time-derivative $\dot{\boldsymbol{\Delta}}$ is the vector of structural velocities. They can be conveniently represented at the axes $\boldsymbol{X_u}$, $\boldsymbol{Y_v}$ and $\boldsymbol{Z_w}$ of the Gw system and simply obtained by $\dot{\boldsymbol{\Delta}}_{\boldsymbol{Gw}} = \boldsymbol{T_{GwLs}}\dot{\boldsymbol{\Delta}}_{\boldsymbol{Ls}}$, i.e., in a 3 DOF format, $\left[\dot{\Delta}_{X_u}, \dot{\Delta}_{Y_v}, \dot{\Delta}_{Z_w}\right]^T = \boldsymbol{T_{GwLs}}\left[\dot{\Delta}_x, \dot{\Delta}_y, \dot{\Delta}_z\right]^T$. The instantaneous relative wind speed is given by eq. (64), whereas its vector representations in the Gw system and in the local dynamic structural $\widetilde{\widetilde{Ls}}$ system (solidary with the rotating body) are given in eqs. (65) and (66).

Motion-dependent quantities:

$$\tilde{\tilde{u}} = u - \dot{\Delta}_{X_u} \quad (61) \qquad \tilde{\tilde{v}} = v - \dot{\Delta}_{Y_v} \quad (62)$$

$$\tilde{\tilde{w}} = w - \dot{\Delta}_{Z_w} \quad (63) \qquad \tilde{\tilde{U}} = \sqrt{(U + \tilde{\tilde{u}})^2 + \tilde{\tilde{v}}^2 + \tilde{\tilde{w}}^2} \quad (64)$$

$$\tilde{\tilde{\boldsymbol{U}}}_{\boldsymbol{Gw}} = \left[U + \tilde{\tilde{u}}, \tilde{\tilde{v}}, \tilde{\tilde{w}}\right]^T \quad (65) \qquad \tilde{\tilde{\boldsymbol{U}}}_{\widetilde{\widetilde{\boldsymbol{Ls}}}} = \left[\tilde{\tilde{U}}_{\tilde{\tilde{x}}}, \tilde{\tilde{U}}_{\tilde{\tilde{y}}}, \tilde{\tilde{U}}_{\tilde{\tilde{z}}}\right]^T = \boldsymbol{T}_{\widetilde{\widetilde{\boldsymbol{Ls}}}\boldsymbol{Ls}} \boldsymbol{T}_{\boldsymbol{LsGw}} \tilde{\tilde{\boldsymbol{U}}}_{\boldsymbol{Gw}} \quad (66)$$

To obtain the transformation from the static structure to the dynamic (rotating) structure $\boldsymbol{T}_{\widetilde{\widetilde{\boldsymbol{Ls}}}\boldsymbol{Ls}}$ at each time step, three chained rotations can be performed if the rotations are assumed small, as in eq. (67). Moreover, when $\boldsymbol{T}_{\widetilde{\widetilde{\boldsymbol{Ls}}}\boldsymbol{Ls}}$ is linearized with respect to Δ_{rx}, Δ_{ry} and Δ_{rz}, these three elemental rotations become commutative and $\boldsymbol{T}_{\widetilde{\widetilde{\boldsymbol{Ls}}}\boldsymbol{Ls}}$ gets further simplified into eq. (68).

$$\boldsymbol{T}_{\widetilde{\widetilde{\boldsymbol{Ls}}}\boldsymbol{Ls}} \approx \left(\boldsymbol{R}_{\boldsymbol{X}}(\Delta_{rx}) \boldsymbol{R}_{\boldsymbol{Y}}(\Delta_{ry}) \boldsymbol{R}_{\boldsymbol{Z}}(\Delta_{rz})\right)^T \quad (67)$$

$$\left(\boldsymbol{R}_{\boldsymbol{X}}(\Delta_{rx}) \boldsymbol{R}_{\boldsymbol{Y}}(\Delta_{ry}) \boldsymbol{R}_{\boldsymbol{Z}}(\Delta_{rz})\right)^T \approx \begin{bmatrix} 1 & \Delta_{rz} & -\Delta_{ry} \\ -\Delta_{rz} & 1 & \Delta_{rx} \\ \Delta_{ry} & -\Delta_{rx} & 1 \end{bmatrix} \quad (68)$$

Given that $\tilde{\tilde{U}}_{\widetilde{\tilde{x}}\tilde{\tilde{y}}} = \sqrt{\tilde{\tilde{U}}_{\tilde{\tilde{x}}}^{\,2} + \tilde{\tilde{U}}_{\tilde{\tilde{y}}}^{\,2}}$, the instantaneous motion-dependent counterparts of β and θ can be obtained from eqs. (69) and (70).

$$\tilde{\tilde{\beta}} = -\arccos\left(\tilde{\tilde{U}}_{\tilde{\tilde{y}}} / \tilde{\tilde{U}}_{\widetilde{\tilde{x}}\tilde{\tilde{y}}}\right) sgn(\tilde{\tilde{U}}_{\tilde{\tilde{x}}}) \quad (69)$$

$$\tilde{\tilde{\theta}} = \arcsin\left(\tilde{\tilde{U}}_{\tilde{\tilde{z}}} / \tilde{\tilde{U}}\right) \quad (70)$$

Two additional right-handed orthogonal coordinate systems are adopted, namely the local instantaneous wind $\widetilde{Lw}$ $(\boldsymbol{X}_{\tilde{\boldsymbol{U}}}, \boldsymbol{Y}_{\tilde{\boldsymbol{U}}}, \boldsymbol{Z}_{\tilde{\boldsymbol{U}}})$ and the local relative instantaneous wind $\widetilde{\widetilde{Lw}}$ $(\boldsymbol{X}_{\tilde{\tilde{\boldsymbol{U}}}}, \boldsymbol{Y}_{\tilde{\tilde{\boldsymbol{U}}}}, \boldsymbol{Z}_{\tilde{\tilde{\boldsymbol{U}}}})$, described by the conditions in eqs. (71) and (72). $\tilde{U}$ and $\tilde{\tilde{U}}$ are represented in $\boldsymbol{X}_{\tilde{\boldsymbol{U}}}$ and $\boldsymbol{X}_{\tilde{\tilde{\boldsymbol{U}}}}$ respectively.

$$\boldsymbol{X}_{\tilde{\boldsymbol{U}}} = \tilde{\boldsymbol{U}}_{\boldsymbol{Gw}} / \left\|\tilde{\boldsymbol{U}}_{\boldsymbol{Gw}}\right\|; \quad \boldsymbol{Y}_{\tilde{\boldsymbol{U}}} \parallel \boldsymbol{xy}\text{-plane} \wedge sgn(\boldsymbol{Z}_{\tilde{\boldsymbol{U}}} \cdot \boldsymbol{z}) > 0; \quad \boldsymbol{Z}_{\tilde{\boldsymbol{U}}} = \boldsymbol{X}_{\tilde{\boldsymbol{U}}} \times \boldsymbol{Y}_{\tilde{\boldsymbol{U}}} \quad (71)$$

$$\boldsymbol{X}_{\tilde{\tilde{\boldsymbol{U}}}} = \tilde{\tilde{\boldsymbol{U}}}_{\boldsymbol{Gw}} / \left\|\tilde{\tilde{\boldsymbol{U}}}_{\boldsymbol{Gw}}\right\|; \quad \boldsymbol{Y}_{\tilde{\tilde{\boldsymbol{U}}}} \parallel \widetilde{\boldsymbol{xy}}\text{-plane} \wedge sgn(\boldsymbol{Z}_{\tilde{\tilde{\boldsymbol{U}}}} \cdot \tilde{\boldsymbol{z}}) > 0; \quad \boldsymbol{Z}_{\tilde{\tilde{\boldsymbol{U}}}} = \boldsymbol{X}_{\tilde{\tilde{\boldsymbol{U}}}} \times \boldsymbol{Y}_{\tilde{\tilde{\boldsymbol{U}}}} \quad (72)$$

These two systems help represent the aerodynamic forces $\tilde{\boldsymbol{f}}_{\boldsymbol{ad,\widetilde{Lw}}}$ and $\tilde{\tilde{\boldsymbol{f}}}_{\boldsymbol{ad,\widetilde{\widetilde{Lw}}}}$ and the respective coefficients $\tilde{\boldsymbol{C}}_{\boldsymbol{\widetilde{Lw}}}(\tilde{\beta},\tilde{\theta})$ and $\tilde{\tilde{\boldsymbol{C}}}_{\boldsymbol{\widetilde{\widetilde{Lw}}}}\left(\tilde{\tilde{\beta}},\tilde{\tilde{\theta}}\right)$ at each time instant, as shown in Section 3.5.

A schematic comparison between the key mean, instantaneous and motion-dependent variables is illustrated in Fig. 9.

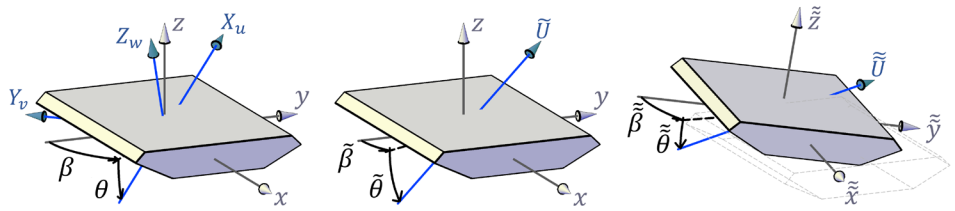

Fig. 9 – Representation of global (mean) wind Gw $(\boldsymbol{X_u}, \boldsymbol{Y_v}, \boldsymbol{Z_w})$, local (static) structural Ls $(\boldsymbol{x}, \boldsymbol{y}, \boldsymbol{z})$ and local dynamic structural $\widetilde{Ls}$ $(\tilde{\boldsymbol{x}}, \tilde{\boldsymbol{y}}, \tilde{\boldsymbol{z}})$ coordinate systems, local instantaneous wind speed $\tilde{U}$ (in the $\boldsymbol{X}_{\tilde{\boldsymbol{U}}}$-axis), local instantaneous relative wind speed $\tilde{\tilde{U}}$ (in the $\boldsymbol{X}_{\tilde{\tilde{\boldsymbol{U}}}}$-axis), and the pairs of angles (β, θ), $(\tilde{\beta}, \tilde{\theta})$ and $\left(\tilde{\tilde{\beta}}, \tilde{\tilde{\theta}}\right)$.

3.5. A 3D buffeting approach for skew winds

A 3D skew wind buffeting analysis requires information on aerodynamic coefficients $\boldsymbol{C}(\beta,\theta)$ that depend on both β and θ. These can be obtained through wind tunnel tests at different yaw angles or through three-dimensional CFD analyses.

3.5.1. Fluctuating wind forces due to turbulence

3.5.1.1. General formulation

The vector of the six aerodynamic forces in the Gs system, for each element and at each time instant, can be simply expressed through eq. (73), using consistent (i.e. represented in a time-invariant system) aerodynamic coefficients $\tilde{\boldsymbol{C}}_{\boldsymbol{Ls}}(\tilde{\beta},\tilde{\theta}) = \left[\tilde{C}_x, \tilde{C}_y, \tilde{C}_z, \tilde{C}_{rx}, \tilde{C}_{ry}, \tilde{C}_{rz}\right]^T$, which depend on the instantaneous $\tilde{\beta}$ and $\tilde{\theta}$.

$$\tilde{\boldsymbol{F}}_{\boldsymbol{ad,Gs}} = L\,\tilde{\boldsymbol{f}}_{\boldsymbol{ad,Gs}} = L\,\boldsymbol{T}_{\boldsymbol{GsLs}}\tilde{\boldsymbol{f}}_{\boldsymbol{ad,Ls}} = L\,\boldsymbol{T}_{\boldsymbol{GsLs}}\,1/2\,\rho\tilde{U}^2\boldsymbol{B}\tilde{\boldsymbol{C}}_{\boldsymbol{Ls}} \tag{73}$$

L is the element length. Uppercase $\boldsymbol{F}$ denotes forces, and lowercase $\boldsymbol{f}$ denotes forces per unit length. ρ is the air density. $\boldsymbol{B} = diag(B, B, B, B^2, B^2, B^2)$ is a diagonal matrix where B is the real cross-section width.

It is however more common to express $\tilde{\boldsymbol{f}}_{\boldsymbol{ad}}$ as a function of aerodynamic coefficients $\tilde{\boldsymbol{C}}_{\widetilde{\boldsymbol{Lw}}}(\tilde{\beta}, \tilde{\theta}) = \left[\tilde{C}_{X_{\tilde{U}}}, \tilde{C}_{Y_{\tilde{U}}}, \tilde{C}_{Z_{\tilde{U}}}, \tilde{C}_{rX_{\tilde{U}}}, \tilde{C}_{rY_{\tilde{U}}}, \tilde{C}_{rZ_{\tilde{U}}}\right]^T$ that are solidary with the instantaneous wind direction $\widetilde{U}$. These forces must therefore be transformed, at each time step, from $\widetilde{Lw}$ to a consistent coordinate system, such as Gw (solidary with U), through $\boldsymbol{T}_{\boldsymbol{Gw\widetilde{Lw}}}$, as expressed in eqs. (74) to (76).

$$\tilde{\boldsymbol{F}}_{\boldsymbol{ad,Gs}} = L\, \boldsymbol{T}_{\boldsymbol{GsGw}} \tilde{\boldsymbol{f}}_{\boldsymbol{ad,Gw}} = L\, \boldsymbol{T}_{\boldsymbol{GsGw}} \boldsymbol{T}_{\boldsymbol{Gw\widetilde{Lw}}}\, 1/2\, \rho \widetilde{U}^2 \boldsymbol{B} \tilde{\boldsymbol{C}}_{\widetilde{\boldsymbol{Lw}}} \tag{74}$$

$$\boldsymbol{T}_{\boldsymbol{Gw\widetilde{Lw}}} = \boldsymbol{T}_{\boldsymbol{GwLs}}\, \boldsymbol{T}_{\boldsymbol{Ls\widetilde{Lw}}} \tag{75}$$

$$\boldsymbol{T}_{\boldsymbol{Ls\widetilde{Lw}}} = \left(\boldsymbol{R}_{\boldsymbol{Y}}(\tilde{\theta})\, \boldsymbol{R}_{\boldsymbol{Z}}(-\tilde{\beta} - \pi/2)\right)^T \tag{76}$$

Note that all coefficients are normalized by B or B^2, for simplicity. The relation between both aerodynamic coefficient representations is expressed in eq. (77), and either or both can be used, as preferred.

$$\tilde{\boldsymbol{C}}_{\boldsymbol{Ls}} = \boldsymbol{T}_{\boldsymbol{Ls\widetilde{Lw}}} \tilde{\boldsymbol{C}}_{\widetilde{\boldsymbol{Lw}}} \tag{77}$$

The aerodynamic forces, first obtained for each finite beam element, can be converted into forces at both local nodes of each element and then converted into global nodal forces, following standard FEM transformation techniques.

Aerodynamic forces $\tilde{\boldsymbol{f}}_{\boldsymbol{ad}}$ are here defined as the sum of the mean wind forces $\boldsymbol{f}_{\boldsymbol{mean}}$ and the time-varying buffeting forces $\tilde{\boldsymbol{f}}_{\boldsymbol{b}}$, so the buffeting part can be retrieved from eq. (78) and linearized when convenient.

$$\tilde{\boldsymbol{f}}_{\boldsymbol{b,Gw}} = \tilde{\boldsymbol{f}}_{\boldsymbol{ad,Gw}} - \boldsymbol{f}_{\boldsymbol{mean,Gw}} = \tilde{\boldsymbol{f}}_{\boldsymbol{ad,Gw}} - 1/2\, \rho U^2 \boldsymbol{B} \boldsymbol{C}_{\boldsymbol{Gw}} \tag{78}$$

Where $\boldsymbol{C}_{\boldsymbol{Gw}}(\beta, \theta)$ depends on the mean β and θ.

3.5.1.2. Linear formulation

Presuming that the time-varying velocities u, v and w are small compared to U, then the local instantaneous yaw angle $\tilde{\beta}$, defined in eq. (57), can be represented as a function of U, u, v, w, β and θ. By performing a first-order Taylor expansion with respect to u, v and w, as in eq. (79), by conveniently separating the two cases of

$\beta \in]-180°, 0°]$ and $\beta \in [0°, 180°]$, and by considering that $\theta \in]-90°, 90°[$, numerous simplifications can be made.

$$\tilde{\beta}(U, u, v, w, \beta, \theta) \approx \tilde{\beta}_{u,v,w=0} + \tilde{\beta}'^{u}_{u,v,w=0} u + \tilde{\beta}'^{v}_{u,v,w=0} v + \tilde{\beta}'^{w}_{u,v,w=0} w \tag{79}$$

Then, equally for both cases of the β-interval, the linear approximation in eq. (80) is obtained. A similar process can be done for $\tilde{\theta}$, $\boldsymbol{T}_{\boldsymbol{Gw\widetilde{Lw}}}$ and $\widetilde{U}^2$, leading to eqs. (81), (82) and (83).

$$\tilde{\beta} = \beta + \widetilde{\Delta\beta} \approx \beta + \frac{v}{U \cos\theta} \tag{80}$$

$$\tilde{\theta} = \theta + \widetilde{\Delta\theta} \approx \theta + \frac{w}{U} \tag{81}$$

$$\boldsymbol{T}_{\boldsymbol{Gw\widetilde{Lw}}} \approx \begin{bmatrix} 1 & -\frac{v}{U} & -\frac{w}{U} \\ \frac{v}{U} & 1 & -\frac{v\tan(\theta)}{U} \\ \frac{w}{U} & \frac{v\tan(\theta)}{U} & 1 \end{bmatrix} = \begin{bmatrix} 1 & -\widetilde{\Delta\beta}\cos\theta & -\widetilde{\Delta\theta} \\ \widetilde{\Delta\beta}\cos\theta & 1 & -\widetilde{\Delta\beta}\sin\theta \\ \widetilde{\Delta\theta} & \widetilde{\Delta\beta}\sin\theta & 1 \end{bmatrix} \tag{82}$$

$$\widetilde{U}^2 \approx U^2 + 2Uu \tag{83}$$

The instantaneous aerodynamic coefficients can also be linearized with respect to the small angle variations $\widetilde{\Delta\beta}$ and $\widetilde{\Delta\theta}$, as in eq. (84).

$$\widetilde{\boldsymbol{C}}_{\widetilde{Lw}} \approx \boldsymbol{C}_{\boldsymbol{Gw}} + \boldsymbol{C}'^{\boldsymbol{\beta}}_{\boldsymbol{Gw}} \widetilde{\Delta\beta} + \boldsymbol{C}'^{\boldsymbol{\theta}}_{\boldsymbol{Gw}} \widetilde{\Delta\theta} \tag{84}$$

Where, for simplicity, $\widetilde{\boldsymbol{C}} = \widetilde{\boldsymbol{C}}(\tilde{\beta}, \tilde{\theta})$, $\boldsymbol{C} = \boldsymbol{C}(\beta, \theta)$, $\boldsymbol{C}'^{\boldsymbol{\beta}} = \frac{\partial \boldsymbol{C}(\beta,\theta)}{\partial \beta}$ and $\boldsymbol{C}'^{\boldsymbol{\theta}} = \frac{\partial \boldsymbol{C}(\beta,\theta)}{\partial \theta}$. When the aerodynamic coefficients $\boldsymbol{C}$ are known for one system, e.g. Gw, they can be converted to another, e.g. Ls, through eq. (85). By partially differentiating both sides of eq. (85), $\boldsymbol{C}'^{\boldsymbol{\beta}}$ and $\boldsymbol{C}'^{\boldsymbol{\theta}}$ can be obtained as in eqs. (86) and (87).

$$\boldsymbol{C}_{\boldsymbol{Ls}} = \boldsymbol{T}_{\boldsymbol{LsGw}} \boldsymbol{C}_{\boldsymbol{Gw}} \tag{85}$$

$$\boldsymbol{C}'^{\boldsymbol{\beta}}_{\boldsymbol{Ls}} = \frac{\partial(\boldsymbol{T}_{\boldsymbol{LsGw}} \boldsymbol{C}_{\boldsymbol{Gw}})}{\partial \beta} = \frac{\partial \boldsymbol{T}_{\boldsymbol{LsGw}}}{\partial \beta} \boldsymbol{C}_{\boldsymbol{Gw}} + \boldsymbol{T}_{\boldsymbol{LsGw}} \boldsymbol{C}'^{\boldsymbol{\beta}}_{\boldsymbol{Gw}} \tag{86}$$

$$\boldsymbol{C}'^{\boldsymbol{\theta}}_{\boldsymbol{Ls}} = \frac{\partial(\boldsymbol{T}_{\boldsymbol{LsGw}} \boldsymbol{C}_{\boldsymbol{Gw}})}{\partial \theta} = \frac{\partial \boldsymbol{T}_{\boldsymbol{LsGw}}}{\partial \theta} \boldsymbol{C}_{\boldsymbol{Gw}} + \boldsymbol{T}_{\boldsymbol{LsGw}} \boldsymbol{C}'^{\boldsymbol{\theta}}_{\boldsymbol{Gw}} \tag{87}$$

Finally, by linearizing the vector of the six buffeting forces per unit length $\tilde{\boldsymbol{f}}_{\boldsymbol{b,Gw}}$, described in eqs. (78) and (74), and by combining eqs. (80) to (84), the buffeting

forces can be approximated by eqs. (88) to (90), as a linear function of the turbulence components vector $\boldsymbol{a_{Gw}}$.

$$\tilde{\boldsymbol{f}}_{\boldsymbol{b,Gw}} \approx \boldsymbol{A_{b,Gw}}\, \boldsymbol{a_{Gw}} \tag{88}$$

$$\boldsymbol{a_{Gw}} = [u, v, w]^T \tag{89}$$

$\boldsymbol{A_{b,Gw}} = 1/2\,\rho U \cdot$

$$\begin{bmatrix} 2BC_{X_u}\chi_{X_u,u} & B\left(C'^{\beta}_{X_u}/\cos\theta - C_{Y_v}\right)\chi_{X_u,v} & B\left(C'^{\theta}_{X_u} - C_{Z_w}\right)\chi_{X_u,w} \\ 2BC_{Y_v}\chi_{Y_v,u} & B\left(C_{X_u} + C'^{\beta}_{Y_v}/\cos\theta - C_{Z_w}\tan\theta\right)\chi_{Y_v,v} & B\; C'^{\theta}_{Y_v}\;\chi_{Y_v,w} \\ 2BC_{Z_w}\chi_{Z_w,u} & B\left(C_{Y_v}\tan\theta + C'^{\beta}_{Z_w}/\cos\theta\right)\chi_{Z_w,v} & B\left(C_{X_u} + C'^{\theta}_{Z_w}\right)\chi_{Z_w,w} \\ 2B^2C_{rX_u}\chi_{rX_u,u} & B^2\left(C'^{\beta}_{rX_u}/\cos\theta - C_{rY_v}\right)\chi_{rX_u,v} & B^2\left(C'^{\theta}_{rX_u} - C_{rZ_w}\right)\chi_{rX_u,w} \\ 2B^2C_{rY_v}\chi_{rY_v,u} & B^2\left(C_{rX_u} + C'^{\beta}_{rY_v}/\cos\theta - C_{rZ_w}\tan\theta\right)\chi_{rY_v,v} & B^2\; C'^{\theta}_{rY_v}\;\chi_{rY_v,w} \\ 2B^2C_{rZ_w}\chi_{rZ_w,u} & B^2\left(C_{rY_v}\tan\theta + C'^{\beta}_{rZ_w}/\cos\theta\right)\chi_{rZ_w,v} & B^2\left(C_{rX_u} + C'^{\theta}_{rZ_w}\right)\chi_{rZ_w,w} \end{bmatrix} \tag{90}$$

Where the function $\chi_{i,j}$, the so-called cross-sectional admittance function, associated with the aerodynamic coefficient C_i and the turbulence component j, is introduced to reflect the sensitivity of the cross-section to different frequency components.

3.5.2. Fluctuating wind forces due to turbulence and structural motions

3.5.2.1. General formulation

The wind action is represented, at each time instant, by a relative wind speed $\tilde{\tilde{U}}$, and the instantaneous motion-dependent yaw and inclination angles $\tilde{\tilde{\beta}}$ and $\tilde{\tilde{\theta}}$. When the wind moves a bridge element, its displaced local axes compose the $\widetilde{\widetilde{Ls}}$ system, as illustrated in Fig. 9. These motion-dependent variables help define the instantaneous vector of motion-dependent aerodynamic forces in eqs. (91) to (93).

$$\tilde{\tilde{\boldsymbol{f}}}_{\boldsymbol{ad,Gw}} = \boldsymbol{T}_{\boldsymbol{Gw\widetilde{\widetilde{Lw}}}}\, 1/2\,\rho\, \tilde{\tilde{U}}^2\, \boldsymbol{B}\, \tilde{\tilde{\boldsymbol{C}}}_{\boldsymbol{\widetilde{\widetilde{Lw}}}} \tag{91}$$

$$\boldsymbol{T}_{\boldsymbol{Gw\widetilde{\widetilde{Lw}}}} = \boldsymbol{T}_{\boldsymbol{GwLs}}\, \boldsymbol{T}_{\boldsymbol{Ls\widetilde{\widetilde{Ls}}}}\, \boldsymbol{T}_{\boldsymbol{\widetilde{\widetilde{Ls}}\widetilde{\widetilde{Lw}}}} \tag{92}$$

$$\boldsymbol{T}_{\widetilde{\widetilde{Ls}}\widetilde{\widetilde{Lw}}} = \left(\boldsymbol{R}_{\boldsymbol{Y}}\left(\tilde{\tilde{\theta}}\right)\boldsymbol{R}_{\boldsymbol{Z}}(-\tilde{\tilde{\beta}} - \pi/2)\right)^{T} \tag{93}$$

$\widetilde{\widetilde{U}}$ is defined in eq. (64), $\boldsymbol{T}_{\boldsymbol{Ls}\widetilde{\widetilde{\boldsymbol{Ls}}}}$ can be obtained through eq. (41) or approximated by eq. (67) or by eq. (68), and $\widetilde{\widetilde{\boldsymbol{C}}}_{\widetilde{\widetilde{\boldsymbol{Lw}}}}\left(\tilde{\tilde{\beta}}, \tilde{\tilde{\theta}}\right)$ is a function of the angles $\tilde{\tilde{\beta}}$ and $\tilde{\tilde{\theta}}$, both defined in eqs. (69) and (70).

3.5.2.2. Linear formulation

The linearization process described in Section 3.5.1.2, with respect to u, v and w, can be expanded to include linearizations of the structural angular displacements and the structural translation velocities. The structural angular displacements are included in $\boldsymbol{\Delta}$ and can be assumed to follow the small angle approximation, whereas the structural translational velocities are included in $\dot{\boldsymbol{\Delta}}$ and can be assumed small relative to the mean wind speed U. These assumptions allow eqs. (69) and (70) to be linearized into eqs. (94) and (95). These expressions are most compact when the structural motions, $\boldsymbol{\Delta}_{\boldsymbol{Gw}}$ and $\dot{\boldsymbol{\Delta}}_{\boldsymbol{Gw}}$, are represented in the Gw system. Similarly, $\boldsymbol{T}_{\boldsymbol{Gw}\widetilde{\widetilde{\boldsymbol{Lw}}}}$ and $\widetilde{\widetilde{U}}^2$ are linearized into eqs. (96) and (97).

$$\tilde{\tilde{\beta}} = \beta + \widetilde{\widetilde{\Delta\beta}} \approx \beta + \frac{\tilde{\tilde{v}}}{U\cos\theta} - \frac{\Delta_{rZ_w}}{\cos\theta} \tag{94}$$

$$\tilde{\tilde{\theta}} = \theta + \widetilde{\widetilde{\Delta\theta}} \approx \theta + \frac{\widetilde{\widetilde{w}}}{U} + \Delta_{rY_v} \tag{95}$$

$$\boldsymbol{T}_{\boldsymbol{Gw}\widetilde{\widetilde{\boldsymbol{Lw}}}} \approx \begin{bmatrix} 1 & -\tilde{\tilde{v}}/U & -\widetilde{\widetilde{w}}/U \\ \tilde{\tilde{v}}/U & 1 & -\Delta_{rX_u} + \left(\Delta_{rZ_w} - \tilde{\tilde{v}}/U\right)\tan(\theta) \\ \widetilde{\widetilde{w}}/U & \Delta_{rX_u} + \left(\tilde{\tilde{v}}/U - \Delta_{rZ_w}\right)\tan(\theta) & 1 \end{bmatrix} \tag{96}$$

$$\widetilde{\widetilde{U}}^2 \approx U^2 + 2U\tilde{u} \tag{97}$$

Where $\left[\Delta_{rX_u}, \Delta_{rY_v}, \Delta_{rZ_w}\right]^T = \boldsymbol{T}_{\boldsymbol{GwLs}}\left[\Delta_{rx}, \Delta_{ry}, \Delta_{rz}\right]^T$.

Again, by linearizing $\widetilde{\widetilde{\boldsymbol{C}}}_{\widetilde{\widetilde{\boldsymbol{Lw}}}} \approx \boldsymbol{C}_{\boldsymbol{Gw}} + \boldsymbol{C}'^{\boldsymbol{\beta}}_{\boldsymbol{Gw}}\widetilde{\widetilde{\Delta\beta}} + \boldsymbol{C}'^{\boldsymbol{\theta}}_{\boldsymbol{Gw}}\widetilde{\widetilde{\Delta\theta}}$, combining eqs. (94) to (97) and linearizing the vector of the six buffeting forces per unit length $\tilde{\tilde{\boldsymbol{f}}}_{\boldsymbol{b,Gw}} = \tilde{\tilde{\boldsymbol{f}}}_{\boldsymbol{ad,Gw}} - \boldsymbol{f}_{\boldsymbol{mean,Gw}}$ (see eqs. (91) and (78)), $\tilde{\tilde{\boldsymbol{f}}}_{\boldsymbol{b,Gw}}$ can be approximated by eqs. (98) to (103), as a linear function of the turbulence components, the structural displacements and the structural velocities.

$$\tilde{\tilde{\boldsymbol{f}}}_{\boldsymbol{b,Gw}} \approx \tilde{\boldsymbol{f}}_{\boldsymbol{b,Gw}} + \boldsymbol{A}_{\boldsymbol{\Delta,Gw}}\,\boldsymbol{\Delta}_{\boldsymbol{Gw}} + \boldsymbol{A}_{\dot{\boldsymbol{\Delta}},\boldsymbol{Gw}}\,\dot{\boldsymbol{\Delta}}_{\boldsymbol{Gw}} \tag{98}$$

$$\boldsymbol{\Delta}_{\boldsymbol{Gw}} = \left[\Delta_{X_u}, \Delta_{Y_v}, \Delta_{Z_w}, \Delta_{rX_u}, \Delta_{rY_v}, \Delta_{rZ_w}\right]^T \tag{99}$$

$$\dot{\boldsymbol{\Delta}}_{\boldsymbol{Gw}} = \left[\dot{\Delta}_{X_u}, \dot{\Delta}_{Y_v}, \dot{\Delta}_{Z_w}, \dot{\Delta}_{rX_u}, \dot{\Delta}_{rY_v}, \dot{\Delta}_{rZ_w}\right]^T \tag{100}$$

$$\boldsymbol{A}_{\boldsymbol{\Delta,Gw}} = \begin{bmatrix}\boldsymbol{0} & \boldsymbol{0} & \boldsymbol{0} & \boldsymbol{A}_{\boldsymbol{\Delta}_{rX_u}} & \boldsymbol{A}_{\boldsymbol{\Delta}_{rY_v}} & \boldsymbol{A}_{\boldsymbol{\Delta}_{rZ_w}}\end{bmatrix} =$$

$$\frac{1}{2}\rho U^2 \begin{bmatrix} 0 & 0 & 0 & 0 & BC'^{\theta}_{X_u} & -BC'^{\beta}_{X_u}/\cos\theta \\ 0 & 0 & 0 & -BC_{Z_w} & BC'^{\theta}_{Y_v} & -B\left(C'^{\beta}_{Y_v} - C_{Z_w}\sin\theta\right)/\cos\theta \\ 0 & 0 & 0 & BC_{Y_v} & BC'^{\theta}_{Z_w} & -B\left(C'^{\beta}_{Z_w} + C_{Y_v}\sin\theta\right)/\cos\theta \\ 0 & 0 & 0 & 0 & B^2C'^{\theta}_{rX_u} & -B^2C'^{\beta}_{rX_u}/\cos\theta \\ 0 & 0 & 0 & -B^2C_{rZ_w} & B^2C'^{\theta}_{rY_v} & -B^2\left(C'^{\beta}_{rY_v} - C_{rZ_w}\sin\theta\right)/\cos\theta \\ 0 & 0 & 0 & B^2C_{rY_v} & B^2C'^{\theta}_{rZ_w} & -B^2\left(C'^{\beta}_{rZ_w} + C_{rY_v}\sin\theta\right)/\cos\theta \end{bmatrix} \tag{101}$$

$$\boldsymbol{A}_{\dot{\boldsymbol{\Delta}},\boldsymbol{Gw}} = \begin{bmatrix}\boldsymbol{A}_{\dot{\boldsymbol{\Delta}}_{\boldsymbol{X_u}}} & \boldsymbol{A}_{\dot{\boldsymbol{\Delta}}_{\boldsymbol{Y_v}}} & \boldsymbol{A}_{\dot{\boldsymbol{\Delta}}_{\boldsymbol{Z_w}}} & \boldsymbol{0} & \boldsymbol{0} & \boldsymbol{0}\end{bmatrix} \tag{102}$$

$$\begin{bmatrix}\boldsymbol{A}_{\dot{\boldsymbol{\Delta}}_{\boldsymbol{X_u}}} & \boldsymbol{A}_{\dot{\boldsymbol{\Delta}}_{\boldsymbol{Y_v}}} & \boldsymbol{A}_{\dot{\boldsymbol{\Delta}}_{\boldsymbol{Z_w}}}\end{bmatrix} = -\boldsymbol{A}_{\boldsymbol{b,Gw}}\left(\chi_{i,j} = 1\right) \tag{103}$$

Where $\tilde{\boldsymbol{f}}_{\boldsymbol{b,Gw}}$ is described and linearized in Section 3.5.1, $\boldsymbol{0} = [0,0,0,0,0,0]^T$ and where $\boldsymbol{A}_{\boldsymbol{b,Gw}}\left(\chi_{i,j} = 1\right)$ is found in eq. (90), for all $\chi_{i,j} = 1$.

Another common alternative is to formulate the motion-dependent forces using Scanlan's flutter derivatives (Scanlan and Tomko, 1971), as shown in eqs. (104) to (108), in the Ls system. These frequency-dependent flutter derivatives can be obtained experimentally, as done in e.g. (Zhu, 2002).

$$\tilde{\tilde{\boldsymbol{f}}}_{\boldsymbol{b,Ls}} \approx \tilde{\boldsymbol{f}}_{\boldsymbol{b,Ls}} + \boldsymbol{A}_{\boldsymbol{\Delta,Ls}}\,\boldsymbol{\Delta}_{\boldsymbol{Ls}} + \boldsymbol{A}_{\dot{\boldsymbol{\Delta}},\boldsymbol{Ls}}\,\dot{\boldsymbol{\Delta}}_{\boldsymbol{Ls}} \tag{104}$$

$$\boldsymbol{\Delta}_{\boldsymbol{Ls}} = \left[\Delta_x, \Delta_y, \Delta_z, \Delta_{rx}, \Delta_{ry}, \Delta_{rz}\right]^T \tag{105}$$

$$\dot{\boldsymbol{\Delta}}_{\boldsymbol{Ls}} = \left[\dot{\Delta}_x, \dot{\Delta}_y, \dot{\Delta}_z, \dot{\Delta}_{rx}, \dot{\Delta}_{ry}, \dot{\Delta}_{rz}\right]^T \tag{106}$$

$$\boldsymbol{A}_{\boldsymbol{Scanlan,\Delta,Ls}} = \frac{1}{2}\rho U^2 k^2 \begin{bmatrix} 0 & 0 & 0 & 0 & 0 & 0 \\ 0 & P_4^* & P_6^* & BP_3^* & 0 & 0 \\ 0 & H_6^* & H_4^* & BH_3^* & 0 & 0 \\ 0 & BA_6^* & BA_4^* & B^2A_3^* & 0 & 0 \\ 0 & 0 & 0 & 0 & 0 & 0 \\ 0 & 0 & 0 & 0 & 0 & 0 \end{bmatrix} \tag{107}$$

$$\boldsymbol{A}_{\boldsymbol{Scanlan,\dot{\Delta},Ls}} = \frac{1}{2}\rho U k \begin{bmatrix} 0 & 0 & 0 & 0 & 0 & 0 \\ 0 & BP_1^* & BP_5^* & B^2P_2^* & 0 & 0 \\ 0 & BH_5^* & BH_1^* & B^2H_2^* & 0 & 0 \\ 0 & B^2A_5^* & B^2A_1^* & B^3A_2^* & 0 & 0 \\ 0 & 0 & 0 & 0 & 0 & 0 \\ 0 & 0 & 0 & 0 & 0 & 0 \end{bmatrix} \tag{108}$$

Here $k = B\omega/U$ is the reduced frequency. In the absence of such experimental results, it is possible to compare Scanlan's expressions with the previously derived expressions for $\boldsymbol{A}_{\boldsymbol{\Delta}}$ and $\boldsymbol{A}_{\dot{\boldsymbol{\Delta}}}$, in the same coordinate system (e.g. through $\boldsymbol{A}_{\boldsymbol{Scanlan,\Delta,Ls}} = \boldsymbol{T}_{\boldsymbol{LsGw}}\boldsymbol{A}_{\boldsymbol{\Delta,Gw}}\boldsymbol{T}_{\boldsymbol{GwLs}}$ and $\boldsymbol{A}_{\boldsymbol{Scanlan,\dot{\Delta},Ls}} = \boldsymbol{T}_{\boldsymbol{LsGw}}\boldsymbol{A}_{\boldsymbol{\dot{\Delta},Gw}}\boldsymbol{T}_{\boldsymbol{GwLs}}$), rendering the quasi-static flutter derivatives in eqs. (109) to (117).

$$\begin{aligned} P_1^* = \; & 1/k\big(C_{X_u}(-\cos^2\beta\cos^2\theta - 1) + C_{Y_v}(2\cos^2\theta - 1)\sin\beta\cos\beta/\cos\theta \\ & + C_{Z_w}(1 - \sin^2\theta\cos^2\beta)\tan\theta + C'^{\beta}_{X_u}\sin\beta\cos\beta \\ & - C'^{\beta}_{Y_v}\sin^2\beta/\cos\theta - C'^{\beta}_{Z_w}\sin\beta\cos\beta\tan\theta \\ & + C'^{\theta}_{X_u}\sin\theta\cos^2\beta\cos\theta - C'^{\theta}_{Y_v}\sin\beta\sin\theta\cos\beta \\ & - C'^{\theta}_{Z_w}\sin^2\theta\cos^2\beta\big) \end{aligned} \tag{109}$$

$$\begin{aligned} P_3^* = \; & 1/k^2\big(C_{Y_v}\sin\beta\cos\beta\tan\theta - C_{Z_w}\sin^2\beta/\cos\theta - C'^{\beta}_{X_u}\sin\beta\sin\theta\cos\beta \\ & + C'^{\beta}_{Y_v}\sin^2\beta\tan\theta + C'^{\beta}_{Z_w}\sin\beta\sin\theta\cos\beta\tan\theta \\ & - C'^{\theta}_{X_u}\cos^2\beta\cos\theta + C'^{\theta}_{Y_v}\sin\beta\cos\beta + C'^{\theta}_{Z_w}\sin\theta\cos^2\beta\big) \end{aligned} \tag{110}$$

$$\begin{aligned} P_5^* = \; & 1/k\big(-C_{X_u}\sin\theta\cos\beta\cos\theta + 2C_{Y_v}\sin\beta\sin\theta + C_{Z_w}(\sin^2\theta + 1)\cos\beta \\ & - C'^{\theta}_{X_u}\cos\beta\cos^2\theta + C'^{\theta}_{Y_v}\sin\beta\cos\theta \\ & + C'^{\theta}_{Z_w}\sin\theta\cos\beta\cos\theta\big) \end{aligned} \tag{111}$$

$$H_1^* = 1/k\big(C_{X_u}(\cos^2\theta - 2) - C_{Z_w}\sin\theta\cos\theta - C'^{\theta}_{X_u}\sin\theta\cos\theta - C'^{\theta}_{Z_w}\cos^2\theta\big) \tag{112}$$

$$\begin{aligned} H_3^* = \; & 1/k^2\big(-C_{Y_v}\sin\beta - C'^{\beta}_{X_u}\sin\beta\sin\theta\tan\theta - C'^{\beta}_{Z_w}\sin\beta\sin\theta \\ & - C'^{\theta}_{X_u}\sin\theta\cos\beta - C'^{\theta}_{Z_w}\cos\beta\cos\theta\big) \end{aligned} \tag{113}$$

$$H_5^* = 1/k\big(-C_{X_u}\sin\theta\cos\beta\cos\theta + C_{Z_w}(\sin^2\theta - 2)\cos\beta + C_{X_u}'^{\beta}\sin\beta\tan\theta + C_{Z_w}'^{\beta}\sin\beta + C_{X_u}'^{\theta}\sin^2\theta\cos\beta + C_{Z_w}'^{\theta}\sin\theta\cos\beta\cos\theta\big) \tag{114}$$

$$A_1^* = 1/k\big(C_{rX_u}\sin\beta\sin\theta\cos\theta + 2C_{rY_v}\sin\theta\cos\beta + C_{rZ_w}(\cos^2\theta - 2)\sin\beta + C_{rX_u}'^{\theta}\sin\beta\cos^2\theta + C_{rY_v}'^{\theta}\cos\beta\cos\theta - C_{rZ_w}'^{\theta}\sin\beta\sin\theta\cos\theta\big) \tag{115}$$

$$A_3^* = 1/k^2\big(-C_{rY_v}\sin^2\beta\tan\theta - C_{rZ_w}\sin\beta\cos\beta/\cos\theta + C_{rX_u}'^{\beta}\sin^2\beta\sin\theta + C_{rY_v}'^{\beta}\sin\beta\cos\beta\tan\theta - C_{rZ_w}'^{\beta}\sin^2\beta\sin\theta\tan\theta + C_{rX_u}'^{\theta}\sin\beta\cos\beta\cos\theta + C_{rY_v}'^{\theta}\cos^2\beta - C_{rZ_w}'^{\theta}\sin\beta\sin\theta\cos\beta\big) \tag{116}$$

$$A_5^* = 1/k\big(C_{rX_u}\sin\beta\cos\beta\cos^2\theta + C_{rY_v}(\sin^2\beta/\cos\theta + 2\cos^2\beta\cos\theta) + C_{rZ_w}\sin\beta\sin^2\theta\cos\beta\tan\theta - C_{rX_u}'^{\beta}\sin^2\beta - C_{rY_v}'^{\beta}\sin\beta\cos\beta/\cos\theta + C_{rZ_w}'^{\beta}\sin^2\beta\tan\theta - C_{rX_u}'^{\theta}\sin\beta\sin\theta\cos\beta\cos\theta - C_{rY_v}'^{\theta}\sin\theta\cos^2\beta + C_{rZ_w}'^{\theta}\sin\beta\sin^2\theta\cos\beta\big) \tag{117}$$

The reduced frequency k cancels out when substituting these quasi-static flutter derivatives in Scanlan's expressions. The remaining flutter derivatives P_i^*, H_i^* and A_i^*, for $i = 2, 4, 6$, are equal to zero.

It should be noted that Scanlan's flutter derivatives were developed for mean winds normal to the bridge girder. These typically consider only 3 DOF, namely $\dot{\Delta}_y, \dot{\Delta}_z$ and Δ_{rx}, and could thus be incomplete for skew wind analyses.

3.6. A 2D (+1D) buffeting approach for skew winds

A 3D buffeting approach (Section 3.5) should be used when possible. It has been observed that buffeting responses vary with β and θ in a way that resembles the same variation of the corresponding aerodynamic coefficients $\boldsymbol{C}(\beta, \theta)$ with β and θ (Zhu, 2002). However, this information is not always available and wind tunnel tests and CFD analyses are commonly only performed for wind normal to the bridge girder, limiting the available information to $\boldsymbol{C}(\beta = 0, \theta)$. For preliminary assessments and comparison purposes, a novel generalization of the 2D normal projection concept is presented, for any β and θ. The (+1D) signature alludes to the option of including the contribution from the axial loads in the longitudinal dimension when an axial force coefficient is available.

The approach presented in this section assumes the validity of decomposing the three-dimensional wind-structure interaction into two independent problems:

a) A two-dimensional wind-structure interaction in the normal plane, where the relevant wind components are those projected onto either the static $\boldsymbol{yz}$-plane or the moving $\widetilde{\widetilde{\boldsymbol{yz}}}$-plane. The aerodynamic coefficients (drag, lift and moment) are only dependent on the normal projections of the inclination angles θ_{yz}, $\tilde{\theta}_{yz}$ and $\tilde{\tilde{\theta}}_{\widetilde{\widetilde{yz}}}$, also called angles-of-attack.

b) A one-dimensional wind-structure interaction in the longitudinal static $\boldsymbol{x}$- or dynamic $\widetilde{\widetilde{\boldsymbol{x}}}$-axis to account for the axial forces (due to e.g. drag forces on railings, bridge equipment, vehicles, other transversal elements, as well as viscous forces along all exposed surfaces).

The present approach is a generalization of the so-called *cosine rule* and *sine rule*, from the domain in which they were derived (for $\theta = 0$), to the more general case of arbitrary values of β and θ. It also expands the motion dependencies from 3 DOF ($\boldsymbol{y}$, $\boldsymbol{z}$ and $\boldsymbol{rx}$), to 6 DOF (e.g. for $\beta = 45°$, a small positive Δ_{rz} will make the bridge more normal to the wind, increasing the normal wind speed and associated forces).

3.6.1. The local normal wind coordinate systems and variables

The mean wind speed projection onto the $\boldsymbol{yz}$-plane, U_{yz}, and its mean angle-of-attack θ_{yz}, as well as their instantaneous (turbulence-dependent) and instantaneous

relative (turbulence- and motion-dependent) counterparts are described in eqs. (118) to (123).

$$U_{yz} = \sqrt{{U_y}^2 + {U_z}^2} \quad (118) \qquad \theta_{yz} = \arcsin\left(U_z/U_{yz}\right) \quad (119)$$

$$\tilde{U}_{yz} = \sqrt{{\tilde{U}_y}^2 + {\tilde{U}_z}^2} \quad (120) \qquad \tilde{\theta}_{yz} = \arcsin\left(\tilde{U}_z/\tilde{U}_{yz}\right) \quad (121)$$

$$\tilde{\tilde{U}}_{\tilde{\tilde{y}}\tilde{\tilde{z}}} = \sqrt{{\tilde{\tilde{U}}_{\tilde{\tilde{y}}}}^2 + {\tilde{\tilde{U}}_{\tilde{\tilde{z}}}}^2} \quad (122) \qquad \tilde{\tilde{\theta}}_{\tilde{\tilde{y}}\tilde{\tilde{z}}} = \arcsin\left(\tilde{\tilde{U}}_{\tilde{\tilde{z}}}/\tilde{\tilde{U}}_{\tilde{\tilde{y}}\tilde{\tilde{z}}}\right) \quad (123)$$

Three additional right-handed orthogonal coordinate systems are adopted, namely the local (mean) normal wind $Lnw\ (\boldsymbol{D}, \boldsymbol{A}, \boldsymbol{L})$ the local instantaneous normal wind $\widetilde{Lnw}\ (\tilde{\boldsymbol{D}}, \tilde{\boldsymbol{A}}, \tilde{\boldsymbol{L}})$ and the local relative instantaneous normal wind $\widetilde{\widetilde{Lnw}}\ \left(\tilde{\tilde{\boldsymbol{D}}}, \tilde{\tilde{\boldsymbol{A}}}, \tilde{\tilde{\boldsymbol{L}}}\right)$. The axes $\boldsymbol{D}$, $\boldsymbol{A}$ and $\boldsymbol{L}$ refer to the drag, axial and lift directions. $\boldsymbol{D}$, $\tilde{\boldsymbol{D}}$ and $\tilde{\tilde{\boldsymbol{D}}}$ describe the direction of the projected wind speeds U_{yz}, $\tilde{U}_{yz}$ and $\tilde{\tilde{U}}_{\tilde{\tilde{y}}\tilde{\tilde{z}}}$, respectively. In a 6 DOF representation of the local normal wind coordinate system, $Lnw\ (\boldsymbol{D}, \boldsymbol{A}, \boldsymbol{L}, \boldsymbol{rD}, \boldsymbol{M}, \boldsymbol{rL})$, the axis $\boldsymbol{M}$ represents the moment, as a rotation about the $\boldsymbol{A}$ axis. These coordinate systems are defined in eqs. (124) to (127) and illustrated in Fig. 10, together with the newly defined variables from eqs. (118) to (123).

$$\boldsymbol{D} = \left(U_y\boldsymbol{y} + U_z\boldsymbol{z}\right)/U_{yz};\ \ \boldsymbol{A} = -\boldsymbol{x}\cdot S;\ \ \boldsymbol{L} = \boldsymbol{D}\times\boldsymbol{A} \quad (124)$$

$$\tilde{\boldsymbol{D}} = \left(\tilde{U}_y\boldsymbol{y} + \tilde{U}_z\boldsymbol{z}\right)/\tilde{U}_{yz};\ \ \tilde{\boldsymbol{A}} = -\boldsymbol{x}\cdot \tilde{S};\ \ \tilde{\boldsymbol{L}} = \tilde{\boldsymbol{D}}\times\tilde{\boldsymbol{A}} \quad (125)$$

$$\tilde{\tilde{\boldsymbol{D}}} = \left(\tilde{\tilde{U}}_{\tilde{\tilde{y}}}\tilde{\tilde{\boldsymbol{y}}} + \tilde{\tilde{U}}_{\tilde{\tilde{z}}}\tilde{\tilde{\boldsymbol{z}}}\right)/\tilde{\tilde{U}}_{\tilde{\tilde{y}}\tilde{\tilde{z}}};\ \ \tilde{\tilde{\boldsymbol{A}}} = -\tilde{\tilde{\boldsymbol{x}}}\cdot\tilde{\tilde{S}};\ \ \tilde{\tilde{\boldsymbol{L}}} = \tilde{\tilde{\boldsymbol{D}}}\times\tilde{\tilde{\boldsymbol{A}}} \quad (126)$$

$$S = sgn(\cos\beta);\ \ \tilde{S} = sgn\left(\cos\tilde{\beta}\right);\ \ \tilde{\tilde{S}} = sgn\left(\cos\tilde{\tilde{\beta}}\right) \quad (127)$$

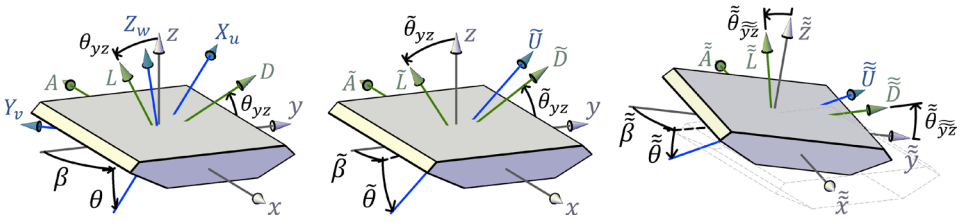

Fig. 10 – Representation of $Gw\ (\boldsymbol{X_u}, \boldsymbol{Y_v}, \boldsymbol{Z_w})$, $Ls\ (\boldsymbol{x}, \boldsymbol{y}, \boldsymbol{z})$, $\widetilde{Ls}\ (\tilde{\boldsymbol{x}}, \tilde{\boldsymbol{y}}, \tilde{\boldsymbol{z}})$, $\tilde{U}$, $\tilde{\tilde{U}}$, (β, θ), $(\tilde{\beta}, \tilde{\theta})$, $\left(\tilde{\tilde{\beta}}, \tilde{\tilde{\theta}}\right)$ and the newly defined angles θ_{yz}, $\tilde{\theta}_{yz}$ and $\tilde{\tilde{\theta}}_{\tilde{\tilde{y}}\tilde{\tilde{z}}}$ and systems $Lnw\ (\boldsymbol{D}, \boldsymbol{A}, \boldsymbol{L})$, $\widetilde{Lnw}\ (\tilde{\boldsymbol{D}}, \tilde{\boldsymbol{A}}, \tilde{\boldsymbol{L}})$ and $\widetilde{\widetilde{Lnw}}\ \left(\tilde{\tilde{\boldsymbol{D}}}, \tilde{\tilde{\boldsymbol{A}}}, \tilde{\tilde{\boldsymbol{L}}}\right)$.

The transformation matrices between Lnw, $\widetilde{Lnw}$, $\widetilde{\widetilde{Lnw}}$ and the previously defined Ls and $\widetilde{\widetilde{Ls}}$ systems can be obtained, for instance, as in eqs. (128) to (130).

$$\boldsymbol{T_{LsLnw}} = \left(\boldsymbol{R_Y}(\theta_{yz})\, \boldsymbol{R_Z}(-S\,\pi/2)\right)^T \tag{128}$$

$$\boldsymbol{T_{Ls\widetilde{Lnw}}} = \left(\boldsymbol{R_Y}(\tilde{\theta}_{yz})\, \boldsymbol{R_Z}(-\tilde{S}\,\pi/2)\right)^T \tag{129}$$

$$\boldsymbol{T_{\widetilde{\widetilde{Ls}}\widetilde{\widetilde{Lnw}}}} = \left(\boldsymbol{R_Y}\left(\tilde{\tilde{\theta}}_{\widetilde{\widetilde{yz}}}\right)\, \boldsymbol{R_Z}\left(-\tilde{\tilde{S}}\,\pi/2\right)\right)^T \tag{130}$$

Finally, it can be convenient to express the turbulence components in the Lnw system as a function of the original components in the Gw system (see eq. (131)).

$$\boldsymbol{a_{Lnw}} = [a_D, a_A, a_L]^T = \boldsymbol{T_{LnwGw}}\, \boldsymbol{a_{Gw}} = \boldsymbol{T_{LsLnw}}^{\boldsymbol{T}}\, \boldsymbol{T_{LsGw}}\, [u, v, w]^T \tag{131}$$

3.6.2. Fluctuating wind forces due to turbulence

3.6.2.1. General formulation

The vector of six aerodynamic forces $\widetilde{\boldsymbol{F}}_{\boldsymbol{ad,Gs}}$ in the Gs system, for each bridge element, can be obtained from eqs. (132) to (133).

$$\widetilde{\boldsymbol{F}}_{\boldsymbol{ad,Gs}} = L\, \boldsymbol{T_{GsLs}}\, \boldsymbol{T_{LsLnw}}\, \tilde{\boldsymbol{f}}_{\boldsymbol{ad,Lnw}} \tag{132}$$

$$\tilde{\boldsymbol{f}}_{\boldsymbol{ad,Lnw}} = \boldsymbol{T_{Lnw\widetilde{Lnw}}}\, 1/2\, \rho\, \tilde{U}_{yz}{}^2\, \boldsymbol{B_{Lnw}} \widetilde{\boldsymbol{C}}_{\widetilde{Lnw}} \tag{133}$$

Where $\boldsymbol{B_{Lnw}} = diag(H, 0, B, 0, B^2, 0)$ is a diagonal matrix and H is the cross-section height as typically used to normalize C_D. $\widetilde{\boldsymbol{C}}_{\widetilde{Lnw}}(\tilde{\theta}_{yz}) = \left[\tilde{C}_{\tilde{D}}, 0, \tilde{C}_{\tilde{L}}, 0, \tilde{C}_{\tilde{M}}, 0\right]^T$ is the vector of aerodynamic coefficients in the $\widetilde{Lnw}$ system, for an instantaneous projected angle of attack $\tilde{\theta}_{yz}$. $\boldsymbol{T_{Lnw\widetilde{Lnw}}} = \boldsymbol{T_{LnwLs}} \boldsymbol{T_{Ls\widetilde{Lnw}}}$ is the transformation matrix from $\widetilde{Lnw}$ to Lnw.

The vector of normal wind buffeting forces per unit length and for each element, containing the time-varying drag, lift and moment forces, is given in eq. (134) by simply subtracting the mean normal wind forces $\boldsymbol{f_{mean,Lnw}}$, where $\boldsymbol{C_{Lnw}}(\theta_{yz}) = [C_D, 0, C_L, 0, C_M, 0]^T$.

$$\tilde{\boldsymbol{f}}_{\boldsymbol{b,Lnw}} = \tilde{\boldsymbol{f}}_{\boldsymbol{ad,Lnw}} - \boldsymbol{f_{mean,Lnw}} = \tilde{\boldsymbol{f}}_{\boldsymbol{ad,Lnw}} - 1/2\, \rho\, U_{yz}{}^2\, \boldsymbol{B_{Lnw}} \boldsymbol{C_{Lnw}} \tag{134}$$

3.6.2.2. Linear formulation

The vector of buffeting forces $\tilde{\boldsymbol{f}}_{\boldsymbol{b,Lnw}}$ is a non-linear function of the turbulence components, either represented as u, v and w, or as a_D, a_A and a_L. The linearization process conducted in Section 3.5.1 can be repeated here.

Limitation: The linear approximations presented in this section should not be used whenever $\widetilde{U}_y$ oscillates between positive and negative values, i.e., in the vicinity of $\beta \sim \pm 90°$. The functions $\boldsymbol{T}_{\boldsymbol{Ls}\widetilde{\boldsymbol{Lnw}}}$ and $\tilde{\theta}_{yz}$ will have singularities at $\tilde{\beta} = \pm 90°$ (Example: when β is close to 90°, the $\boldsymbol{y}$-projected turbulence can be larger than the $\boldsymbol{y}$-projected mean wind, which can abruptly change the instantaneous drag direction $\widetilde{\boldsymbol{D}}$ at each time instant). It is thus assumed that $\tilde{S} = S$ for all time steps.

By conveniently adopting a representation that uses a_D, a_A and a_L, instead of u, v and w, the linearization of ${\widetilde{U}_{yz}}^2$, $\tilde{\theta}_{yz}$, $\boldsymbol{T}_{\boldsymbol{Lnw}\widetilde{\boldsymbol{Lnw}}}$ (assuming $S = \tilde{S}$) and $\widetilde{\boldsymbol{C}}_{\widetilde{\boldsymbol{Lnw}}}$ follows in eqs. (135) to (138).

$$ {\widetilde{U}_{yz}}^2 \approx {U_{yz}}^2 + 2U_{yz}a_D \tag{135} $$

$$ \tilde{\theta}_{yz} = \theta_{yz} + \widetilde{\Delta\theta}_{yz} \approx \theta_{yz} + \frac{a_L}{U_{yz}} \tag{136} $$

$$ \boldsymbol{T}_{\boldsymbol{Lnw}\widetilde{\boldsymbol{Lnw}}}(\tilde{S} = S) = \left(\boldsymbol{R}_{\boldsymbol{Y}}(\tilde{\theta}_{yz})\, \boldsymbol{R}_{\boldsymbol{Y}}(-\theta_{yz})\right)^T \approx \begin{bmatrix} 1 & 0 & -\widetilde{\Delta\theta}_{yz} \\ 0 & 1 & 0 \\ \widetilde{\Delta\theta}_{yz} & 0 & 1 \end{bmatrix} \tag{137} $$

$$ \widetilde{\boldsymbol{C}}_{\widetilde{\boldsymbol{Lnw}}} \approx \boldsymbol{C}_{\boldsymbol{Lnw}} + \boldsymbol{C}'_{\boldsymbol{Lnw}}\, \widetilde{\Delta\theta}_{yz} \tag{138} $$

Where $\boldsymbol{C}'_{\boldsymbol{Lnw}} = \frac{\partial \boldsymbol{C}_{\boldsymbol{Lnw}}(\theta_{yz})}{\partial \theta_{yz}} = [C'_D, 0, C'_L, 0, C'_M, 0]^T$ is the vector of aerodynamic coefficient derivatives with respect to the angle-of-attack, at a mean angle θ_{yz}.

The vector of linearized normal buffeting forces due to the $\boldsymbol{yz}$-projected wind, $\tilde{\boldsymbol{f}}_{\boldsymbol{b,Lnw}}$, after being linearized with respect to the turbulence components, can then be separated into a coefficient matrix $\boldsymbol{A}_{\boldsymbol{b,Lnw}}$ and the turbulence components vector $\boldsymbol{a}_{\boldsymbol{Lnw}} = [a_D, a_A, a_L]^T$, as in eqs. (139) and (140).

$$ \tilde{\boldsymbol{f}}_{\boldsymbol{b,Lnw}} \approx \boldsymbol{A}_{\boldsymbol{b,Lnw}}\, \boldsymbol{a}_{\boldsymbol{Lnw}} \tag{139} $$

$$\boldsymbol{A_{b,Lnw}} = \frac{1}{2}\rho U_{yz}\begin{bmatrix} 2HC_D\chi_{D,a_D} & 0 & (HC'_D - BC_L)\chi_{D,a_L} \\ 0 & 0 & 0 \\ 2BC_L\chi_{L,a_D} & 0 & (BC'_L + HC_D)\chi_{L,a_L} \\ 0 & 0 & 0 \\ 2B^2C_M\chi_{M,a_D} & 0 & B^2C'_M\chi_{M,a_L} \\ 0 & 0 & 0 \end{bmatrix} \tag{140}$$

Where $\chi_{i,j}$ are the cross-sectional admittance functions associated with the aerodynamic coefficient C_i and the turbulence component j.

Alternative representations of the $\boldsymbol{A_b}$ matrix can be easily obtained by pre- and/or post-multiplication with the right transformation matrices.

Example 1: To obtain the $\boldsymbol{A_{b,LnwGw}}$ matrix, which instead is to be post-multiplied with $\boldsymbol{a_{Gw}}$, $\boldsymbol{A_{b,Lnw}}$ can be simply post-multiplied by $\boldsymbol{T_{LnwGw}}$ (eq. (141)).

$$\tilde{\boldsymbol{f}}_{\boldsymbol{b,Lnw}} \approx \boldsymbol{A_{b,Lnw}}\,\boldsymbol{a_{Lnw}} = \boldsymbol{A_{b,Lnw}}\,\boldsymbol{T_{LnwGw}}\,\boldsymbol{T_{GwLnw}}\,\boldsymbol{a_{Lnw}} = \boldsymbol{A_{b,LnwGw}}\,\boldsymbol{a_{Gw}} \tag{141}$$

Example 2: For the same matrix to return forces in the Ls system, it can be pre-multiplied by $\boldsymbol{T_{LsLnw}}$ (eq. (142)).

$$\tilde{\boldsymbol{f}}_{\boldsymbol{b,Ls}} \approx \boldsymbol{A_{b,LsGw}}\,\boldsymbol{a_{Gw}} = \boldsymbol{T_{LsLnw}}\boldsymbol{A_{b,LnwGw}}\,\boldsymbol{a_{Gw}} \tag{142}$$

3.6.3. Fluctuating wind forces due to turbulence and structural motions

3.6.3.1. General formulation

Analogously to Section 3.5.2, and using the variables defined in Section 3.6.1, the turbulence- and motion-dependent vector of aerodynamic forces, per unit length, at each element and at each time step, represented in the Lnw system, is described by eqs. (143) and (144).

$$\tilde{\tilde{\boldsymbol{f}}}_{\boldsymbol{ad,Lnw}} = \boldsymbol{T}_{\boldsymbol{Lnw}\widetilde{\widetilde{\boldsymbol{Lnw}}}}\, 1/2\,\rho\, \tilde{\tilde{U}}_{\widetilde{\widetilde{yz}}}^{\,2}\, \boldsymbol{B_{Lnw}}\, \tilde{\tilde{\boldsymbol{C}}}_{\widetilde{\widetilde{\boldsymbol{Lnw}}}} \tag{143}$$

$$\boldsymbol{T}_{\boldsymbol{Lnw}\widetilde{\widetilde{\boldsymbol{Lnw}}}} = \boldsymbol{T_{LnwLs}}\,\boldsymbol{T}_{\boldsymbol{Ls}\widetilde{\widetilde{\boldsymbol{Ls}}}}\,\boldsymbol{T}_{\widetilde{\widetilde{\boldsymbol{Ls}}}\widetilde{\widetilde{\boldsymbol{Lnw}}}} \tag{144}$$

Where $\tilde{\tilde{\boldsymbol{C}}}_{\widetilde{\widetilde{\boldsymbol{Lnw}}}}\left(\tilde{\tilde{\theta}}_{\widetilde{\widetilde{yz}}}\right) = \left[\tilde{\tilde{C}}_{\tilde{\tilde{D}}}, 0, \tilde{\tilde{C}}_{\tilde{\tilde{L}}}, 0, \tilde{\tilde{C}}_{\tilde{\tilde{M}}}, 0\right]^T$ is the vector of aerodynamic coefficients, represented in the $\widetilde{\widetilde{Lnw}}$ system and dependent on $\tilde{\tilde{\theta}}_{\widetilde{\widetilde{yz}}}$.

3.6.3.2. Linear formulation

The vector of turbulence- and motion-dependent aerodynamic forces $\tilde{\tilde{\boldsymbol{f}}}_{\boldsymbol{ad,Lnw}}$ is a non-linear function of u, v, w, $\boldsymbol{\Delta}$ and $\dot{\boldsymbol{\Delta}}$. The linearization process conducted in Section 3.5.2 can then be repeated here.

Limitation: Analogously to the limitation described for the linear expressions in Section 3.6.2, the linear approximations presented in this section should not be used whenever $\tilde{\tilde{U}}_{\tilde{y}}$ oscillates between positive and negative values, i.e. in the vicinity of $\beta \sim \pm 90°$, since the functions $\boldsymbol{T}_{\boldsymbol{Lnw}\tilde{\tilde{\boldsymbol{Lnw}}}}$ and $\tilde{\tilde{\theta}}_{\tilde{\tilde{y}}\tilde{\tilde{z}}}$ will have singularities at $\tilde{\tilde{\beta}} = \pm 90°$. It is thus assumed that $\tilde{\tilde{S}} = \tilde{S} = S$ for all time steps.

Analogously to the definition of $\tilde{\tilde{u}}$, $\tilde{\tilde{v}}$ and $\tilde{\tilde{w}}$, when a_D, a_A and a_L account for the relative velocity between the wind and the structure, they are denoted $\tilde{\tilde{a}}_D$, $\tilde{\tilde{a}}_A$ and $\tilde{\tilde{a}}_L$, as in eqs. (145) to (147).

$$\tilde{\tilde{a}}_D = a_D - \dot{\Delta}_D \tag{145}$$

$$\tilde{\tilde{a}}_A = a_A - \dot{\Delta}_A \tag{146}$$

$$\tilde{\tilde{a}}_L = a_L - \dot{\Delta}_L \tag{147}$$

With the newly defined variables, following the same linearization principles as in Section 3.5.2.2 and representing the structural motions in the Lnw system as $\boldsymbol{\Delta}_{\boldsymbol{Lnw}} = [\Delta_D, \Delta_A, \Delta_L, \Delta_{rD}, \Delta_M, \Delta_{rL}]^T = \boldsymbol{T}_{\boldsymbol{LnwLs}}\boldsymbol{\Delta}_{\boldsymbol{Ls}}$ and $\dot{\boldsymbol{\Delta}}_{\boldsymbol{Lnw}} = [\dot{\Delta}_D, \dot{\Delta}_A, \dot{\Delta}_L, \dot{\Delta}_{rD}, \dot{\Delta}_M, \dot{\Delta}_{rL}]^T = \boldsymbol{T}_{\boldsymbol{LnwLs}}\dot{\boldsymbol{\Delta}}_{\boldsymbol{Ls}}$, then $\tilde{\tilde{U}}_{\tilde{\tilde{y}}\tilde{\tilde{z}}}^{\ 2}$, $\tilde{\tilde{\theta}}_{\tilde{\tilde{y}}\tilde{\tilde{z}}}$, $\boldsymbol{T}_{\boldsymbol{Lnw}\tilde{\tilde{\boldsymbol{Lnw}}}}$ and $\tilde{\tilde{\boldsymbol{C}}}_{\tilde{\tilde{\boldsymbol{Lnw}}}}$ can be simplified into eqs. (148) to (151).

$$\tilde{\tilde{U}}_{\tilde{\tilde{y}}\tilde{\tilde{z}}}^{\ 2} \approx U_{yz}\left(U_{yz} + 2\tilde{\tilde{a}}_D + 2SU\Delta_{rL}\sin\beta\cos\theta\right) \tag{148}$$

$$\tilde{\tilde{\theta}}_{\tilde{\tilde{y}}\tilde{\tilde{z}}} = \theta_{yz} + \tilde{\tilde{\Delta\theta}}_{\tilde{\tilde{y}}\tilde{\tilde{z}}} = \theta_{yz} + \Delta_M + \left(\tilde{\tilde{a}}_L - SU\Delta_{rD}\sin\beta\cos\theta\right)/U_{yz} \tag{149}$$

$$\boldsymbol{T}_{\boldsymbol{Lnw}\tilde{\tilde{\boldsymbol{Lnw}}}}\left(\tilde{\tilde{S}} = S\right) \approx \begin{bmatrix} 1 & -\Delta_{rL} & -\tilde{\tilde{\Delta\theta}}_{\tilde{\tilde{y}}\tilde{\tilde{z}}} + \Delta_M \\ \Delta_{rL} & 1 & -\Delta_{rD} \\ \tilde{\tilde{\Delta\theta}}_{\tilde{\tilde{y}}\tilde{\tilde{z}}} - \Delta_M & \Delta_{rD} & 1 \end{bmatrix} \tag{150}$$

$$\tilde{\tilde{\boldsymbol{C}}}_{\tilde{\tilde{\boldsymbol{Lnw}}}} \approx \boldsymbol{C}_{\boldsymbol{Lnw}} + \boldsymbol{C}'_{\boldsymbol{Lnw}}\,\tilde{\tilde{\Delta\theta}}_{\tilde{\tilde{y}}\tilde{\tilde{z}}} \tag{151}$$

Note that $\boldsymbol{T}_{\boldsymbol{Lnw}\tilde{\tilde{\boldsymbol{Lnw}}}}$ is independent of Δ_M since such a bridge rotation leaves both the wind projection and the drag, axial and lift directions unchanged.

Finally, the vector of linearized wind forces due to the normal-projected wind and the structural motions, $\tilde{\tilde{\boldsymbol{f}}}_{\boldsymbol{b,Lnw}} = \tilde{\tilde{\boldsymbol{f}}}_{\boldsymbol{ad,Lnw}} - \boldsymbol{f}_{\boldsymbol{mean,Lnw}}$, can be linearized into eqs. (152) to (156).

$$\tilde{\tilde{\boldsymbol{f}}}_{\boldsymbol{b,Lnw}} \approx \tilde{\boldsymbol{f}}_{\boldsymbol{b,Lnw}} + \boldsymbol{A}_{\boldsymbol{\Delta,Lnw}}\,\boldsymbol{\Delta}_{\boldsymbol{Lnw}} + \boldsymbol{A}_{\dot{\boldsymbol{\Delta}},\boldsymbol{Lnw}}\,\dot{\boldsymbol{\Delta}}_{\boldsymbol{Lnw}} \tag{152}$$

$$\boldsymbol{A}_{\boldsymbol{\Delta,Lnw}} = [\boldsymbol{0} \quad \boldsymbol{0} \quad \boldsymbol{0} \quad \boldsymbol{A}_{\boldsymbol{\Delta}_{rD}} \quad \boldsymbol{A}_{\boldsymbol{\Delta}_{M}} \quad \boldsymbol{A}_{\boldsymbol{\Delta}_{rL}}] \tag{153}$$

$$[\boldsymbol{A}_{\boldsymbol{\Delta}_{rD}} \quad \boldsymbol{A}_{\boldsymbol{\Delta}_{M}} \quad \boldsymbol{A}_{\boldsymbol{\Delta}_{rL}}] = \frac{1}{2}\rho {U_{yz}}^2 \cdot$$

$$\begin{bmatrix} S(BC_L - HC_D')\sin\beta\cos\theta\, U/U_{yz} & HC_D' & 2SHC_D\sin\beta\cos\theta\, U/U_{yz} \\ -BC_L & 0 & HC_D \\ -S(HC_D + BC_L')\sin\beta\cos\theta\, U/U_{yz} & BC_L' & 2SBC_L\sin\beta\cos\theta\, U/U_{yz} \\ 0 & 0 & -B^2C_M \\ -SB^2C_M'\sin\beta\cos\theta\, U/U_{yz} & B^2C_M' & 2SB^2C_M\sin\beta\cos\theta\, U/U_{yz} \\ B^2C_M & 0 & 0 \end{bmatrix} \tag{154}$$

$$\boldsymbol{A}_{\dot{\boldsymbol{\Delta}},\boldsymbol{Lnw}} = [\boldsymbol{A}_{\dot{\boldsymbol{\Delta}}_{\boldsymbol{D}}} \quad \boldsymbol{A}_{\dot{\boldsymbol{\Delta}}_{\boldsymbol{A}}} \quad \boldsymbol{A}_{\dot{\boldsymbol{\Delta}}_{\boldsymbol{L}}} \quad \boldsymbol{0} \quad \boldsymbol{0} \quad \boldsymbol{0}] \tag{155}$$

$$[\boldsymbol{A}_{\dot{\boldsymbol{\Delta}}_{\boldsymbol{D}}} \quad \boldsymbol{A}_{\dot{\boldsymbol{\Delta}}_{\boldsymbol{A}}} \quad \boldsymbol{A}_{\dot{\boldsymbol{\Delta}}_{\boldsymbol{L}}}] = -\boldsymbol{A}_{\boldsymbol{b,Lnw}}(\chi_{i,j} = 1) \tag{156}$$

Where $\tilde{\boldsymbol{f}}_{\boldsymbol{b,Lnw}}$ is described and linearized in Section 3.6.2, $\boldsymbol{0} = [0,0,0,0,0,0]^T$ and $\boldsymbol{A}_{\boldsymbol{b,Lnw}}(\chi_{i,j} = 1)$ is found in eq. (140) with all $\chi_{i,j} = 1$. Note that both Δ_{rD} and Δ_{rL} cause a change in the normal plane, from $\boldsymbol{yz}$ to $\tilde{\tilde{\boldsymbol{yz}}}$, which consequently changes the normal projection of the wind.

3.6.4. Axial force contribution

3.6.4.1. General formulation

The mean axial force $\boldsymbol{f}_{\boldsymbol{mean,axial}}$, the instantaneous axial force $\tilde{\boldsymbol{f}}_{\boldsymbol{ad,axial}}$ and the motion-dependent instantaneous axial force $\tilde{\tilde{\boldsymbol{f}}}_{\boldsymbol{ad,axial}}$ are described in eqs. (157) to (159), for each bridge element, as vectors in the consistent Ls system.

$$\boldsymbol{f}_{\boldsymbol{mean,axial,Ls}} = [1/2\,\rho U_x|U_x|BC_x, 0,0,0,0,0]^T \tag{157}$$

$$\tilde{\boldsymbol{f}}_{\boldsymbol{ad,axial,Ls}} = \left[1/2\,\rho\tilde{U}_x\left|\tilde{U}_x\right|BC_x, 0,0,0,0,0\right]^T \tag{158}$$

$$\tilde{\tilde{\boldsymbol{f}}}_{\boldsymbol{ad,axial,Ls}} = \boldsymbol{T}_{\boldsymbol{Ls\tilde{\tilde{Ls}}}}\left[1/2\,\rho\tilde{\tilde{U}}_{\tilde{\tilde{x}}}\left|\tilde{\tilde{U}}_{\tilde{\tilde{x}}}\right|BC_x, 0,0,0,0,0\right]^T \tag{159}$$

In this section, $C_x = C_x(\beta = -\pi/2\,, \theta = 0)$ can be directly obtained for the case when the wind is parallel to the bridge girder. It is normalized by B (or alternatively by the perimeter of the cross-section), non-negative and assumed independent of both β and θ (the β-dependecy of the force is already considered in U_x). This results in maximum axial forces when the wind is parallel to the longitudinal axis. However, it should be noted that the maximum axial force may occur for skew angles (see e.g. (Veritas, 2010) and their reference to (Eames, 1968) with respect to inclined cylinders). Alternatively, C_x can be obtained by curve fitting the results of different skew wind cases.

Each of the force vectors $\boldsymbol{f_{mean,axial}}$, $\tilde{\boldsymbol{f}}_{\boldsymbol{ad,axial}}$ and $\tilde{\tilde{\boldsymbol{f}}}_{\boldsymbol{ad,axial}}$ can be then added to their (non-axial) counterparts in sections 3.6.2 and 3.6.3, within the same coordinate system.

3.6.4.2. Linear formulation

The linearized axial force contribution is most conveniently expressed in the Ls system (in the Lnw system, the $\widetilde{\boldsymbol{A}}$ and $\widetilde{\tilde{\boldsymbol{A}}}$ axes invert in the vicinity of $\tilde{\beta} \sim \pm 90°$ and $\tilde{\tilde{\beta}} \sim \pm 90°$). The vector of turbulence components in the Ls system, $\boldsymbol{a_{Ls}}$, and the linearized expressions for $\widetilde{U}_x\left|\widetilde{U}_x\right|$ and $\widetilde{\widetilde{U}}_{\tilde{\tilde{x}}}\left|\widetilde{\widetilde{U}}_{\tilde{\tilde{x}}}\right|$ are introduced in eqs. (160) to (162).

$$\boldsymbol{a_{Ls}} = \left[a_x, a_y, a_z\right]^T = \left[\widetilde{U}_x - U_x, \widetilde{U}_y - U_y, \widetilde{U}_z - U_z\right]^T = \boldsymbol{T_{LsGw}}[u, v, w]^T \tag{160}$$

$$\widetilde{U}_x\left|\widetilde{U}_x\right| \approx U_x|U_x| + 2|U_x|a_x \tag{161}$$

$$\widetilde{\widetilde{U}}_{\tilde{\tilde{x}}}\left|\widetilde{\widetilde{U}}_{\tilde{\tilde{x}}}\right| \approx U_x|U_x| + 2|U_x|\left(\left(a_x - \dot{\Delta}_x\right) + U_y\Delta_{rz} - U_z\Delta_{ry}\right) \tag{162}$$

Then, the linear approximations of $\tilde{\boldsymbol{f}}_{\boldsymbol{ad,axial,Ls}}$ and $\tilde{\tilde{\boldsymbol{f}}}_{\boldsymbol{ad,axial,Ls}}$ are expressed in eqs. (163) to (169).

$$\tilde{\boldsymbol{f}}_{\boldsymbol{ad,axial,Ls}} \approx \boldsymbol{f}_{\boldsymbol{mean,axial,Ls}} + \boldsymbol{A}_{\boldsymbol{b,axial,Ls}}\,\boldsymbol{a_{Ls}} \tag{163}$$

$$\tilde{\tilde{\boldsymbol{f}}}_{\boldsymbol{ad,axial,Ls}} \approx \tilde{\boldsymbol{f}}_{\boldsymbol{ad,axial,Ls}} + \boldsymbol{A}_{\boldsymbol{\Delta,axial,Ls}}\boldsymbol{\Delta_{Ls}} + \boldsymbol{A}_{\boldsymbol{\dot{\Delta},axial,Ls}}\boldsymbol{\dot{\Delta}_{Ls}} \tag{164}$$

$$\boldsymbol{A_{b,axial,Ls}} = 1/2\rho B|U_x|\begin{bmatrix} 2C_x\,\chi_{x,a_x} & 0 & 0 \\ 0 & 0 & 0 \\ 0 & 0 & 0 \\ 0 & 0 & 0 \\ 0 & 0 & 0 \\ 0 & 0 & 0 \end{bmatrix} \tag{165}$$

$$\boldsymbol{A_{\Delta,axial,Ls}} = \begin{bmatrix} \mathbf{0} & \mathbf{0} & \mathbf{0} & \boldsymbol{A_{\Delta_{rx}}} & \boldsymbol{A_{\Delta_{ry}}} & \boldsymbol{A_{\Delta_{rz}}} \end{bmatrix}_{axial} \tag{166}$$

$$\begin{bmatrix} \boldsymbol{A_{\Delta_{rx}}} & \boldsymbol{A_{\Delta_{ry}}} & \boldsymbol{A_{\Delta_{rz}}} \end{bmatrix}_{axial} = 1/2\rho B|U_x| \begin{bmatrix} 0 & -2U_zC_x & 2U_yC_x \\ 0 & 0 & U_xC_x \\ 0 & -U_xC_x & 0 \\ 0 & 0 & 0 \\ 0 & 0 & 0 \\ 0 & 0 & 0 \end{bmatrix} \tag{167}$$

$$\boldsymbol{A_{\dot{\Delta},axial,Ls}} = \begin{bmatrix} \boldsymbol{A_{\dot{\Delta}_x}} & \boldsymbol{A_{\dot{\Delta}_y}} & \boldsymbol{A_{\dot{\Delta}_z}} & \mathbf{0} & \mathbf{0} & \mathbf{0} \end{bmatrix}_{axial} \tag{168}$$

$$\begin{bmatrix} \boldsymbol{A_{\dot{\Delta}_x}} & \boldsymbol{A_{\dot{\Delta}_y}} & \boldsymbol{A_{\dot{\Delta}_z}} \end{bmatrix}_{axial} = -\boldsymbol{A_{b,axial,Ls}}(\chi_{x,a_x} = 1) \tag{169}$$

Where $\mathbf{0} = [0,0,0,0,0,0]^T$ and χ_{x,a_x} is the cross-sectional admittance function associated with the aerodynamic coefficient C_x and the $\boldsymbol{x}$-projected turbulence a_x.

3.7. Response analysis

3.7.1. Time domain approach

In the time domain, the equation of motion for a dynamic structural system under forced vibration is expressed by eq. (170), with the global buffeting forces on the right-hand side.

$$\boldsymbol{M^G}\ddot{\boldsymbol{\Delta}}^{\boldsymbol{G}}(t) + \boldsymbol{C^G}\dot{\boldsymbol{\Delta}}^{\boldsymbol{G}}(t) + \boldsymbol{K^G}\boldsymbol{\Delta^G}(t) = \boldsymbol{F_b^G}(t) \tag{170}$$

Here $\boldsymbol{M^G}$, $\boldsymbol{C^G}$ and $\boldsymbol{K^G}$ are the global mass, damping and stiffness matrices, with size $[6N_N \times 6N_N]$, with N_N as the number of structural nodes in a FEM model, where each node has 6 DOF; $\boldsymbol{\Delta^G}$, $\dot{\boldsymbol{\Delta}}^{\boldsymbol{G}}$ and $\ddot{\boldsymbol{\Delta}}^{\boldsymbol{G}}$ are the global vectors of structural displacements, velocities, and accelerations, with size $[6N_N]$; $\boldsymbol{F_b^G}$ is the global vector of nodal buffeting forces, with size $[6N_N]$, assembled from all the elemental $\widetilde{\boldsymbol{F}}_{\boldsymbol{b}} = L\,\widetilde{\boldsymbol{f}}_{\boldsymbol{b}}$ or $\widetilde{\widetilde{\boldsymbol{F}}}_{\boldsymbol{b}} = L\,\widetilde{\widetilde{\boldsymbol{f}}}_{\boldsymbol{b}}$ vectors. These global matrices and vectors are assembled following standard FEM techniques and are represented in a global and consistent coordinate system such as the Gs system.

To numerically simulate the turbulent wind field, the turbulence simulator *TurbSim* (Jonkman, 2009) or the freely available *MATLAB* code by Etienne Cheynet (Cheynet, 2020) can be used.

To solve the equation of motion, a numerical integration method, such as the Newmark-beta method (Newmark, 1959), can be used.

In a linearized format, the motion-dependent force coefficient matrices $\boldsymbol{A_{\Delta}}$ and $\boldsymbol{A_{\dot{\Delta}}}$ can be moved to the left-hand side of the equation of motion, joining the other $\boldsymbol{\Delta}$ and $\dot{\boldsymbol{\Delta}}$ dependencies, instead of contributing to the global vector $\boldsymbol{F_b^G}$. Thus, they can be converted into the so-called aerodynamic stiffness $\boldsymbol{K_{AE}^G}$ and aerodynamic damping $\boldsymbol{C_{AE}^G}$ global matrices. $\boldsymbol{K_{AE}^G}$ and $\boldsymbol{C_{AE}^G}$ are expressed in the Gs system so that they can be added to the structural stiffness $\boldsymbol{K_S^G}$ and structural damping $\boldsymbol{C_S^G}$ global matrices, as in eqs. (171) and (172).

$$\boldsymbol{K^G} = \boldsymbol{K_S^G} + \boldsymbol{K_{AE}^G} \tag{171}$$

$$\boldsymbol{C^G} = \boldsymbol{C_S^G} + \boldsymbol{C_{AE}^G} \tag{172}$$

They have the size $[6N_N \times 6N_N]$ and can be assembled from the individual $\boldsymbol{K_{AE}}$ and $\boldsymbol{C_{AE}}$ matrices representative of each element, with size $[6 \times 6]$. $\boldsymbol{K_{AE}}$ and $\boldsymbol{C_{AE}}$ are obtained through eqs. (173) and (174).

$$\boldsymbol{K_{AE}} = -L\,\boldsymbol{T_{GsGw}}\boldsymbol{A_{\Delta,Gw}}\boldsymbol{T_{GwGs}} \tag{173}$$

$$\boldsymbol{C_{AE}} = -L\,\boldsymbol{T_{GsGw}}\boldsymbol{A_{\dot{\Delta},Gw}}\boldsymbol{T_{GwGs}} \tag{174}$$

$\boldsymbol{K_{AE}}$ and $\boldsymbol{C_{AE}}$ can also be estimated in a frequency-dependent format. To express such frequency-dependent forces in the time domain, as well as the frequency-dependent cross-sectional admittance functions $\chi_{i,j}$, one approach is given in e.g. Chapter 4.7 in (Xu, 2013). In a frequency domain analysis, $\boldsymbol{K_{AE}}$ and $\boldsymbol{C_{AE}}$ can be transformed to modal coordinates and added to the modal stiffness and damping matrices, inside the modal frequency response function.

3.7.2. Frequency domain approach

The frequency domain approach is a Fourier transform of its time domain counterpart. In the time domain, a displacement vector $\boldsymbol{\Delta}$ is estimated, whereas in the frequency domain, a cross-spectral density matrix of the displacement response $\boldsymbol{S_{\Delta\Delta}}(\omega)$ is estimated. From known modal analyses and buffeting theory solution schemes (see e.g. (Chopra, 2007; Clough and Penzien, 2003; Strømmen, 2010; Xu, 2013)) it follows that eqs. (175) to (180) can be used to obtain the standard deviation of the displacement response $\boldsymbol{\sigma_{\Delta}}$. The response is here given for the Gs system, as a function of $\boldsymbol{S_{aa}}(\omega)$ which is naturally expressed in the Gw system. Single-sided spectra are used. The superscript $^{\boldsymbol{G}}$ is omitted when there is no ambiguity.

$$\boldsymbol{\sigma_{\Delta}} = \sqrt{\int_0^{\infty} \boldsymbol{S_{\Delta}}(\omega)\, d\omega} \tag{175}$$

$$\boldsymbol{S_{\Delta\Delta}}(\omega) = \boldsymbol{\Phi}\, \boldsymbol{S_{\widehat{\eta}\widehat{\eta}}}(\omega)\, \boldsymbol{\Phi}^T \tag{176}$$

$$\boldsymbol{S_{\widehat{\eta}\widehat{\eta}}}(\omega) = \widehat{\boldsymbol{H}}^*(\omega)\, \boldsymbol{S_{\widehat{F}\widehat{F}}}(\omega)\, \widehat{\boldsymbol{H}}^T(\omega) \tag{177}$$

$$\boldsymbol{S_{\widehat{F}\widehat{F}}}(\omega) = \boldsymbol{\Phi}^T\, \boldsymbol{P_b^{G^*}}\, \boldsymbol{S_{aa}}(\omega)\, \boldsymbol{P_b^{G^T}}\, \boldsymbol{\Phi} \tag{178}$$

$$\widehat{\boldsymbol{H}}(\omega) = \left[-\omega^2 \widehat{\boldsymbol{M}} + i\omega \widehat{\boldsymbol{C}} + \widehat{\boldsymbol{K}}\right]^{-1} \tag{179}$$

$$\boldsymbol{P_b} = L\, \boldsymbol{A_{b,GsGw}} = L\, \boldsymbol{T_{GsGw}} \boldsymbol{A_{b,Gw}} \tag{180}$$

Here $\boldsymbol{\sigma_{\Delta}}$ is the standard deviation of the response with size $[6N_N]$, with N_N as the number of nodes. $\boldsymbol{S_{\Delta}}(\omega)$ is the auto-spectral density vector of the nodal displacement response. It can be extracted from the diagonal elements of $\boldsymbol{S_{\Delta\Delta}}(\omega)$ and has size $[6N_N]$. ω is the angular frequency. $\boldsymbol{S_{\Delta\Delta}}(\omega)$ is the cross-spectral density matrix of the nodal displacement response, with size $[6N_N \times 6N_N]$. $\boldsymbol{\Phi}$ is the matrix of mode shapes with size $[6N_N \times N_M]$, with N_M as the number of modes. $\boldsymbol{S_{\widehat{\eta}\widehat{\eta}}}(\omega)$ is the cross-spectral density matrix of the modal displacement response with size $[N_M \times N_M]$. $\widehat{\boldsymbol{H}}(\omega)$ is the modal frequency response function matrix with size $[N_M \times N_M]$. In the absence of modal coupling, it becomes a diagonal matrix. $\boldsymbol{S_{\widehat{F}\widehat{F}}}(\omega)$ is the cross-spectral density matrix of the modal buffeting loads with size $[N_M \times N_M]$. $\boldsymbol{S_{aa}}(\omega)$ is the cross-spectral density matrix of the turbulence components u, v and w, with size $[3N_N \times 3N_N]$. One possible formulation of $\boldsymbol{S_{aa}}(\omega)$ can be found in (Zhu and Xu, 2005). $\boldsymbol{P_b^G}$ is the global coefficient matrix of buffeting forces assembled from each elemental $\boldsymbol{P_b}$, and it has size $[6N_N \times 3N_N]$. $\boldsymbol{P_b}$ is the coefficient matrix of buffeting forces, representing one element, with size $[6 \times 3]$. It can be frequency-dependent when the cross-sectional admittance functions $\chi_{i,j}$ are included. $\widehat{\boldsymbol{M}}$ is the modal mass matrix. It can be frequency-dependent, e.g. due to hydrodynamic forces, and it has size $[N_M \times N_M]$. $\widehat{\boldsymbol{C}}$ and $\widehat{\boldsymbol{K}}$ are the modal damping and modal stiffness matrices. They can also be frequency-dependent and have size $[N_M \times N_M]$ each. *(superscript) represents the complex conjugate. i is the imaginary unit.

To express the response in the Ls system instead, for each element, the $\boldsymbol{S_{\Delta\Delta}}(\omega)$ in eq. (176) can be converted to an elemental format, and then pre- and post-multiplied by $\boldsymbol{T_{LsGs}}$ and $\boldsymbol{T_{GsLs}}$, accordingly.

3.8. Summary

Previous literature, through experimental and field measurements, has revealed an important impact of skew winds on the response of bridges. Two theoretical models to estimate the skew wind buffeting loads, here named 3D and 2D, are found in the literature. The 3D approach, which requires aerodynamic coefficients that depend on both yaw and inclination angles, is preferred but not always feasible. The 2D approach, where only the normal projection of the wind is considered, has previously underestimated the buffeting response of straight bridges to some extent, raising further questions for bridges with more complex geometries.

A revised version of the bridge buffeting theory for skew winds is introduced here for both turbulence- and motion-dependent forces. The 3D approach presented consists of a partial revision and a complement to the comprehensive and pioneering work by Le-Dong Zhu. Through the use of convenient coordinate systems, an intuitive and systematic use of transformation matrices, and with the help of modern mathematical tools, a few key improvements were achieved for the 3D approach:

a) A simplified and accurate description of the wind velocities, yaw angles, inclination angles and transformation matrices, as functions of both the turbulence and the structural motions.

b) A clear and compact representation of the linearized buffeting forces.

c) A more accurate description of the quasi-static motion-dependent forces, in both general non-linear and linear forms.

Additionally, for the cases where the 3D approach is not feasible and in order to establish a better framework of comparison, a comprehensive 2D approach is developed:

a) The cosine rule is expanded to include wind directions that are both yawed and inclined.

b) An optional axial force contribution, when the axial coefficient has been estimated, is included, accounting for both turbulence- and motion-dependent forces.

c) The motion dependencies are expanded from the typical 3 DOF in the normal plane to a complete 6 DOF formulation.

d) Linearizations of all relevant forces and variables are successfully achieved and presented in a conveniently compact form.

Further work is necessary to evaluate the impact of skew winds on bridges with different geometries, compare the differences between the two approaches and evaluate the improvements and generalizations introduced here. Some of these aspects are addressed in Chapter 5, where the planned bridge for Bjørnafjorden, first introduced in Chapter 4, is used as a case study.

The main differences between the original theory (Zhu, 2002) and the present theory are summarized in Table 1.

Table 1 – Key differences between the original and the present theory.

Original theory (Zhu, 2002)	**The present theory**
Local static structural coordinate systems:	
Use of both a Ls $(\boldsymbol{x}, \boldsymbol{y}, \boldsymbol{z})$ and a Lr $(\boldsymbol{q}, \boldsymbol{p}, \boldsymbol{h})$ system for each element. The direction of the $\boldsymbol{p}$-axis is dependent on the mean wind such that $\bar{\beta} \leq 90°$.	Use of only one Ls $(\boldsymbol{x}, \boldsymbol{y}, \boldsymbol{z})$ system that is consistent regardless of mean wind direction, i.e., for $\beta \in]-180°, 180°]$. This consistency leads to simpler expressions.
Mean wind coordinate systems:	
Use of both a local $L\overline{w}$ $(\overline{\boldsymbol{q}}, \overline{\boldsymbol{p}}, \overline{\boldsymbol{h}})$ system and a global Gw $(\boldsymbol{X_u}, \boldsymbol{Y_v}, \boldsymbol{Z_w})$ system to represent the mean wind.	The $L\overline{w}$ $(\overline{\boldsymbol{q}}, \overline{\boldsymbol{p}}, \overline{\boldsymbol{h}})$ system is discarded (redundant) and only Gw $(\boldsymbol{X_u}, \boldsymbol{Y_v}, \boldsymbol{Z_w})$ is used for the mean wind.
Local dynamic structural coordinate systems:	
Not included. Element rotations and their effects on motion-dependent forces must be explicitly defined.	Inclusion of a $\widetilde{\widetilde{Ls}}$ $(\widetilde{\widetilde{\boldsymbol{x}}}, \widetilde{\widetilde{\boldsymbol{y}}}, \widetilde{\widetilde{\boldsymbol{z}}})$ system, solidary with the moving element, helping define the motion-dependent loads.
Instantaneous and relative wind coordinate systems:	
The $\widetilde{\boldsymbol{p}}$ in the $L\widetilde{w}$ $(\widetilde{\boldsymbol{q}}, \widetilde{\boldsymbol{p}}, \widetilde{\boldsymbol{h}})$ system follows the instantaneous wind. No system is dedicated to the relative instantaneous wind (relative to the bridge in motion).	The $\boldsymbol{X}_{\widetilde{U}}$ in the $\widetilde{Lw}$ $(\boldsymbol{X}_{\widetilde{U}}, \boldsymbol{Y}_{\widetilde{U}}, \boldsymbol{Z}_{\widetilde{U}})$ system is aligned with the instantaneous wind $(\widetilde{U})$. The $\boldsymbol{X}_{\widetilde{\widetilde{U}}}$ in the $\widetilde{\widetilde{Lw}}$ $(\boldsymbol{X}_{\widetilde{\widetilde{U}}}, \boldsymbol{Y}_{\widetilde{\widetilde{U}}}, \boldsymbol{Z}_{\widetilde{\widetilde{U}}})$ system is aligned with the relative instantaneous wind $\left(\widetilde{\widetilde{U}}\right)$.
Transformation matrices:	
Transformation matrices are deduced from 9 angles between the axes of both systems, which must be previously defined.	An intuitive formulation using chained rotations is also included.

Linearization of the aerodynamic loads:	
$\overline{\boldsymbol{A}}^{\boldsymbol{b}}$, $\Delta\beta$, $\Delta\theta$, $\boldsymbol{T}_{\boldsymbol{L\bar{w}L\tilde{w}}}$ are formulated as functions of U, v, w, the nine entries t_{ij} of the transformation matrix $\boldsymbol{T}_{\boldsymbol{LrGw}}$ and six expressions s_i of these. $\overline{\boldsymbol{A}}^{\boldsymbol{b}}$ "transforms" $\boldsymbol{a} = [u, v, w]^T$ from the Gw system into forces in the $L\bar{w}$ system.	$\boldsymbol{A_b}$, $\widetilde{\Delta\beta}$, $\widetilde{\Delta\theta}$, $\boldsymbol{T}_{\boldsymbol{Gw\widetilde{Lw}}}$ are clearly formulated as functions of only U, v, w, β and θ, in a compact form and without loss of generality. $\boldsymbol{A_b}$ and $\boldsymbol{a} = [u, v, w]^T$ are both represented in the Gw system.
Motion-dependent forces:	
It is implicitly assumed (see section 5.4.3 in (Zhu, 2002), in particular in eq. 5.12b) that: $\tilde{\tilde{\beta}} \approx \beta + \frac{v}{U\cos\theta} - \Delta_{rz}$ $\tilde{\tilde{\theta}} \approx \theta + \frac{w}{U} + \Delta_{rY_v}$ The quasi-static expressions of P_3^*, H_3^* and A_3^* in eq. 5-16 are inaccurate: there is an inaccuracy in $\tilde{\tilde{\beta}}$ with respect to the bridge rotation ($\Delta_{rz} \neq \frac{\Delta_{rZ_w}}{\cos\theta}$, for $\theta \neq 0$), and a motion-dependent $\boldsymbol{T}_{\boldsymbol{L\bar{w}L\tilde{w}}}$ (analogous to $\boldsymbol{T}_{\boldsymbol{Gw\widetilde{Lw}}}$) is missing in the second term of the right side of eq. 5-13. Some motion dependencies are thus overlooked. After eq. 5-13, it is mentioned that $\overline{\boldsymbol{A}}^{\boldsymbol{se}} = \overline{\boldsymbol{A}}^{\boldsymbol{b}}(\chi_{i,j} = 1)$, where the relevant $\boldsymbol{T}_{\boldsymbol{L\bar{w}L\tilde{w}}}$ effects have been included. This confines the inaccuracies to the aerodynamic stiffness only, not the aerodynamic damping. A typo in P_5^* in eq. 5-16: $[\sin\bar{\beta}\cos\bar{\beta}]C'^{\theta}_{C_{\bar{q}}}$ should be corrected to $[\sin\bar{\beta}\cos\bar{\theta}]C'^{\theta}_{C_{\bar{q}}}$.	A simple non-linear quasi-static description of motion-dependent forces is first provided in eq. (91). Linear approximations of $\tilde{\tilde{\beta}}$ and $\tilde{\tilde{\theta}}$ are derived and revised to: $\tilde{\tilde{\beta}} \approx \beta + \frac{v - \dot{\Delta}_{Y_v}}{U\cos\theta} - \frac{\Delta_{rZ_w}}{\cos\theta}$ $\tilde{\tilde{\theta}} \approx \theta + \frac{w - \dot{\Delta}_{Z_w}}{U} + \Delta_{rY_v}$ A $\boldsymbol{T}_{\boldsymbol{Gw\widetilde{Lw}}}$ is derived and used, and a linear approximation is also provided. Comprehensive formulations of $\boldsymbol{A_\Delta}$ and $\boldsymbol{A_{\dot{\Delta}}}$ are provided. Accurate quasi-static Scanlan's flutter derivatives are provided as an alternative.
Alternative approach when $\boldsymbol{C}(\beta, \theta)$ have not been estimated but $\boldsymbol{C}(0, \theta)$ are known:	
A cosine rule $\boldsymbol{C_{Ls}}(\beta, \theta) = \boldsymbol{C_{Ls}}(0, \theta)\cos^2\beta$, originally intended for $\theta = 0$, is used to compare equivalent aerodynamic coefficients for different β (0 to 35°) and θ (-10 to 10°) (see also (Zhu et al., 2002b)). $C_{D_p}(= C_y)$ show moderate deviations. $C_{L_h}(= C_z)$ show erratic deviations. $C_{M_\alpha}(= C_{rx})$ show large deviations, especially for $\theta = \pm 10°$.	A novel generalization of the cosine rule approach is introduced, for generic β and θ, allowing contributions from axial and motion-dependent forces, due to all in- and out-of-plane motions. All the relevant variables, deductions and linearizations are presented. This approach is still only intended for preliminary analyses as it is presumably inferior to the 3D $\boldsymbol{C}(\beta, \theta)$ approach.

4. The Bjørnafjord Bridge

4.1. Bridge description

A brief history of the Bjørnafjord crossing project is included in Appendix A, where the various crossing solutions proposed throughout the project are introduced, as well as the floating bridge alternatives currently under consideration. One of those alternatives is used herein as a case study to demonstrate the application of the theory presented in Chapter 3.

The floating bridge alternative used in this case study is a single-curvature floating bridge, without mooring lines. It corresponds to the alternative a) shown in Fig. A.16. This solution was chosen for the sake of simplicity, relatability and generality of the results, and is further illustrated in Fig. 11.

Fig. 11 – Illustration of the floating bridge alternative used as a case study (Norwegian Public Roads Administration, 2019a).

Two concrete abutments, one on the South and one on the North side of the bridge, fix the bridge at both ends. According to the N400 standard (Norwegian Public Roads Administration, 2015), no hinges or kinks are allowed in the road alignment when the driving speed limit is over 70 km/h. The bridge girder is continuous with the adjoining road, and there are no hinges or expansion joints. The bridge behaves like an arch in the horizontal plane. The curvature and the high slenderness of the bridge in the horizontal plane give it enough flexibility for thermal deformations to occur with only limited stresses. The bridge girder must also take other deformations such as those from tides.

The bridge has two traffic lanes in each direction, each 3.5 m wide, with 1.5 m wide outside shoulders and 0.5 m wide inside shoulders. The cross-section of the orthotropic steel box deck used in the modelling is shown in Fig. 12.

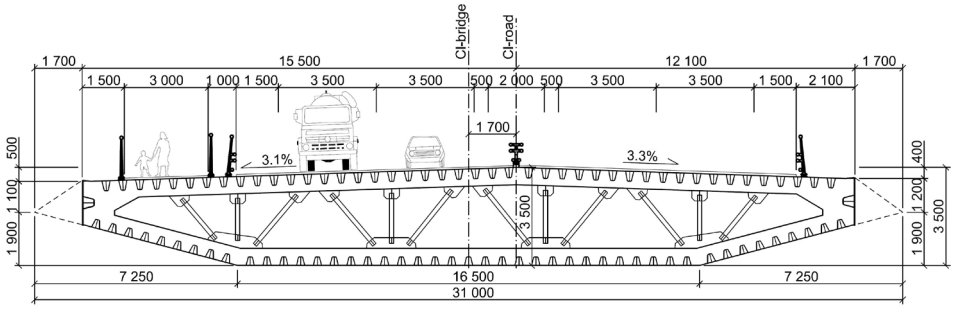

Fig. 12 – Cross-section of the case study [mm] (Norwegian Public Roads Administration, 2017b).

The minimum vertical clearance for ship traffic is set to 45 m in the main cable-stayed span and 11.5 m in the floating spans. The minimum horizontal clearance in the main span is set to 250 m, and no requirements are set for the side spans. The shear centre of the bridge deck is located at around 50 m above sea level in the cable-stayed part of the bridge, and it goes down to approximately 14.5 m above sea level in the following 1.5 km, where it remains until nearly the end of the floating bridge. The steel columns are relatively stiff and provide a rigid link between the girder and the steel pontoons. The design life of the bridge is 100 years.

4.2. Numerical model

4.2.1. Main properties

The numerical model created and used in this research is a simplification of the floating bridge described in Section 4.1. The cable-stayed part of the bridge is discarded, and the bridge girder axis is assumed to be at a constant height above sea level of 14.5 m. The simplified model has 49 pontoons, with an even spacing of 100 m between them, and the total bridge length is 5000 meters, with a curvature radius of also 5000 meters. This is illustrated in Fig. 13, together with the defined global structural coordinate system.

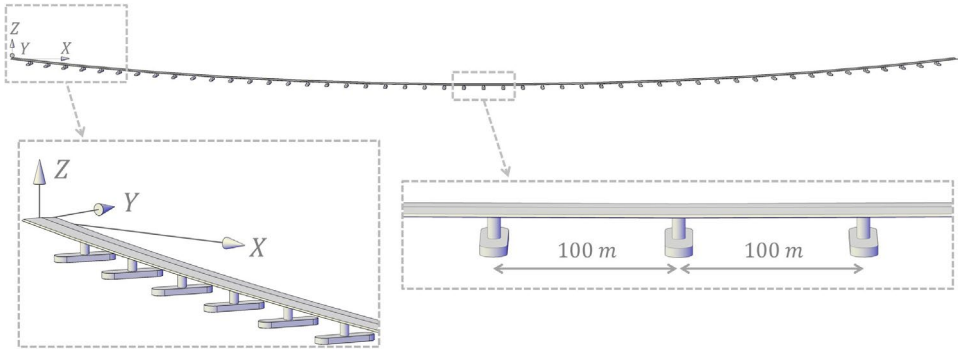

Fig. 13 – Illustration of the simplified floating bridge model implemented and the global structural (Gs) coordinate system ($\boldsymbol{X}$, $\boldsymbol{Y}$, $\boldsymbol{Z}$).

Some of the bridge properties implemented in this numerical model are taken from the Phase 3 reports of the Bjørnafjord crossing project (Norwegian Public Roads Administration, 2017a). Different cross-sectional properties have since been proposed by two different consortia in Phase 5 of the project, but these agree well with each other and with the values from Phase 3 since only minor cross-sectional optimizations were performed.

In order to define the structural properties, the local structural axes of the bridge girder, columns and pontoons are defined first, following Fig. 14.

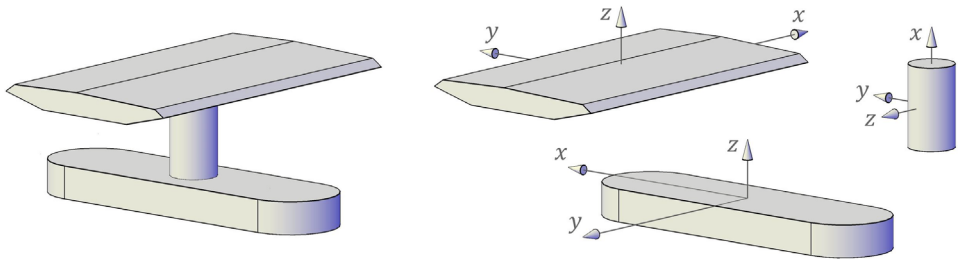

Fig. 14 – Representation of the local structural (Ls) coordinate systems ($\boldsymbol{x}$, $\boldsymbol{y}$, $\boldsymbol{z}$) of the girder, pontoons and columns of the numerical model.

The bridge girder is discretized into 25-meter-long segments. This was found to be a good compromise between computational efficiency and result accuracy (further details are given in the sensitivity analysis in Section 4.2.5). Each column is modelled as a single finite element between a pontoon node and the girder node above, with a 14.5 m height, which is also considered a good approximation. Due to their low slenderness, the columns behave like rigid elements. Every single floating pontoon is modelled as a node, at the water plane level, with equivalent mass, damping and stiffness properties. In total, the 5000-meter-long bridge model is composed of 200 bridge elements, 201 bridge girder nodes, 49 pontoon nodes and 49 column elements.

With respect to the boundary conditions, both ends of the bridge model are fixed. The first girder node in the South and the last girder node in the North are fixed for all degrees of freedom (DOF), using stiff springs with $10^{15}\ N/m$ and $10^{15}\ Nm/rad$, respectively for translational components ($\boldsymbol{x}$, $\boldsymbol{y}$, $\boldsymbol{z}$) and rotational ones ($\boldsymbol{rx}$, $\boldsymbol{ry}$, $\boldsymbol{rz}$).

The properties of the cross-section, the weight loads and the material of the bridge girder and columns that were implemented in the model are described in Table 2.

Table 2 – Girder and column properties implemented in the model

	Cross-sectional						Weight	Material	
Quantity [units]	B $[m]$	H $[m]$	A $[m^2]$	I_y $[m^4]$	I_z $[m^4]$	J $[m^4]$	$DL+SDL$ $[ton/m]$	E $[GPa]$	G $[GPa]$
Girder	31	3.5	1.43	2.67	114.8	6.88	17.85	210	80.77
Column	7.16	7.16	0.872	5.53	5.53	11.06	7.20		

In Table 2, B is the width; H is the height; A is the area; I_y and I_z are the second moments of area with respect to the $\boldsymbol{y}$- and $\boldsymbol{z}$-axis respectively (shown in Fig. 14); J is the torsional constant; DL are the dead loads, i.e., self-weight of the structure; SDL are the superimposed dead loads, e.g. asphalt and railings; DL and SDL are

taken together when creating the mass matrix; E is the Young's modulus and G is the shear modulus representing the steel properties. Traffic loads are not considered since the bridge is expected to close for traffic during environmental events with a 100-year return period.

The frequency-independent pontoon properties were obtained from a Phase 5 report (Norwegian Public Roads Administration, 2019d). These are summarized in Table 3. The pontoons only provide hydrostatic stiffness in three of the six DOF because the pontoons, if not attached to the bridge, can float freely in the surge ($\boldsymbol{x}$) and sway ($\boldsymbol{y}$) directions and are also free to have yaw rotations ($\boldsymbol{rz}$).

Table 3 – Pontoon properties implemented in the model

Axis	x	y	z		rx	ry	rz	
Mass	985			$[ton]$	33100	252000		$[ton\ m^2]$
Stiffness	0	0	7459	$[kN/m]$	36637	1467900	0	$[kNm/rad]$

Additionally, the pontoons have crucial frequency-dependent properties that must be included in the model, namely the hydrodynamic added mass and potential damping matrices. To estimate these, a numerical model of a pontoon is subjected to forced harmonic rigid body motions, in each DOF. Steady-state hydrodynamic forces and moments are then obtained from the integration of the resultant fluid pressure forces over the pontoon surfaces. These forces and moments are separated into those that are velocity dependent (potential damping) and those that are acceleration dependent (added mass). These were obtained with the software Ansys Aqwa 2019R1 during Phase 5 of the Bjørnafjord crossing project, and they are described in Fig. 15. The two left-most plots show the diagonal entries of these matrices concerning the three translations ($\boldsymbol{x}$, $\boldsymbol{y}$, $\boldsymbol{z}$). The two plots in the middle show the remaining diagonal entries concerning rotations ($\boldsymbol{rx}$, $\boldsymbol{ry}$, $\boldsymbol{rz}$). The two remaining right-most plots show the two most relevant off-diagonal entries, $\boldsymbol{x}$-$\boldsymbol{ry}$ and $\boldsymbol{y}$-$\boldsymbol{rx}$. For simplicity, the effects of sea current are neglected, and since the pontoons have zero mean forward speed (e.g. unlike a vessel), both the added mass and potential damping matrices become symmetric (Faltinsen, 1993).

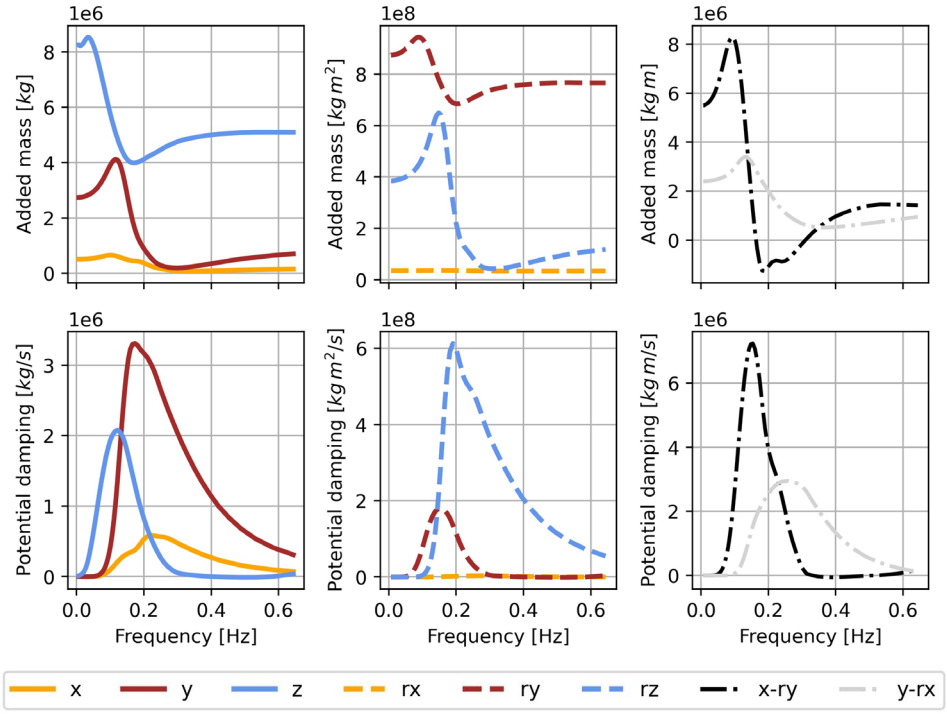

Fig. 15 – Hydrodynamic frequency-dependent added mass and potential damping matrices of the pontoons. The six diagonal entries (***x***, ***y***, ***z***) and (***rx***, ***ry***, ***rz***) are shown, as well as the two most relevant off-diagonal entries, ***x-ry*** and ***y-rx***.

Pontoon translations along pontoon axes that are perpendicular to large pontoon surfaces tend to displace larger volumes of water and thus tend to be associated with larger values of hydrodynamic added mass and damping, but there are other factors contributing to the fluid pressures (e.g. pontoon shape, sharp edge locations, motion frequencies). A similar reasoning can be made for the three pontoon rotations.

More information about these hydrodynamic loads (described in e.g. (Faltinsen, 1993)) can be found in (Norwegian Public Roads Administration, 2019d). The hydrodynamic interaction between pontoons, studied for the same bridge in (Xiang et al., 2018)), was not considered in this study.

The floating bridge studied has additional important damping sources, such as non-linear hydrodynamic viscous forces due to the pontoons' response relative to the local sea current. The consideration of these forces was left outside the scope of this study as it would further add complexity to the analysis and reduce the interpretability of the results. The numerical model is not intended for an absolute

assessment of the response but rather for a relative assessment of the different load models.

In order to include all the properties described in this section, the finite element method (FEM) is used to create the bridge model and define its nodes, its elements and all mass, damping and stiffness matrices.

4.2.2. Node coordinates

Table 4 presents a short Python code for generating all the node coordinates of the simplified FEM model studied with 201 bridge girder nodes and 49 pontoons. This considers that free online Python compilers are readily available and avoids presenting an extensive table with the coordinates of each node.

Table 4 – Python code to print the node coordinates of the simplified FEM model, in the global structural (Gs) coordinate system ($\boldsymbol{X}$, $\boldsymbol{Y}$, $\boldsymbol{Z}$)

```
import numpy as np

arc_length = 5000
arc_radius = 5000
span = 100
bridge_height = 14.5
elem_length = 25
num_girder_nodes = int(arc_length/elem_length) + 1
arc_angle = arc_length / arc_radius
elem_angle = elem_length / arc_radius
node_angles = -arc_angle/2 + np.cumsum([0]+[elem_angle]*(num_girder_nodes-1))
X = arc_radius * np.sin(node_angles)
Y = -arc_radius * np.cos(node_angles)
X, Y = X-X[0], Y-Y[0]
Z = [bridge_height]*num_girder_nodes
girder_coords = np.array([X, Y, Z]).T
elem_p_span = int(span/elem_length)
pontoon_coords = girder_coords[elem_p_span:-elem_p_span:elem_p_span].copy()
pontoon_coords[:, 2] *= 0
print('Bridge girder node coordinates: \n', girder_coords)
print('Pontoon coordinates: \n', pontoon_coords)
```

This code snippet is tailored for printing the node coordinates only. If the input values are changed, additional assertions should be implemented (e.g. assert that the arc length is a multiple of the span and that both are a multiple of the element length). More functionality and flexibility can be incorporated into the code to allow for other model characteristics and for sensitivity studies. A comprehensive

implementation in Python of the current numerical model is made freely available on GitHub: https://github.com/costabm. These nodal coordinates are useful inputs when implementing the wind loads described in sections 3, 5 and 6 of the thesis.

4.2.3. Mass, damping and stiffness matrices

The FEM discretizes the structure into finite elements. The bridge girder and the columns can be numerically modelled as an assembly of beam (line-like) elements with 12 degrees of freedom (DOF) (as in, e.g. (Strømmen, 2014)). Following the 12 DOF defined in Fig. 16, and assuming the first three DOF to be parallel to the local structural (Ls) coordinate systems ($\boldsymbol{x}$, $\boldsymbol{y}$, $\boldsymbol{z}$) from Fig. 14, the local stiffness matrix can be defined according to eqs. (181) through (184), for each finite element of the bridge.

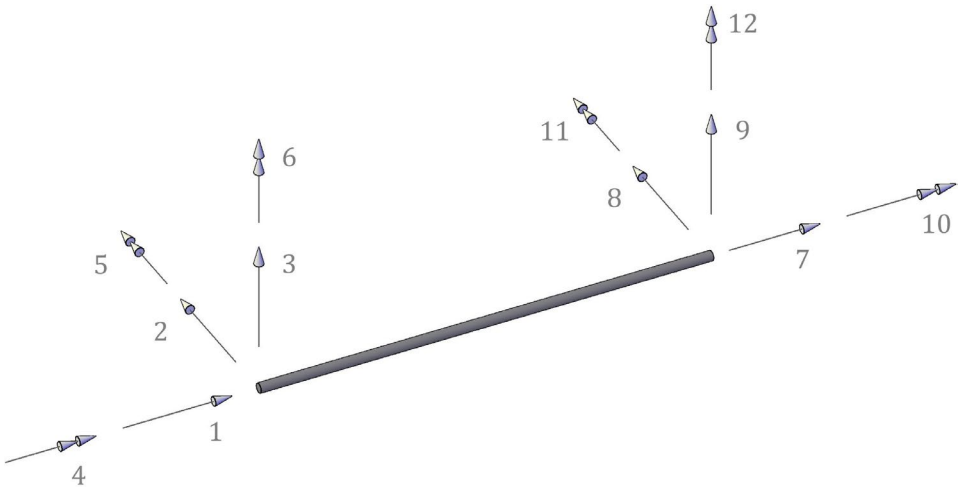

Fig. 16 – Line-like element and its twelve degrees of freedom.

$$K_{Ls} = \begin{bmatrix} K_{Ls,11} & K_{Ls,12} \\ K_{Ls,21} & K_{Ls,22} \end{bmatrix} \tag{181}$$

$$K_{Ls,11} = \begin{bmatrix} EA/L & 0 & 0 & 0 & 0 & 0 \\ & 12EI_z/L^3 & 0 & 0 & 0 & 6EI_z/L^2 \\ & & 12EI_y/L^3 & 0 & -6EI_y/L^2 & 0 \\ & & & GJ/L & 0 & 0 \\ & sym. & & & 4EI_y/L & 0 \\ & & & & & 4EI_z/L \end{bmatrix} \tag{182}$$

$$K_{Ls,12} = K_{Ls,21} =$$

$$= \begin{bmatrix} -EA/L & 0 & 0 & 0 & 0 & 0 \\ 0 & -12EI_z/L^3 & 0 & 0 & 0 & 6EI_z/L^2 \\ 0 & 0 & -12EI_y/L^3 & 0 & -6EI_y/L^2 & 0 \\ 0 & 0 & 0 & -GJ/L & 0 & 0 \\ 0 & 0 & 6EI_y/L^2 & 0 & 2EI_y/L & 0 \\ 0 & -6EI_z/L^2 & 0 & 0 & 0 & 2EI_z/L \end{bmatrix} \quad (183)$$

$$K_{Ls,22} = \begin{bmatrix} EA/L & 0 & 0 & 0 & 0 & 0 \\ & 12EI_z/L^3 & 0 & 0 & 0 & -6EI_z/L^2 \\ & & 12EI_y/L^3 & 0 & 6EI_y/L^2 & 0 \\ & & & GJ/L & 0 & 0 \\ & sym. & & & 4EI_y/L & 0 \\ & & & & & 4EI_z/L \end{bmatrix} \quad (184)$$

L is the length of the finite beam element. The remaining variables were already defined below Table 2. Due to the bridge curvature, some loads such as the mean wind, sea current and wave drift can induce significant axial forces in the bridge girder, which in turn increase (when in tension) or decrease (when in compression) its effective stiffness $K_{eff} = K - K_{Geom}$. The geometric stiffness matrix K_{Geom}, in local structural coordinates Ls, is defined in eqs. (185) to (188), for each finite element.

$$K_{Geom,Ls} = \begin{bmatrix} K_{Geom,Ls,11} & K_{Geom,Ls,12} \\ K_{Geom,Ls,21} & K_{Geom,Ls,22} \end{bmatrix} \quad (185)$$

$$K_{Geom,Ls,11} = \begin{bmatrix} 0 & 0 & 0 & 0 & 0 & 0 \\ & 36\bar{N}/30L & 0 & -\overline{M_y} & 0 & \bar{N}/10 \\ & & 36\bar{N}/30L & -\overline{M_z} & -\bar{N}/10 & 0 \\ & & & \bar{N}{e_0}^2 & 0 & 0 \\ & sym. & & & 2\bar{N}L/15 & 0 \\ & & & & & 2\bar{N}L/15 \end{bmatrix} \quad (186)$$

$$K_{Geom,Ls,12} = K_{Geom,Ls,21} =$$

$$= \begin{bmatrix} 0 & 0 & 0 & 0 & 0 & 0 \\ 0 & -36\bar{N}/30L & 0 & \overline{M_y} & 0 & \bar{N}/10 \\ 0 & 0 & -36\bar{N}/30L & \overline{M_z} & -\bar{N}/10 & 0 \\ 0 & \overline{M_y} & \overline{M_z} & -\bar{N}{e_0}^2 & 0 & 0 \\ 0 & 0 & \bar{N}/10 & 0 & \bar{N}L/30 & 0 \\ 0 & -\bar{N}/10 & 0 & 0 & 0 & -\bar{N}L/30 \end{bmatrix} \quad (187)$$

$$K_{Geom,Ls,22} = \begin{bmatrix} 0 & 0 & 0 & 0 & 0 & 0 \\ & 36\bar{N}/30L & 0 & -\overline{M_y} & 0 & -\bar{N}/10 \\ & & 36\bar{N}/30L & -\overline{M_z} & \bar{N}/10 & 0 \\ & & & \bar{N}{e_0}^2 & 0 & 0 \\ & sym. & & & 2\bar{N}L/15 & 0 \\ & & & & & 2\bar{N}L/15 \end{bmatrix} \quad (188)$$

Where ${e_0}^2 = {i_y}^2 + {i_z}^2 + e_y + e_z$; i_y and i_z are the radius of gyration about axes y and z ; e_y and e_z are the coordinates of the shear centre with respect to the centroid; $\bar{N}$ is the time-averaged axial force and $\overline{M_y}$ and $\overline{M_z}$ are the time-averaged bending moments about axes $\boldsymbol{y}$ and $\boldsymbol{z}$, which are also averaged along the sufficiently short element i.

Next, the consistent mass matrix, for each finite element, is defined in the same Ls coordinate system, according to eqs. (189) to (192).

$$M_{Ls} = \begin{bmatrix} M_{Ls,11} & M_{Ls,12} \\ M_{Ls,21} & M_{Ls,22} \end{bmatrix} \quad (189)$$

$M_{Ls,11}$

$$= \frac{L}{420}\begin{bmatrix} 140m_x & 0 & 0 & 0 & 0 & 0 \\ & 156m_y & 0 & -147m_y e_z & 0 & 22m_y L \\ & & 156m_z & 147m_z e_y & -22m_z L & 0 \\ & & & 140m_\theta & -21m_z L e_y & -21m_y L e_z \\ & sym. & & & 4m_z L^2 & 0 \\ & & & & & 4m_y L^2 \end{bmatrix} \quad (190)$$

$M_{Ls,12} = M_{Ls,21} =$

$$= \frac{L}{420}\begin{bmatrix} 70m_x & 0 & 0 & 0 & 0 & 0 \\ 0 & 54m_y & 0 & -63m_y e_z & 0 & -13m_y L \\ 0 & 0 & 54m_z & 63m_z e_y & 13m_z L & 0 \\ 0 & -63m_y e_z & 63m_z e_y & 70m_\theta & 14m_z L e_y & -14m_y L e_z \\ 0 & 0 & -13m_z L & -14m_z L e_y & -3m_z L^2 & 0 \\ 0 & 13m_y L & 0 & -14m_y L e_z & 0 & -3m_y L^2 \end{bmatrix} \quad (191)$$

$$M_{Ls,22} = \frac{L}{420}\begin{bmatrix} 140m_x & 0 & 0 & 0 & 0 & 0 \\ & 156m_y & 0 & -147m_y e_z & 0 & -22m_y L \\ & & 156m_z & 147m_z e_y & 22m_z L & 0 \\ & & & 140m_\theta & 21m_z L e_y & 21m_y L e_z \\ & sym. & & & 4m_z L^2 & 0 \\ & & & & & 4m_y L^2 \end{bmatrix} \quad (192)$$

m_x, m_y and m_z are the translational masses per unit length, in the $\boldsymbol{x}$, $\boldsymbol{y}$ and $\boldsymbol{z}$ directions (SI base units: kg); m_θ is the rotational mass per unit length (SI base units: $kg\ m^2$).

So far, only local mass and stiffness matrices have been defined. The next step is to transform each of these matrices from their local structural coordinate systems ($\boldsymbol{x}$, $\boldsymbol{y}$, $\boldsymbol{z}$) to the common and consistent global structural coordinate system ($\boldsymbol{X}$, $\boldsymbol{Y}$, $\boldsymbol{Z}$), defined in Fig. 13. These local matrices, for one beam element, when expressed in global coordinates, can then be assembled together into a global matrix, for all nodes of the bridge model. In order to express these local matrices in the global structural coordinate system Gs, the transformations in eqs. (193) and (194) can be used.

$$K_{Gs} = T_{GsLs}\, K_{eff,Ls} = T_{GsLs}(\, K_{Ls} - K_{Geom,Ls}\,) \quad (193)$$

$$M_{Gs} = T_{GsLs}\ M_{Ls} \quad (194)$$

Here, T_{GsLs} is the transformation matrix, from the local structural coordinate system, Ls, to the global structural coordinate system Gs. There is a unique transformation matrix T_{GsLs} for each of the girder and column finite elements of the model.

All the local element matrices, when expressed in the global coordinate system, such as K_{Gs} and M_{Gs}, each with size $[12 \times 12]$, can then be assembled into one global matrix, such as K_{Gs}^{G} and M_{Gs}^{G}, both with size $[6N_N \times 6N_N]$, representing the whole structure, in the same global coordinate system Gs. N_N is the total number of nodes in the FEM model. The superscript G refers to the global model, i.e., including all nodes of the FEM model in one global matrix, which should not be confused with the global coordinate system notation Gs used in the subscript.

In Table 5, a schematic and generic procedure is provided that can be used to assemble both the global stiffness matrix K_{Gs}^{G} and the global mass matrix M_{Gs}^{G},

provided as input all the local matrices of each finite element K_{Gs} and M_{Gs}, in the same consistent global coordinate system Gs. In Table 5, the notations $g1$, $g2$, $g3$, $g4$ ... are used to represent the local matrices of the girder elements 1, 2, 3, 4 ... . The notations $c1, c2, c3$ ... are used for the column elements 1, 2, 3 ... . The notation b is used here to represent the boundary condition (only applicable for the stiffness matrix). The notations $p1, p2, p3$ ... are used to represent the pontoons 1, 2, 3 ... (e.g. mass and added mass could be included together here). The local element matrices of the girder and columns have size $[12 \times 12]$ and are therefore each subdivided into four sub-matrices with size $[6 \times 6]$ using the notations 11, 12, 21, 22 in the subscript. The boundary b and pontoon p matrices are nodal matrices, so they already have size $[6 \times 6]$. Each cell in Table 5 corresponds to a $[6 \times 6]$ sub-matrix of the global $[6N_N \times 6N_N]$ matrix and $\mathbf{0}$ represents a $[6 \times 6]$ sub-matrix filled with zeros. For the sake of compactness and simplicity, the less discretized model with 50-m-long elements shown in Fig. 17 is used in the assembly procedure in Table 5, but the procedure can be easily extended to more discretized models.

The pontoons share the same node as the first node of the columns. The columns' second node is shared with two adjacent bridge elements. If the suggested assembling procedure is used for the model used in this research, with 201 bridge nodes, 200 bridge elements, 49 column elements and 49 pontoon nodes, then the first $6 \times 201 = 1206$ rows and columns of the global matrix concern the bridge girder nodes, and the last $6 \times 49 = 294$ rows and columns concern the pontoon nodes. Sub-matrices, such as the $c1_{21}$, $c1_{12}$, $c2_{21}$ and $c2_{12}$ shown in Table 5, ensure the correct modelling of the columns, i.e., the structural link between girder and pontoon nodes. These sub-matrices are sparsely located in the global matrix, usually far from the diagonal. The b matrix is a diagonal matrix filled with 10^{15} values (N/m or Nm/rad) that is only applicable for the global stiffness matrix.

Fig. 17 – Example of a coarse FEM model representation. Girder (g) and column (c) finite elements are combined with boundary (b) and pontoon (p) node properties when assembling the global model matrices, as further described in Table 5.

Table 5 – Assembling procedure for the global stiffness K_{Gs}^{G} and global mass M_{Gs}^{G} matrices with size $[6N_N \times 6N_N]$, from the girder (g) and column (c) element matrices $[12 \times 12]$ and from the nodal matrices $[6 \times 6]$ of the boundary (b) and pontoon (p) properties. The coarse FEM model in Fig. 17 is used in this example for simplicity.

$g1_{11} + b1$	$g1_{12}$	**0**	**0**	**0**	…	…	**0**	**0**	**0**	…
$g1_{21}$	$g1_{22} + g2_{11}$	$g2_{12}$	**0**	**0**	…	…	**0**	**0**	**0**	…
0	$g2_{21}$	$g2_{22} + c1_{22} + g3_{11}$	$g3_{12}$	**0**	…	…	$c1_{21}$	**0**	**0**	…
0	**0**	$g3_{21}$	$g3_{22} + g4_{11}$	$g4_{12}$	…	…	**0**	**0**	**0**	…
0	**0**	**0**	$g4_{21}$	$g4_{22} + c2_{22} + g5_{11}$	…	…	**0**	$c2_{21}$	**0**	…
…	…	…	…	…	…	…	**0**	**0**	**0**	…
…	…	…	…	…	…	…	…	…	…	…
0	**0**	$c1_{12}$	**0**	**0**	**0**	…	$c1_{11} + p1$	**0**	**0**	…
0	**0**	**0**	**0**	$c2_{12}$	**0**	…	**0**	$c2_{11} + p2$	**0**	…
0	**0**	**0**	**0**	**0**	**0**	…	**0**	**0**	$c3_{11} + p3$	…
…	…	…	…	…	…	…	…	…	…	…

To estimate the global matrix of the hydrodynamic potential damping provided by all pontoons, the individual damping matrices, in local structural pontoon coordinates of each pontoon, are estimated first and then individually transformed to global structural coordinates. These then represent the $p1, p2, p3$ ... matrices in Table 5, so the same assembly procedure can be used, where all other matrices are zero.

In addition to the global hydrodynamic damping C_{Hydro}^{G}, the global structural damping C_{Struct}^{G} can also be included. In this study, the Rayleigh damping formulation was used, which depends on both the global mass and global stiffness matrices. This is described in eqs (195) and (196). These global matrices should still be represented in global structural coordinates, but the subscript Gs is omitted for simplicity.

$$C^G = C^G_{Hydro} + C^G_{Struct} = C^G_{Hydro} + (a_0 M^G + a_1 K^G) \quad (195)$$

$$\xi_k = a_0 \frac{1}{2\omega_k} + a_1 \frac{\omega_k}{2} \quad (196)$$

Here a_0 and a_1 are the Rayleigh coefficients and ξ_k is the damping ratio of the eigenmode k with angular frequency ω_k. If two desired damping ratios at two different eigenfrequencies are known (or assumed), then the Rayleigh coefficients a_0 and a_1 can be solved with a system of two linear equations, each with the form of eq. (196). In this study, $\xi_k = 0.005$ is assumed for two periods ($T = 2\pi/\omega$) of $120\ s$ and $2\ s$. This level of structural damping is assumed to be representative of the steel bridge.

By assembling the global matrices presented here in a computer code format, greater flexibility for parametric studies and optimizations can be achieved.

For simplicity, the incoming wave loads were disregarded in this study. All permanent loads and corresponding buoyancy forces were also disregarded. This means the skew wind buffeting analysis assumes an initially undeformed structure.

4.2.4. Modal analysis

The linear bridge response can be calculated via a frequency-domain analysis, which is typically faster than a time-domain analysis. For this, the modal properties of the structure must be first estimated, namely its natural mode shapes and frequencies. A detailed procedure to obtain these inherent dynamic structural properties can be found in, e.g. Chapter 10 of (Chopra, 2007). In practice, this involves computing the eigenvalues and eigenvectors of the square matrix $(M_{Gs}^{-1} K_{Gs})$.

The natural mode shapes and periods $(T = 1/f)$ of the simplified FEM model are given in Fig. 18 and Fig. 19, for the first 100 modes, in the three main local DOF ($\boldsymbol{x}$, $\boldsymbol{y}$ and $\boldsymbol{rx}$). These are all the modes considered in the frequency-domain analyses presented in sections 5 and 6.

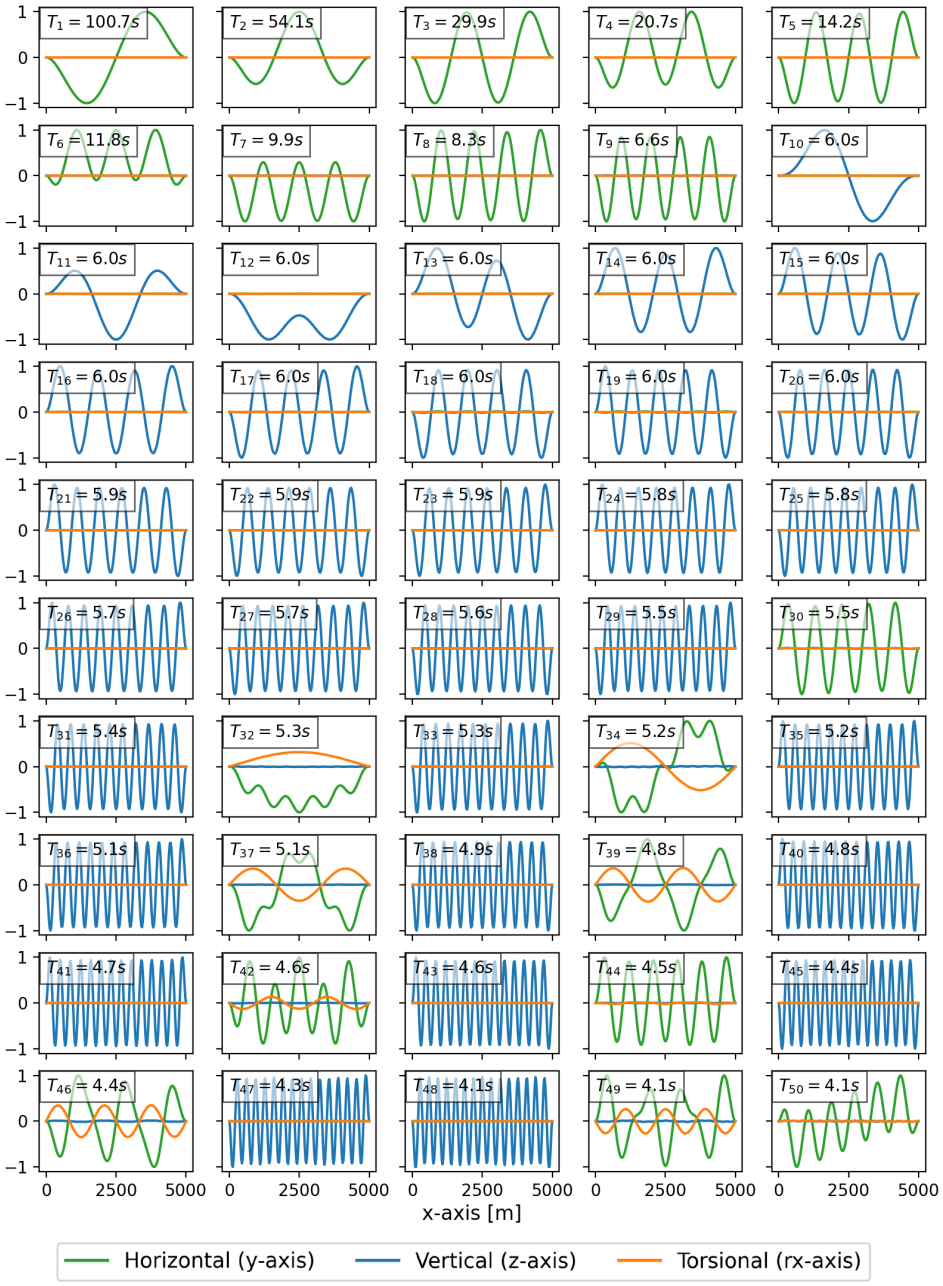

Fig. 18 – Modes shapes 1 to 50 of the girder of the simplified FEM model and respective eigenperiods.

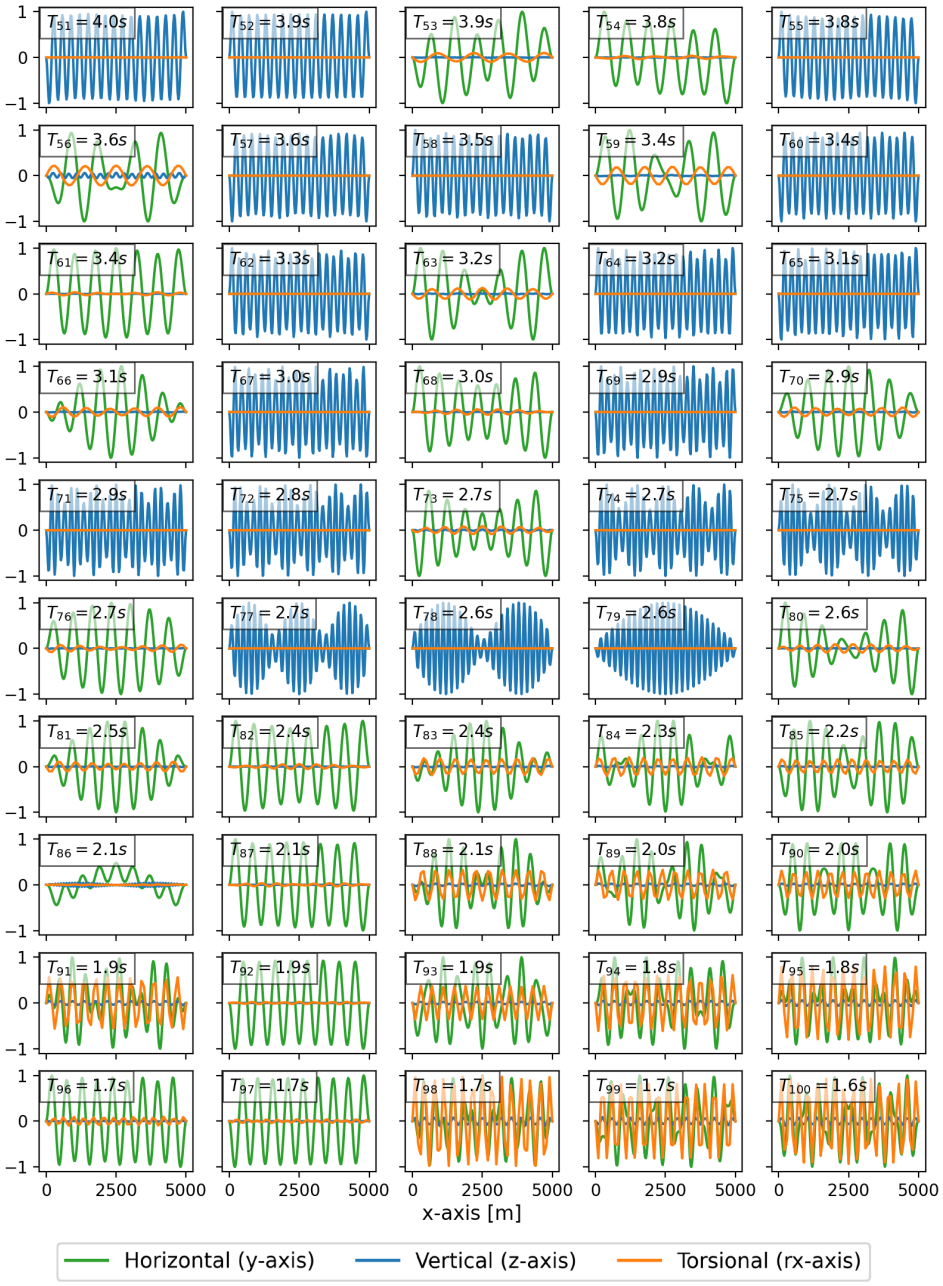

Fig. 19 – Modes shapes 51 to 100 of the girder of the simplified FEM model and respective eigenperiods.

The obtained mode shapes and eigenperiods resemble those reported in the latest design reports (concept *K11* in, e.g. (Norwegian Public Roads Administration, 2019b)). Mean wind forces can significantly affect the first few modes of this particular structure. Mean wind directions that cause mean tension forces in the girder reduce the eigenperiods of these modes, whereas mean wind directions that lead to mean compression forces increase them due to geometric stiffness effects. It can also be noted that modes 6 and 7 include significant axial deformations, as indicated by the nearly strictly positive (or negative) horizontal deformations associated with those modes and as a consequence of the arc shape, which may have implications for dynamic buckling and parametric resonance analyses. For simplicity, static wind effects were not included in the analysis.

A few of the main horizontal, vertical and torsional modes are illustrated in more detail in Fig. 20, where the mode shapes are plotted in global structural coordinates instead, in the horizontal (***XY***) and vertical (***XZ***) plan. The pontoon nodes are included in the plot. The unitary mode shapes are multiplied by 200 (meters) for visualization purposes. These are the first horizontal and axial modes (modes 1 to 7), the first two vertical modes (modes 10 and 11) with nearly identical mode periods, the two first torsional modes (modes 32 and 34) and one of the last relevant vertical modes (mode 79) that still mobilizes the pontoons, meaning that most of the vertical response comes from a narrow band between the periods of 6.0 and 2.6 seconds.

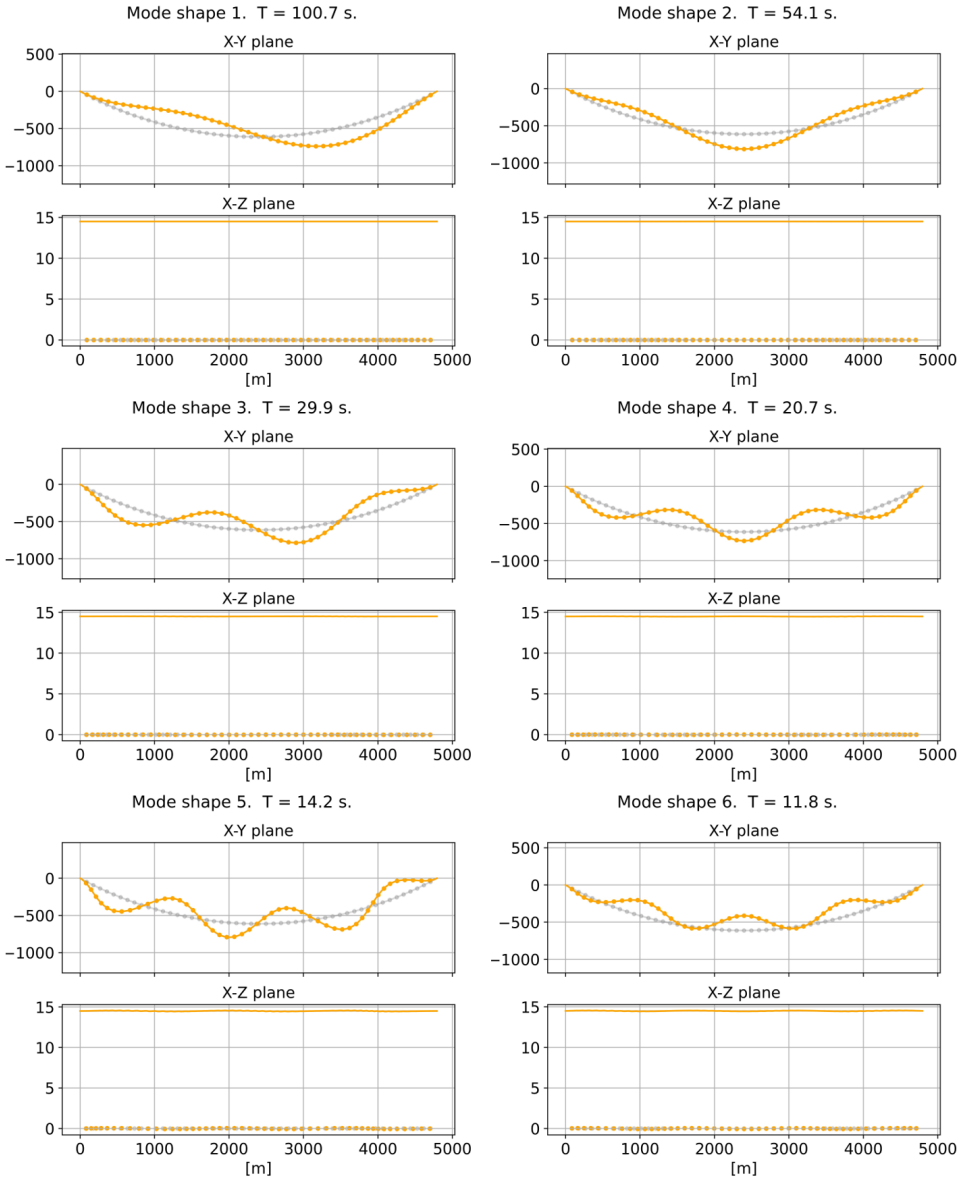

Fig. 20 – Selected mode shapes of the simplified finite element model.

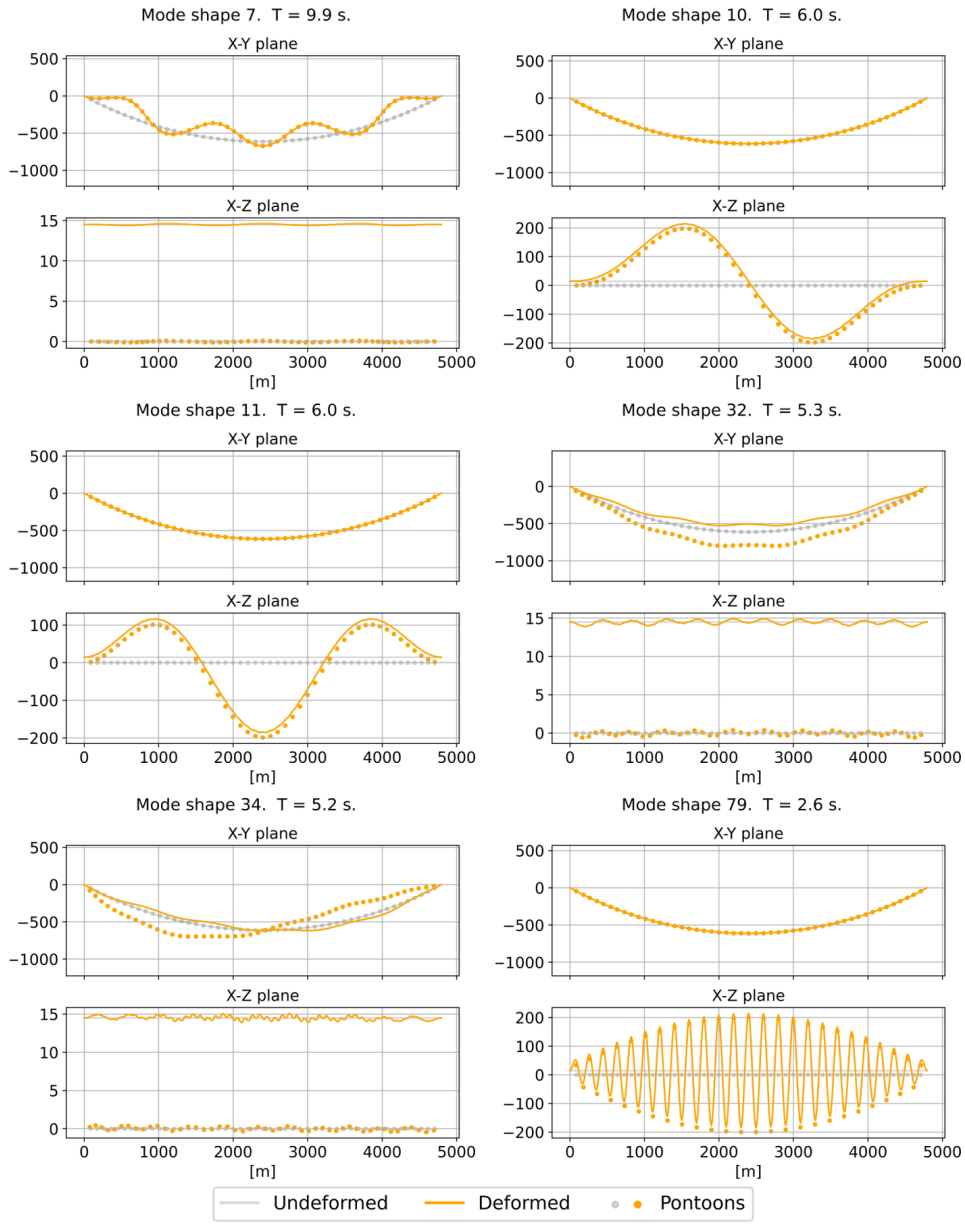

Fig. 20 (cont.) – Selected mode shapes of the simplified finite element model.

4.2.5. Sensitivity analysis

In this section, a sensitivity analysis is performed in the frequency domain to verify some of the key input parameters of the numerical model by checking the sensitivity of the model response to changes in the same input parameters.

The model parameters analysed here are the following:

a) Num. of nodes in the FEM model of the bridge girder.

b) Num. of eigenmodes considered in the frequency-domain analysis.

c) Num. of frequency bins used in the frequency discretization, using a uniform discretization (i.e., $\Delta f = const.$).

d) Highest frequency cut-off (using a uniform frequency discretization).

e) Lowest frequency cut-off (using a uniform frequency discretization).

f) Num. of frequency bins used in the frequency discretization, using a more efficient equal-area discretization (i.e., $\Delta f \neq const.$, being smaller at frequencies that contribute more to the response).

The sensitivity analysis is performed for two different wind load cases:

- Load case 1: Mean wind from W ($\beta_{Cardinal} = 280°$), perpendicular to the bridge girder at its global mid-point.
- Load case 2: Mean wind from NNW ($\beta_{Cardinal} = 340°$).

For both load cases, the sensitivity of the response is evaluated separately for each of the three main local DOF, namely the horizontal $\boldsymbol{y}$-axis, the vertical $\boldsymbol{z}$-axis and the torsional $\boldsymbol{rx}$-axis. The response sensitivity is shown for the a), b), and c) parameters in Table 6, Table 7 and Table 8. For each load case, DOF and input parameter, these tables indicate the bridge displacement response, relative to a reference response, in percentage (i.e., $\Delta_i/\Delta_{i,ref.} \times 100$ [%]). Each of these three tables has a reference (ref.) row. The relative response values marked in bold are respective to the parameter value adopted in the numerical simulations.

In Table 6, it is shown that, when adopting 25 m long finite girder elements, the torsional and vertical responses are within a 3% error margin of the results from higher-resolution models with converged results. The horizontal response, dominated by very long mode shapes, has virtually a 0% difference between the chosen 25 m resolution model and higher-resolution models.

In Table 7, the choice of considering 100 eigenmodes is found to be suitable for the analysis.

In Table 8, different uniform frequency discretizations (number of frequency bins in the frequency domain) are tested, and the results are then used as a reference for Table 9, Table 10 and Table 11.

In Table 9, the bridge response sensitivity to the highest frequency considered in the frequency-domain analysis is evaluated. This is similar to a low-pass filter cut-off frequency. It should be noted that a change in this cut-off frequency, without changing the total number of frequency bins, significantly changes the position of all frequency bins. So, to effectively select the optimal cut-off frequency from this sensitivity analysis, attention should be given distinctly to the horizontal response, dominated by lower frequencies, and to the vertical and torsional responses, dominated by higher frequencies. On the one hand, regarding the highest allowed frequency, a low value compromises the contribution of the higher frequency modes. On the other hand, assuming a uniform frequency discretization and having a limited number of frequency bins, a high value can compromise the fine discretization required at the very low frequencies of this bridge. Thus, a balance is pursued, and the value of 0.5 Hz is chosen for the highest frequency considered.

Regarding the choice of the lowest frequency considered, i.e., the high-pass filter cut-off frequency, shown in Table 10, a very small value does not affect the vertical and torsional response, as opposed to the effect of the low-pass filter on the horizontal response. This assumes a uniform frequency discretization. The value of 0.002 Hz was found appropriate for the lowest frequency considered.

In order to improve the computational efficiency of the numerous frequency-domain simulations performed in this thesis, an alternative frequency discretization was adopted. First, a base case was established, using uniform and finely discretized frequency bins to compute the bridge response (load case 1 was used as the base case). This base case was then used to calculate the displacement response spectrum of all bridge girder nodes. The spectrum with the highest real value of all nodes was extracted. This was done separately for the horizontal response and all the other DOF. These spectra were then sliced into equal-area slices, and the resulting frequency bins were combined. For example, with 128 bins, 64 bins are used to discretize the horizontal response, and 64 bins are used to discretize all other DOF of the response. A non-overlapping combination of all bins is then performed to obtain the final frequency array. To improve confidence in this method, a sensitivity analysis on the number of equal-area frequency bins

considered is shown in Table 11, having the uniform and finely (4096 bins) discretized case from Table 8 as a reference. With this method, only roughly $1/10$ of the bins are necessary to achieve the same accuracy.

Table 6 – Response sensitivity to the length of the FEM bridge girder elements.						
Finite element length of the bridge girder [m]	Relative bridge displacement response [%]					
	Load case 1			Load case 2		
	y	z	rx	y	z	rx
100	100.4%	127.8%	136.5%	100.2%	111.9%	128.9%
50	100.1%	107.7%	111.8%	100.0%	102.9%	108.8%
33.33	100.0%	103.4%	105.3%	100.0%	101.2%	103.9%
25 [*1]	**100.0%**	**101.7%**	**102.9%**	**100.0%**	**100.6%**	**102.1%**
20	100.0%	101.0%	101.7%	100.0%	100.4%	101.2%
16.67	100.0%	100.6%	101.0%	100.0%	100.2%	100.7%
14.29	100.0%	100.4%	100.6%	100.0%	100.1%	100.4%
12.5	100.0%	100.2%	100.3%	100.0%	100.1%	100.2%
10 (ref.) [*2]	100.0%	100.0%	100.0%	100.0%	100.0%	100.0%

Table 7 – Response sensitivity to the number of eigenmodes considered.						
Number of eigenmodes considered	Relative bridge displacement response [%]					
	Load case 1			Load case 2		
	y	z	rx	y	z	rx
1	98.9%	0.0%	2.9%	98.5%	0.0%	3.0%
2	99.9%	0.1%	5.6%	99.8%	0.0%	6.1%
10	100.1%	36.0%	6.9%	100.0%	35.1%	7.7%
25	100.1%	87.3%	6.9%	100.0%	90.4%	7.7%
50	100.0%	96.7%	90.8%	100.0%	97.7%	92.5%
100 [*1]	**100.0%**	**99.0%**	**99.7%**	**100.0%**	**99.2%**	**99.5%**
250	100.0%	99.8%	99.7%	100.0%	99.9%	99.5%
500	100.0%	100.0%	100.0%	100.0%	100.0%	100.0%
1000 (ref.) [*2]	100.0%	100.0%	100.0%	100.0%	100.0%	100.0%

Table 8 – Response sensitivity to the number of frequency bins. Uniform discretization.						
Number of frequency bins	Relative bridge displacement response [%]					
	Load case 1			Load case 2		
	y	z	rx	y	z	rx
16	33.2%	101.7%	100.2%	29.1%	101.5%	100.5%
32	107.1%	100.1%	101.4%	99.4%	100.0%	100.2%
64	318.8%	100.0%	100.2%	371.5%	100.0%	100.7%
128	213.4%	100.0%	100.2%	237.6%	100.0%	100.5%
256	147.5%	100.0%	99.9%	158.0%	100.0%	100.1%
512	111.4%	100.0%	100.0%	114.8%	100.0%	100.0%
1024	98.6%	100.0%	100.0%	96.6%	100.0%	100.0%
2048	99.8%	100.0%	100.0%	99.1%	100.0%	100.0%
4096 (ref.) [*2, *3]	100.0%	100.0%	100.0%	100.0%	100.0%	100.0%

Table 9 – Response sensitivity to the low-pass cut-off frequency						
Highest allowed frequency [Hz]	Relative[*4] bridge response [%]					
	Load case 1			Load case 2		
	y	z	rx	y	z	rx
0.1	100.0%	54.7%	49.0%	100.0%	48.9%	49.4%
0.25	100.0%	98.3%	92.6%	100.0%	98.0%	94.1%
0.5 [*1]	**99.8%**	**100.0%**	**100.0%**	**99.1%**	**100.0%**	**100.0%**
0.75	99.6%	100.0%	100.4%	98.5%	100.0%	100.4%
1	99.3%	100.0%	100.4%	98.0%	100.0%	100.4%
2	113.1%	100.0%	100.4%	117.9%	100.0%	100.4%

Table 10 – Response sensitivity to the high-pass cut-off frequency						
Lowest allowed frequency [Hz]	Relative[*4] bridge response [%]					
	Load case 1			Load case 2		
	y	z	rx	y	z	rx
0.01	62.3%	98.1%	97.3%	62.8%	98.8%	97.5%
0.008	96.6%	98.5%	97.9%	98.6%	99.1%	98.1%
0.006	98.2%	99.0%	98.5%	98.5%	99.4%	98.6%
0.004	99.0%	99.5%	99.2%	98.4%	99.7%	99.3%
0.002 [*1]	**99.8%**	**100.0%**	**100.0%**	**99.1%**	**100.0%**	**100.0%**
0.001	100.2%	100.3%	100.4%	99.5%	100.2%	100.4%
0	100.3%	100.5%	100.9%	99.9%	100.3%	100.8%

Table 11 – Response sensitivity to the num. of frequency bins. Equal-area discretization.						
Number of frequency bins	Relative*4 bridge displacement response [%]					
	Load case 1			Load case 2		
	y	z	rx	y	z	rx
8	1138.6%	146.3%	194.0%	1194.5%	142.3%	206.8%
16	260.2%	109.4%	129.8%	271.5%	107.5%	128.2%
32	121.6%	103.0%	113.4%	116.2%	101.9%	109.9%
64	104.5%	101.1%	105.6%	107.1%	100.5%	105.8%
128 *1	**100.3%**	**100.4%**	**102.3%**	**99.7%**	**100.1%**	**102.7%**
256	99.8%	100.1%	100.8%	99.1%	100.0%	100.9%
512	99.9%	100.0%	100.5%	99.3%	100.0%	100.4%
1024	99.9%	100.0%	100.1%	99.3%	100.0%	100.1%
2048	99.9%	100.0%	100.0%	99.3%	100.0%	100.0%

*1 – Value adopted in the numerical investigations.
*2 – Value used to obtain the reference response to which all relative responses in that table are compared.
*3 – Value used to obtain the reference response to which all relative responses in Table 9, Table 10 and Table 11 are compared.
*4 – The last row results of Table 8 are used as the reference.

4.3. Wind characteristics

The Bjørnafjord is a relatively wide fjord. Using approximate distances and heights, the planned bridge location can be described as having a 5 km fetch of water towards the West and a 20 km fetch of water towards the East. Small islands with 50 m heights are found towards the ocean in the West, whereas 800 m high hills can be found from 20 km to the East, followed by 1500 m high mountains 20 km further towards the East. North of the bridge site, there is a cluster of islands 50-200 m high, extending over the nearest 5 km towards the North. South of the bridge site, there are 100 m high hills within 1 km which extend to 300 m high hills within 4 km from the bridge. These hills are usually covered by forests. The frequency distributions of the mean wind speed and direction at the planned bridge location are represented by a wind rose in Fig. 21. Synthetic wind speed and direction data from a high-resolution Weather Research and Forecasting (WRF) model was used to produce the results (further details about the model are given in Section 6.4.2).

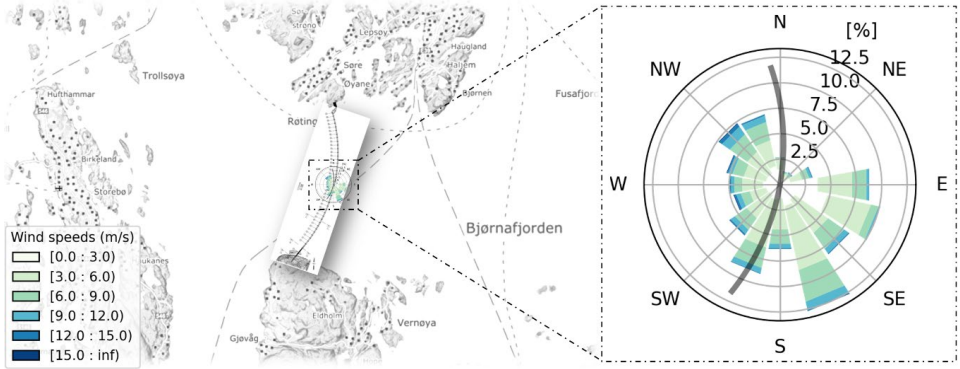

Fig. 21 – Planned bridge site. Wind rose of the distributions of the mean wind speeds and directions at the centre of the Bjørnafjord (60°06'N 5°22'E), obtained from long-term synthetic data using a WRF model and corrected by nearby wind measurements.

According to the design basis of the project, which follows the Eurocode (Norwegian Standard, 2009) and the national bridge design manual N400 (Norwegian Public Roads Administration, 2015), the vertical profile of 10-min mean wind speeds can be given by eqs. (197) to (199).

$$U(z) = c_r(z)\, c_0(z)\, U_b\, c_{prob} \tag{197}$$

$$c_r(z) = \begin{cases} k_r\, ln\left(\dfrac{z}{z_0}\right) & for \quad z_{min} \le z \le 200\, m \\ c_r(z_{min}) & for \quad z \le z_{min} \end{cases} \tag{198}$$

$$c_{prob} = \left(\frac{1 - K \cdot \ln\left(-\ln(1-p)\right)}{1 - K \cdot \ln\left(-\ln(0.98)\right)}\right)^n \tag{199}$$

U is the 10-min mean wind speed; z is the height above ground; c_r is the roughness factor; c_0 is the orography factor, taken as 1.0; U_b is the 10-min basic wind velocity at 10 m height, taken as $26\, m/s$, with a reference 50-year return period and a reference terrain category II; k_r is the terrain factor, taken as 0.17; z_0 is the roughness length, taken as 0.01, assuming for the bridge site a terrain category I; z_{min} is the minimum height, taken as 1 m; c_{prob} is the probability factor to adjust for a probability p for an annual exceedance, where $p = 1 - e^{-1/(RP)}$, and where RP is the return period in years; K and n are taken as 0.2 and 0.5, respectively.

Based on eqs. (197) to (199), the 10-min mean wind speed at $z = 10\, m$, with the return period of the bridge of 100 years, is found to be $31.7\, m/s$, and at the considered height of the girder in the floating spans, $z = 14.5\, m$, is found to be $33.4\, m/s$.

For simplicity, the wind field is first considered a stationary, homogenous stochastic process with equal velocity, turbulence, and coherence properties, for all mean wind directions. This simplification isolates the effect of the wind direction on the bridge aerodynamics and the resulting structural response.

Single-point and two-point spectra are used to model the properties of the wind field in the Bjørnafjord. The single-point spectrum used, shown in eq. (200), is given by the Norwegian bridge design manual (Norwegian Public Roads Administration, 2015), which is a "blunt model" (Olesen et al., 1984) inspired by the Kaimal spectrum (Kaimal et al., 1972). The normalized co-spectrum used, whose diagonal and off-diagonal entries are shown in eqs. (201a) and (201b), respectively, is a root sum of squares adaptation of that in (Davenport, 1961b) to consider the three-dimensionality of the wind field. The correlation between different turbulence components was assumed to be zero to comply with the design manual and for simplicity. However, the effects of a non-zero S_{uw} are potentially relevant, in particular for low natural frequencies, as suggested by (Øiseth et al., 2013) and by another ongoing study. The relevant parameters are summarized in Table 12, for $\mathrm{Z} = 14.5\ m$ (above sea level).

$$\frac{f\,S_i(f)}{\sigma_i^2} = \frac{A_i \hat{f}_i}{\left(1 + 1.5 A_i \hat{f}_i\right)^{\frac{5}{3}}}\,; \quad where:\ \hat{f}_i = \frac{f\,L_{i,X_u}}{U}\,; \quad for\ i = u, v, w \tag{200}$$

$$\frac{Re\left(S_{ii}(f, \Delta X_u, \Delta Y_v, \Delta Z_w)\right)}{S_i(f)} = \exp\left(-\sqrt{\left(K_{i,X_u}\frac{f\Delta X_u}{U}\right)^2 + \left(K_{i,Y_v}\frac{f\Delta Y_v}{U}\right)^2 + \left(K_{i,Z_w}\frac{f\Delta Z_w}{U}\right)^2}\right) \tag{201a}$$

$$\frac{Re\left(S_{i_1 i_2}(f, \Delta X_u, \Delta Y_v, \Delta Z_w)\right)}{\sqrt{S_{i_1}(f) \cdot S_{i_2}(f)}} = 0, \qquad for\ i, i_1, i_2 = u, v, w \quad and \quad i_1 \neq i_2 \tag{201b}$$

S_i is the single-point spectrum of the turbulence component i, which is then normalized by the frequency f, in Hertz, and the variance σ_i^2 of the considered turbulence component. A_i is a non-dimensional parameter used to regulate the frequency distribution of the turbulence component i and L_{i,X_u} is its characteristic length scale, in the $\boldsymbol{X_u}$ direction, which is equivalent to its average eddy size. S_{ii} and $S_{i_1 i_2}$ represent the diagonal and off-diagonal entries of the wind cross-spectral matrix, respectively. $\Delta X_u, \Delta Y_v$ and ΔZ_w are the distances between two reference

points in the Gw (Global wind) coordinate system. $K_{i,j}$ represents the non-dimensional exponential decay coefficient of the turbulent component i, used to decrease its coherence with increasing frequency and increasing distance in the direction $j = X_u, Y_v, Z_w$.

The values adopted for each parameter of the case study are presented in Table 12, where $I_i = \sigma_i / U$ is the turbulence intensity of i. These values were obtained following the latest available version of the project-related design basis (Norwegian Public Roads Administration, 2018), except for the three decay coefficients K_{i,X_u} which were taken from an aerodynamic design report (Norwegian Public Roads Administration, 2019c).

Table 12 – Input parameters for the wind simulation.

$A_u = 6.8$	$A_v = 9.4$	$A_w = 9.4$
$L_{u,X_u} = 111.8\ m$	$L_{v,X_u} = 27.9\ m$	$L_{w,X_u} = 9.3\ m$
$K_{u,X_u} = 3.0$	$K_{v,X_u} = 6.0$	$K_{w,X_u} = 3.0$
$K_{u,Y_v} = 10.0$	$K_{v,Y_v} = 6.5$	$K_{w,Y_v} = 6.5$
$K_{u,Z_w} = 10.0$	$K_{v,Z_w} = 6.5$	$K_{w,Z_w} = 3.0$
$I_u = 0.137$	$I_v = 0.115$	$I_w = 0.082$
$U = 33.4\ m/s\ (Z = 14.5\ m)$		

The wind field can be then generated numerically through, e.g. the procedure shown in (Shinozuka, 1972) and (Deodatis, 1996), and used in time-domain simulations of the response. Various methods to compute the wind field have been proposed, e.g. (Di Paola, 1998; Hémon and Santi, 2003; Tao et al., 2021), with different computational efficiency. The target and the generated non-dimensional auto-spectral densities of each turbulence component, using the parameters from Table 12, are illustrated in Fig. 22 (left-hand plot). The first diagonal entry of the co-spectrum (concerning the u component) is also illustrated in its normalized form and zoomed for the frequencies of interest (right-hand plot). It is a function of the frequency and the vector of distances $(\Delta X_u, \Delta Y_v, \Delta Z_w)$ between the two reference points, which in this example are assumed to be colinear with the $\boldsymbol{Y_v}$ axis for illustration purposes. 3-hour long Monte Carlo simulations of the wind field, with a sampling frequency of 4 Hz, were used. The Welch method, with 20 non-overlapping windows, was used in both plots of Fig. 22 for a better visual comparison (reducing the noise at the cost of lower frequency resolution). The wind simulations for this study were performed in *Python*. A compromise between computational time and accuracy was found by simulating several independent 10-minute-long "wind blocks". In order to prevent abrupt changes in the wind

velocities, these blocks are concatenated with 8-second-long overlapping periods and with a linear transition between the velocities of adjacent blocks.

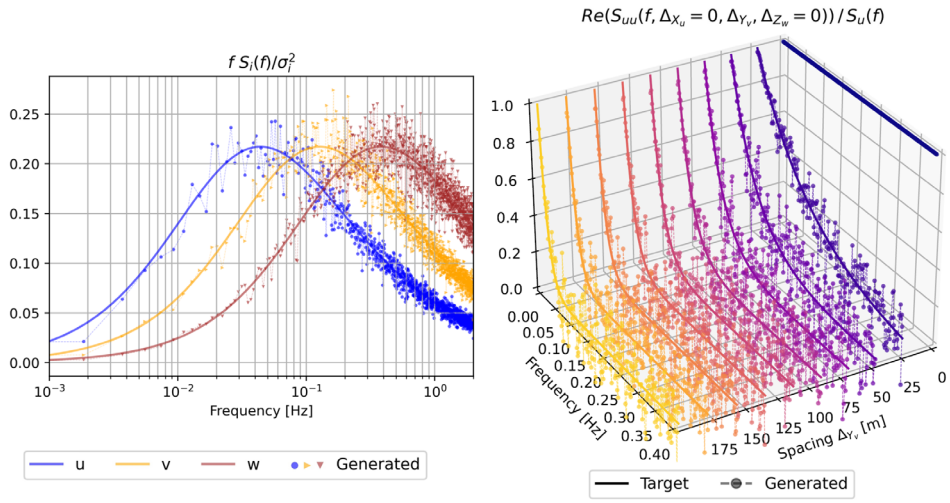

Fig. 22 – Comparison between the target and numerically generated values for the normalized auto-spectra of turbulence components and for one normalized co-spectrum of u as a function of the frequency and the distance of two colinear reference points along the $\boldsymbol{Y_v}$ axis, using the parameters from Table 12. Welch's method was used in this figure (with 20 non-overlapping windows) for a better visual comparison.

5. Skew wind buffeting application

5.1. Preface

This chapter is reproduced from a published article (Costa et al., 2022b). The formatting has been adapted to the thesis, and some of the content was removed to avoid repeating information given in previous chapters. The removed parts of the paper are related to: a) the motivations, b) the description of existing skew wind buffeting models, c) the previous literature findings, d) the Bjørnafjord project, e) the floating bridge description, f) the wind site description, g) the wind field modelling, h) the adopted coordinate systems, and i) the FEM model and its modal analysis. The remaining parts of the paper were rearranged, but their content remains mostly unchanged. The full reference of the paper is:

Costa, B.M., Wang, J., Jakobsen, J.B., Øiseth, O.A., Snæbjörnsson, J.Þ., 2022b. Bridge buffeting by skew winds: A quasi-steady case study. Journal of Wind Engineering and Industrial Aerodynamics 227, 105068.
https://doi.org/10.1016/j.jweia.2022.105068

5.2. Abstract

The buffeting response of a 5000-meter-long curved floating bridge is investigated for different mean wind directions, with emphasis on the wind load formulations and use of experimental data. Wind tunnel tests, with a section model of the bridge girder, provided six aerodynamic coefficients for different yaw and inclination angles. A comprehensive 3D buffeting formulation with bivariate polynomial fits of the coefficients is proposed and investigated. For cases when the skew wind data is not available, alternative 2D formulations, including the traditional “cosine rule”, are examined. A finite element model is established together with the three-dimensional wind field, in both frequency- and time-domain, and the structural

response is analysed. The response is compared for: linear and non-linear coefficient formulations, different buffeting load formulations, different fitting methods, different coefficients considered and different quasi-steady motion-dependent force formulations. The case study demonstrates limitations of the 2D buffeting formulations, in particular of the "cosine rule", and further supports the use of 3D buffeting formulations, the gathering of comprehensive data for skew wind loads and the use of constrained polynomials when fitting and extrapolating the data. This study also provides valuable insight on how to perform these analyses and overcome some of the practical challenges.

5.3. Introduction

Bridges in steep surroundings are often subject to wind channelling effects, marked by narrow distributions of mean wind directions, which can differ drastically from those observed in nearby offshore measurements. This observation is seen to a different extent in Lysefjord (Cheynet et al., 2020), Hardangerfjord (Castellon et al., 2021), and Sulafjord (Midjiyawa et al., 2021). Contrastingly, near-flat surroundings such as at the Donghai Bridge allow wider and more uniform distributions of mean wind directions (Zhou et al., 2020). The Bjørnafjord, shown in Fig. 11 and Fig. 21, exhibits topography effects that lie in between the examples mentioned, with moderate wind channelling effects and multiple relevant wind directions (Cheynet et al., 2018). The planned bridge deck is curved in the horizontal plane, and it also includes vertical curvatures and slopes. This geometry naturally gives rise to skew winds along most or all of its length.

The study of skew wind effects on a bridge response is important for the safe and cost-effective design of wind-sensitive bridges exposed to strong skew winds. Understanding these effects can also assist full-scale studies, which deal with wind and bridge response data for arbitrary mean wind directions, fatigue analyses, which require a comprehensive understanding of the environmental loads, and bridge operation and maintenance decision support. This chapter provides an application of the various skew wind buffeting models presented in Chapter 3, using the floating bridge and finite element model presented in Chapter 4 as a case study.

A third party, *Svend Ole Hansen ApS*, conducted wind tunnel experiments on a section model of the bridge girder studied. The gathered data is presented and used in this study. Aerodynamic coefficients at 30 different combinations of β and θ are estimated. Despite obtaining results for β up to $50°$, beyond a range previously

documented in the literature, significant extrapolations are still necessary for a full description of the buffeting response under skew winds. The challenges of fitting the data and extrapolating the results are carefully presented and discussed. Constrained polynomial fits are proposed and compared with their unconstrained counterparts. A comparison is made between the univariate polynomial fits that do not consider the skew wind data at $\beta \neq 0°$ and the bivariate polynomial fits that consider all the data. The traditional "Cosine rule" extrapolation is also included for comparison.

Buffeting analyses are conducted and compared in both frequency and time domain. Analyses that use general non-linear formulations of the skew wind loads are compared with their linearized counterparts. The different skew wind formulations, namely 2D, 2D + 1D and 3D, and the different fitting methods are compared in terms of bridge response. The effects of the different aerodynamic coefficients on the response are also compared. Finally, the effects of the quasi-steady motion-dependent forces are assessed using the formulation presented in (Zhu, 2002) and the main and alternative formulations presented in Chapter 3.

5.4. Wind tunnel experiment

Svend Ole Hansen ApS performed a series of wind tunnel tests in connection with the Bjørnafjord floating bridge project, including static section model tests under skew winds (Norwegian Public Roads Administration, 2019e). The test results and the raw data were provided to the authors and were further examined. The model is 2.40 meters long, has a geometric scale of 1:80, and has an aspect ratio of 6.2 (length/width). A straight strip theory is assumed valid due to the large curvature radius of the bridge and the relatively rapid decaying coherence of the wind. The cross-section of the model is illustrated in Fig. 12, and the relevant static model setup is described in Fig. 23, Fig. 24 and Fig. 25.

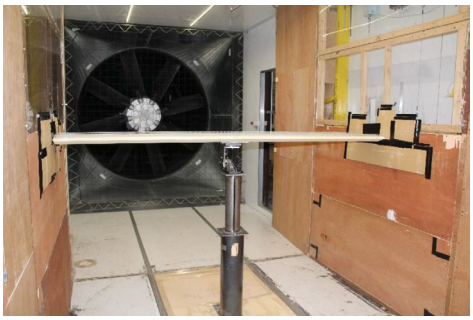

Fig. 23 – Model setup for $(\beta, \theta) = (0°, 0°)$

Fig. 24 – Model setup for $(\beta, \theta) = (50.94°, -1.89°)$

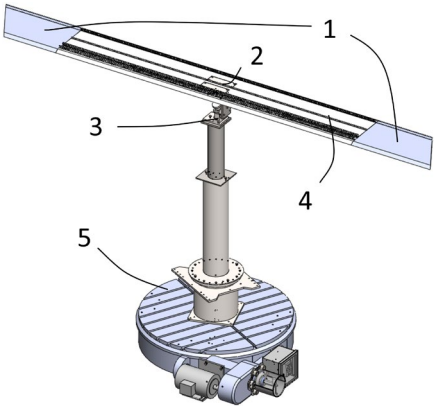

Fig. 25 – Model parts: 1) disconnected pseudo ends; 2) 6 DOF force sensor; 3) rotary joint for rx; 4) bridge girder; 5) rotary table for rZ.

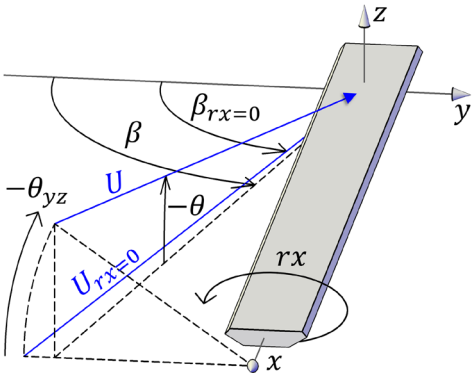

Fig. 26 – Schematic relation between the rotation rx, the mean wind vectors $U_{rx=0}$ (before the rotation) and U, and the angles $\beta_{rx=0}$, β, θ and θ_{yz}.

In a wind tunnel setting, it is often practical to perform rotations of the bridge girder model around its longitudinal $\boldsymbol{x}$ axis, denoted as a rx rotation, to access the wind loading at different wind angles. For skew winds, the effects of such a rotation on the local wind angles are shown in Fig. 26. A rx rotation of the girder causes the $\boldsymbol{y}$ and $\boldsymbol{z}$ axes to rotate as well but, equivalently and for better illustration purposes, the mean wind vector is rotated instead in Fig. 26, as it is the relative angles between the mean wind and the structure that are of interest. Note that rx is directly correlated with θ_{yz}, with opposite sign, and not with θ. The mean wind vectors, before and after the rx rotation, are denoted $\boldsymbol{U_{rx=0}}$ and $\boldsymbol{U}$ respectively. Also, the yaw angle may change with rx, from an initial value $\beta_{rx=0}$ to β. From an initial unrotated position with $\theta = \theta_{yz} = 0°$ and with given values of $\beta_{rx=0}$ and rx, it is possible to estimate the resulting β, θ and θ_{yz} using eqs. (202), (203) and (204), which are valid for $\beta_{rx=0} \in [-90°, 90°] \wedge rx \in [-90°, 90°]$.

$$\beta = \arctan\left(\frac{\tan(\beta_{rx=0})}{\cos(rx)}\right) \tag{202}$$

$$\theta = -\arcsin(\cos(\beta_{rx=0})\sin(rx)) \tag{203}$$

$$\theta_{yz} = -rx \tag{204}$$

Also, it may be helpful to obtain θ_{yz} from known values of β and θ, through eq. (205).

$$\theta_{yz} = \arcsin\left(\sin\theta/\sqrt{1-\sin^2\beta\cos^2\theta}\right) \tag{205}$$

In 2D analyses, i.e., with only the wind components in the normal plane, the aerodynamic loads are traditionally represented in the Drag, Lift and Moment directions. However, in 3D analyses, different representations of the wind forces have been used. In Chapter 3, representing the aerodynamic coefficients in the global wind system Gw $(\boldsymbol{X_u}, \boldsymbol{Y_v}, \boldsymbol{Z_w})$ leads to a more compact formulation of the buffeting and self-excited forces. However, in the present case study, the local structural system Ls $(\boldsymbol{x}, \boldsymbol{y}, \boldsymbol{z})$ is used to represent the aerodynamic coefficients, together with a normalization by the total mean wind speed squared U^2 and the cross-section width B (or B^2), such that the vector of mean aerodynamic forces per unit length in the Ls system $\boldsymbol{f_{mean,Ls}}$ is expressed by eq. (206).

$$\boldsymbol{f_{mean,Ls}} = 1/2\,\rho\,U^2\boldsymbol{B}\,\boldsymbol{C_{Ls}}(\beta,\theta) = 1/2\,\rho\,U^2\begin{bmatrix} B & 0 & 0 & 0 & 0 & 0 \\ 0 & B & 0 & 0 & 0 & 0 \\ 0 & 0 & B & 0 & 0 & 0 \\ 0 & 0 & 0 & B^2 & 0 & 0 \\ 0 & 0 & 0 & 0 & B^2 & 0 \\ 0 & 0 & 0 & 0 & 0 & B^2 \end{bmatrix}\begin{bmatrix} C_x \\ C_y \\ C_z \\ C_{rx} \\ C_{ry} \\ C_{rz} \end{bmatrix}_{(\beta,\theta)} \tag{206}$$

Wind- and structure-based coordinate systems have pros and cons, which the user should weigh. The Ls $(\boldsymbol{x}, \boldsymbol{y}, \boldsymbol{z})$ system representation was used here, with the following advantages:

a) It is consistent regardless of wind direction, avoiding transformations between instantaneous and mean wind directions when describing the aerodynamic forces.

b) It is practical in both the experimental setup and the FEM implementation.

c) It enables intuitive and easily defined constraints on the polynomials for fitting the aerodynamic coefficients, as shown in Section 5.5.

d) It describes well the axial direction with $\boldsymbol{x}$ and $\boldsymbol{rx}$, as well as the perpendicular ($\boldsymbol{y}$) and vertical ($\boldsymbol{z}$) directions, and it isolates the two often negligible coefficients C_{ry} and C_{rz}, as opposed to a wind-oriented coordinate system.

e) A normal-projection coordinate system representation (such as Drag, Moment and Lift) would lead to extra non-linearities due to the projections, and it would be discontinuous at certain regions (e.g. at $\beta = \pm 90°$, an inversion of the normal drag direction occurs). Also, it is often associated with an inconsistent normalization (e.g. Drag normalized by H and Lift normalized by B) that could lead to mistakes (and also lose meaning at large angles).

Note that when C_y is plotted as a function of θ, it can concave downwards, contrary to the more traditional drag coefficient that usually concaves upwards for similar cross-sections (the reason for this is that the second derivative of C_y, evaluated at $\theta = 0$, depends on the slope of the Lift, the second derivative of the Drag, and the Drag itself, though this is not relevant for the analysis).

A mean wind speed of approximately 5 m/s was used in the experiments, together with a turbulent flow setting where horizontal and vertical turbulence intensities were measured at 10% and 7%, respectively. The static aerodynamic coefficients were obtained by averaging the measured forces over 60 seconds, at a 500 Hz sample rate, for each mean wind direction. A 6 DOF "*ATI Industrial Automation Mini45* force/torque sensor" was used.

The tests were conducted for six initial angles of $\beta_{rx=0}$ (0°, 9.90°, 19.90°, 29.90°, 39.90° and 49.90°) and, for each of them, five different rx rotations ($-3.0°$, $-1{,}5°$, 0°, 1.5° and 3.0°). The tested angles, expressed in β and θ, and the measured coefficients are presented in the following tables, from Table 13 to Table 19.

Table 13 – 30 tested pairs of angles (β, θ) in degrees.

(0.00, 3.00)	(9.91, 2.96)	(19.93, 2.82)	(29.93, 2.60)	(39.94, 2.30)	(49.94, 1.93)
(0.00, 1.50)	(9.90, 1.48)	(19.91, 1.41)	(29.91, 1.30)	(39.91, 1.15)	(49.91, 0.97)
(0.00, 0.00)	(9.90, 0.00)	(19.90, 0.00)	(29.90, 0.00)	(39.90, 0.00)	(49.90, 0.00)
(0.00, -1.50)	(9.90, -1.48)	(19.91, -1.41)	(29.91, -1.30)	(39.91, -1.15)	(49.91, -0.97)
(0.00, -3.00)	(9.91, -2.96)	(19.93, -2.82)	(29.93, -2.60)	(39.94, -2.30)	(49.94, -1.93)

Table 14 – Measured $C_x(\beta,\theta)$ with β and θ pairs from Table 13.

0.00E+2*	-4.91E-3	-1.07E-2	-1.87E-2	-2.01E-2	-2.22E-2
0.00E+2*	-6.75E-3	-1.41E-2	-2.09E-2	-1.73E-2	-2.42E-2
0.00E+2*	-7.18E-3	-1.52E-2	-2.19E-2	-2.33E-2	-1.95E-2
0.00E+2*	-8.53E-3	-1.71E-2	-2.06E-2	-2.27E-2	-2.58E-2
0.00E+2*	-2.82E-3	-1.72E-2	-2.67E-2	-2.61E-2	-2.80E-2

Table 15 – Measured $C_y(\beta,\theta)$ with β and θ pairs from Table 13.

7.32E-2	7.31E-2	6.45E-2	5.90E-2	4.95E-2	3.19E-2
7.40E-2	7.46E-2	6.81E-2	6.08E-2	5.95E-2	3.79E-2
7.11E-2	7.60E-2	7.11E-2	6.30E-2	5.53E-2	4.03E-2
7.07E-2	7.51E-2	6.67E-2	6.62E-2	5.45E-2	4.10E-2
6.39E-2	6.86E-2	6.57E-2	5.52E-2	5.35E-2	3.90E-2

Table 16 – Measured $C_z(\beta,\theta)$ with β and θ pairs from Table 13.

4.27E-2	5.99E-2	9.74E-2	1.18E-1	1.51E-1	1.60E-1
-5.51E-2	-2.79E-2	6.39E-3	4.88E-2	6.76E-2	1.02E-1
-1.47E-1	-1.16E-1	-7.03E-2	-3.75E-2	3.80E-2	2.74E-2
-2.41E-1	-2.15E-1	-1.54E-1	-1.09E-1	-1.95E-2	2.66E-2
-3.29E-1	-3.12E-1	-2.26E-1	-1.63E-1	-7.26E-2	-1.44E-2

Table 17 – Measured $C_{rx}(\beta,\theta)$ with β and θ pairs from Table 13.

-6.17E-2	-6.20E-2	-6.16E-2	-5.33E-2	-4.81E-2	-3.81E-2
-3.74E-2	-3.90E-2	-3.96E-2	-3.54E-2	-3.56E-2	-2.64E-2
-1.20E-2	-1.82E-2	-2.07E-2	-1.73E-2	-2.21E-2	-1.61E-2
1.55E-2	1.09E-2	1.75E-3	1.04E-3	-7.79E-3	-6.62E-3
4.22E-2	3.89E-2	2.61E-2	2.08E-2	6.35E-3	2.30E-3

Table 18 – Measured $C_{ry}(\beta,\theta)$ with β and θ pairs from Table 13.

0.00E+2*	-3.03E-2	-3.65E-2	6.58E-3	1.93E-2	4.44E-3
0.00E+2*	-1.05E-2	4.03E-3	1.26E-2	2.01E-2	1.79E-2
0.00E+2*	-3.05E-2	-2.38E-2	3.85E-2	1.22E-2	2.04E-2
0.00E+2*	-5.96E-3	-9.29E-3	6.38E-3	2.50E-2	3.78E-2
0.00E+2*	4.86E-5	-2.88E-2	1.39E-2	6.36E-3	2.32E-2

Table 19 – Measured $C_{rz}(\beta, \theta)$ with β and θ pairs from Table 13.

0.00E+2*	-2.73E-3	-1.09E-3	2.46E-3	1.07E-3	2.19E-3
0.00E+2*	-1.94E-3	-8.82E-4	3.23E-3	1.62E-4	1.42E-3
0.00E+2*	-3.17E-3	-5.52E-4	1.78E-3	-2.80E-3	-8.24E-3
0.00E+2*	-8.42E-4	1.84E-3	1.51E-3	5.16E-4	1.03E-3
0.00E+2*	-1.69E-3	1.61E-3	5.51E-3	1.75E-3	1.87E-3

* Small, measured values marked with * were forced to 0 due to symmetry assumptions at $\beta = 0$.

The results from the wind tunnel tests need to be interpolated and extrapolated in order to be used in the buffeting analyses of the finite element model at different instantaneous values of $\tilde{\beta}$ and $\tilde{\theta}$ (variables represented with a tilde accent are time- and turbulence-dependent).

To assess the $\tilde{\theta}$-interval of interest, 1 million samples of u, v and w were generated in Fig. 27, assuming them to be independent of each other, normally distributed, with $\sigma_i = I_i\, U$ obtained from Table 12, with an arbitrary global (homogeneous) mean wind direction. The joint and marginal probability density functions of the instantaneous $\tilde{\theta} = \arcsin\left(\tilde{U}_z/\tilde{U}\right)$ and $\tilde{\beta} = atan2\left(-\tilde{U}_x/\tilde{U}_y\right)$ are plotted, where $\tilde{U} = \sqrt{(U+u)^2 + v^2 + w^2}$ and where $\tilde{U}_x$, $\tilde{U}_y$ and $\tilde{U}_z$ are the local x, y and z components of $\tilde{U}$. The $\boldsymbol{yz}$-plane projection of the instantaneous inclination angle, $\tilde{\theta}_{yz}$, is also included for reference. The 10th and 90th percentiles (P10 and P90) are included for both $\tilde{\theta}$ and $\tilde{\theta}_{yz}$.

The domain and variance of $\tilde{\theta}_{yz}$ increase strongly as $\tilde{\beta}$ approaches $\pm 90°$, as anticipated. On the other hand, the tested domain of θ of $[-3°, 3°]$ covers 50.5% of all occurring $\tilde{\theta}$-values. An interval of $[-10°, 10°]$ would cover 97.2% of the occurring $\tilde{\theta}$-values and is the interval used to illustrate the aerodynamic coefficient fits in Section 5.5.

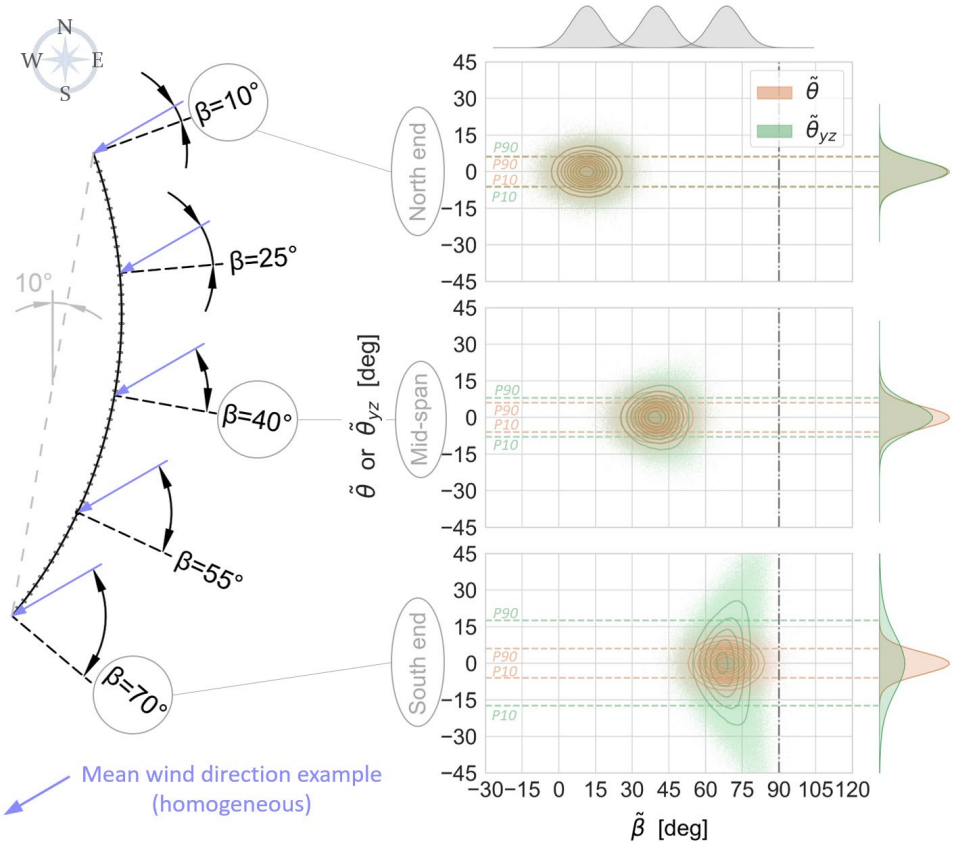

Fig. 27 – Left: Example of one homogeneous mean wind direction and associated local mean yaw angles β along the curved floating bridge. Right: Example of joint and marginal probability density functions of the instantaneous yaw and inclination angles, $\tilde{\beta}$ and $\tilde{\theta}$, due to turbulence, at three different bridge nodes. The $\boldsymbol{yz}$-plane projection of inclination angle, $\tilde{\theta}_{yz}$, is also included for reference.

Lastly, it should be mentioned that alternative model test setups could be considered when studying very large yaw angles. A rotatable girder with elongated pseudo ends on a large rotary table in a large wind tunnel or the cantilevered setup presented in (Zhu et al., 2002b) are two possibilities. A strip section perpendicular to the $\boldsymbol{x}$ axis was tested, but an oblique strip section, aligned with the wind, could also be considered. Local flow effects caused by the small air gaps or eccentricities between the girder and the pseudo ends, were neglected. These effects were assessed in (Zhu et al., 2002b) and (Zhu, 2002), by estimating the six aerodynamic coefficients with different air gap alignments relative to the wind, using different oblique strips. Small differences were observed for some of the DOF ($\boldsymbol{X_u}$, $\boldsymbol{Z_w}$, $\boldsymbol{rX_u}$), and larger differences were observed for the other DOF ($\boldsymbol{Y_v}$, $\boldsymbol{rY_v}$, $\boldsymbol{rZ_w}$) that were associated with smaller valued coefficients.

5.5. Approximations and fits of the aerodynamic coefficients

5.5.1. Initial considerations

The basic mean wind load expressions for the different skew wind formulations, namely the 2D approach, the traditional "Cosine rule", which is a further simplification of the 2D approach (more details are given in Section 5.5.3), and the preferred 3D approach, are recalled in eqs. (207) to (209).

$$f_{mean,i}^{2D} = \begin{cases} 1/2\,\rho \boldsymbol{B} {U_{yz}}^2 C_i\left(\beta = 0°, \theta_{yz}\right), & for\ i = y,z,rx \\ 0, & for\ i = x,ry,rz \end{cases} \tag{207}$$

$$f_{mean,i}^{Cosine\ rule} = \begin{cases} 1/2\,\rho \boldsymbol{B} U^2 \cos^2\beta\, C_i(\beta = 0°, \theta), & for\ i = y,z,rx \\ 0, & for\ i = x,ry,rz \end{cases} \tag{208}$$

$$f_{mean,i}^{3D} = 1/2\,\rho \boldsymbol{B} U^2 C_i(\beta, \theta), \qquad for\ i = x,y,z,rx,ry,rz \tag{209}$$

Where θ_{yz} is defined in eq. (205) and U_{yz} in eq. (210).

$$U_{yz} = U\sqrt{1 - \sin^2\beta \cos^2\theta} \tag{210}$$

For comparison purposes, all coefficients can be re-normalized by $1/2\,\rho \boldsymbol{B} U^2$, as in the 3D approach. A direct comparison of the quantities $\boldsymbol{C}\left(\beta = 0°, \theta_{yz}\right){U_{yz}}^2/U^2$, $\boldsymbol{C}(\beta = 0°, \theta)\cos^2\beta$ and $\boldsymbol{C}(\beta, \theta)$ is then possible, where the first two quantities are denoted $\boldsymbol{C^{2D}}(\beta, \theta)$ and $\boldsymbol{C^{Cosine\ rule}}(\beta, \theta)$, to distinguish them from the $\boldsymbol{C}(\beta, \theta)$ coefficients that were estimated in a skew wind configuration for the 3D approach. This is expressed in eqs. (211) and (212).

$$C_i^{2D}(\beta, \theta) = \begin{cases} C_i\left(\beta = 0°, \theta_{yz}\right){U_{yz}}^2/U^2, & for\ i = y,z,rx \\ 0, & for\ i = x,ry,rz \end{cases} \tag{211}$$

$$C_i^{Cosine\ rule}(\beta, \theta) = \begin{cases} C_i(\beta = 0°, \theta)\cos^2\beta\,, & for\ i = y,z,rx \\ 0, & for\ i = x,ry,rz \end{cases} \tag{212}$$

Since no experimental data was yet available for $\beta \in [90°, 180°]$ at the current project phase, the present cross-section is assumed to have a vertical plane of symmetry ($\boldsymbol{xz}$ plane). Then, the extrapolation of the coefficient fits from $\beta \in [0°, 90°]$ to the desired domain of $\beta \in\,]-180°, 180°]$ is performed through the symmetry transformations described in eq. (213) and Fig. 28.

$$\boldsymbol{C_{Ls}}(\beta,\theta) = \boldsymbol{T_{sym}}\boldsymbol{C_{Ls}}(\beta^*,\theta) \tag{213}$$

Where β^* is the smallest angle between $\boldsymbol{U_{xy}}$ (mean wind vector projection onto the $\boldsymbol{xy}$ plane) and the $\boldsymbol{y}$ axis, such that $\beta^* \in [0°, 90°]$. β^* and $\boldsymbol{T_{sym}}$ are both given in Fig. 28 for different β-intervals. One possible explanation for non-zero C_{ry} and C_{rz} is the eccentricity of the axial force, $f_{mean,x}$, along the $\boldsymbol{z}$ and $\boldsymbol{y}$ axes.

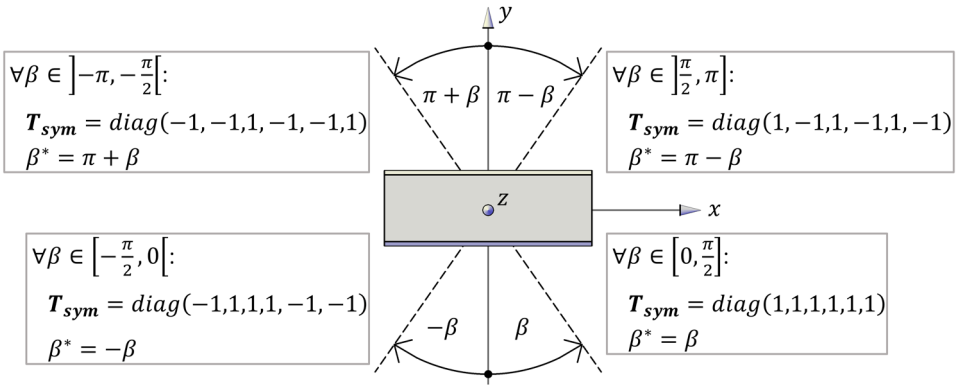

Fig. 28 – Values of $\boldsymbol{T_{sym}}$ and β^* to be used in eq. (213), for different β-intervals, to impose symmetry from the tested domain $\beta \in [0°, 90°]$ to the domain $\beta \in]-180°, 180°]$, assuming a vertical $\boldsymbol{xz}$ plane of symmetry.

The different polynomial fits to the experimentally obtained aerodynamic coefficients are now presented for the different skew wind load approaches. The coefficients of determination R^2 are included for the different polynomial degrees considered.

5.5.2. 2D approach vs measurements

In both the 2D approach and its Cosine rule approximation, only the five data points at $\beta = 0°$ are considered since these are the only available ones in a traditional wind tunnel test experiment with the mean wind normal to the girder. A univariate polynomial, as a function of θ, is fitted exclusively to these five points at $\beta = 0°$, using the least-squares method, for each coefficient, and extrapolated onto the β-dimension through eq. (211) and through the β-dependencies of θ_{yz} and U_{yz}. A comparison between the resulting values $\boldsymbol{C^{2D}}(\beta,\theta)$ and the measured values $\boldsymbol{C}(\beta,\theta)$ is shown in Fig. 29. The calculated R^2 values, which include all the 30 data points, are a measure of the goodness-of-fit of such a simplified β-extrapolation that is implicitly assumed in a 2D buffeting load formulation.

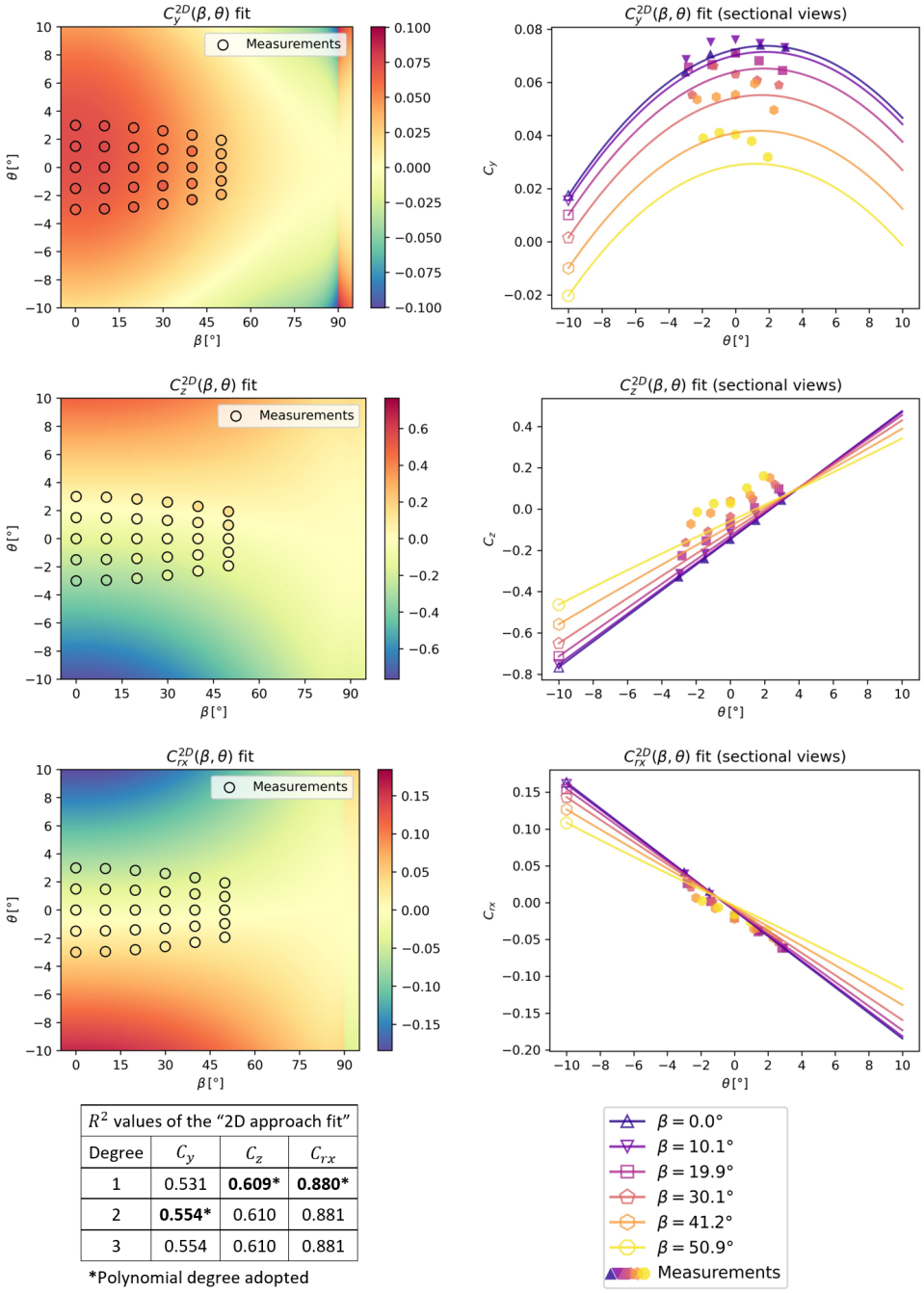

R^2 values of the "2D approach fit"			
Degree	C_y	C_z	C_{rx}
1	0.531	**0.609***	**0.880***
2	**0.554***	0.610	0.881
3	0.554	0.610	0.881

*Polynomial degree adopted

Fig. 29 – Comparing the $\boldsymbol{C^{2D}(\beta,\theta)}$ fit with the measurements $\boldsymbol{C}(\beta,\theta)$. The fit was obtained with an n^{th} degree univariate polynomial at $(\beta = 0°, \theta)$ and a 2D approach extrapolation to other β as in eq. (211).

As expected, the data points at $\beta = 0°$ are well fitted, but the poor fit at the remaining data points reinforces the idea that the 2D approach is a poor approximation of the actual three-dimensional wind flow and the corresponding skew wind load acting on a static bridge girder. Moreover, inconvenient discontinuities are obtained at $\beta = 90° \wedge \theta \neq 0$ for C_y and C_{rx} as a result of the $\boldsymbol{yz}$ projections in eq. (211) and the symmetry transformations.

5.5.3. Cosine rule vs measurements

The Cosine rule is a further simplification of the 2D approach. It implicitly assumes that $U_{yz} \approx U \cos\beta$ and that $\theta_{yz} \approx \theta$. The adequacy of these approximations is investigated in Fig. 30.

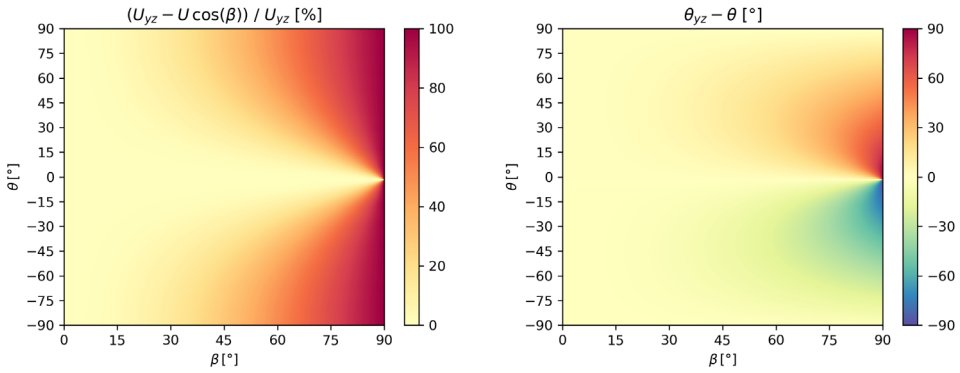

Fig. 30 – Assessing the two assumptions of the Cosine rule approximation of the 2D approach, namely that $U_{yz} \approx U cos\,\beta$ (left plot) and $\theta_{yz} \approx \theta$ (right plot).

The Cosine rule is identical to the 2D approach when $\theta = 0$, but even in $\theta = 0$ conditions, non-zero θ values need to be tested to e.g. estimate the derivatives of the aerodynamic coefficients. In the domain of the experimental data ($\beta \in [0°, 50°] \wedge \theta \in [-3°, 3°]$), both the 2D approach and its Cosine rule approximation give similar results, meaning that the experimental data is insufficient to compare both these approaches accurately. However, a "Cosine rule fit" is also included for comparison since it gives significantly different results beyond that domain. A univariate polynomial fit is first performed exclusively on the five data points at $\beta = 0°$, as in the 2D approach, followed by the extrapolation onto the β-dimension through $\cos^2\beta$, as in eq. (212). The resulting values $\boldsymbol{C}^{\boldsymbol{Cosine\ rule}}(\beta, \theta)$ and the measured values $\boldsymbol{C}(\beta, \theta)$ are compared in Fig. 31 and the R^2 values are provided.

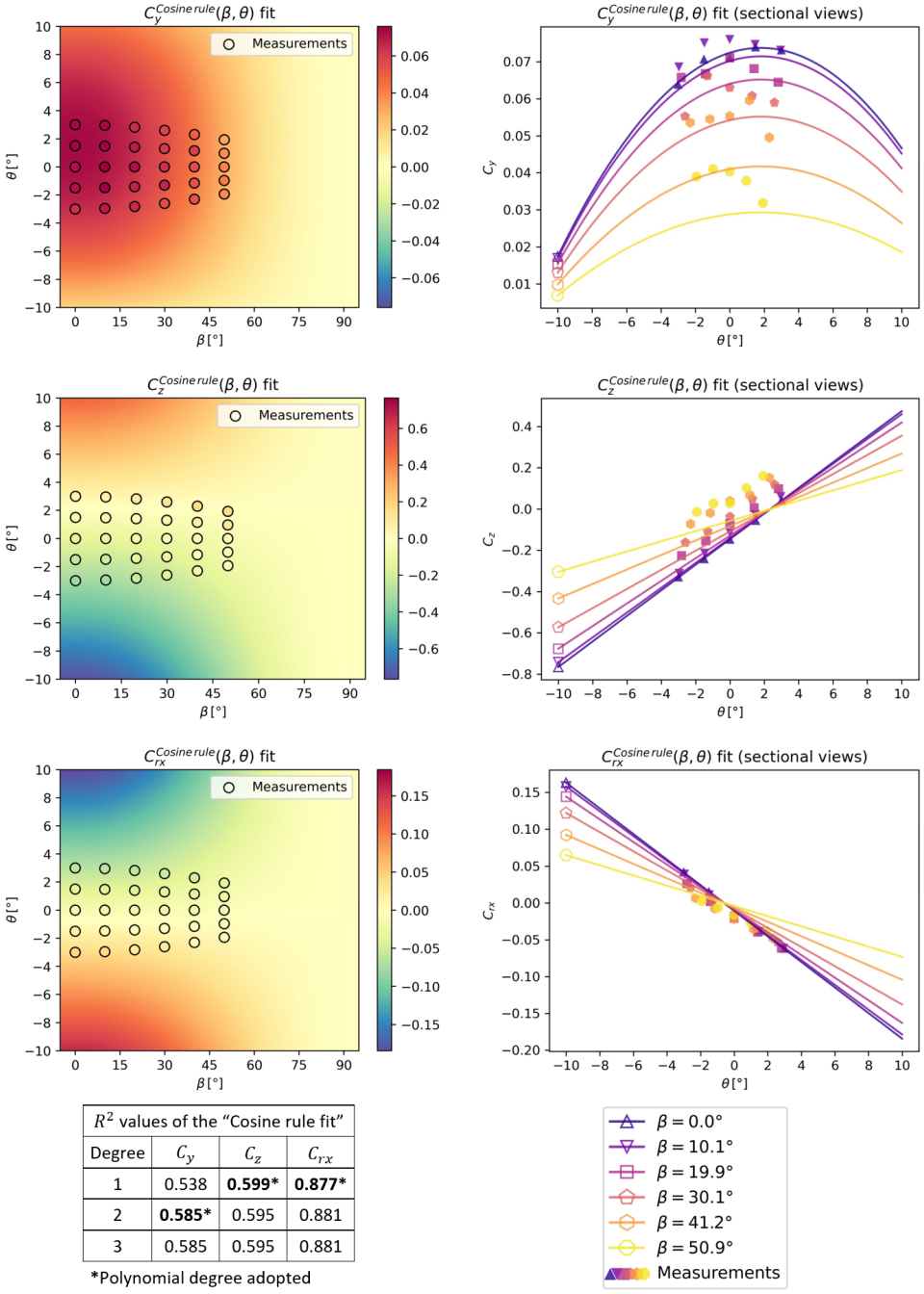

R^2 values of the "Cosine rule fit"			
Degree	C_y	C_z	C_{rx}
1	0.538	**0.599***	**0.877***
2	**0.585***	0.595	0.881
3	0.585	0.595	0.881

*Polynomial degree adopted

Fig. 31 – Comparing the $\boldsymbol{C^{Cosine\ rule}(\beta,\theta)}$ fit with the measurements $\boldsymbol{C(\beta,\theta)}$. The fit was obtained with an n^{th} degree univariate polynomial at $(\beta = 0°, \theta)$ and a Cosine rule extrapolation to other β as in eq. (212).

Both the 2D approach and the Cosine rule give similar comparisons and similar R^2 values, as expected. One advantage of using the Cosine rule approximation is that it provides continuous and smooth coefficients throughout the domain as a consequence of using $\cos^2\beta$. On the other hand, the principle on which the Cosine rule is based (a wind projection onto the 2D normal plane) is not valid for large values of β and θ (as shown in Fig. 30).

5.5.4. Bivariate polynomial fits

Bivariate (β, θ) polynomials are now fitted to the entire experimental dataset and later used as input for the 3D approach formulation. An example of a *maximum* 2nd degree polynomial is shown in eq. (214) (where, e.g. a *total* 4th degree monomial $\beta^2\theta^2$ is allowed). Hereafter, "degree" refers to the highest degree used in the polynomial.

$$P(\beta,\theta) = c_{00} + c_{01}\theta + c_{02}\theta^2 + c_{10}\beta + c_{11}\beta\theta + c_{12}\beta\theta^2 + c_{20}\beta^2 + c_{21}\beta^2\theta + c_{22}\beta^2\theta^2 \tag{214}$$

The c constants are found with the least-squares solution by minimizing $\sum_{k=1}^{m}\left(P_i(\beta_k,\theta_k) - C_i(\beta_k,\theta_k)\right)^2$, where k iterates over each of the m experimental data points of the aerodynamic coefficient C_i. It can be useful to reformulate the function to be minimized as $\sum_{k=1}^{m}(\boldsymbol{Ax}-\boldsymbol{b})_k^2$. The parameters $\boldsymbol{A}$, $\boldsymbol{x}$ and $\boldsymbol{b}$ are exemplified in eqs. (215) to (217), using the same 2nd degree polynomial example.

$$\boldsymbol{A} = \begin{bmatrix} 1 & \theta_1 & \theta_1^2 & \beta_1 & \beta_1\theta_1 & \beta_1\theta_1^2 & \beta_1^2 & \beta_1^2\theta_1 & \beta_1^2\theta_1^2 \\ \cdots & \cdots & \cdots & \cdots & \cdots & \cdots & \cdots & \cdots & \cdots \\ 1 & \theta_m & \theta_m^2 & \beta_m & \beta_m\theta_m & \beta_m\theta_m^2 & \beta_m^2 & \beta_m^2\theta_m & \beta_m^2\theta_m^2 \end{bmatrix} \tag{215}$$

$$\boldsymbol{x} = [c_{00} \quad c_{01} \quad c_{02} \quad c_{10} \quad c_{11} \quad c_{12} \quad c_{20} \quad c_{21} \quad c_{22}]^T \tag{216}$$

$$\boldsymbol{b} = [C_{i,1} \quad \cdots \quad C_{i,m}]^T \tag{217}$$

Then, the Jacobian row matrix of $\sum_{k=1}^{m}(\boldsymbol{Ax}-\boldsymbol{b})_k^2$ becomes simply $2(\boldsymbol{Ax}-\boldsymbol{b})^T\boldsymbol{A}$, and the Hessian matrix becomes $2\boldsymbol{A}^T\boldsymbol{A}$, which can be valuable inputs for an efficient minimization.

5.5.4.1. Free polynomials

In Fig. 32, free (unconstrained) polynomials are fitted to all six aerodynamic coefficients and compared with the measured values.

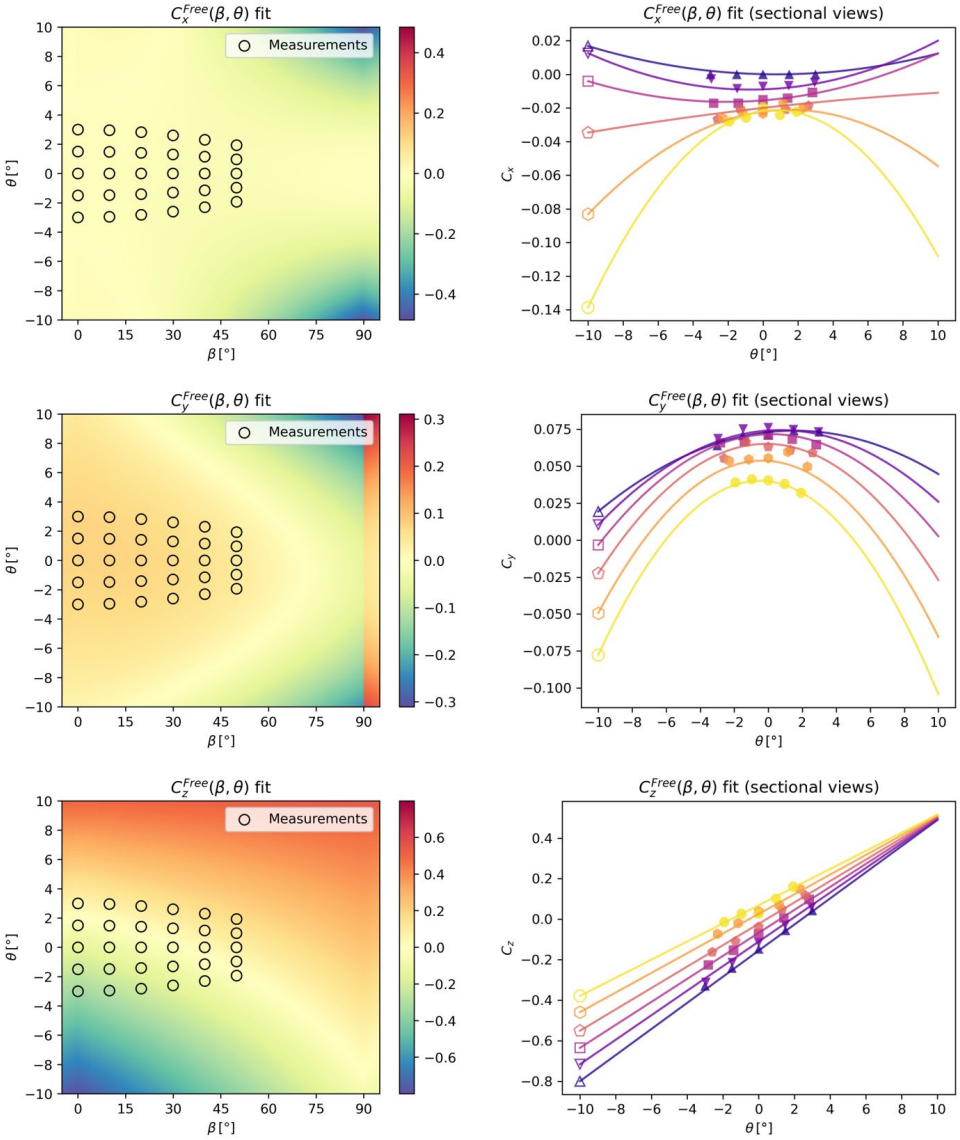

Fig. 32 – Free bivariate polynomial fits of the aerodynamic coefficients.

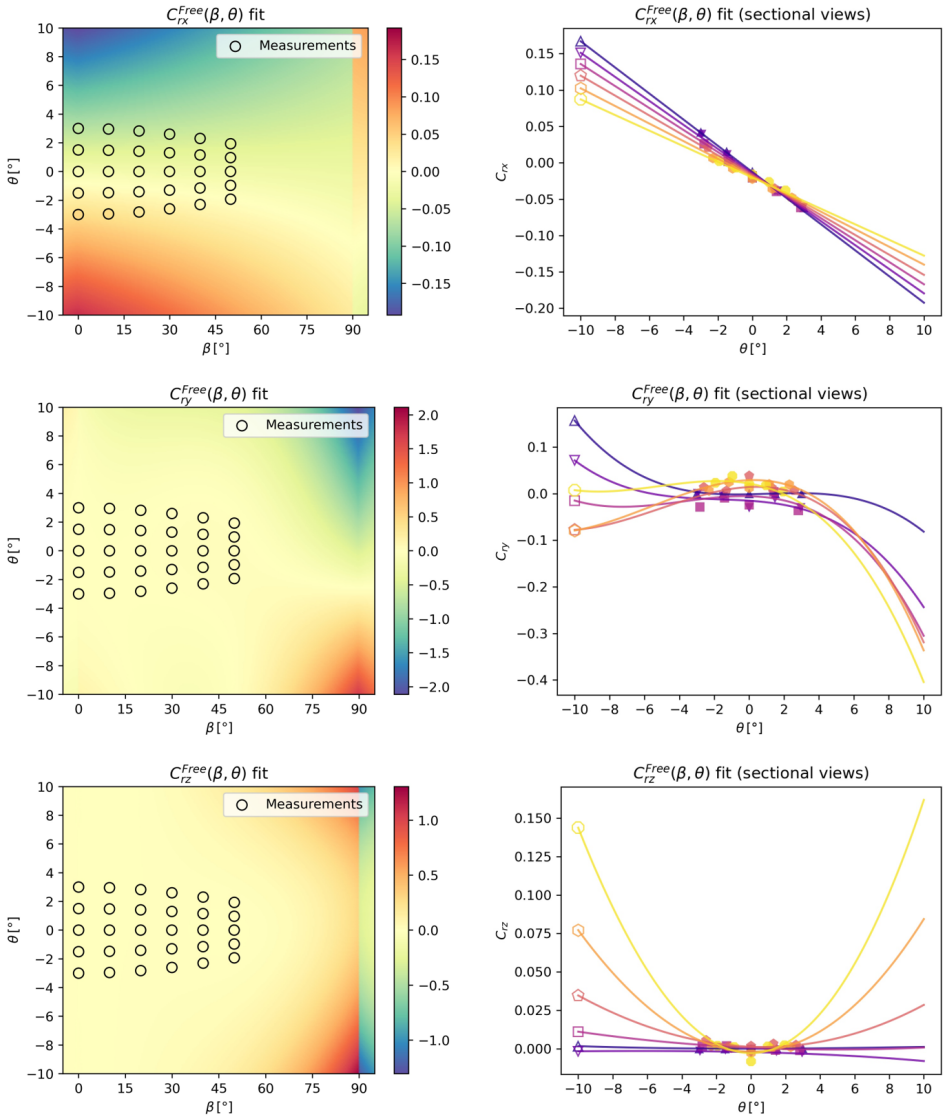

R^2 values of the n^{th} degree free polynomial fit						
Degree	C_x	C_y	C_z	C_{rx}	C_{ry}	C_{rz}
1	0.880	0.815	**0.990***	**0.991***	0.383	0.052
2	**0.962***	**0.969***	0.994	0.997	0.532	0.437
3	0.965	0.971	0.996	0.997	**0.728***	0.499
4	0.978	0.985	0.996	0.997	0.734	**0.648***
5	0.980	0.986	0.997	0.999	0.827	0.676
6	0.981	0.986	0.997	0.999	0.828	0.676

*Polynomial degree adopted

Fig. 32 (cont.) – Free bivariate polynomial fits of the aerodynamic coefficients.

It is clear that bivariate polynomials provide good fits to the measurement data for the four main coefficients C_x, C_y, C_z and C_{rx}, even with low-degree polynomials. The measured values of C_{ry} and C_{rz} are relatively small and irregular. The higher-degree polynomials adopted for these two coefficients result in somewhat larger extrapolated values, but their effect on the response is still small, as shown in Section 5.6.4.

One disadvantage of these free bivariate polynomials is that they provide discontinuous or non-differentiable results at the β-boundaries (see, e.g. a discontinuity at $C_y(90°, \theta)$ or, less noticeably, of $\partial C_z/\partial\beta$ at $(0°, \theta)$ and $(90°, \theta)$, which is more clearly illustrated in Fig. 34). Also, due to the lack of data at higher values of β and θ, unrealistic values are estimated for some of the coefficients in these regions.

5.5.4.2. Constrained polynomials – the proposed fitting method

The present case study and buffeting analysis cover a large domain of yaw angles β from $-180°$ to $180°$ (and inclination angles θ from roughly $-10°$ to $10°$), which has only been partly covered by experimental data. This shortage of data is the first indication of a need to control the shape of the polynomials where no data is available, by imposing key physical principles at the boundaries. It should be noted that neither the present experiment nor previous literature has presented aerodynamic coefficients of bridge decks at yaw angles larger than $50°$, and even if data was abundant, the aerodynamic coefficients $C(\beta, \theta)$ should still follow certain principles, such as continuity, differentiability and symmetry, in order to provide stable and reliable linearized numerical buffeting analyses. For example, simply mirroring a free polynomial fit from a tested domain (e.g. $\beta \in [0°, 90°]$) to an extrapolated domain (e.g. $\beta \in [90°, 180°]$) can compromise these principles. Hence, different shape constraints were introduced for different polynomial fits based on the expected aerodynamic behaviour at the boundaries of β and θ. Together with the symmetry transformations already introduced, these constraints enable smooth transitions of the fits at the boundaries (at $\beta = -90°, 0°, 90°$ and $\pm 180°$), ensuring continuous and differentiable aerodynamic coefficients throughout the domain, as well as enforcing certain assumed polynomial shapes and encouraging the polynomials to remain within reasonable values. The boundary constraints adopted are presented in Table 20, for each fitted coefficient, within the domain $\beta \in [0°, 90°] \wedge \theta \in [-90°, 90°]$. They are considered valid for bridge section models with a constant cross-section along the $\boldsymbol{x}$ axis.

Table 20 – Boundary constraints adopted for the polynomial fits $P(\beta, \theta)$ of each C_i.

No.	Constraint equation	C_x	C_y	C_z	C_{rx}	C_{ry}	C_{rz}
1	$P(0°, \theta) = 0$	X[*1]				X[*1]	X[*1]
2	$P(90°, \theta) = 0$		X[*2]		X[*2]		X[*2]
3	$P(90°, 0°) = 0$		X[*1*3]	X[*1]	X[*1*3]		X[*2*3]
4	$P(\beta, -90°) = 0$	X[*1]	X[*2]		X[*2]	X[*1]	X[*1]
5	$P(\beta, 90°) = 0$	X[*1]	X[*2]		X[*2]	X[*1]	X[*1]
6	$P(\beta, -90°) = -1.9$			X[*4]			
7	$P(\beta, 90°) = 1.9$			X[*4]			
8	$\partial P/\partial \beta\ (0°, \theta) = 0$		X[*5]	X[*5]	X[*5]		
9	$\partial P/\partial \beta\ (90°, \theta) = 0$	X[*6]		X[*6]		X[*6]	
10	$\partial P/\partial \beta\ (90°, 0°) = 0$	X[*3]	X[*7]	X[*3]	X[*7]	X[*3]	

X – adopted constraint.

[*1] Required by symmetry for any cross-section.

[*2] Required by symmetry for a cross-section with a vertical plane ($\boldsymbol{xz}$) of symmetry.

[*3] Redundant constraint since it is a subset of another applied constraint.

[*4] Adopted by assuming that the cross-section grossly behaves as a flat plate at $\theta = \pm 90°$.

[*5] Adopted due to: 1) symmetry (for any cross-section), and 2) assumption of smoothness (differentiability class C^1) at the current boundary.

[*6] Same as [*5], but only valid for a cross-section with a vertical plane of symmetry.

[*7] Adopted by assuming that the independence principle is valid locally.

The two constraints X[*4] prevent the polynomial fit from attaining extremely high or low values at the θ boundaries, which are very far from any data point. In the domain of interest, the polynomial is not sensitive to moderate variations around the chosen value of 1.9 (flat plate drag coefficient for $Re > 10^4$ according to (Veritas, 2010)). These two constraints lead to higher linearity of C_z with respect to θ, in the θ-interval of interest, resembling the shape of C_z at $\beta = 0°$ of other comparable bridge cross-sections (such as the proposed Langenuen, Julsundet and new Sotra bridges) while still providing an accurate fit. The constraint X[*7] can be explained in more detail as follows:

A 2D approach, which assumes the independence principle, implies, for $\beta \in [0°, 90°]$, that:

- $C_y(\beta, \theta) \approx C_y\big(\beta = 0°, \theta_{yz}\big)\, {U_{yz}}^2/U^2$
- $C_{rx}(\beta, \theta) \approx C_{rx}\big(\beta = 0°, \theta_{yz}\big)\, {U_{yz}}^2/U^2$

Where θ_{yz} and U_{yz} are expressed in eqs. (205) and (210). Then, in the subdomain where $\beta = 90°$:

- $\partial\left({U_{yz}}^2/U^2\right)/\partial\beta = 0$

And, at the point $\beta = 90° \wedge \theta = 0°$:

- $\partial\theta_{yz}/\partial\beta = 0$

This means that the polynomial fits of C_y and C_{rx} also comply with the constraint $\partial P/\partial\beta\ (90°, 0°) = 0$. This assumption aims to mitigate the data insufficiency at $\beta \approx 90°$ when other arguments (e.g. smoothness assumption) are not applicable. Note that $\partial\theta_{yz}/\partial\beta$ does not exist at $\beta = 90° \wedge \theta \neq 0°$.

Additionally, inequality constraints (e.g. $P(\beta, \theta) > 0$) could also be employed. Equality and inequality constraints can then be combined and fed into minimization algorithms to minimize the residual sum of squares already described. The Byrd and Omojokun's trust region algorithm was adopted using *SciPy v1.6.1* (Virtanen et al., 2020), a toolbox available for *Python*. The software implementation of this algorithm is described in (Lalee et al., 1998)). Whenever the available tools are insufficient to automatically convert an inequality constraint on the polynomial into a system of inequalities of the polynomial coefficients (which is often the required format), the work by (Wahl and Espinasse, 2014) provides a useful procedure for some common constraints on multivariate polynomials.

The constrained polynomial fits are finally presented in Fig. 33. Constrained bivariate polynomials also provide good fits of the measurements for the four main coefficients C_x, C_y, C_z and C_{rx}. As expected, they provide continuous and smooth estimations, and they constrain the results to reasonable values while preserving high R^2 values.

Particular attention is given to C_z and $\partial C_z/\partial\theta$ at high values of β, where no data is available to the authors' knowledge, and to the adopted constraints No. 6 and No. 7 (X^{*4}). A Cosine rule considers that $\partial C_z/\partial\theta = 0$ at $\beta = 90°$, which is a non-conservative assumption as any changes in $\tilde{\theta}$ should lead to changes in the instantaneous vertical forces. This naturally affects the vertical response of the case studied at high yaw angles and is also deemed important for other bridges where the wind speed at high angles and the vertical turbulence are significant.

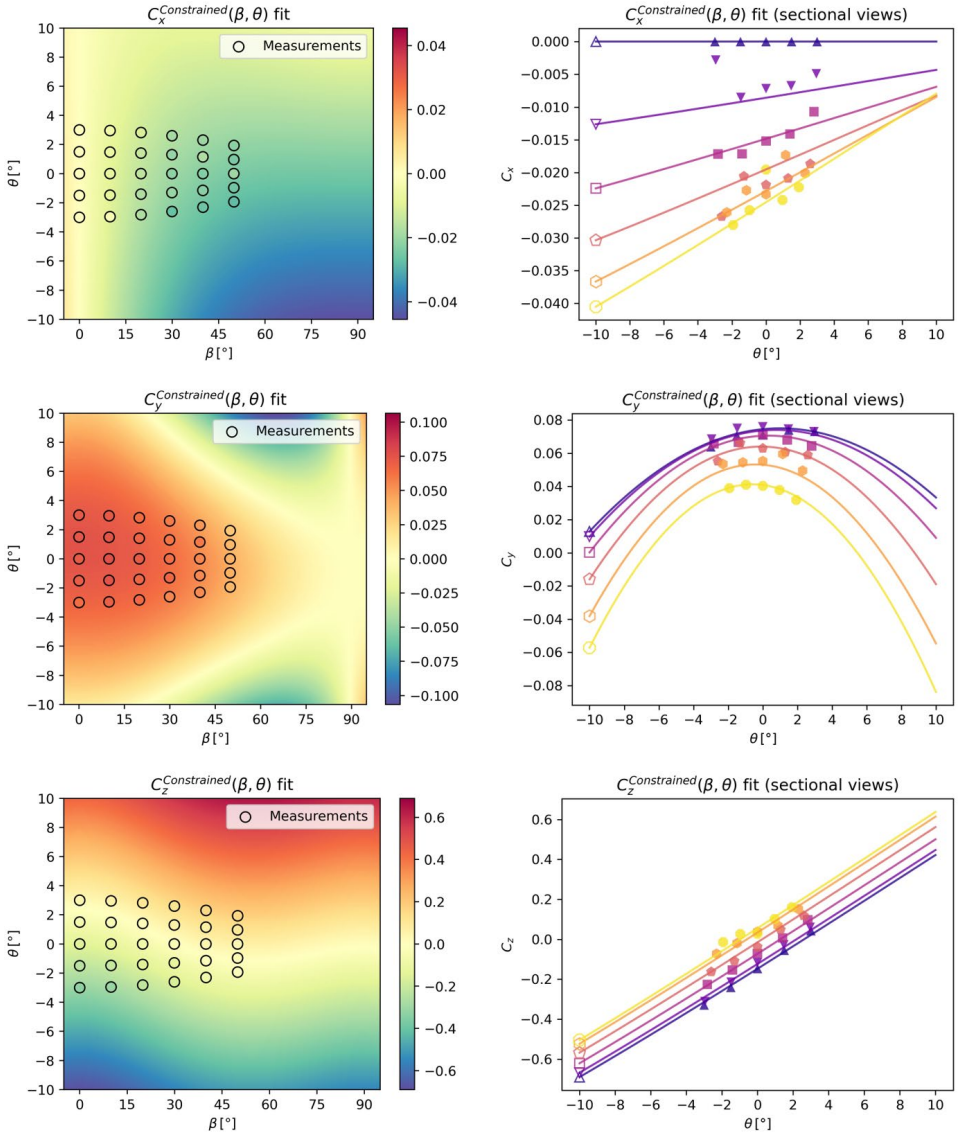

Fig. 33 – Constrained bivariate polynomial fits of the aerodynamic coefficients.

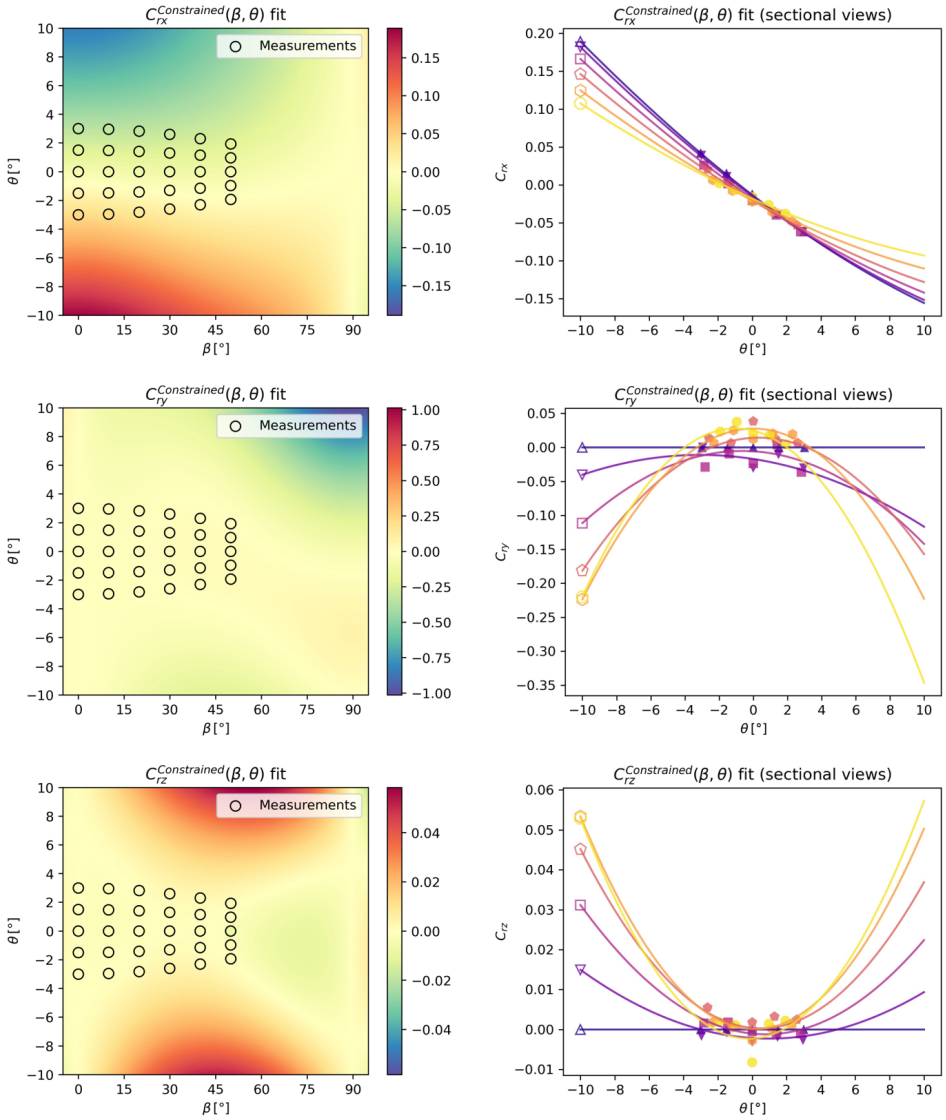

R^2 values of the n^{th} degree constrained polynomial fit						
Degree	C_x	C_y	C_z	C_{rx}	C_{ry}	C_{rz}
1	-2.55	-24.20	0.274	-0.331	-0.027	-0.003
2	0.888	-24.20	0.274	-0.331	0.168	0.021
3	**0.945***	0.758	0.766	0.939	0.479	0.073
4	0.960	**0.961***	**0.983***	**0.996***	**0.724***	**0.453***
5	0.975	0.967	0.983	0.996	0.727	0.536
6	0.979	0.968	0.982	0.996	0.802	0.665

*Polynomial degree adopted

Fig. 33 (cont.) – Constrained bivariate polynomial fits of the aerodynamic coefficients.

5.5.5. Additional comparisons

Some of the constraints and smoothness assumptions discussed can be better visualized in Fig. 34, where θ is fixed at $\theta = 0°$. The free polynomials are intentionally left out of the visible window for C_{ry} and C_{rz} where they attain disproportionally large values. Also, at $\theta = 0°$, there are no differences between the 2D approach and the Cosine rule, so only the former is presented.

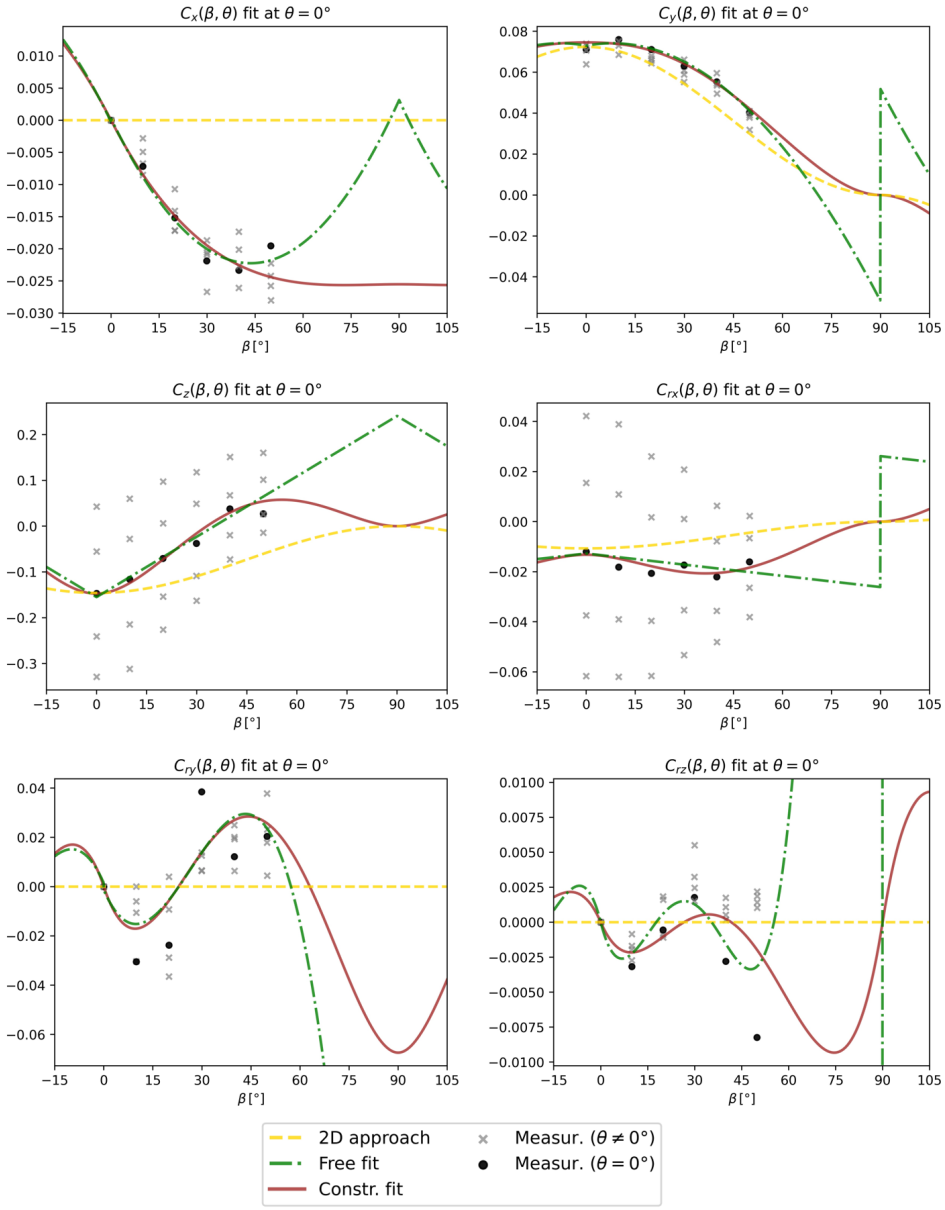

Fig. 34 – Sectional view, at a fixed $\theta = 0°$, of the different fits of $C(\beta, \theta)$.

The yaw angle of the resultant mean wind force $\beta_{\vec{F}}$ is plotted in Fig. 35 as a function of the mean wind yaw angle β, at a fixed inclination angle $\theta = 0°$, estimated from the different fits based on the measurements. This indicates whether the mean wind force is aligned with the mean wind $\boldsymbol{X_u Z_w}$ plane or not. The assumption of such a yaw alignment $\beta_{\vec{F}} = \beta$ (which could eventually be used in e.g. 2D CFD simulations that are performed on oblique cross-sections coplanar with the wind $\boldsymbol{X_u Z_w}$ plane) is not recommended, since $\beta_{\vec{F}} \neq \beta$ for most yaw angles β.

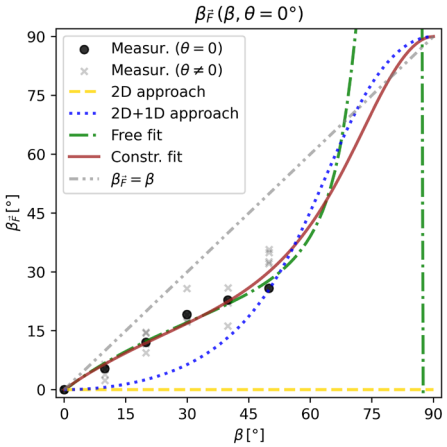

Fig. 35 – Yaw angle of the mean resultant wind force $\beta_{\vec{F}}$ for different mean wind yaw angles β, at $\theta = 0°$.

5.6. Buffeting response analysis

5.6.1. Methodology and validation

In the following sections, the established finite element model of the floating bridge presented in Section 4.2 is subjected to different skew wind buffeting load models using the wind properties defined in Section 4.3. First, an illustrative example of the frequency-domain response analysis performed, using the previously introduced constrained polynomial fits and the 3D approach, is shown in Fig. 36. The Complete Quadratic Combination (CQC) method was used. In this example, the mean wind cardinal direction $\beta_{Cardinal} = 280°$ is adopted, which corresponds to having $\beta = 180°$ at the middle of the bridge, as illustrated. A linearized 3D buffeting analysis then provides the auto-spectral densities of the nodal displacement response, shown for $\boldsymbol{y}$, $\boldsymbol{z}$ and $\boldsymbol{rx}$, at different positions along the bridge girder. The integrated response follows, also presented along the bridge

girder. Then, by noting the maximum response values along the bridge, and iterating this process for all possible mean wind directions, a final polar plot of the maximum standard deviation σ_{Δ_i} of the relevant response components can be presented, providing an overview of the bridge behaviour for all mean wind directions.

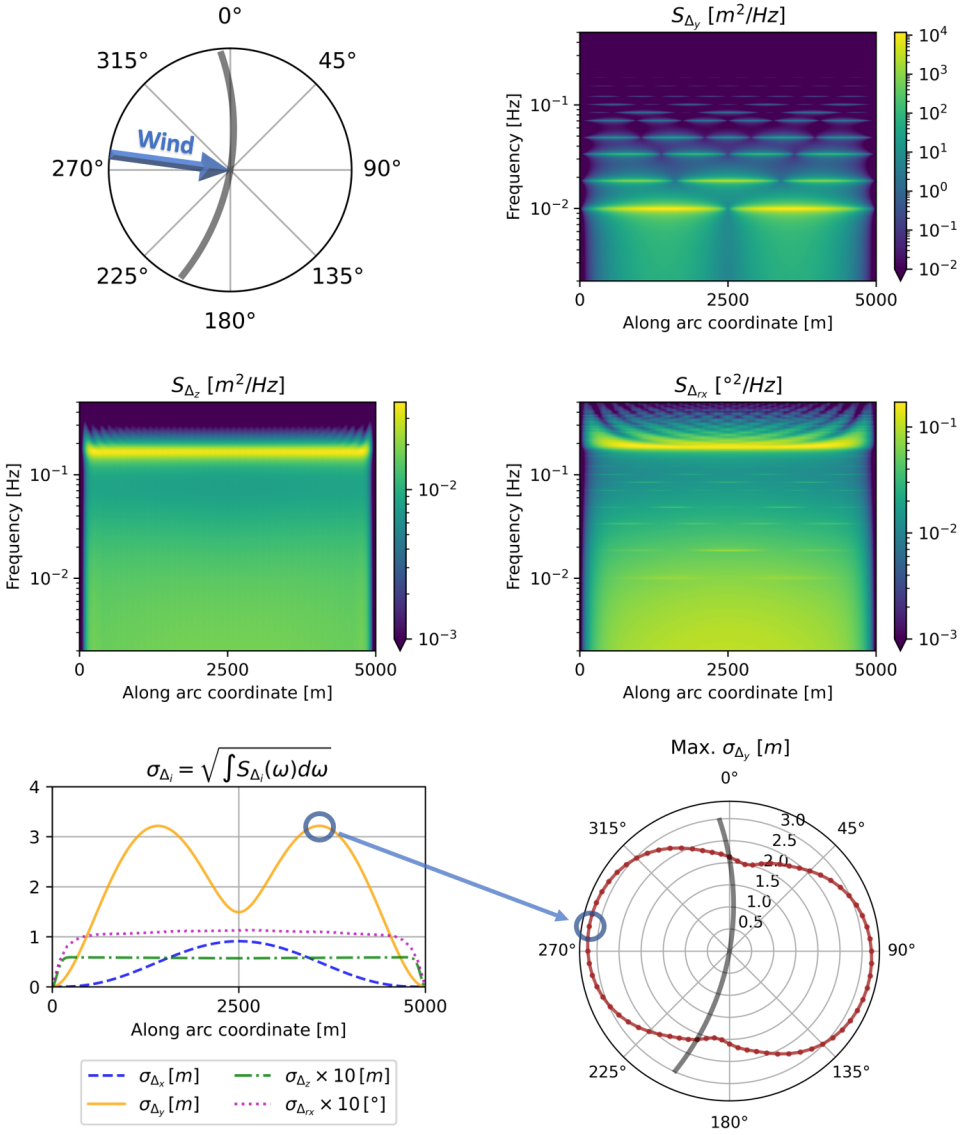

Fig. 36 – 3D buffeting response analysis example, in the frequency-domain, using constrained polynomial fits, for a mean wind cardinal direction $\beta_{Cardinal} = 280°$. Auto-spectral densities of the nodal displacement responses for $\boldsymbol{y}$, $\boldsymbol{z}$, and $\boldsymbol{rx}$. Standard deviation of the response along the bridge girder for $\boldsymbol{x}$, $\boldsymbol{y}$, $\boldsymbol{z}$, and $\boldsymbol{rx}$. Maximum standard deviation of the response in $\boldsymbol{y}$, for each global mean wind direction.

Time-domain simulations of the wind field and the structural response are also implemented as a tool to validate the results of the frequency-domain simulations. In both the time- and frequency-domain analyses being compared in this section, the frequency-dependent added mass and damping were set at fixed frequency values corresponding to the dominant eigenfrequencies of each DOF, for simplicity and to improve computational efficiency, with reasonable accuracy. These frequency dependencies are fully accounted for in the following sections 5.6.2 to 5.6.5, where only computationally efficient frequency-domain analyses are performed. A representative example of one 3-hour long simulation is illustrated in Fig. 37, for the same mean wind direction $\beta_{Cardinal} = 280°$.

A time step of 0.25 seconds was used. The time windows plotted (left side) are centred at the maximum obtained Δ_i values during the simulation and show a time range proportional to the relevant eigenmodes depicted. The respective spectral analyses (right side) of the time-domain response reflect the entire 3-hour simulation, which starts after an initial 20-minute transient period, with colour ranges matching those from the frequency domain for a direct comparison. There is an apparent similarity between the spectral response in the frequency domain and the spectral analysis of the time-domain response in the example given, supporting their validity.

Then, ten different time-domain simulations are performed for each global mean wind direction. The mean values and standard deviations (by using error bars) of all ten simulations' maximum responses are noted and plotted in Fig. 38 for each direction, where a comparison is made with the frequency-domain results. Additionally, the assumption of linearized coefficients, i.e., $\tilde{C}(\tilde{\beta}, \tilde{\theta}) \approx C(\beta, \theta) + C'^{\beta}(\beta, \theta)\Delta\beta + C'^{\theta}(\beta, \theta)\Delta\theta$, is also assessed in the time domain where instantaneous $\tilde{\beta}$ and $\tilde{\theta}$ are easily obtained at each time step. The two different types of analyses and the linear and non-linear coefficient formulations provide reasonably similar results.

A series of sensitivity studies were also conducted in the time domain to ensure convergence of the present time-domain response results. Besides the parameters described in Section 4.2.5, the time step, the simulation duration and the transient period duration were also assessed here for their sensitivity and convergence.

The effects of the admittance functions are conservatively disregarded in this study. These effects could be relevant for the higher vertical and torsional modes, whereas, for the first horizontal mode, the wavelength of the relevant turbulence components (U/f) is roughly 100 times the cross-section width, and thus, the effect should be

negligible. The wind has a major role in the horizontal response of this case study, but the vertical and torsional responses are dominated by wave loads, which are not considered in this study.

Sections 5.6.2 to 5.6.5 present the various findings of the skew wind buffeting analyses performed.

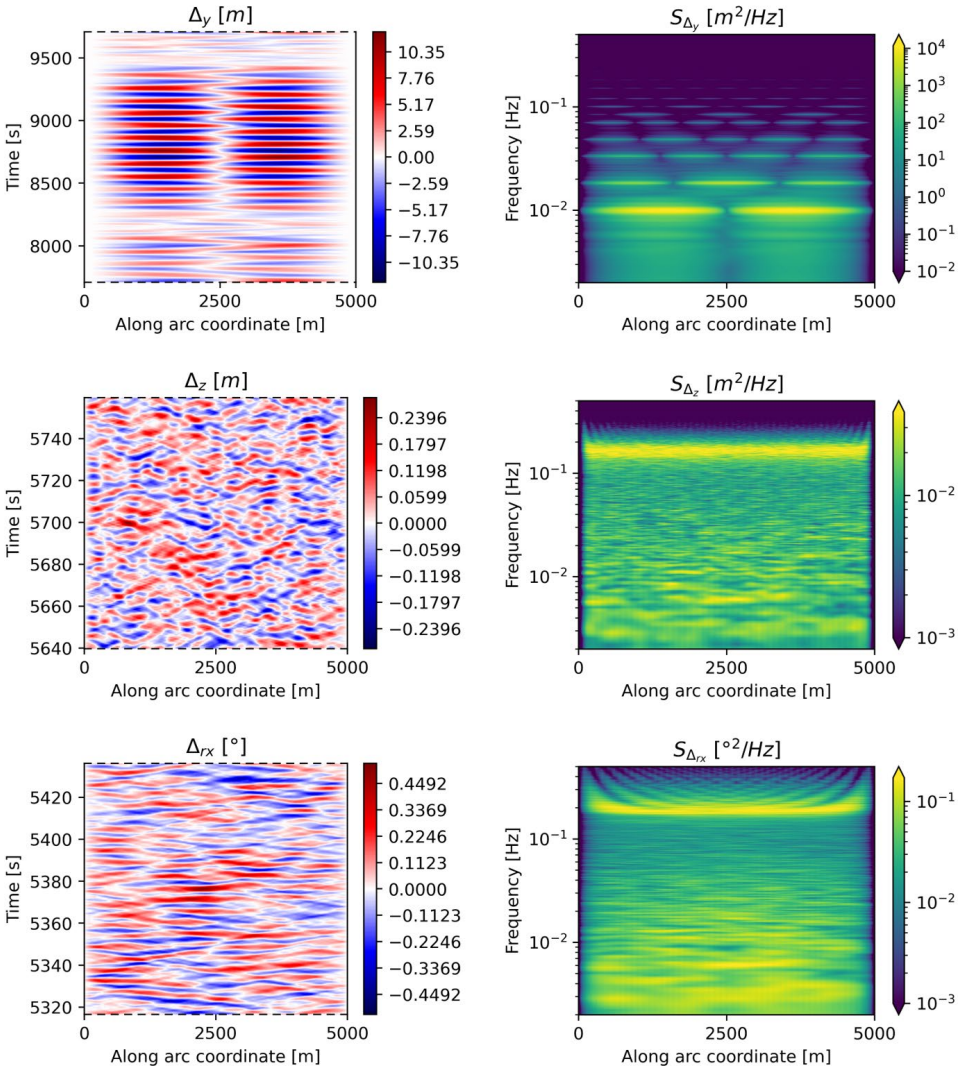

Fig. 37 – Example of a 3-hour time-domain simulation and respective spectral analysis of the response, for $\beta_{Cardinal} = 280°$. The time windows (left) are centred at the maximum obtained values, with a time range proportional to the relevant eigenmodes depicted. For a direct comparison, the colour range of the spectra (right) is the same as in Fig. 36.

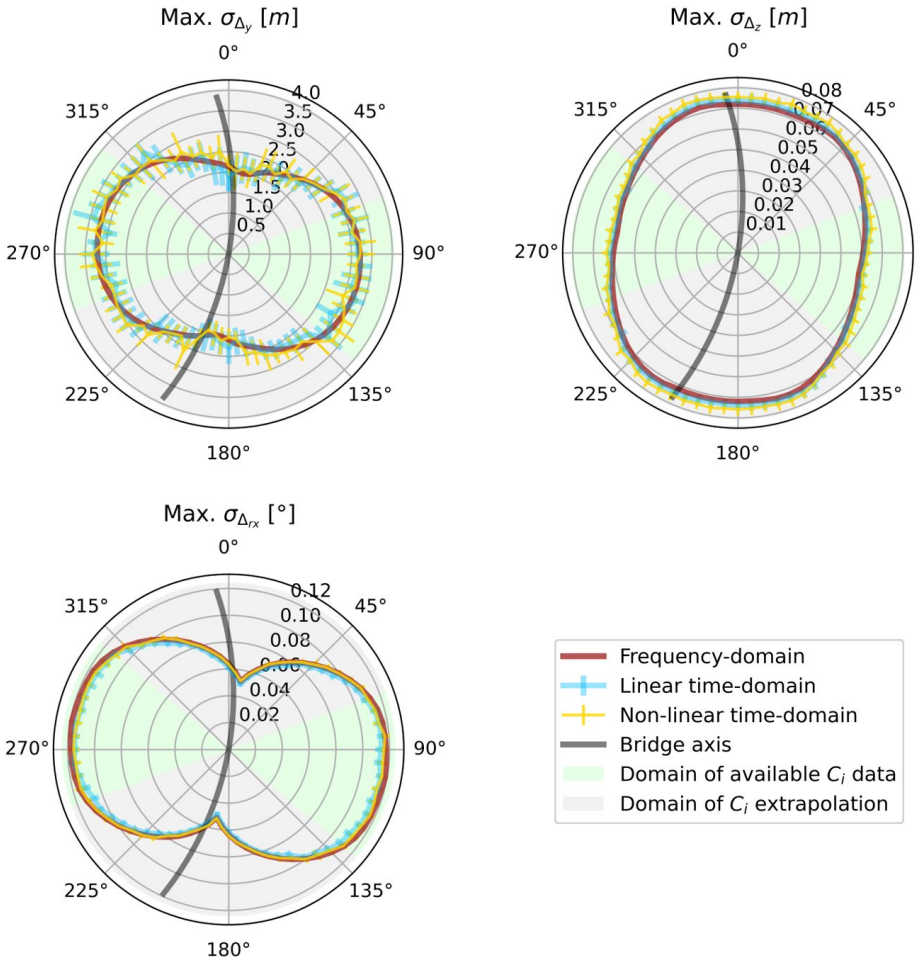

Fig. 38 – Comparison between 3D frequency-domain and time-domain analyses (mean of 10 simulations, for each direction, whose standard deviation is indicated by the error bars). "Non-linear" refers to the general formulation, with aerodynamic coefficients as functions of instantaneous $\tilde{\beta}$ and $\tilde{\theta}$, instead of using a Taylor approximation.

5.6.2. Comparing skew wind buffeting formulations

The 2D, 2D + 1D, and 3D buffeting formulations are compared in Fig. 39 in terms of maximum response obtained. The same constrained polynomial fits are used in all three cases in order to keep the focus on the different buffeting formulations. Note that only the 3D approach can use the data at $\beta \neq 0°$, except for the 2D + 1D formulation which simply imports the estimated value of C_x at $\beta = 90° \wedge \theta = 0°$ and additionally considers the wind projection onto the $\boldsymbol{x}$ axis. The maximum $\boldsymbol{x}$

axis response is omitted in the following plots as it closely resembles the shape of the maximum $\boldsymbol{y}$ axis response, only with smaller amplitudes.

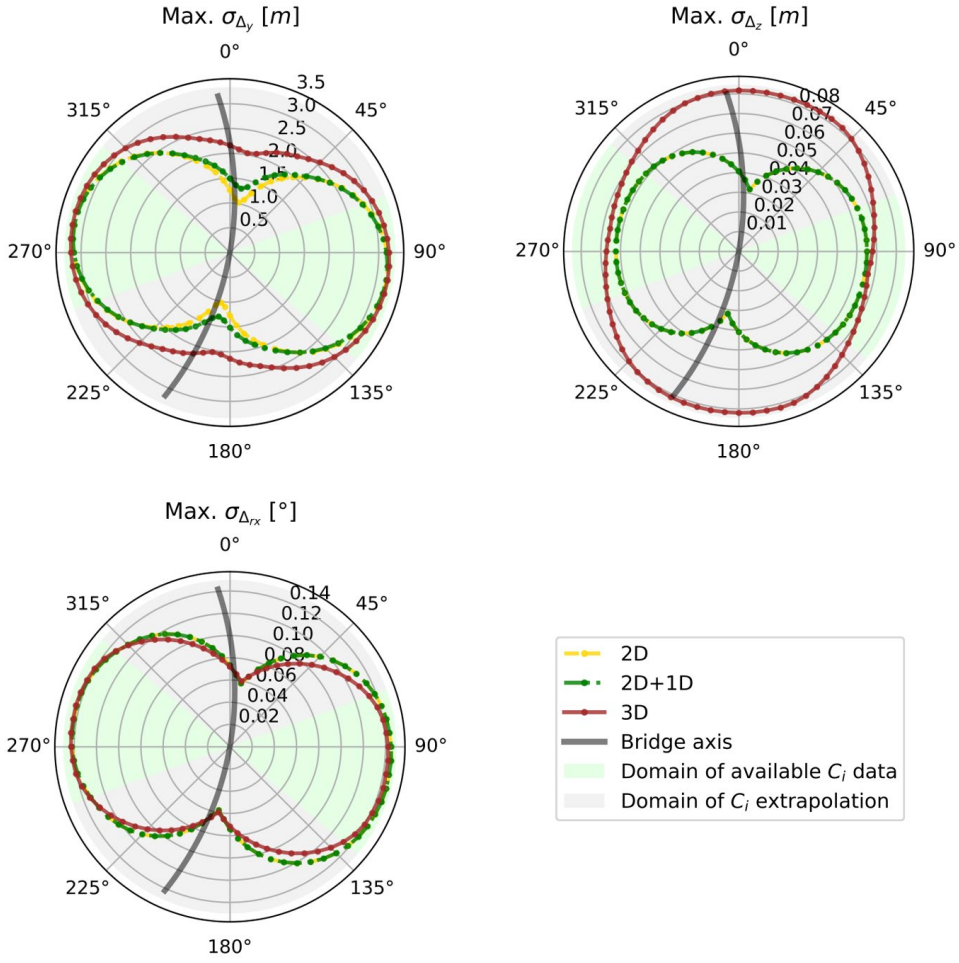

Fig. 39 – Maximum bridge responses, for each mean wind direction, for different theoretical models of the skew wind buffeting. The same constrained polynomial fits of the aerodynamic coefficients are used.

Despite the inherent uncertainty of the C_i coefficients at large yaw angles, it is clear that there are important differences between the response estimates of the different buffeting load formulations. The vertical response, in particular, can be strikingly different. In the 3D approach, the maximum vertical response is estimated to occur at high yaw angles, and a large vertical response is observed on a wide range of yaw angles. These results require validation through more extensive wind tunnel tests, but it seems plausible that small changes in $\tilde{\theta}$ can lead to changes in the vertical forces with similar (or perhaps larger) importance for large β as for small

β. In other words, it seems plausible that $C_z'^{\theta}(0°, 0°) \approx C_z'^{\theta}(90°, 0°)$ despite that the latter one often goes unnoticed in literature and design practices. Also, it might be interesting to investigate the vertical response at large yaw angles in bridges with a significant vertical curvature of the deck, which would be overlooked using a Cosine rule approach. In Fig. 39, it can also be seen that adding the axial dimension (+ 1D) to the 2D approach affects the horizontal response at large yaw angles.

5.6.3. Comparing aerodynamic coefficient fitting methods

The maximum bridge response for the different fitting methods previously introduced is shown in Fig. 40. The 3D approach formulation is used in all four cases to determine how the choice of a fitting method affects the response.

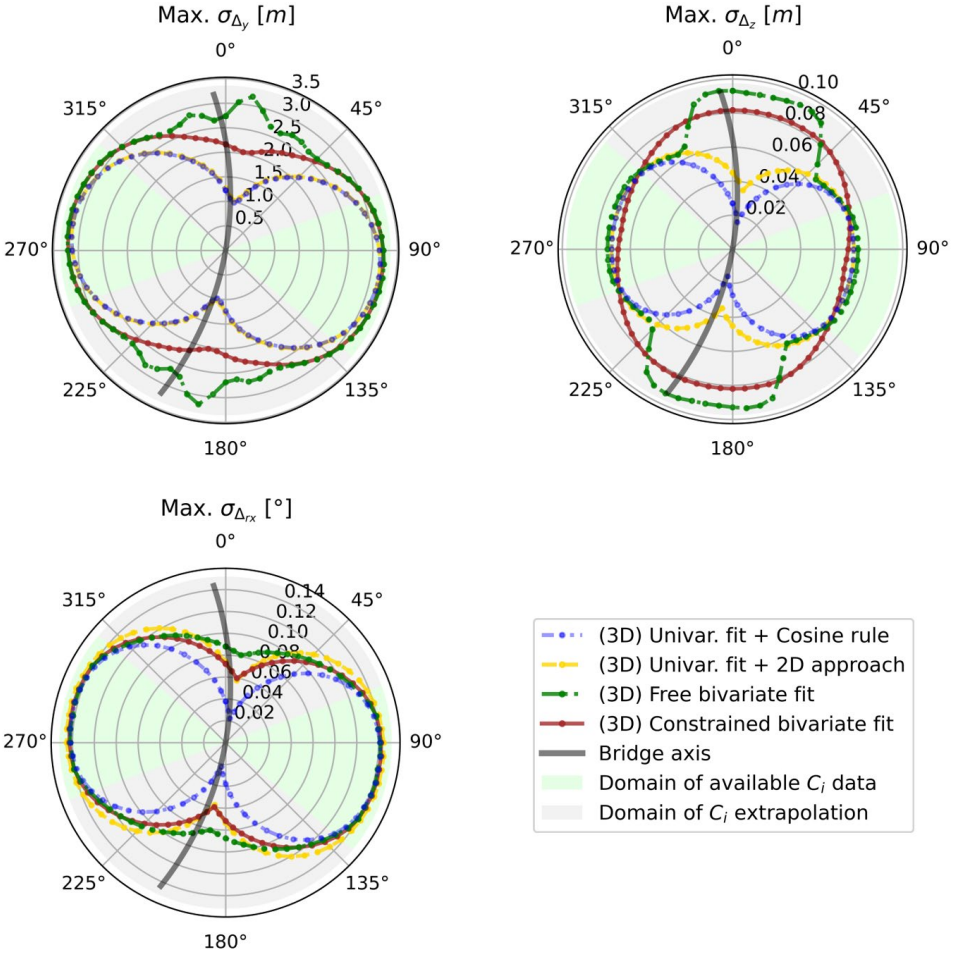

Fig. 40 – Maximum bridge responses, for each mean wind direction, for different aerodynamic coefficient fitting methods. The 3D buffeting load formulation is used.

The main differences between the fitted coefficients of the "Univariate fit + Cosine rule" and the "Univariate fit + 2D approach" are found at large yaw angles β and at $\theta \neq 0°$, which thus affects the coefficients' partial θ derivatives at $\theta = 0°$. The impact of such differences in the horizontal response is only up to 3%, but they can be larger than 100% for the vertical and torsional responses. This is the first attempt in the literature to suggest that the Cosine rule should be replaced by the 2D approach when experimental data is only available at $\beta = 0°$ since the 2D approach is seemingly more conservative and closer to the 3D bivariate estimates that utilize the data at $\beta \neq 0°$. For a straight and non-horizontal bridge girder, larger differences could be obtained. As for the preferred bivariate approaches, significant deviations are also obtained as expected, directly related to the fitting differences already discussed in Section 5.5. For the reasons already explained there, the constrained fit is believed to give the most reliable results. The important differences between the univariate and the bivariate polynomial fitting models are closely related to the 2D and 3D differences shown in Fig. 39. But note that introducing new data points to a polynomial fit can change the entire fit. This effect was suppressed in Fig. 39, where all approaches purposedly used the same constrained polynomial fits for comparison, but it is naturally included in Fig. 40 (each univariate fit considered only the 5 data points at $\beta = 0°$, whereas each bivariate fit considered all 30 data points).

5.6.4. Comparing different coefficient contributions to the response

The next step in the analysis is to assess the isolated effects of including the axial coefficient C_x as well as the two last rotational coefficients C_{ry} and C_{rz}, by using the 3D approach and the constrained polynomial fits for all three cases. The results are shown in Fig. 41. As expected, the axial coefficient C_x contributes to the horizontal response at large yaw angles, which is also a result of having a curved bridge. On the other hand, the effects of including the C_{ry} and C_{rz} coefficients seem relatively small despite the uncertainty from the poor fits obtained. The minor effects of C_{ry}, which mostly affect the vertical response, can be detected in the vertical response plot at large yaw angles. The C_{rz}, which should mostly affect the horizontal response, has practically unnoticeable effects there.

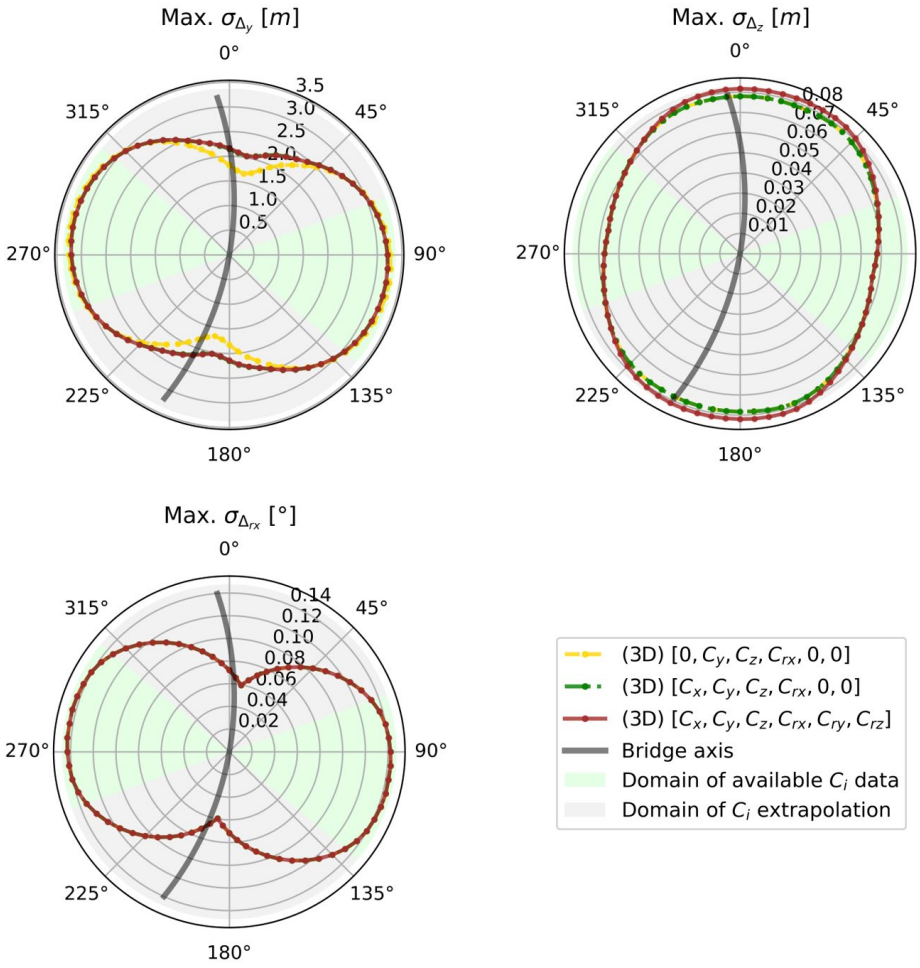

Fig. 41 – Maximum bridge responses, for each mean wind direction, considering (or not) C_x, C_{ry} and C_{rz}. The 3D buffeting load formulation is used together with constrained polynomial fits.

5.6.5. Comparing quasi-steady motion-dependent force formulations

This section investigates the effects of including the quasi-steady (QS) self-excited forces. Since the unsteady flutter derivatives under skew winds were not available for the case studied, the quasi-steady theory was assumed to be a sufficient approximation, given the low eigenfrequencies and high mean wind speeds. This approximation should be investigated in a future study.

Three different QS formulations of the self-excited forces are compared in Fig. 42. "(QS) Zhu" is the formulation introduced in (Zhu, 2002). "(QS) Costa et al. (6 DOF)" is the formulation later proposed in (Costa et al., 2022a) (presented in Chapter 3) which considers all six degrees of freedom, further improved the aerodynamic stiffness terms and made a minor correction to the P_5^* term. The alternative "(QS) Costa et al. (3 DOF)" formulation is the same as the "(QS) Costa et al. (6 DOF)" formulation when only the three main DOF, namely $\boldsymbol{y}$, $\boldsymbol{z}$ and $\boldsymbol{rx}$, are considered, as in (Scanlan and Tomko, 1971).

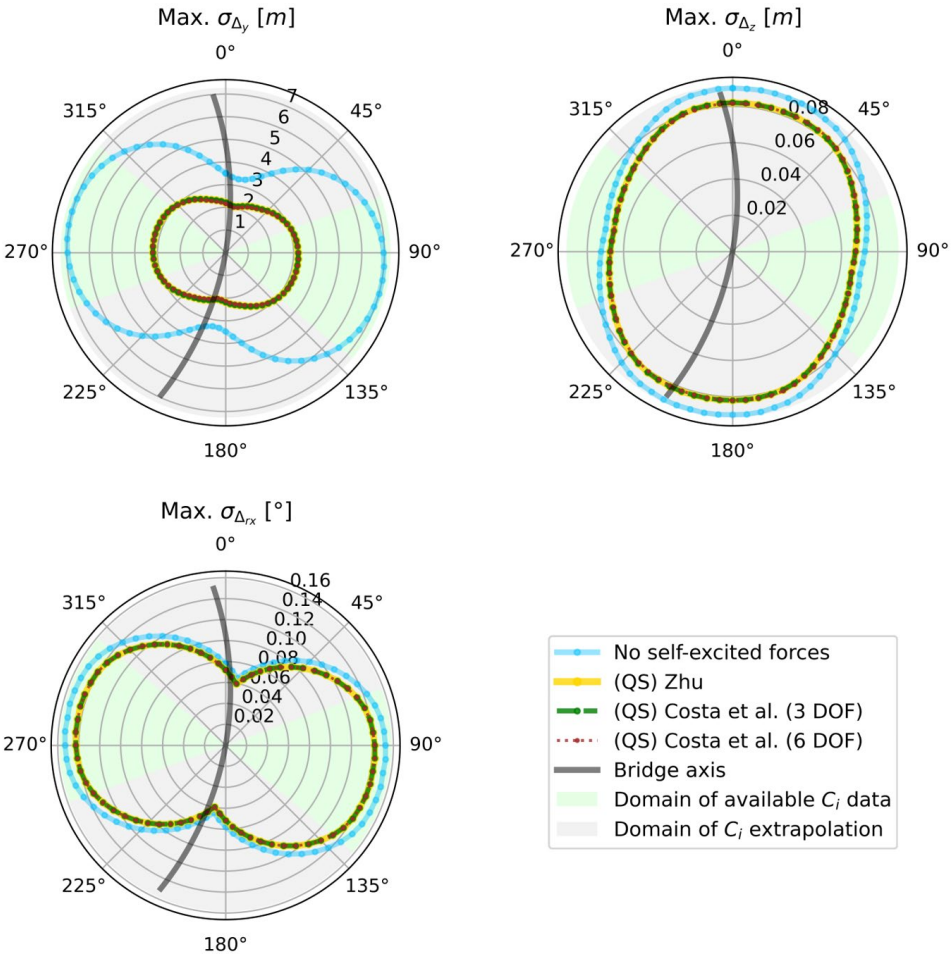

Fig. 42 – Maximum bridge responses, for each mean wind direction, considering (or not) different formulations of the quasi-steady (QS) self-excited forces.

It is noted that neglecting the quasi-steady self-excited forces changes the response substantially, particularly the horizontal response, which would be increased between 60% and 120%. These motion-dependent forces are an important source

of damping for the first eigenmodes where the hydrodynamic potential damping is very low. The vertical and torsional responses also see a significant increase, between 7% and 10%. For this case study, the three different formulations of the quasi-steady self-excited forces provide similar results. The "(QS) Zhu" and "(QS) Costa et al. (3 DOF)" formulations provide virtually the same results (less than 0.1% differences). The recommended "(QS) Costa et al. (6 DOF)" formulation is also similar, with differences up to 2.5% for the horizontal response, up to 1% for the vertical response and smaller than 0.1% for the torsional response.

5.7. Summary

One proposed floating bridge solution to cross the Bjørnafjord in Norway was modelled through a simplified finite element model. It is important to carefully investigate this bridge buffeting response for all possible mean wind directions due to its curvature, long eigenperiods, relatively open surroundings and also for fatigue considerations.

Wind tunnel test results of a section model of the bridge girder were analysed for different combinations of the mean wind yaw angle β and inclination angle θ. Some of the challenges faced in the wind tunnel testing and data interpretation are discussed. Static aerodynamic coefficients were obtained for all six DOF. Despite the domain of yaw angles tested (up to $50°$) being larger than what is available in the current literature, it was still necessary to significantly extrapolate the results for a complete $360°$ assessment of the skew wind buffeting response. Thus, different extrapolation approaches are presented, using univariate and bivariate polynomial fits of the coefficients. Several possible constraints are investigated and applied to the bivariate polynomials, imposing key physical principles at the boundaries. The suggested constrained polynomials fit reasonably well the measured coefficients in the four main DOF, they provide sensible estimates in the challenging regions of β and θ that are far from the available data, and also, together with the appropriate symmetry transformations, they ensure smooth functions in the entire β and θ domain, as required by a linear approach.

Previously established theoretical models for the skew wind buffeting are grouped into so-called 2D, 2D + 1D and 3D approaches, depending on whether they only consider the wind components in the plane that is normal to the bridge girder (2D), additionally consider an independent axial component (+1D) or fully account for the three-dimensionality of the wind flow (3D). The present article provides the first comparison of these three methodologies. The three-dimensional wind field

and the structural response were investigated in both frequency- and time-domain to increase confidence in the results.

The theoretical buffeting models and fitting methods that only consider the aerodynamic data at $\beta = 0°$ underestimated the response of the case studied at large yaw angles, relative to the models and methods that consider all the data. The large differences in the vertical response are particularly interesting, indicating a need for more comprehensive wind tunnel tests that can estimate $C_z'^{\theta}$ at large yaw angles. The traditional "Cosine rule" approximation of the 2D approach is believed to be particularly non-conservative at large yaw angles. Therefore, this work further consolidates the support for a 3D approach.

The bivariate aerodynamic coefficients are thought to be most conveniently represented in the local structural coordinate system. For the case study, the axial coefficient C_x was of some importance at large yaw angles and should be included in the analyses. On the other hand, the rotational C_{ry} and C_{rz} coefficients were found to have a small impact on the response, with C_{rz} being particularly negligible.

Finally, three different quasi-steady formulations of the motion-dependent aerodynamic forces were compared, namely the original formulation by Le-Dong Zhu and the main and alternative formulations proposed in a preceding article (Costa et al., 2022a) and presented in Chapter 3. These self-excited forces have a large impact on the bridge response. However, the differences between the three different quasi-steady formulations are smaller than 2.5% for this particular case study.

6. Long-term response to inhomogeneous skew winds

6.1. Preface

This chapter is reproduced from a manuscript submitted for journal publication (Costa et al., 2022c). The formatting has been adapted to the thesis, and some background information has been removed to avoid repetition with previous chapters. The remaining content of the manuscript remains essentially unchanged. The preliminary reference of the paper is:

Costa, B.M., Wang, J., Jakobsen, J.B., Snæbjörnsson, J.Þ., Øiseth, O.A., 2022c. Long-term response of a floating bridge to inhomogeneous wind fields. Manuscript submitted for publication.

6.2. Abstract

A numerical model of a 5 km long curved floating bridge, planned for the Bjørnafjord, in Norway, is subjected to strong wind events with stationary mean properties that vary along the bridge axis. A Weather Research and Forecasting model (WRF) is used to estimate the mean wind speeds and directions in the fjord, with a 500-meter resolution, during a 20-year period. The wind turbulence intensities are estimated as functions of the position along the bridge and the wind direction, using an artificial neural network trained on nearby sonic anemometer data and formulations given in the national annex of the Eurocode. A skew wind buffeting formulation is used to estimate the linear static response and the linear quasi-steady buffeting response in the frequency domain. The response under inhomogeneous winds is compared with the response under equivalent homogeneous winds. The inhomogeneous wind response is, on average, 1.5% to

47% larger, depending on the type of analysis and response component, but a high variability is observed, with much larger differences for some wind cases. These findings motivate case-specific investigations of inhomogeneous wind effects to improve fatigue and extreme response predictions of long wind-sensitive structures.

6.3. Introduction

Advancing the knowledge of wind loads and effects should allow for more innovative, reliable, durable and cost-effective structures. This investigation concerns the record-breaking floating bridge presented in Chapter 4. More specifically, it aims to study the effects of the wind field inhomogeneity, which are usually not fully accounted for in traditional bridge engineering (e.g. (Davenport, 1961a; Strømmen, 2010)). The homogeneity (or uniformity) assumption states that the wind properties (e.g. mean wind speed, direction, turbulence intensity, coherence and spectral content) are constant along the entire bridge length. Inhomogeneous wind, also denoted non-homogeneous or non-uniform wind, hereby refers to wind with stationary time-averaged properties that vary in space, particularly in the horizontal direction along the bridge axis. The extreme length of this floating bridge and the heterogeneity of the topography make this an appropriate case study to further investigate the implications of the wind homogeneity assumption. An example of inhomogeneous mean wind speed vectors varying along the bridge in magnitude and direction is illustrated in Fig. 43.

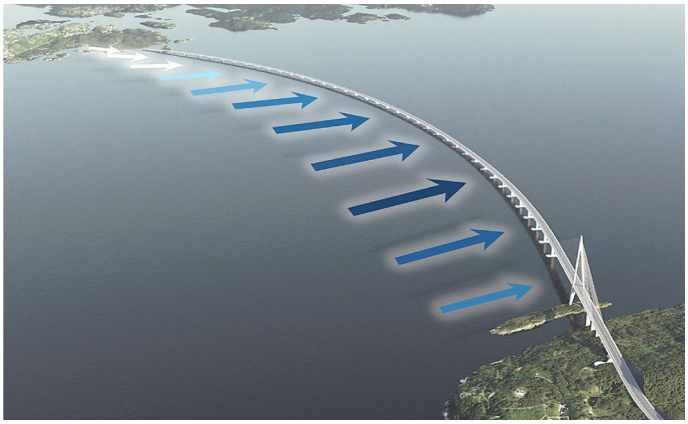

Fig. 43 – Planned floating bridge for the Bjørnafjord, with a sketched example of mean wind speed vectors that vary along the bridge in magnitude and direction (i.e., inhomogeneous wind).

Previous work provides valuable insight into inhomogeneous wind effects on straight cable-stayed and suspension bridges with up to 1.5 km long spans. Terrain models in wind tunnels and full-scale measurements are commonly used to describe inhomogeneous wind fields. The literature findings vary largely with the chosen assumptions, the extent of the inhomogeneities, the equivalent homogeneous wind cases being compared, and the properties of the structure being studied. Some of these findings are summarized and briefly discussed below.

In (Zhang, 2007), non-uniform horizontal wind profiles perpendicular to the bridge girder were applied to a numerical model of the Runyang Bridge, resulting in slightly larger horizontal, similar vertical, and slightly smaller torsional aerostatic responses than the uniform case. They also resulted in improved flutter stability. However, it should be noted that the non-uniform profiles tested had lower mean wind speeds than the uniform profile.

In (Arena et al., 2014), different Gaussian spatial distributions of the wind speed were assessed, with different shape and amplitude parameters such that all distributions were energy-equivalent. The non-uniform wind profiles led to up to 10% increased and down to 3% decreased flutter wind speeds. Regarding the inhomogeneous wind buffeting, a so-called one-cosine gust model was used, and for some of the non-uniform wind profiles, the torsional response was up to 55% higher, and the vertical response was up to 160% higher.

In (Cheynet et al., 2016), measurements from anemometers at different positions along the bridge girder were used as single-point inputs for the computed buffeting response of the Lysefjord Bridge. This led to large variations in the results, indicating the presence of important inhomogeneity in the wind action along the bridge. A later study of the Lysefjord (Cheynet et al., 2020) further assessed those inhomogeneities using complementary 3D Reynolds-averaged Navier–Stokes (RANS) computational fluid dynamics (CFD) simulations. Four different main wind directions were simulated, indicating, respectively, variations of mean wind speeds of 8, 30, 18 and 7%, variations of mean wind directions of 13, 12, 6 and 8°, and variations of mean attack-angles of 10, 2, 2 and 3° along the bridge girder.

In (Hu et al., 2017), adding a weakly inhomogeneous profile (spanwise) of mean wind speeds increased the response by 3%. The mean wind speeds varied between –2% and 9% and less than that for most of the span.

A study by (Forbord and Hjellvik, 2017) attempted to compare full-scale response measurements of the Hardanger bridge with equivalent numerical model responses under inhomogeneous and homogeneous wind cases. In both cases, the response

misestimations were too large to confidently conclude on the effects of modelling the inhomogeneities.

In (Lystad et al., 2018b), the wind inhomogeneities were also studied for the Hardanger bridge. Full-scale measurements along the girder showed spatial variations of up to 50% of the mean wind speed and up to 100% of the mean along-wind turbulence intensity. Nearby anemometric measurements show that, depending on wind direction, there is 5 to 14% higher mean turbulence intensity at the anemometer location (45 m above ground level, 165 m above sea level) compared with measurements at the centre of the bridge (60 m above sea level). The bridge is located in rather complex topography.

The response of the Hardanger Bridge to inhomogeneous winds was later studied in (Lystad et al., 2018a). Two functions with three terms each (one constant, one linear and one trigonometric) were fitted to each measured spanwise wind speed profile and spanwise wind turbulence profile. Then, the constant parameters were adjusted so that all functions had the same mean values. Joint probability density functions of the linear and trigonometric fitted parameters were estimated. Then, two pairs of profiles, one for wind from the East and one for wind from the West, with extreme linear and trigonometric parameter values, were used to estimate the associated buffeting response under extreme inhomogeneous wind conditions. This response was then compared with that under equivalent homogeneous wind conditions, and differences of up to 25% were observed.

A full long-term extreme analysis, analysing all available wind profiles, was left out for further work, which could potentially lead to different results. This is because wind profiles representing extreme inhomogeneity may not represent the extreme unfavourable distribution and combination of mean wind speeds and turbulence, which is important but unknown a priori. To overcome this, the present study estimates the response of the planned floating bridge for Bjørnafjord to all 670 1-hour-long strong wind events in the last 20 years, thus allowing for the first long-term extreme inhomogeneous wind buffeting analysis in literature.

A comprehensive study (Shen et al., 2021) used a 1:1000 reduced-scale model of a trumpet-shaped mountainous terrain in a wind tunnel. One-point wind statistics were obtained along the planned position of the bridge axis, namely the time-averaged wind speeds, attack angles, yaw angles, integral length scales and frequency-regulating parameters of the single-point spectrum. Shen et al. used the simplified “cosine rule” to model skew wind loads, suggesting for further work the implementation of a skew wind buffeting formulation.

The present study utilizes the yaw- and inclination-angle-dependent aerodynamic coefficients obtained under skew winds in a wind tunnel and presented in Chapter 5. It also uses the 3D formulation of the skew wind buffeting theory described in Chapter 3. In order to represent the effects of inhomogeneous winds, some notations, coordinate systems and angles are adapted for this study. These are briefly introduced and described in Section 6.4.1.

A mesoscale numerical weather research and forecasting (WRF) model is described and used for the first time in the context of inhomogeneous wind loads on ultra-long span bridges. The WRF model was used to estimate the mean wind speeds and mean wind directions along the 5 km long floating bridge. This model complements the full-scale measurements. It provides wind data for time periods and locations that are not easily accessible, such as past wind events that occurred in the middle of a fjord, with full data availability. It can readily provide simulations that reflect the true long-term wind statistics. This model is further described in Section 6.4.2. In order to estimate the wind turbulence intensities across the fjord, the procedure described in Appendix B is adopted, together with the implementation details provided in Section 6.4.3. Then, Section 6.4.4 proposes an estimation of equivalent homogeneous wind cases for a meaningful comparison of both inhomogeneous and homogeneous wind analyses. Section 6.4.5 describes the buffeting formulation used, adapted for inhomogeneous winds. The results, discussions and conclusions follow in sections 6.5 to 6.7, providing new insights into the importance of modelling the long-term inhomogeneities of the wind field.

6.4. Methods

6.4.1. The adopted coordinate systems and wind angles

In order to properly describe the buffeting loads on a moving structure, a set of coordinate systems must be established.

The global structural, Gs, local structural, Ls, and (homogeneous) global mean wind, Gw, coordinate systems introduced in Chapter 3 are also adopted here. The (homogeneous) global mean yaw and inclination angles β_G (updated here to β_{Gs}) and θ_G (updated here to θ_{Gs}) are also adopted, as well as the (homogeneous) local mean yaw and inclination angles, β (updated here to β_{Ls}) and θ (updated here to θ_{Ls}). The small updates in these notations help clarify the "global" and "local" terms, which can now be used in the context of the coordinate systems and the

context of inhomogeneity. In order to further expand the scope to inhomogeneous wind buffeting analyses, the following is also defined:

- Superscripts I and H. These are included, as needed, to distinguish between quantities that are estimated in inhomogeneous and homogeneous wind conditions, respectively. The former quantities are defined for each bridge element (or node), and the latter concern the entire bridge.
- Local inhomogeneous mean wind coordinate system, Lw, $(\boldsymbol{x_u}, \boldsymbol{y_v}, \boldsymbol{z_w})$. The axis $\boldsymbol{x_u}$ is aligned with the local mean wind direction and the local turbulence component u, and the axes $\boldsymbol{y_v}$ and $\boldsymbol{z_w}$ are aligned with the local turbulence components v and w, respectively. By definition, these local axes vary across the fjord.
- Local inhomogeneous yaw and inclination angles β^I and θ^I. These can be respective to either the Gs or the Ls system (as indicated by a subscript). They can also be represented in a cardinal system (0° for wind from the North, 90° from the East, 180° from the South and 270° from the West). To convert β_{Gs} to $\beta_{Cardinal}$, eq. (218) is valid for the present case study (where $\beta_{Gs} = 0°$ corresponds to $\beta_{Cardinal} = 100°$), and it could be easily adapted to other choices of the Gs system.

$$\beta_{Cardinal} = \begin{cases} 100° - \beta_{Gs} & if \ -180° < \beta_{Gs} \leq 100° \\ 100° - \beta_{Gs} + 360° & if \ 100° < \beta_{Gs} \leq 180° \end{cases} \tag{218}$$

The homogeneity-related coordinate systems and angles, previously introduced in Chapter 3, are illustrated again in Fig. 44, where the mean angles now include the superscript H and the subscripts Gs or Ls to indicate the coordinate system they refer to.

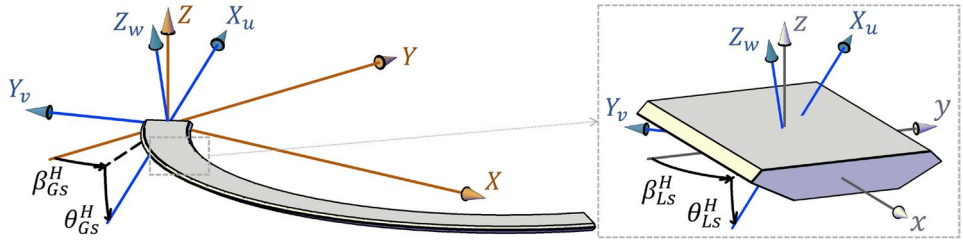

Fig. 44 – Homogeneous global mean wind, Gw, $(\boldsymbol{X_u}, \boldsymbol{Y_v}, \boldsymbol{Z_w})$, global structural, Gs, $(\boldsymbol{X}, \boldsymbol{Y}, \boldsymbol{Z})$ and local structural, Ls, $(\boldsymbol{x}, \boldsymbol{y}, \boldsymbol{z})$ coordinate systems. Homogeneous mean yaw and inclination angles, β^H_{Gs}, θ^H_{Gs} and β^H_{Ls}, θ^H_{Ls}, relative to Gs and Ls, respectively.

The inhomogeneity-related coordinate systems and angles are introduced in Fig. 45, where the superscript I is used. Two cross-sections are illustrated to exemplify the different local axes and angles.

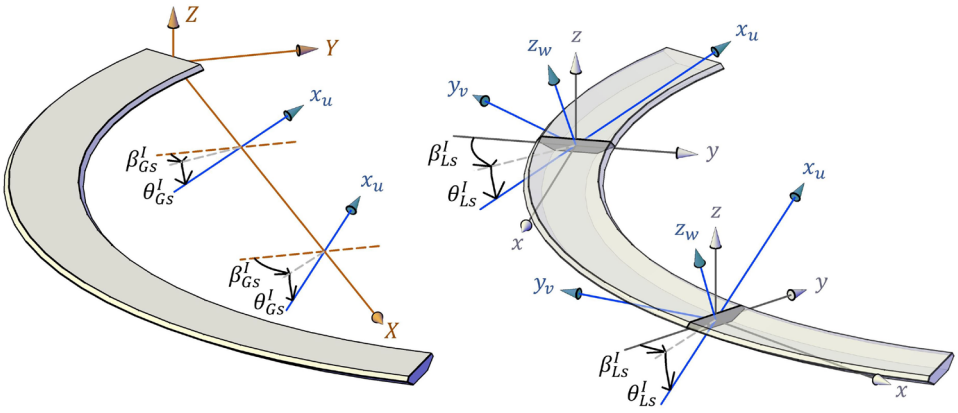

Fig. 45 – Inhomogeneous local mean wind, Lw, $(\boldsymbol{x_u}, \boldsymbol{y_v}, \boldsymbol{z_w})$ coordinate systems. Inhomogeneous mean yaw and inclination angles, β^I_{Gs}, θ^I_{Gs} and β^I_{Ls}, θ^I_{Ls}, relative to Gs and Ls, respectively.

6.4.2. Inhomogeneous mean wind speeds and directions

A Weather Research and Forecasting (WRF) model, version 3.2.1, was used by (Kjeller Vindteknikk AS, 2016) to estimate the mean wind properties in the Bjørnafjord region. The model, described in (Skamarock et al., 2008), is a state-of-the-art mesoscale numerical weather prediction system. It solves coupled equations for all important physical processes in the atmosphere (e.g. wind, temperature, stability, clouds, radiation), given the initial field values and lateral boundary data. The global ERA-Interim reanalysis data (e.g. (Dee et al., 2011)) is used at the boundaries. Details about the modelling structure, numerical routines and physical packages available can also be found in other publications (e.g. (Klemp et al., 2007; Michalakes et al., 2001)).

Meteorological data and geographical data are used as model inputs. The latter is provided by the *National Oceanic and Atmospheric Administration* (NOAA) and includes surface data, albedo, vegetation and topography. These parameters significantly affect the predicted wind speeds closer to the ground. National databases from the Norwegian (N50 series) and Swedish (GSD-General Map) mapping authorities are used to update the local surface type and roughness.

A WRF 500 m model was adopted with four different horizontal resolutions, namely 22.5 km, 4.5 km, 1.5 km and 500 m, with nested domains of decreasing size. The WRF 500 m model provided data from 2000 to 2020. One reference node from a previously established WRF 4 km model, providing data from 1979 to 2020, was also used to adjust the long-term predictions of the WRF 500 m model. A good agreement was found between the WRF data and the data from nearby mast measurements (Kjeller Vindteknikk AS, 2018). The grids of both WRF models utilized are illustrated in Fig. 46.

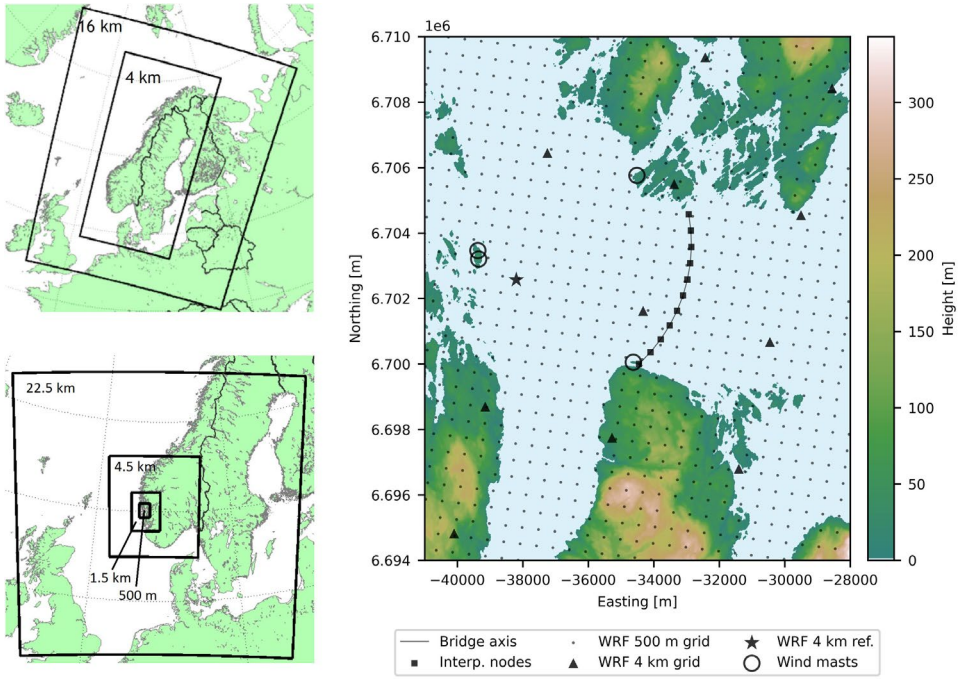

Fig. 46 – Top-left: WRF 4 km model setup (1979-2020). Bottom-left: WRF 500 m model setup (2000-2020). Right: Bjørnafjord map (EUREF89, UTM zone 33, EPSG: 25833); planned bridge axis with selected interpolation nodes; WRF 500 m grid nodes, used as input for the interpolation; WRF 4 km grid nodes, including one reference node for long-term corrections; nearby mast locations.

The double-moment microphysics scheme by (Thompson et al., 2004) was adopted to improve precipitation modelling in cold weather. Two different planetary boundary layer schemes were used to represent the turbulent fluxes of momentum, heat and moisture. In the WRF 4 km model, the *MYJ* (Janić, 2001) scheme is used, while in the WRF 500 m model, the YSU (Hong et al., 2006) scheme is used. Both models are equally discretized in the vertical direction into 32 layers, with the first four being located at 18, 58, 117 and 197 meters above ground level (AGL). Only the data from the layer at 18 meters AGL is used as input in the current study,

despite the centre of the bridge girder being modelled at 14.5 meters above mean sea level (the cross-section height is 3.5 meters). This is considered a reasonable practical approximation. The WRF model layers are located at fixed heights AGL, but the ground level naturally varies with the topography. Thus, the height of the WRF model layers, relative to a reference mean sea level, also varies with the topography.

The 20 years of data are filtered to analyse relevant strong wind events only. A threshold of 18 m/s was used. Only 1-hour wind events that had a measured mean wind speed of 18 m/s or higher, in at least one point along the bridge, were stored for further analysis. This means that significantly lower wind speeds can still be observed in the strong wind data due to the wind inhomogeneity. In total, 670 strong wind events were kept for analysis. In Section 6.4.3, the 11 selected interpolation nodes from Fig. 46, which are 500 meters apart, are used to represent the wind roses that concern only these strong wind events. These nodes are also used to estimate the wind turbulence intensities.

It is noted that testing a terrain model in a wind tunnel is a viable alternative or complement to the WRF model. This would then require a large wind tunnel facility to accommodate all the relevant topographic features of the wide Bjørnafjord region on a reasonable scale. That, and a comparison of both models, is suggested for future work.

6.4.3. Inhomogeneous turbulence intensities

The WRF models described in Section 6.4.2 do not provide direct information about wind turbulence. Vertical wind profiles could be estimated at different locations within the Bjørnafjord, using the mean wind speed data at different heights AGL. However, extracting accurate turbulence information from such profiles would be unfeasible due to the terrain heterogeneity (the wind profiles are often not fully developed) and due to an inadequate vertical resolution and scope of the WRF models.

The along wind turbulence intensity I_u is predicted at 11 equidistant points along the bridge girder using two combined approaches, namely the Eurocode (NS-EN 1991-1-4:2005+NA:2009) and the Artificial Neural Network (ANN) described in Appendix B. First, turbulence is predicted at 48 meters AGL, using the ANN, because only the wind measurements at 48 meters AGL, from six different wind masts, were used to train the ANN model. This avoids near-ground flow distortions from nearby objects such as tall trees and buildings. Then, Eurocode predictions

are made for those 11 equidistant points, at both 48 meters and 18 meters AGL, to establish a transfer function between the two different heights. This transfer function is then applied to the ANN predictions, rendering the final ANN predictions at the desired height of 18 meters AGL. This transfer function was the preferred method to extrapolate the wind turbulence predictions to new heights AGL. Contrary to using simple logarithmic or exponential wind profiles (e.g. eq. 4.7 of the NS-EN 1991-1-4:2005+NA:2009), this transfer function is able to consider the effects of variations in fetch and roughness of the upstream terrain. For a given node location and a given mean wind direction, the associated upstream terrain varies between terrain roughness category 0 (sea water) and III (forests in relatively small hills), with a greatly varying fetch. Further details on the implementation of Section NA.4.3.2 (2) (901.2.2) of the NS-EN 1991-1-4:2005+NA:2009 can be found in Appendix B. Weak wind events were removed from the training data of the ANN for it to train only on turbulence samples that are likely dominated by friction, instead of local thermal effects.

Wind roses representing the strong wind events described in Section 6.4.2, together with the ANN predictions of the along-wind turbulence intensities I_u, associated with each mean wind direction, at 18 meters AGL, are illustrated in Fig. 47. The Eurocode predictions are included for reference. I_u values, between 0.11 and 0.31, are predicted.

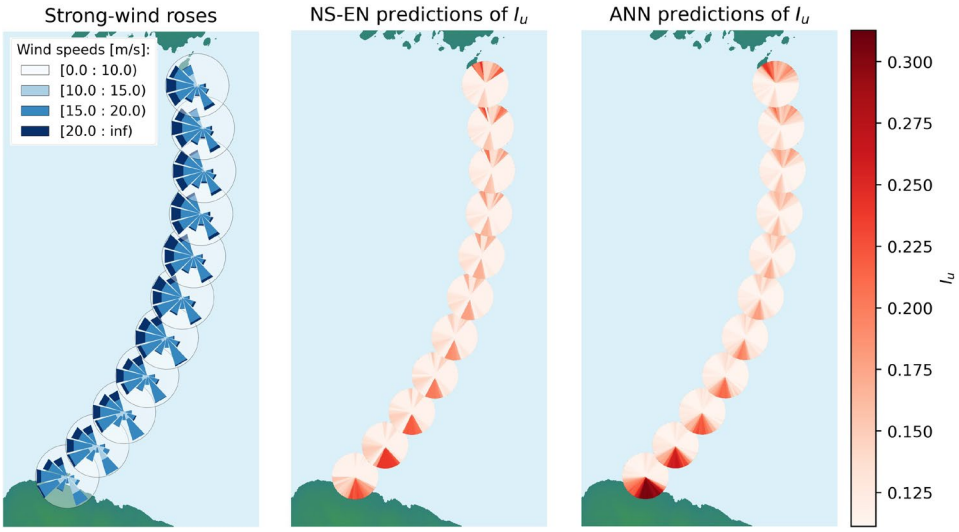

Fig. 47 – Left: wind roses of the 670 strong wind events (where U ≥ 18 m/s in at least one node) at the selected 11 interpolation nodes along the bridge axis. Right: Eurocode (NS-EN 1991-1-4) and artificial neural network (ANN) predictions of the wind turbulence intensities, as a function of the mean wind direction (360 sectors).

Regarding the across-wind I_v and upward I_w turbulence components, eqs. (219) and (220) were established based on the project-related design basis (Norwegian Public Roads Administration, 2018).

$$I_v = 0.84 \times I_u \tag{219}$$

$$I_w = 0.60 \times I_u \tag{220}$$

6.4.4. Generating equivalent homogeneous mean wind properties

Sections 6.4.2 and 6.4.3 described the methods used to estimate the inhomogeneous wind conditions. In this section, a separate analogous set of homogeneous wind conditions is generated so that an adequate comparison of both inhomogeneous and homogeneous wind analyses can take place. These are hereby denoted as "equivalent" homogeneous winds. For each inhomogeneous wind case analysed, one equivalent homogeneous wind case is also analysed in order to conclude on the importance of considering the wind inhomogeneity. By definition, these equivalent homogeneous wind properties are identical for all points along the bridge.

For each inhomogeneous strong wind event, the equivalent homogenous mean wind speed U^H, and the corresponding global mean yaw angle β_{Gs}^H and inclination angle θ_{Gs}^H, can be assumed determined in different ways. The chosen method to obtain these equivalent homogeneous properties is presented in eqs. (221) to (226). In these equations, the transformation matrix $\boldsymbol{T_{GsLw,n}}$, from the Lw to the Gs system, is obtained in the same way as $\boldsymbol{T_{GsGw}}$ (as defined in Chapter 3), but by replacing global β_G and θ_G with local $\beta_{Gs,n}^I$ and $\theta_{Gs,n}^I$, where n refers to a particular bridge node or element). N is the total number of bridge nodes (or elements).

$$\boldsymbol{U_{Lw,n}^{I,Q}} = \left[U^{I^2}, 0, 0\right]_n \tag{221}$$

$$\boldsymbol{U_{Gs,n}^{I,Q}} = \boldsymbol{T_{GsLw,n}} \boldsymbol{U_{Lw,n}^{I,Q}} \tag{222}$$

$$\boldsymbol{U_{Gs}^{H,Q}} = \left[U_X^{H,Q}, U_Y^{H,Q}, U_Z^{H,Q}\right] = \frac{1}{N} \sum_n^N \boldsymbol{U_{Gs,n}^{I,Q}} \tag{223}$$

$$U^H = \sqrt{\sqrt{U_X^{H,Q^2} + U_Y^{H,Q^2} + U_Z^{H,Q^2}}} \tag{224}$$

$$\beta_{Gs}^{H} = arctan\left(-U_X^{H,Q}/U_Y^{H,Q}\right) \tag{225}$$

$$\theta_{Gs}^{H} = arcsin\left(U_Z^{H,Q}/U^{H^2}\right) \tag{226}$$

This method consists in averaging the vectors that represent the quadratic (with superscript Q) mean wind speeds and directions of the inhomogeneous wind field along the bridge girder.

It should be noted that other methods are also possible. Possible alternatives include averaging the vectors representing instead the linear wind speeds and directions, or directly performing an arithmetic mean of the mean wind speeds, linear or quadratic, and performing circular means of the yaw and inclination angles, weighed by the linear or quadratic wind speeds. Using more advanced mathematical methods is also possible (e.g. (Gramkow, 2001; Kapić et al., 2021)).

The bridge response to static wind loads is proportional to U^2. A typical linear buffeting response is proportional to Uu, Uv and Uw, so the equivalent homogeneous turbulence intensities I_u^H, I_v^H and I_w^H were simply estimated with eq. (227).

$$\begin{gathered} U^H \sigma_i^H = \frac{1}{N}\sum_n^N \left(U_n^I \sigma_{i,n}^I\right) \Leftrightarrow U^{H^2} I_i^H = \frac{1}{N}\sum_n^N \left(U_n^{I^2} I_{i,n}^I\right) \Leftrightarrow \\ \Leftrightarrow I_i^H = \frac{\sum_n^N \left(U_n^{I^2} I_{i,n}^I\right)}{N U^{H^2}}, \qquad for\ i = u, v, w \end{gathered} \tag{227}$$

6.4.5. Inhomogeneous wind buffeting formulation

The simplified finite element model (FEM) of the floating bridge presented in Section 4.2 is used. Wind properties, other than the inhomogeneous mean wind speed, direction and turbulence intensities, were taken from Section 4.3. The state-of-the-art 3D skew wind buffeting formulation, described in Chapter 3 and applied in Chapter 5, is adopted in this chapter. The constrained polynomial fits of the aerodynamic coefficients, obtained from the wind tunnel tests and procedure described in Chapter 5, are used as inputs for the model.

Also in this chapter, the linear quasi-steady approach was used since flutter derivatives and aerodynamic admittance functions have not yet been measured experimentally for the current floating bridge. Its horizontal modes of vibration have extremely low natural frequencies. The wavelength of the most relevant

turbulence component for the first mode is U / f = 33.4 [m/s] / 0.01 [Hz] = 3340 m, which is more than 100 times the width of the cross-section (31 m). This means that the quasi-steady theory should provide a decent approximation of the forces that depend on these very slow motions. Still, an unsteady theory should improve the vertical and torsional response predictions, where the relevant turbulence components are roughly 200 m long. In this study, the aerodynamic admittances are also conservatively disregarded, and a quasi-steady theory is considered to have sufficient accuracy to compare inhomogeneous and homogeneous wind buffeting responses. It is recalled that the unsteady hydrodynamic radiation forces are available and included in the model, via frequency-dependent mass and damping matrices added to the respective structural and aerodynamic matrices.

To consider the decay of the wind coherence with increasing distances, it is common to use nine non-dimensional exponential decay coefficients, $K_{i,j}$, for i in u, v, w and for j as one of the three relevant wind-oriented axes. In this study, these pre-defined $K_{i,j}$ coefficients, suited for homogeneous wind analyses, were also adopted in the inhomogeneous wind analysis for the following reasons: 1) simplicity and availability; 2) the underlying wind measurement data and equipment (described in Appendix B) are insufficient to estimate accurately $K_{i,j}$ coefficients that additionally depend on inhomogeneous wind parameters such as ΔU, $\Delta\beta$ and $\Delta\theta$; 3) "if the non-uniformity of the mean wind velocity is not too large, the coherence model can remain unchanged" (Cheynet et al., 2016); 4) for the present case study, the wind coherence drops to nearly zero at the scales where the mean wind inhomogeneity starts to develop. Similarly, for reasons 1) to 3), the non-dimensional $A_{i,n}$ parameters and the integral length scales L_{i,x_u} used in the single-point spectra were also kept homogeneous.

When determining the normalized co-spectra of the wind, $Re\left(S_{i_1 n_1 i_2 n_2}\right)/\sqrt{S_{i_1 n_1}\, S_{i_2 n_2}}$, between wind components i_1 and i_2 (for i in u, v, w) and between two reference nodes n_1 and n_2, it is necessary to input the distances, in wind coordinates, between both reference nodes. However, the inhomogeneous wind-oriented axes, $\boldsymbol{x_u, y_v, z_w}$, are local, as they vary in space. To overcome this, an averaging method is used again. The method shown in eqs. (221) to (226) was used to find the average wind coordinate systems, hereby denoted $\overline{Lw}$ ($\overline{\boldsymbol{x_u}}, \overline{\boldsymbol{y_v}}, \overline{\boldsymbol{z_w}}$), that are obtained for each pair of nodes and their respective Lw systems. This method was used to obtain the values of the average yaw $\overline{\beta_{Gs}}$ and inclination angles $\overline{\theta_{Gs}}$ for the pair of nodes n_1 and n_2, with $\overline{\beta_{Gs}}$ as β_{Gs}^H and $\overline{\theta_{Gs}}$ as θ_{Gs}^H, with $N = 2$. These angles are then used to estimate $\boldsymbol{T_{\overline{Lw}Gs}}$ in the same way as $\boldsymbol{T_{GwGs}}$ is estimated in Chapter 3. It should be noted that a simple component-wise average of two

coordinate systems can lead to non-orthogonal systems. The required input distances, in averaged wind coordinates, $\Delta\overline{x_u}$, $\Delta\overline{y_v}$ and $\Delta\overline{z_w}$ are thus obtained from eq. (228), for each pair of nodes n_1 and n_2.

$$[\Delta\overline{x_u}, \Delta\overline{y_v}, \Delta\overline{z_w}]^T = \boldsymbol{T}_{\overline{\boldsymbol{LwGs}}}[\Delta X, \Delta Y, \Delta Z]^T \tag{228}$$

where ΔX, ΔY and ΔZ are the known distances between nodes n_1 and n_2, in the consistent global structural axes X, Y and Z.

The average mean wind speed, necessary in the normalized co-spectra formulation, is also obtained with the method shown in eqs. (221) to (226), with $\overline{U}$ as U^H, for n in n_1 and n_2 ($N = 2$). The single-point spectrum, associated with node n, and the two-point inhomogeneous normalized co-spectrum, associated with nodes n_1 and n_2, can be then updated from the homogeneous case, in eqs. (200) and (201), to the more general inhomogeneous case shown in eqs. (229) and (230).

$$\frac{f\,S_{i,n}(f)}{\sigma_{i,n}^2} = \frac{A_{i,n}\hat{f}_{i,n}}{(1 + 1.5A_{i,n}\hat{f}_{i,n})^{5/3}}\;; \quad where:\;\; \hat{f}_{i,n} = \frac{f\,L_{i,x_u}}{U_n}\;; \quad for\; i = u, v, w \tag{229}$$

$$\begin{aligned} &\frac{Re\left(S_{i_1 n_1 i_2 n_2}(f, \Delta\overline{x_u}, \Delta\overline{y_v}, \Delta\overline{z_w})\right)}{\sqrt{S_{i_1 n_1}(f)\,S_{i_2 n_2}(f)}} = \\ &= \begin{cases} \exp\left(-\dfrac{f}{\overline{U}}\sqrt{\left(K_{i,X_u}\Delta\overline{x_u}\right)^2 + \left(K_{i,Y_v}\Delta\overline{y_v}\right)^2 + \left(K_{i,Z_w}\Delta\overline{z_w}\right)^2}\right), & if\;\; i_1 = i_2 \\ 0, & if\;\; i_1 \neq i_2 \end{cases} \end{aligned} \tag{230}$$

The correlation between two different turbulence components was neglected in this study for simplicity. However, important effects, in particular from S_{uw}, may occur, as seen in, e.g. (Øiseth et al., 2013). These should be evaluated separately in future work.

6.5. Results and discussion

This section presents detailed analyses of the 670 strong wind events accumulated for the Bjørnafjord area. However, first, two selected examples of how inhomogeneous winds can affect the maximum bridge response are discussed.

The first inhomogeneous wind example is a 1-hour-long strong wind event that occurred on the 27th of November 2011, at 15:00:00. This event has the 15th largest

observed mean wind speed, at any point along the bridge, during the 20-year simulation period. This event is selected as an example since it causes the largest predicted linear static horizontal response of the bridge, out of all the 670 strong wind events studied. This event is dominated by winds from the North-West, relatively homogeneous in mean direction (maximum deviation of 4°), but with strongly varying mean wind speeds along the bridge, between 12.5 m/s and 24.6 m/s. The stronger winds meet the south part of the bridge nearly perpendicularly, whereas the weaker ones in the north meet the bridge at large yaw angles. This inhomogeneous wind event is illustrated in Fig. 48. The equivalent homogeneous wind is also illustrated in Fig. 48, as well as the static response to both cases. In this event, the unfavourable combination of skewness and inhomogeneity creates a strongly varying static wind load along the bridge. Since the floating bridge behaves like an arch in the horizontal plane, it is vulnerable to antisymmetric loads. The maximum static horizontal response, along the bridge, to inhomogeneous winds, $|\Delta_y|^I_{max}$, is 2.53 m, whereas the analogous homogeneous response $|\Delta_y|^H_{max}$ is 1.33 m. The ratio $|\Delta_y|^I_{max}/|\Delta_y|^H_{max} = 1.90$ indicates, for this case, a 90% increase in response when considering the wind inhomogeneity.

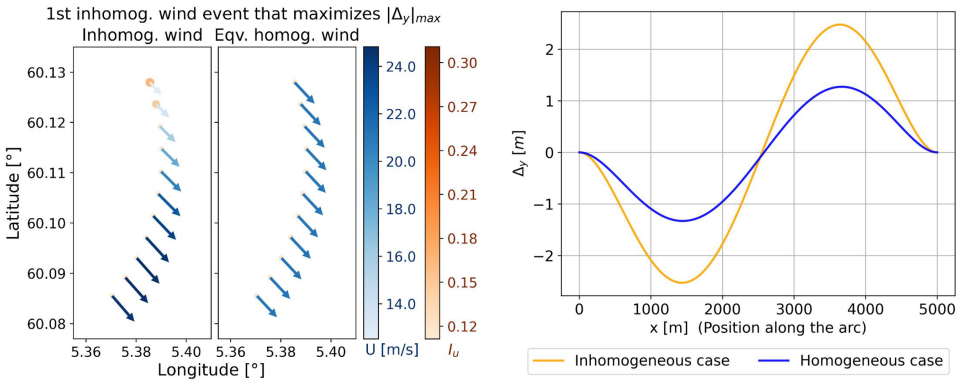

Fig. 48 – Left: Inhomogeneous wind event that maximizes the static horizontal response. The equivalent homogeneous wind event is also included for comparison. Right: Static wind response to both cases.

The second example represents an inhomogeneous wind event which occurred on the 12th of January 2005, at 12:00:00. This 1-hour-long event is only the 63rd strongest in terms of maximum wind speed. However, it yields the largest predicted vertical buffeting response out of all the 670 strong wind events studied and is illustrated in Fig. 49. This southerly wind is significantly more turbulent, especially in the south part of the fjord, due to the hills located south of the planned fjord crossing. This local turbulence is then able to locally excite the bridge in the vertical

plane, in which stiffness is mainly provided by the floating pontoons, leading to a maximum response of $|\Delta_z|^I_{max} = 0.044\,m$. The response to the equivalent homogeneous wind case is $|\Delta_z|^H_{max} = 0.036\,m$, and so the ratio $|\Delta_z|^I_{max}/|\Delta_z|^H_{max} = 1.22$ indicates a 22% increase in response.

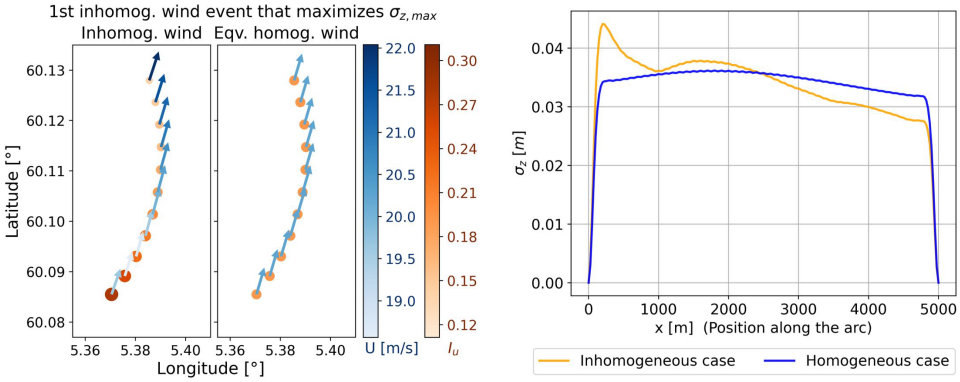

Fig. 49 – Left: Inhomogeneous wind event that maximizes the vertical buffeting response. The equivalent homogeneous wind event is also included for comparison. Right: Buffeting response to both cases.

Next, the results from all 670 strong wind events are presented. The five most critical inhomogeneous wind events have been identified, concerning the static and buffeting response, respectively, for each of the three most relevant degrees of freedom (horizontal, vertical and torsional). An overview of the properties of these events is provided in a separate Section 6.6.

The general results from the linear static and frequency-domain buffeting analyses are conveniently compiled and presented in figures, as summarized in Table 21.

Table 21. Bridge response figures, by analysis type and response component

	Horizontal	Vertical	Torsional
Static analysis	Fig. 50	Fig. 51	Fig. 52
Buffeting analysis	Fig. 53	Fig. 54	Fig. 55

Each of these figures is then subdivided into five plots, comparing all 670 1-hour inhomogeneous wind events and their equivalent homogeneous wind events as indicated next:

- The first plot (right side, top row) – Displacement response, plotted as a function of the position along the bridge girder.

- The second plot (left side, middle row) – Maximum displacement response (along the entire bridge girder, in absolute value) as a function of the equivalent homogeneous wind speed U^H that is associated with each event, i.e., associated with each pair of comparable inhomogeneous and homogeneous winds. The markers used in this scatter plot are arrows that indicate the wind direction, i.e., the equivalent homogeneous yaw angle, $\beta^H_{Cardinal}$, with respect to the cardinal directions that the wind blows from (see eq. (218)). These directions are in conformity with the polar axis of the third plot.

- The third plot (right side, middle row) – The results in this plot are the same as in the second plot but presented instead as a function of $\beta^H_{Cardinal}$. The size of the circular markers is proportional to U^H. The bridge axis is also illustrated. Together, the second and third plots attempt to depict the response with respect to both U^H and $\beta^H_{Cardinal}$.

- The fourth plot (left side, bottom row) – Direct comparison between the maximum responses along the bridge under the inhomogeneous and equivalent homogeneous wind of each event. It indicates the correlation, the bias and the variation between both responses.

- The fifth plot (right side, bottom row) – Cumulative distribution functions (CDF) of maximum response along the bridge. It helps quantify the response underestimation of a homogeneous wind analysis with respect to its inhomogeneous counterpart, for each probability value.

The ratio between the inhomogeneous wind response and the equivalent homogeneous wind response, for each single wind event, is partially described in the abovementioned fourth and fifth plots. This ratio is further described in Fig. 56 and Fig. 57 for the static and buffeting analyses, respectively, where it is plotted as a function of U^H and $\beta^H_{Cardinal}$, for each response component.

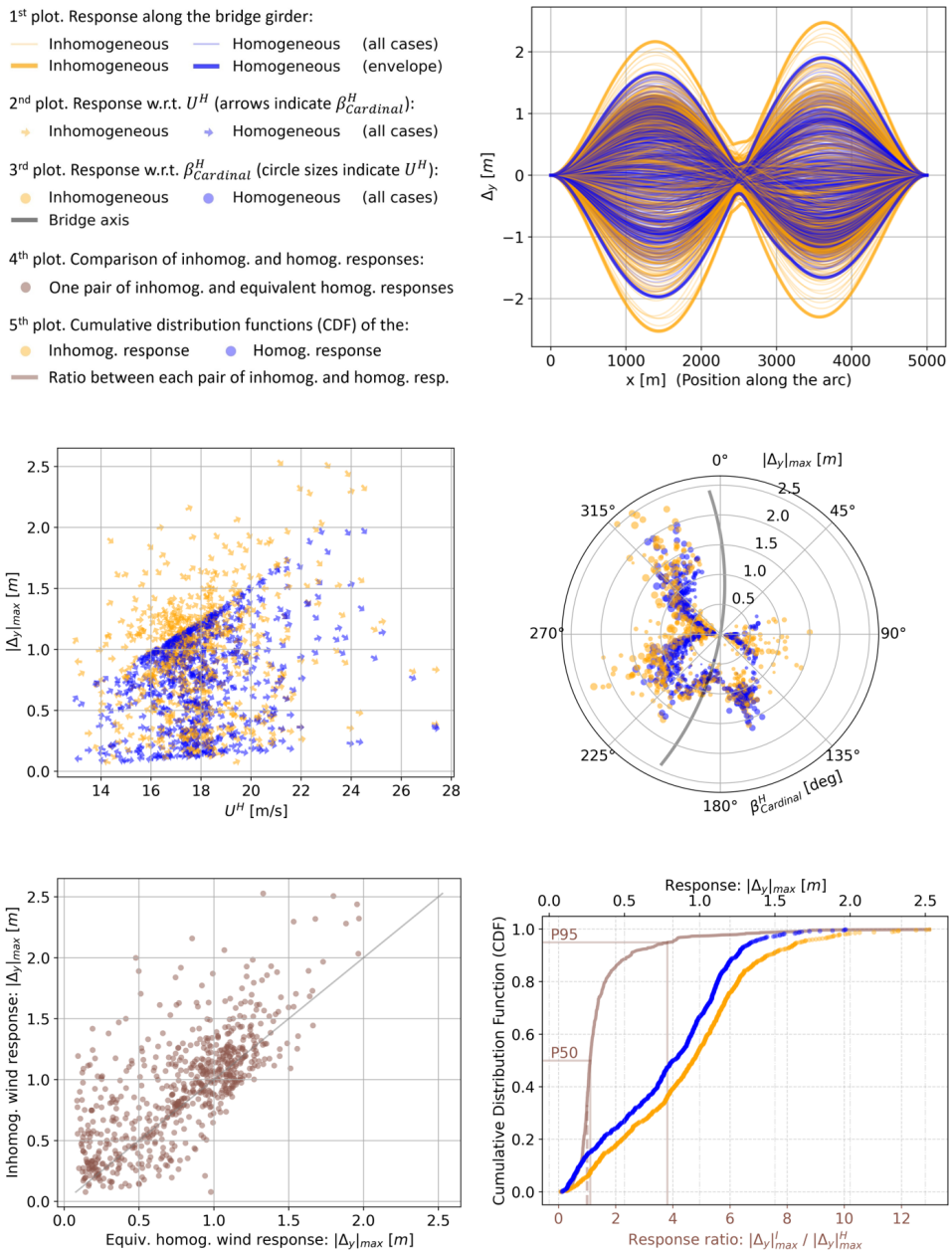

Fig. 50 – Horizontal response plots from static wind loads for all 670 strong wind events.

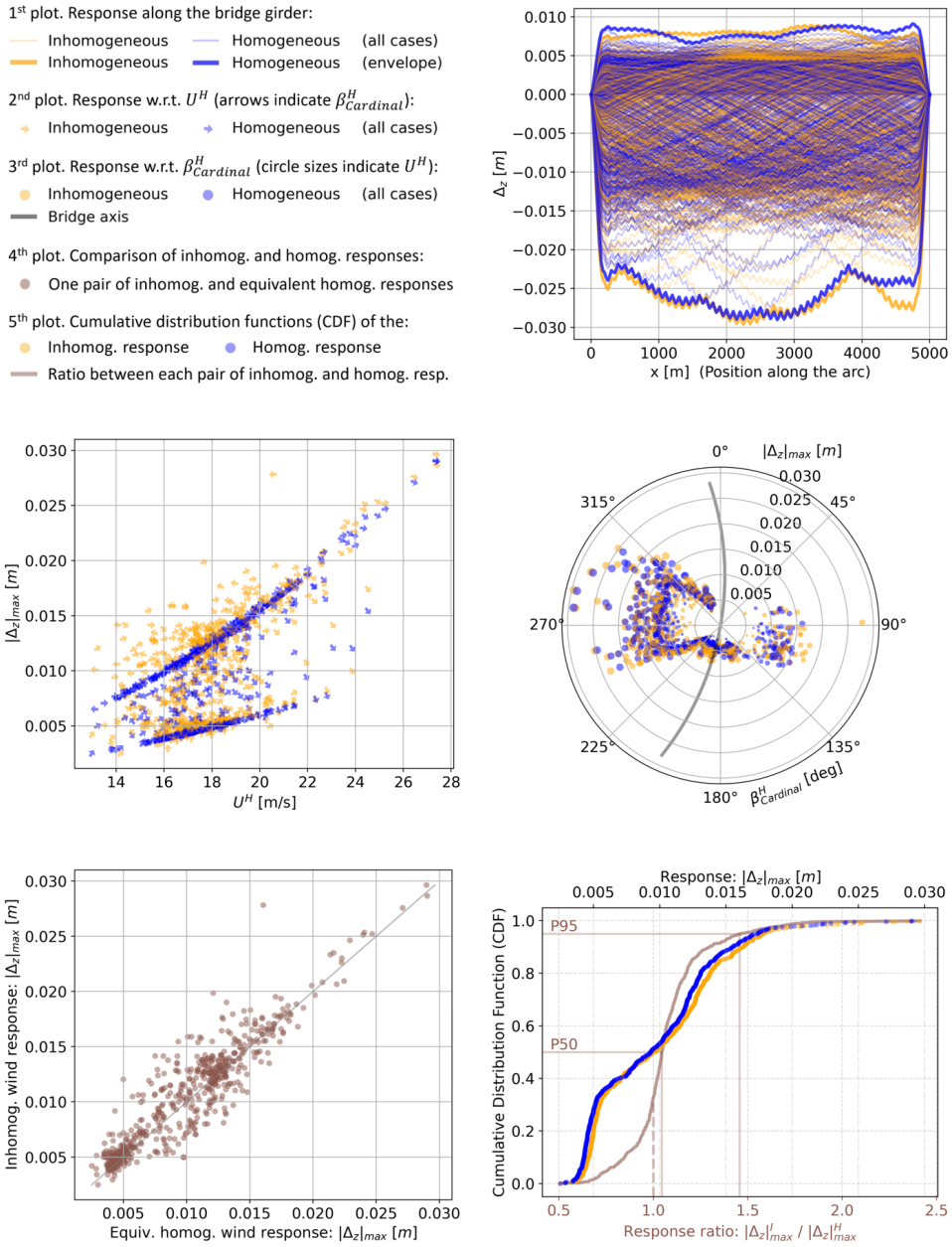

Fig. 51 – Vertical response plots from static wind loads for all 670 strong wind events.

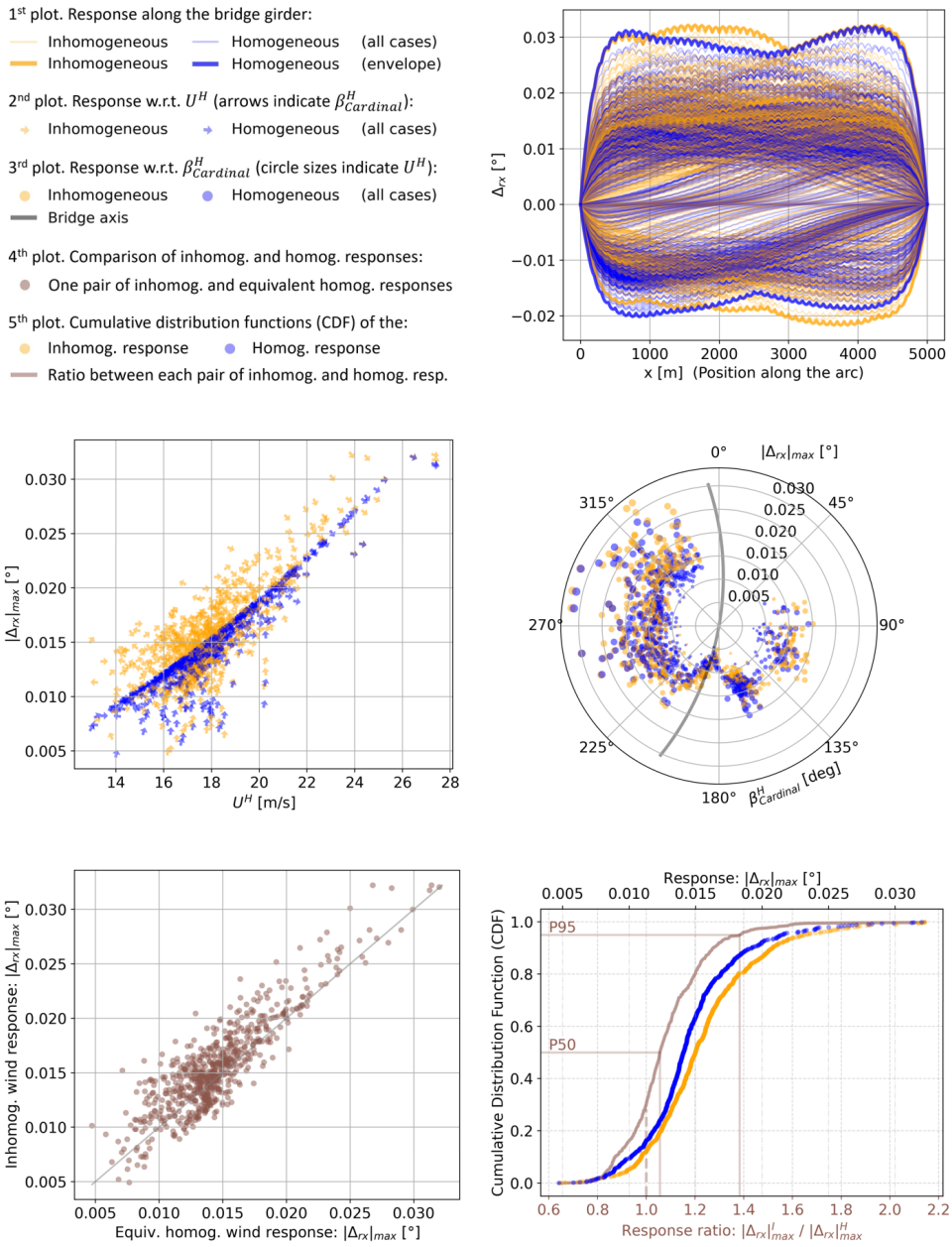

Fig. 52 – Torsional response plots from static wind loads for all 670 strong wind events.

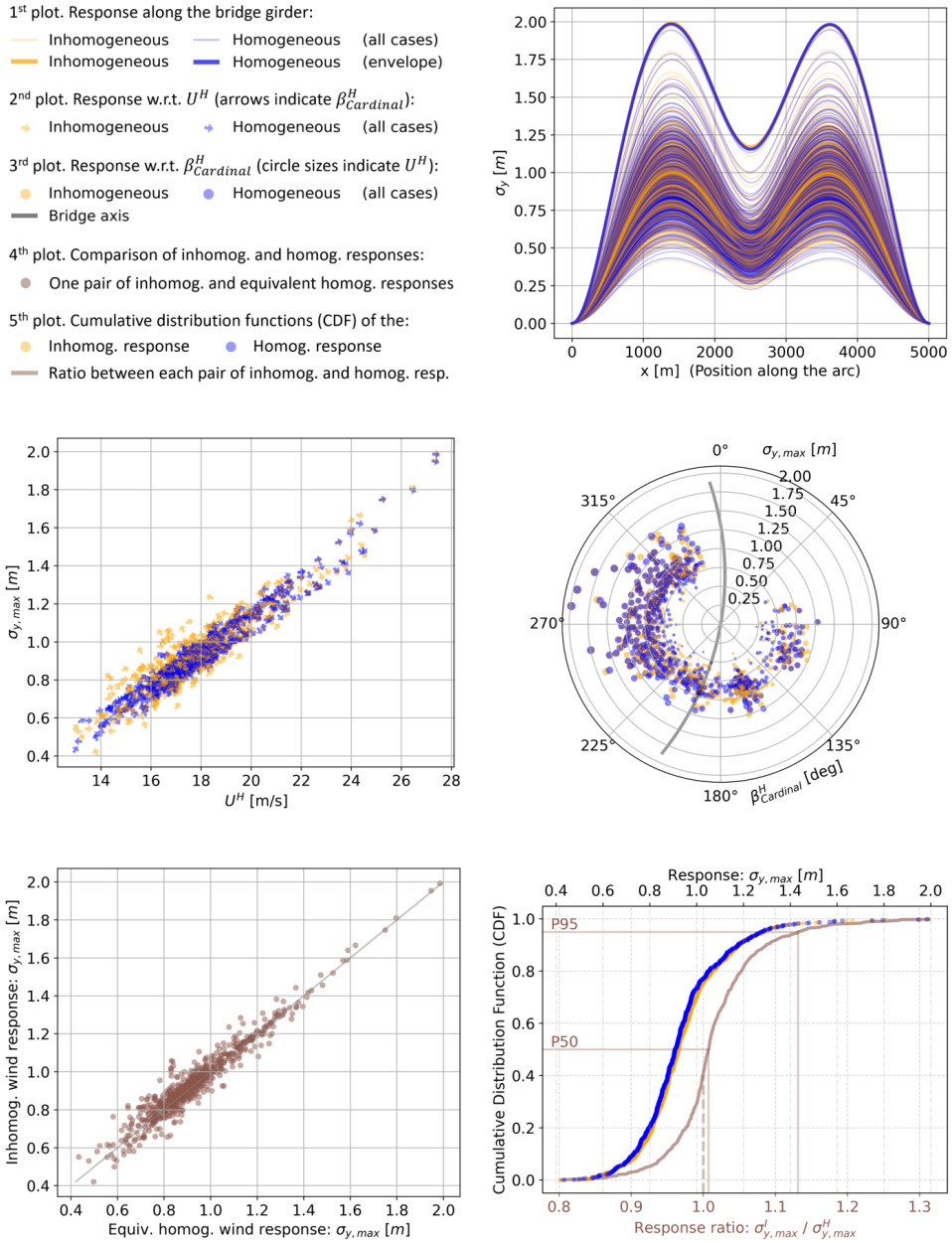

Fig. 53 – Horizontal response plots from buffeting wind loads for all 670 strong wind events.

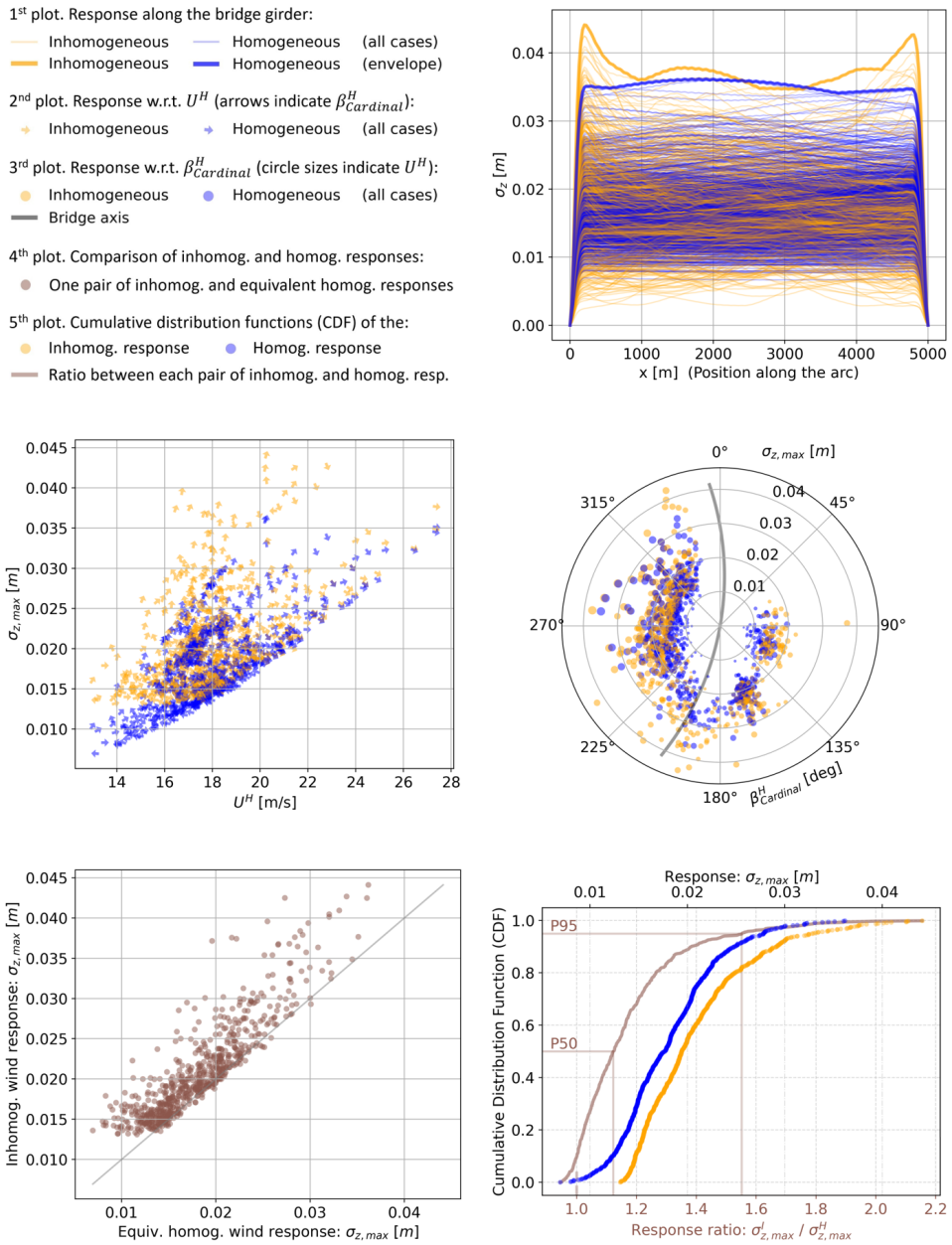

Fig. 54 – Vertical response plots from buffeting wind loads for all 670 strong wind events.

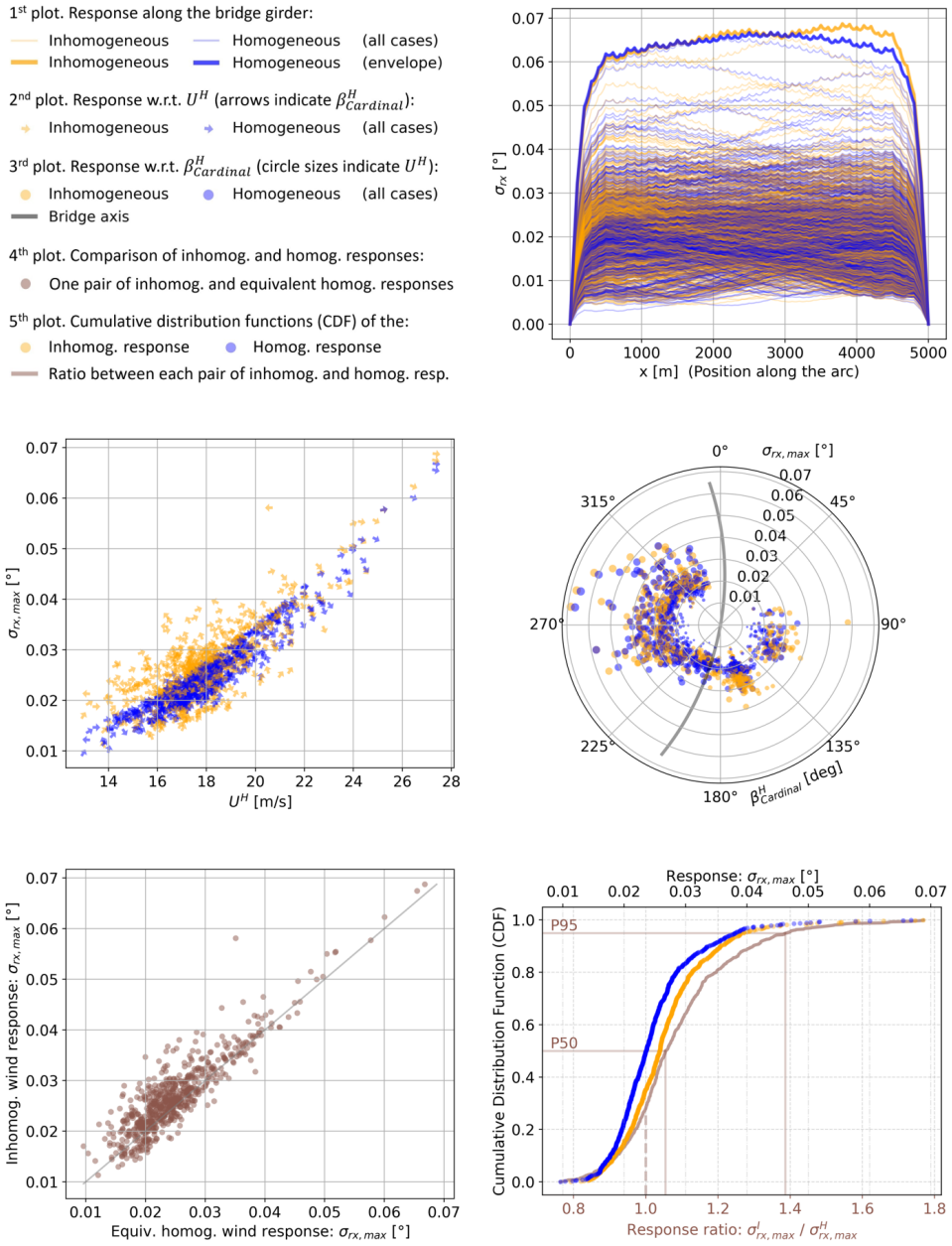

Fig. 55 – Torsional response plots from buffeting wind loads for all 670 strong wind events.

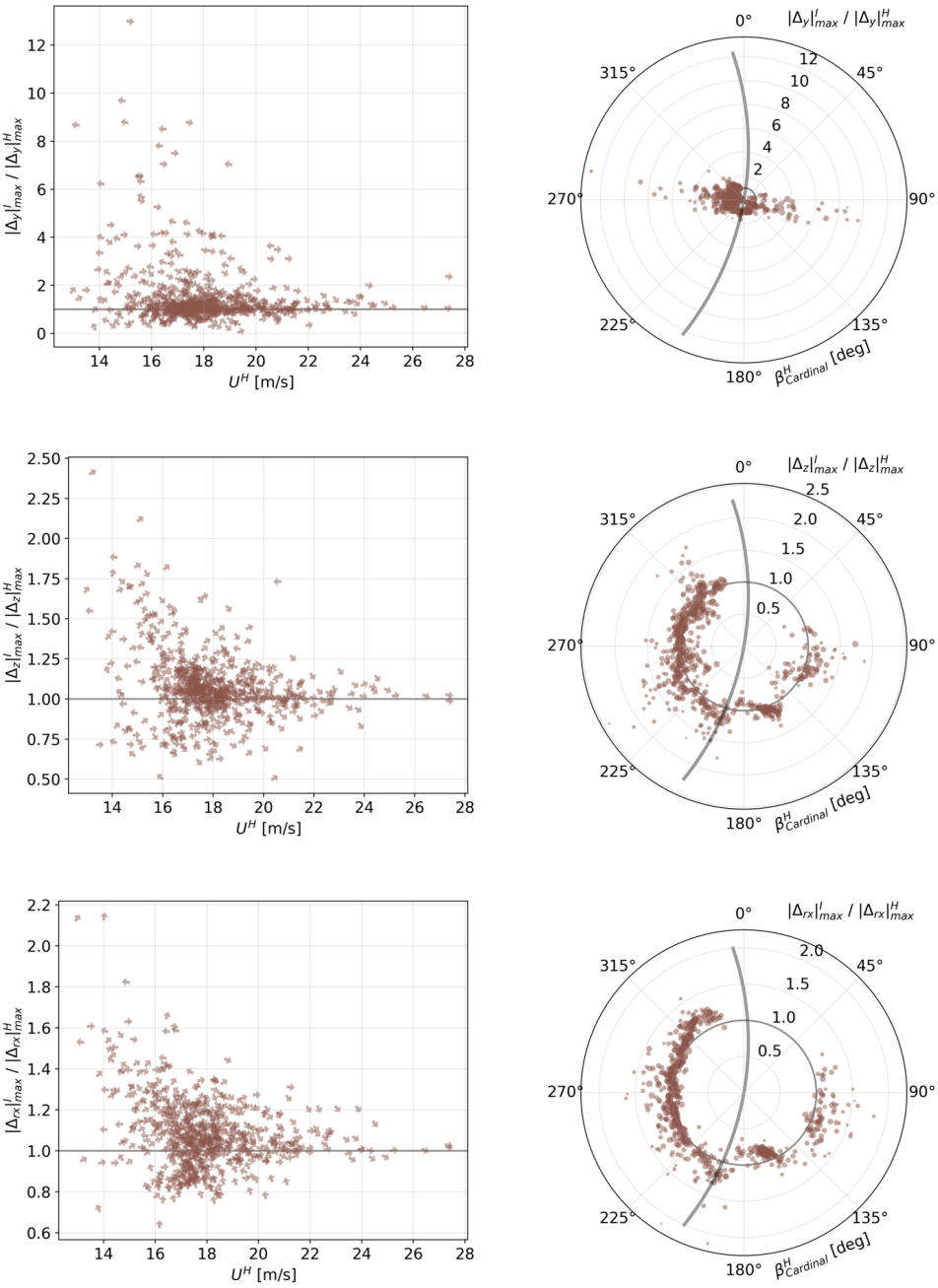

Fig. 56 – Response ratio, for the static analysis, between the inhomogeneous wind response and the equivalent homogeneous response, for each strong wind event, for the lateral, vertical and torsional components.

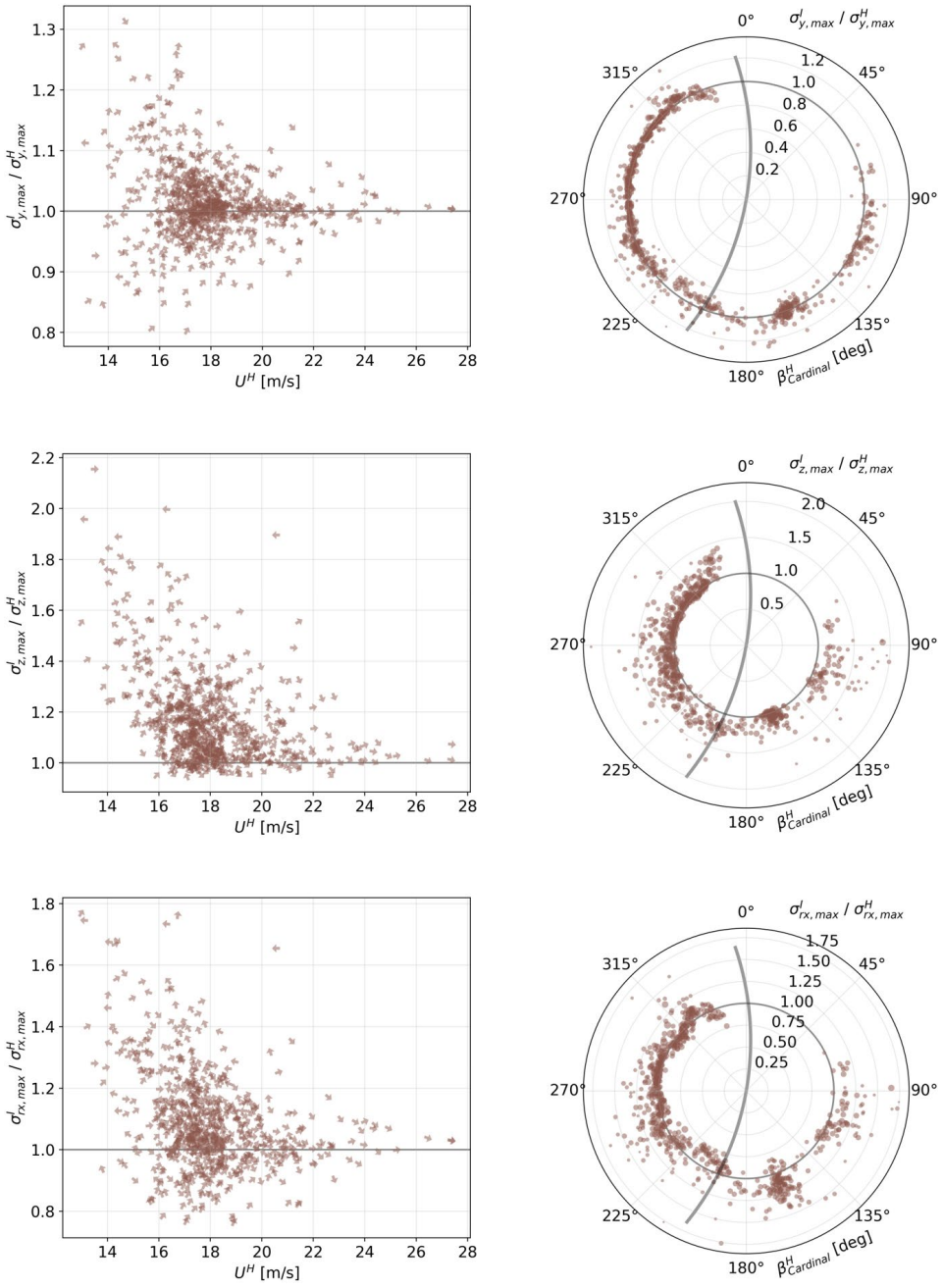

Fig. 57 – Response ratio, for the buffeting analysis, between the inhomogeneous wind response and the equivalent homogeneous response, for each strong wind event, for the lateral, vertical and torsional components.

A summary of the above results is given in Table 22. Key statistics such as the 50th, 90th, 95th and 99th percentiles are provided for the bridge response to all the 670 strong wind events, where $U \geq 18\,m/s$ in at least one point along the bridge. The minimum, average and maximum response values are also included. These statistics are given for the three main response components (lateral, vertical and torsional), for the linear static and buffeting analyses, and for both inhomogeneous and equivalent homogeneous formulations. Statistics of the response ratio between these two formulations are also included to highlight their potential differences, where each ratio concerns one inhomogeneous wind event and its equivalent homogeneous wind event.

Table 22. Key statistics of the static and buffeting wind responses to all 670 strong wind events ($U \geq 18m/s$).

Quantity	Units	P50	P90	P95	P99	Min	Avg.	Max
$\lvert\Delta_y\rvert^I_{max}$	m	0.956	1.446	1.655	2.197	0.077	0.925	2.528
$\lvert\Delta_y\rvert^H_{max}$	m	0.822	1.246	1.340	1.667	0.085	0.784	1.970
$\lvert\Delta_y\rvert^I_{max}/\lvert\Delta_y\rvert^H_{max}$	m	1.105	2.501	3.806	7.594	0.079	**1.470**	12.98
$\lvert\Delta_z\rvert^I_{max}$	m	0.010	0.016	0.018	0.025	0.002	0.010	0.030
$\lvert\Delta_z\rvert^H_{max}$	m	0.009	0.015	0.017	0.023	0.003	0.009	0.029
$\lvert\Delta_z\rvert^I_{max}/\lvert\Delta_z\rvert^H_{max}$	m	1.045	1.297	1.457	1.748	0.507	**1.070**	2.412
$\lvert\Delta_{rx}\rvert^I_{max}$	deg	0.015	0.021	0.023	0.029	0.005	0.016	0.032
$\lvert\Delta_{rx}\rvert^H_{max}$	deg	0.014	0.019	0.021	0.027	0.005	0.015	0.032
$\lvert\Delta_{rx}\rvert^I_{max}/\lvert\Delta_{rx}\rvert^H_{max}$	deg	1.056	1.273	1.383	1.594	0.641	**1.079**	2.143
$\sigma^I_{y,max}$	m	0.923	1.181	1.286	1.587	0.421	0.945	1.993
$\sigma^H_{y,max}$	m	0.908	1.177	1.274	1.574	0.434	0.933	1.985
$\sigma^I_{y,max}/\sigma^H_{y,max}$	m	1.007	1.087	1.131	1.227	0.803	**1.015**	1.313
$\sigma^I_{z,max}$	m	0.019	0.029	0.033	0.040	0.013	0.021	0.044
$\sigma^H_{z,max}$	m	0.018	0.025	0.028	0.032	0.007	0.018	0.036
$\sigma^I_{z,max}/\sigma^H_{z,max}$	m	1.123	1.381	1.552	1.798	0.946	**1.167**	2.155
$\sigma^I_{rx,max}$	deg	0.026	0.036	0.039	0.055	0.011	0.027	0.069
$\sigma^H_{rx,max}$	deg	0.024	0.034	0.038	0.050	0.010	0.025	0.067
$\sigma^I_{rx,max}/\sigma^H_{rx,max}$	deg	1.054	1.297	1.387	1.659	0.764	**1.088**	1.769

The statistics presented in Table 22 show that, for this case study, on average, an inhomogeneous wind analysis leads to a 47% increase in the maximum horizontal response when compared with the equivalent and traditional homogeneous wind analysis. As discussed in the first wind case example (Fig. 48), this increase can be explained by the inhomogeneous mean wind speeds and directions, which can

further increase the asymmetry of the skew wind loads. This may lead to both fatigue life and extreme value underestimations.

The next most important effect is observed for the vertical response under buffeting loads. An average increase of the maximum response by 17% is observed when the inhomogeneity of the wind is considered. This floating bridge has dozens of vertical eigenmodes within a narrow frequency band ($\sim 0.17\ Hz$), as shown in Section 4.2.4. Even if the bridge girder is a symmetric structure (with a vertical plane of symmetry at half its length), the off-diagonal terms of the cross-spectral density matrices of the modal buffeting loads and modal displacement response may induce an asymmetric response of the bridge. This asymmetric buffeting response occurs when the bridge is subjected to asymmetric loads, such as those from skew winds on a curved bridge and those from inhomogeneous winds. Inhomogeneous winds impose, by definition, larger nodal buffeting forces in some parts of the bridge and smaller ones in other parts, so the associated vertical response will also vary accordingly along the bridge. Thus, the inhomogeneous wind buffeting response will often have larger local maxima than its homogeneous equivalent, which has implications for the bridge design. In particular, at the south and north ends of the bridge, when the wind comes from land, it is significantly more turbulent than in the middle of the fjord, so the maximum vertical buffeting response is often found there, similarly to what was shown in the example in Fig. 49. Note that, in these cases, the winds are usually very skewed, but the derivative of the relevant aerodynamic coefficient ($C_z'^{\theta}$) is still large at large skew angles, according to the wind tunnel tests and extrapolations described in Chapter 5. On the other hand, the vertical response of this floating structure can be largely conditioned by incident wave loads rather than wind loads. In this study, only the outgoing waves, generated by the motion of the pontoons, were considered, as unsteady hydrodynamic radiation forces that help to dampen the response.

A non-negligible increase in response, of roughly 7 to 9%, on average, is also observed for the static vertical and torsional response, as well as the torsional buffeting response. As for the average of the horizontal buffeting response, only a 1.5% difference is observed.

The scatter results in Fig. 56 and Fig. 57 seem to indicate that the response ratio tends to 1.0 with increasing mean wind speeds. This is partly explained by a varying extent of wind inhomogeneity among the different wind events, as a function of U^H. By definition, wind events with U^H significantly lower than $18\ m/s$ only pass the strong wind event criterion ($U \geq 18\ m/s$ in at least one point along the bridge)

if they are significantly inhomogeneous. Moreover, the number of data points on the highest U^H values is insufficient to support this trend.

The homogeneous wind results, when plotted with respect to U^H (second plots in Fig. 50 to Fig. 55), have upper bounds that increase with the wind speed. This is because these results depend only on U^H and β^H (I^H is estimated as a function of position and β^H). By contrast, inhomogeneous winds cannot be described by just a few global parameters, and their response often spreads beyond these bounds. These scattered results then lead to an important varying level of misestimation of the homogeneous wind analyses. For individual events, extraordinary underestimations and overestimations can be attained, as indicated in Table 22 by the *Min*, *P90*, *P95*, *P99* and *Max* values of the ratios $|\Delta_i|^I_{max}/|\Delta_i|^H_{max}$ and $\sigma^I_{i,max}/\sigma^H_{i,max}$, for $i = y, z, rx$.

6.6. Wind events that maximize the bridge response

On the following left-side plots, the mean properties of the five first inhomogeneous 1-hour-long strong wind events that maximize the static horizontal $|\Delta_y|_{max}$, vertical $|\Delta_z|_{max}$, and torsional $|\Delta_{rx}|_{max}$ responses are presented at 11 points, 500 meters apart, along the bridge girder. The properties of the equivalent homogenous wind cases, used for comparison in Section 6.5, are included. Regarding the right-side plots, the mean wind properties that maximize the buffeting horizontal $\sigma_{y,max}$, vertical $\sigma_{z,max}$, and torsional $\sigma_{rx,max}$ responses, are presented instead.

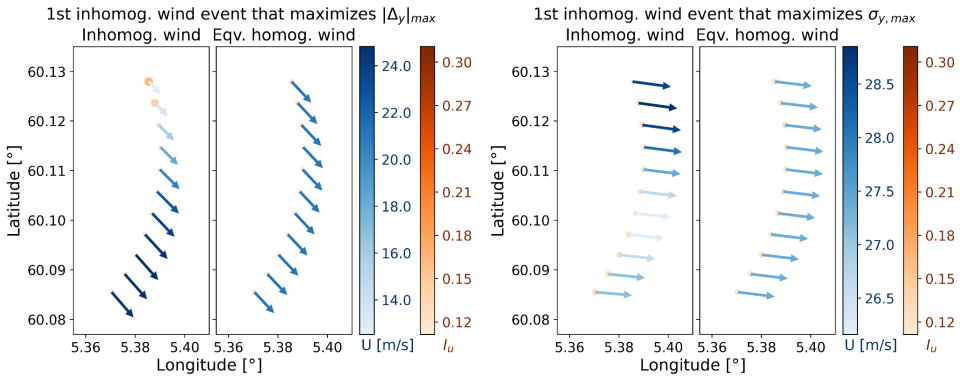

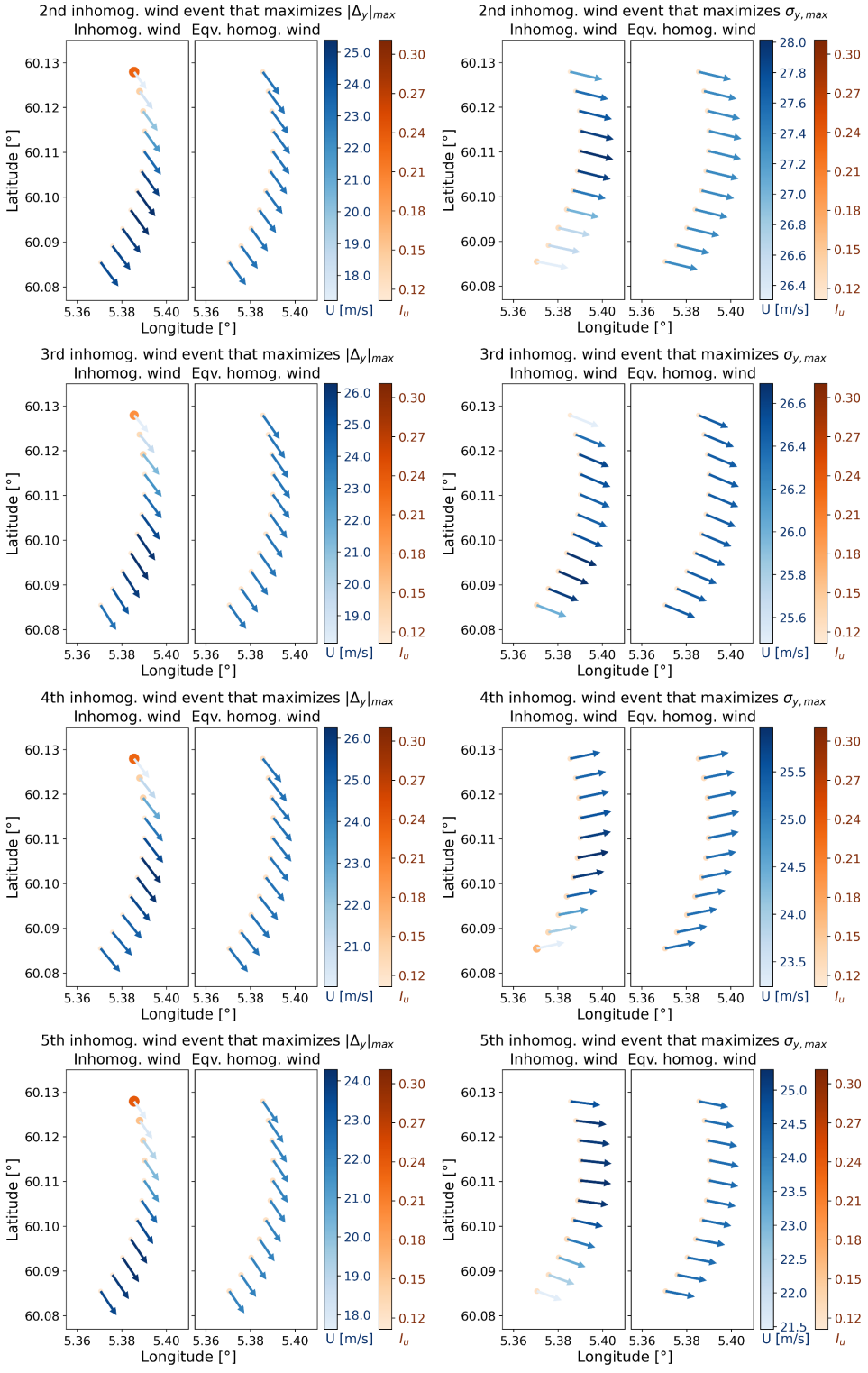
2nd inhomog. wind event that maximizes $|\Delta_y|_{max}$
Inhomog. wind
Eqv. homog. wind
2nd inhomog. wind event that maximizes $\sigma_{y,max}$
Inhomog. wind
Eqv. homog. wind
3rd inhomog. wind event that maximizes $|\Delta_y|_{max}$
Inhomog. wind
Eqv. homog. wind
3rd inhomog. wind event that maximizes $\sigma_{y,max}$
Inhomog. wind
Eqv. homog. wind
4th inhomog. wind event that maximizes $|\Delta_y|_{max}$
Inhomog. wind
Eqv. homog. wind
4th inhomog. wind event that maximizes $\sigma_{y,max}$
Inhomog. wind
Eqv. homog. wind
5th inhomog. wind event that maximizes $|\Delta_y|_{max}$
Inhomog. wind
Eqv. homog. wind
5th inhomog. wind event that maximizes $\sigma_{y,max}$
Inhomog. wind
Eqv. homog. wind
Latitude [°]
Longitude [°]
U [m/s]
I_u

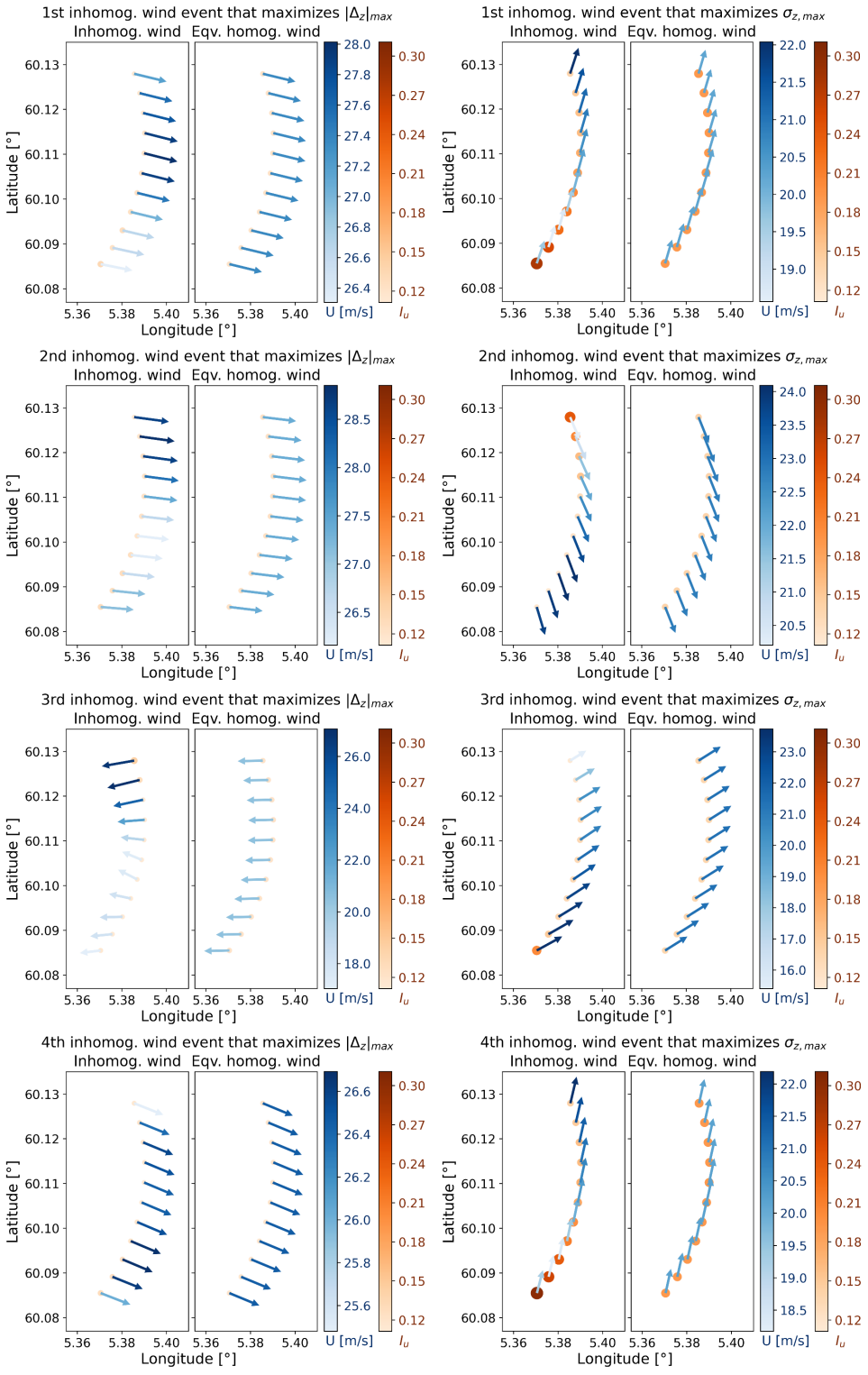
1st inhomog. wind event that maximizes $|\Delta_z|_{max}$
Inhomog. wind
Eqv. homog. wind
1st inhomog. wind event that maximizes $\sigma_{z,max}$
Inhomog. wind
Eqv. homog. wind
2nd inhomog. wind event that maximizes $|\Delta_z|_{max}$
Inhomog. wind
Eqv. homog. wind
2nd inhomog. wind event that maximizes $\sigma_{z,max}$
Inhomog. wind
Eqv. homog. wind
3rd inhomog. wind event that maximizes $|\Delta_z|_{max}$
Inhomog. wind
Eqv. homog. wind
3rd inhomog. wind event that maximizes $\sigma_{z,max}$
Inhomog. wind
Eqv. homog. wind
4th inhomog. wind event that maximizes $|\Delta_z|_{max}$
Inhomog. wind
Eqv. homog. wind
4th inhomog. wind event that maximizes $\sigma_{z,max}$
Inhomog. wind
Eqv. homog. wind
Latitude [°]
Longitude [°]
U [m/s]
I_u

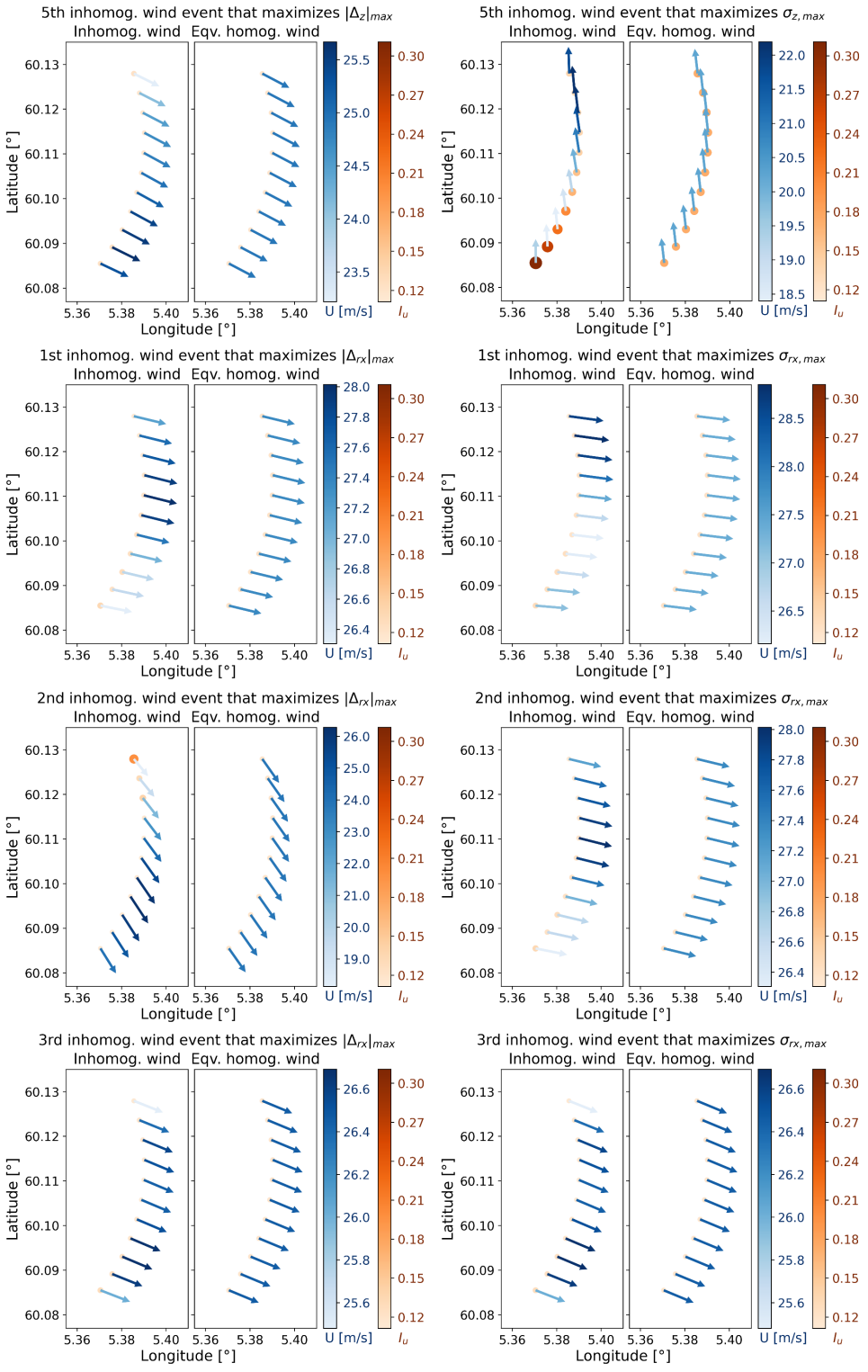
5th inhomog. wind event that maximizes $|\Delta_z|_{max}$
Inhomog. wind
Eqv. homog. wind
5th inhomog. wind event that maximizes $\sigma_{z,max}$
1st inhomog. wind event that maximizes $|\Delta_{rx}|_{max}$
1st inhomog. wind event that maximizes $\sigma_{rx,max}$
2nd inhomog. wind event that maximizes $|\Delta_{rx}|_{max}$
2nd inhomog. wind event that maximizes $\sigma_{rx,max}$
3rd inhomog. wind event that maximizes $|\Delta_{rx}|_{max}$
3rd inhomog. wind event that maximizes $\sigma_{rx,max}$
Latitude [°]
Longitude [°]
U [m/s]
I_u

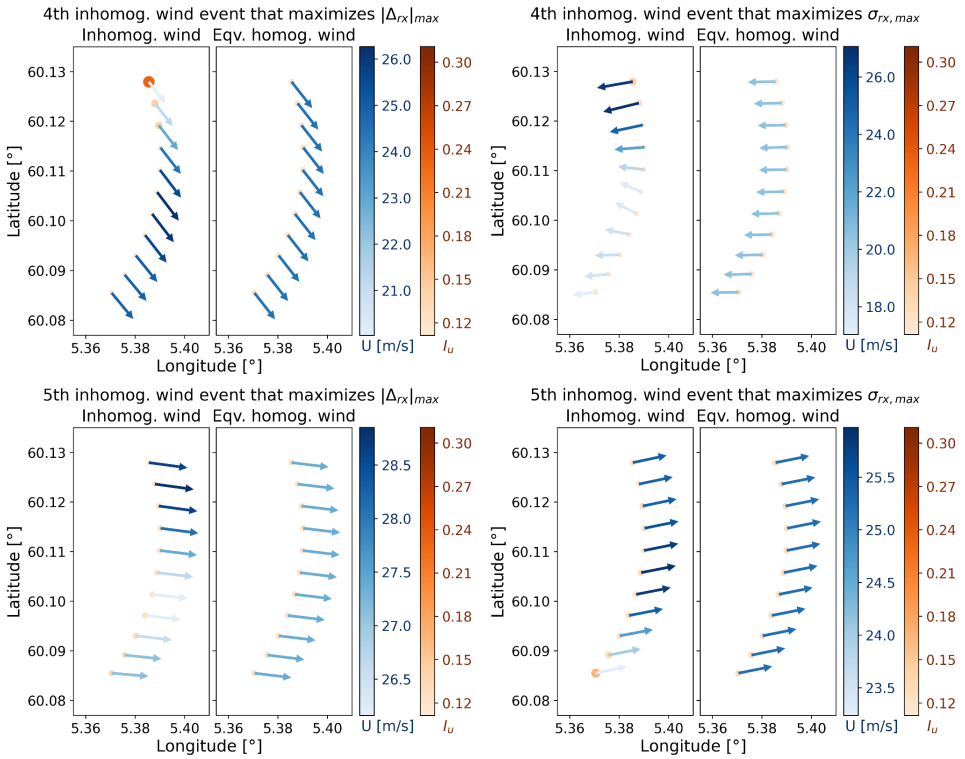

6.7. Summary

A numerical model of a 5 km long and curved floating bridge is subjected to extreme wind loads, and the effects of the wind-field homogeneity assumption are studied.

A Weather Research and Forecasting (WRF) model is used to build a realistic 20-year database of 670 inhomogeneous strong wind events. With a 500 m resolution, the WRF model provides a novel alternative to other data acquisition methods for ultra-long span bridges. This database consists of mean wind speeds and directions along the bridge girder. Additionally, wind turbulence intensities are estimated as functions of the position along the bridge and wind direction, using a hybrid method combining a European standard with a data-driven approach based on nearby wind mast measurements. A database of equivalent homogeneous wind events is also established for comparison purposes.

A linear quasi-steady frequency-domain analysis was used to efficiently compute the buffeting response to all wind events. The linear static response was also

included in the analysis. Yaw- and inclination-angle-dependent aerodynamic coefficients are used together with a skew wind buffeting formulation. Two-point co-spectra are adapted to consider the wind field inhomogeneity.

The novel long-term extreme response results presented here highlight the limitations of the traditional homogeneity assumption. On average, from all 670 strong wind events, it is shown that the maximum response along the bridge increases significantly for the inhomogeneous wind analysis. The largest average increase in maximum response was observed for the horizontal static response (47%), followed by the vertical buffeting response (17%), the torsional buffeting response (9%), the vertical and torsional static response (7 to 8%) and the horizontal buffeting response (1.5%). Most importantly, in addition to this bias, there is also a very large variance in the accuracy of the predictions under the homogeneity assumption. For some particular wind events, individual response components can be either underestimated or overestimated by more than one order of magnitude when the inherent inhomogeneity of the wind is ignored.

These results depend on the type of structure studied, the modelling assumptions, the homogenization method chosen, the local topography and the properties of the long-term strong wind events, so they are case-specific. Nonetheless, these findings help to understand the inconsistencies in the response analyses found in previous literature, which are not based on long-term bridge response data. These results encourage careful long-term investigations of the homogeneity assumption for each case study.

7. Conclusions

7.1. Main findings

Several aspects related to the aerodynamic loading of bridges and their response have been investigated in the preceding chapters, and the most relevant findings are summarized here.

Previous literature has described the importance of skew wind effects on bridges and demonstrated that traditional skew wind load models, such as the cosine rule, are inaccurate at large yaw angles. This research was instigated to further study the importance of three-dimensional skew wind effects on the response of long and wind-sensitive bridges.

The formulations of the skew winds and their effects introduced herein, together with the use of modern mathematical tools, have helped to achieve revised wind load models that can both represent a simplified and a general approach. An in-house simplified finite element model of the Bjørnafjord floating bridge was established in this research to provide a flexible and computationally efficient framework for the analyses. The bridge response was evaluated for both homogeneous and inhomogeneous wind fields.

First, the wind field was assumed to be homogeneous and with equal properties for all wind directions. In an attempt to improve the cosine rule, using the same input information, a 2D approach is developed. This approach uses a more rigorous projection of the instantaneous skew winds onto the plane that is normal to the bridge deck and includes all in- and out-of-plane motion-dependent forces. Compared to the cosine rule, the 2D approach leads to larger vertical and torsional responses that are closer to those estimated by the preferred 3D approach. The 2D approach is thus proposed as a replacement for the cosine rule for improved response estimation.

In order to consider the three-dimensional interaction between the wind and the bridge deck, a 3D approach is introduced, utilizing six aerodynamic coefficients obtained in a wind tunnel under skew winds. This approach leads to an increase in the horizontal response and a further increase in the vertical response predictions at large yaw angles, relative to the 2D approach. The maximum vertical bridge response was found to occur at large yaw angles. It should be noted that the linear vertical response depends on $C_z'^{\theta}$, i.e., the derivative of the vertical force coefficient with respect to the inclination angle. Experimental results and extrapolations support the hypothesis that $C_z'^{\theta}(\beta \approx 0°, \theta = 0°) \approx C_z'^{\theta}(\beta \approx 90°, \theta = 0°)$, although the term on the right-hand side, at $\beta \approx 90°$, is often neglected. This hypothesis leads to a large vertical response in a large domain of yaw angles. This can directly affect the ultimate and fatigue limit state design, depending on the real directional distributions of wind speed and turbulence at a given bridge location. The contribution of the axial aerodynamic coefficient, C_x, was found to be relevant for the horizontal response of the curved bridge at large yaw angles only. The moment coefficients C_{ry} and C_{rz} were found to have only minor contributions to the response, as expected, with the latter being particularly negligible. The inclusion of quasi-steady self-excited forces in the model significantly reduced the bridge response, particularly the horizontal response, for all wind directions. Different formulations of the quasi-steady self-excited forces showed similar results. Both linear and non-linear quasi-steady buffeting formulations also led to similar response results (where "non-linear" refers to the general force formulation, with aerodynamic coefficients as functions of the instantaneous wind angles).

Then, the inhomogeneity of the wind and its effects on the bridge response were assessed. First, a data-driven method was developed using an artificial neural network to predict the mean wind turbulence intensities along the bridge girder, for each wind direction, under strong winds. The model uses upstream terrain topography as input, and it is trained on a database of wind measurements and topography obtained elsewhere. The predictions outperformed those evaluated using the relevant European standard. Secondly, a high-resolution Weather Research and Forecasting (WRF) model was used to produce synthetic but realistic wind field data during a 20-year-long period. 670 inhomogeneous strong wind events were extracted, and 670 analogous homogeneous events were created to establish a basis for comparison. The 3D skew wind approach was updated to consider the wind field inhomogeneity. Linear static and linear quasi-steady frequency-domain buffeting analyses were performed. When averaging all 670 events, the bridge response under inhomogeneous winds is larger than that under the equivalent homogeneous wind cases: the static horizontal, vertical and torsional

responses increased by 47%, 7% and 8%, and the buffeting horizontal, vertical and torsional responses increased by 1.5%, 17% and 9%, respectively. However, much larger variations were observed for single wind events, demonstrating the poor accuracy of the homogeneity assumption. Investigation of the validity of the homogeneity assumption for the long-term local wind environment is thus encouraged for each case study.

7.2. Scientific contributions

The present research project and thesis provide the following scientific contributions:

a) A reproduction of the normal wind buffeting theory in a format that can be conveniently generalized to skew winds.

b) A revised 3D skew wind buffeting theory. This includes:

- A comprehensive choice of coordinate systems, consistent for all wind directions, and an intuitive and systematic use of transformation matrices, expanding a previous limitation of the yaw angle interval, from -90 to 90 deg, to -180 to 180 deg. This allows for linear buffeting analyses where the wind can come from both sides of the bridge, which is relevant for near parallel winds, for curved bridges and for inhomogeneous winds.
- The achievement of simpler and more compact formulations, especially for the linearized forces.
- Rectifications of previous quasi-steady motion-dependent skew wind force formulations.

c) An alternative 2D skew wind buffeting theory for the cases where only conventional aerodynamic coefficients (obtained under normal wind) are known. Despite the 3D theory being the preferred option, the 2D alternative consists of a novel generalization and improvement of the cosine rule, which is commonly used in practice. The 2D alternative allows for non-zero inclination angles. It can consider contributions from axial forces and from motion-dependent forces due to all in- and out-of-plane motions. It is presented in both non-linear and linearized forms.

d) A simplified finite element model of the floating bridge, developed in Python. Its properties, assembling process and verifications are described.

The model and all wind load formulations are made freely available on GitHub (https://github.com/costabm).

e) An application of the skew wind theory, with numerous novelties:

- First 360 deg assessment of skew wind effects.
- First assessment of skew wind effects on a curved bridge, and on a floating bridge.
- First aerodynamic coefficients that are estimated at yaw angles up to 50 deg, obtained with an alternative setup of static wind tunnel tests under skew winds. All values are provided.
- New and detailed proposal of fitting the aerodynamic coefficients with physics-informed piecewise constrained bivariate polynomials.
- First application of the state-of-the-art quasi-steady skew wind theories, for all 2D, 2D+1D and 3D approaches. First-time comparison between these and the cosine rule.
- First-time identification of potentially large and important differences in the vertical response between the traditional cosine rule and the improved 2D and 3D approaches.
- First-time assessment of the skew wind effects due to different coefficient fitting and extrapolation methods, considering different coefficient components and different quasi-steady self-excited force formulations.

f) A novel method of estimating wind turbulence intensities, under strong winds, at locations where no wind measurements are available, given only the relevant upstream terrain topography and a pre-existing database of wind measurements and topography elsewhere.

g) The application of a Weather Research and Forecasting (WRF) model to estimate long-term wind field properties for bridge engineering.

h) A combined assessment of inhomogeneous and skew wind effects.

i) The first long-term inhomogeneous wind response analysis of a bridge. It is also the first long-term bridge response analysis to consider 3D skew wind effects.

j) A detailed up-to-date history of the Bjørnafjorden bridge project.

7.3. Suggestions for further work

A few recommendations for further work are summarized. First, concerning the skew wind buffeting analysis:

a) Wind tunnel tests could be performed for a larger domain of yaw and inclinations angles to better extrapolate the aerodynamic coefficients and more accurately compare the different fitting methods.

b) The effects of the non-stationarity of the mean wind speeds and other wind field properties could be investigated, particularly for bridges with very long eigenperiods such as the one studied.

c) Different formulations of the normalized co-spectra of the wind turbulence could be pursued and their effects on the response compared. A non-zero spectral density between different wind components (e.g. S_{uw}) should also be considered.

d) The estimation of the axial coefficient C_x in the wind tunnel could be further improved to consider all bridge equipment and design cases where the wind loads and traffic are concomitant. For instance, the cumulative effect of many fast-moving vehicles against the wind could be considered for such long and continuous bridge girders as the one studied.

e) An accurate estimation of the aerodynamic admittance functions, which were conservatively disregarded in this study, could be pursued, with a possible impact on the buffeting analysis, particularly for the vertical and torsional responses.

f) Unsteady flutter derivatives under skew winds should provide more accurate motion-dependent forces. They could be estimated and compared with the quasi-steady formulation used. They have been previously estimated in (Zhu et al., 2002a). In the same study, an approximate method by (Scanlan, 1999), requiring only the unsteady flutter derivatives under normal wind, was included for comparison. The accuracy of the method by Scanlan was found to decrease with increasing wind speeds. A hybrid method could be pursued using Scanlan's method and imposing quasi-steady asymptotes at larger values of reduced wind velocities and yaw angles.

Regarding the machine learning application to the prediction of mean wind turbulence intensities, a few suggestions on how to expand the current work are as follows:

a) Wind measurements at different heights above ground should be collected to expand the scope of the model and capture the turbulence relationship with the height above ground.

b) More terrain categories, or a continuous roughness parameter, could be directly estimated as in (Mah et al., 2013; Mills and Fotopoulos, 2013), using, e.g. the finer point cloud models available in (Kartverket) (0.25×0.25 m resolution).

c) The crosswind and vertical turbulence intensities, often assumed to have a linear relationship with the along-wind turbulence, could be included in the model.

d) Expanding the inputs to "see" a wider upstream topography, such as a $\pm 15°$ sector around the wind direction, could improve the predictions and capture effects such as wind deflection around hills and the horizontal diffusion of turbulence. All-around topographies could also be considered to capture channelling and downstream blockage effects. However, in the present study and with the limited data available, this resulted in no obvious gains in accuracy.

e) Convolutional neural networks and other state-of-the-art computer vision models could be used to capture the spatial information of the expanded inputs mentioned above.

f) A hybrid ANN + Eurocode model could be pursued, where the Eurocode predictions could be added to the ANN inputs.

g) Predefined probability density functions of wind turbulence could be predicted instead of the sectoral mean turbulence intensity. Attempts in the present study have shown that functions with more parameters resulted in a better representation of the real data, but led to worse predictions, and vice-versa, presumably due to the lack of data in some wind sectors and the small number of mast locations in the database.

Appendix A: History of the Bjørnafjord crossing project

Floating bridges, or pontoon bridges, have been built since ancient times. In the Classic of Poetry (also known as Shijing, or the Book of Odes), which dates from the 11th to 7th centuries BCE, it is mentioned that the King Wen of Zhou, in the Wei River in China, "arranged boats to form a bridge; amply illustrious was the splendour" (Karlgren, 1950). Bridges supported by boats, as long as 2 and 3 km, dating back to the 6th and 5th century BCE, once crossed the Bosphorus and Hellespont (Dardanelles Strait) in modern-day Turkey, according to the history of Herodotus (Rawlinson and Wilkinson, 1861). Brief historical reviews of floating bridges can be found in, e.g. (Viuff, 2020; Watanabe, 2003). A list of floating road bridges currently in use worldwide as part of a lasting modern infrastructure can be found in (Kvåle, 2017).

In Norway, in 1948, the regional road director from the county of Sogn og Fjordane commissioned a report entitled "The West Coast Route", depicted in Fig. A.1 and described in (Eidem, 2016). While bridges were expected to cross narrow fjords, ferries were proposed to cross wider ones such as the Bjørnafjord (also denoted Bjørnefjord, Bjørnefjorden or Bjørnafjorden, where the suffix "en" corresponds to the definite article "the", as in "the Bjørnafjord").

Before the introduction of cars, the fjords facilitated transport by boats, but gradually they started being perceived as transport barriers when cars became more mainstream. The bridge engineering field started making rapid progress worldwide, with longer bridge spans being realized. Suspension bridges, such as the Golden Gate Bridge in 1937, the Verrazzano-Narrows Bridge in 1964 and the Humber Bridge in 1981 were breaking the longest span records, and the Lacey V. Murrow Memorial Bridge in 1940, the Hood Canal Bridge in 1961 and the Evergreen Point Floating Bridge in 1963 marked an important progress for floating bridges.

Norway started its offshore industry in the late 1960s and 1970s (Ryggvik, 2015). The pursuit of oil in increasingly deeper waters meant the development of increasingly more complex marine structures. Major technological advancements in both the bridge engineering and the marine engineering fields would soon help shape the transportation strategies of Norway.

From 1985 to 1991, the West Coast Route project was developed further (Eidem, 2016). A group of bridge engineers and road planners from the Norwegian Public Roads Administration (NPRA) proposed replacing the ferry connections along the route with submerged floating tube bridges, floating bridges and sub-sea rock tunnels. An initial sketch of these solutions is shown in Fig. A.2.

Fig. A.1 – "The West Coast Route" proposal in 1948, with ferry crossings.

Fig. A.2 – "The Coastal Highway Route" work in 1985, with ferry-free crossings.

Shortly after this period, two floating bridges were built in Norway. The Bergsøysund Bridge in 1992, and the Nordhordland Bridge in 1994, are shown in Fig. A.3 and Fig. A.4, respectively. They became the longest floating bridges without mooring lines supporting them, owing much of their horizontal stiffness to their curvature instead.

Fig. A.3 – Bergsøysund floating bridge. Opened in 1992.

Fig. A.4 – Nordhordland floating bridge. Opened in 1994.

In 1995, the Norwegian government sent a report to the parliament showing apprehension towards a complete ferry-free highway within a foreseeable future due to high costs (Samferdselsdepartementet, 1995). Instead, recommendations were made for each of the road alignment alternatives and each of the remaining fjord crossings. At the time, a 17.6 km long sub-sea rock tunnel was being considered for crossing the Bjørnafjord, which the government dismissed as unrealistic in their report to the parliament.

It took 15 years for the project to be brought up again for consideration by the government. In 2010, the Ministry of Transportation commissioned the NPRA to study the potential impact of a ferry-free highway route on businesses and associated living and working regions, as well as to evaluate technological solutions for the fjord crossings (Norwegian Public Roads Administration, 2012). This route, designated as the ferry-free E39, would stretch from Kristiansand to Trondheim, along the coast, as shown on the left-hand side of Fig. A.5.

In 2011, several road alignments with different bridge and tunnel solutions were again proposed for the Bjørnafjord and its vicinity. These can be found in a few public summary reports (Norwegian Public Roads Administration, 2011, 2012) and other internal reports (e.g. (Jermstad and Johansen, 2011)). A summary of the alternative road alignments is shown on the right-hand side of Fig. A.5, categorized by the relevant fjord crossing solutions.

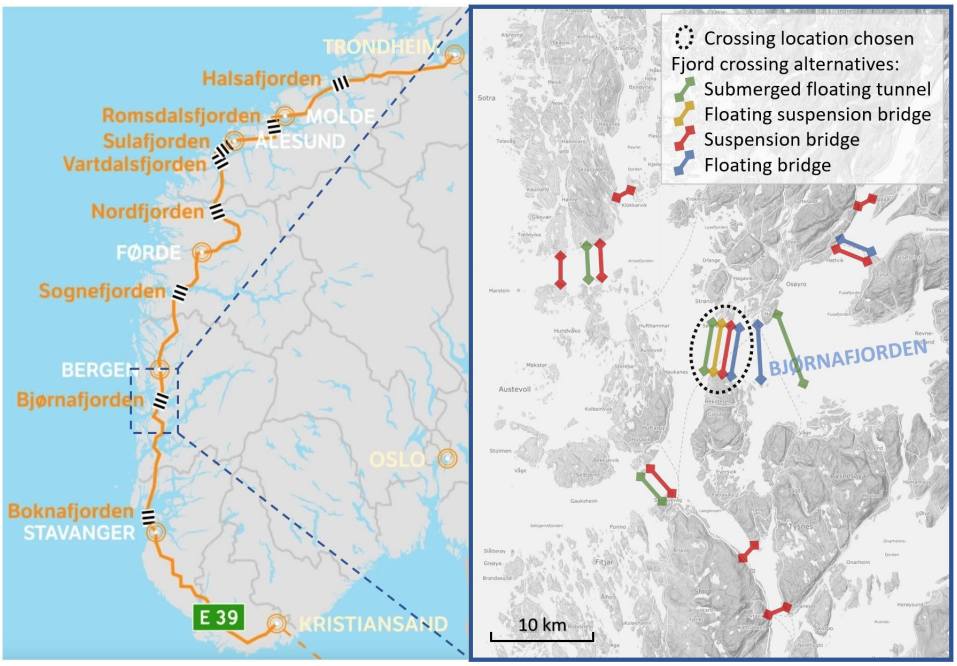

Fig. A.5 – Norway's Coastal Highway Route E39 project (left). Bjørnafjorden, with the bridge location currently chosen and other fjord crossing studies in 2011 (right).

Four fjord crossing alternatives were studied for Bjørnafjorden in addition to the sub-sea rock tunnel dismissed in 1995. These are shown in Fig. A.6 and consist of:

a) A submerged floating tube bridge (also called a submerged floating tunnel).

b) A floating bridge, with a girder supported by floating pontoons.

c) A suspension bridge.

d) A floating suspension bridge, i.e., a multi-span suspension bridge with tension-leg platforms (TLP) supporting (some of) the tower(s).

In alternative a), one submerged tube was proposed to carry the traffic in both directions, at different levels within the tube. The buoyant tube is kept submerged at a 20-50 meters depth by using inclined tensioned tethers anchored to the sea bottom, or, alternatively, by using floating pontoons at the sea surface and columns connecting the tube and the pontoons.

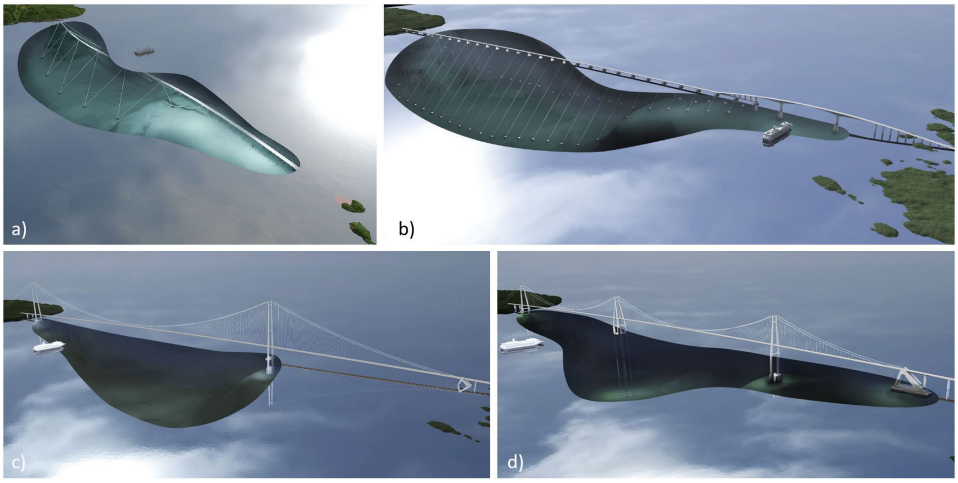

Fig. A.6 – Fjord crossing alternatives in 2011: a) submerged floating tunnel, b) floating bridge, c) suspension bridge, d) floating suspension bridge (TLP).

In the floating bridge example shown in alternative b), the horizontal stiffness of the straight girder is given by mooring lines anchored to the sea bottom. In the vertical plane, the pontoons provide the necessary support, and the bridge design resembles that of a conventional girder bridge. This way, the bridge can have relatively small spans, except for one reserved for the ship navigation channel traffic. Some of the floating bridge solutions considered in 2011 are shown in Fig. A.7.

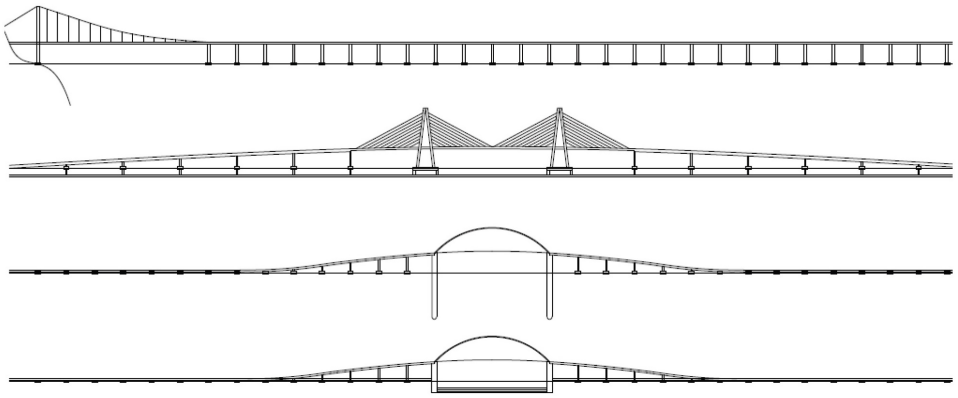

Fig. A.7 – Various fjord crossing floating bridge solutions in 2011.

In alternative c), a suspension bridge with a 3300-meter-long main span is proposed, which is 65% larger than the current world record. Despite still being a conventional bridge solution, its extreme span leads to very large self-weight loads. Then, most of the stress capacity in the main steel cables is used by their own weight.

In alternative d), a multi-span suspension bridge is proposed, which relies on one (or more) floating TLP to support its intermediate tower (or towers). These tension-leg platforms are vertically moored to the seabed and are normally used in deep water for oil and gas production. With their support, conventional suspension spans can then be considered in this alternative, as opposed to alternative c).

Another floating bridge alternative was also proposed in 2011, namely a chained floating bridge (Opgård and Allievi, 2014), as shown in Fig. A.8. This consists of a floating bridge composed of multiple segments that are connected by swivel joints. These joints allow small rotations around the vertical and transverse axes of the bridge, preventing bending moments from being transferred through them. The external loads must be then supported by tension forces in the bridge, as in a horizontal catenary or chain.

Other generic fjord crossing technologies were also studied, where a floating bridge, a submerged floating tunnel, or a hybrid combination of both could be anchored to an artificial seabed (Søreide et al., 2013). This solution is shown in Fig. A.9 and can be useful when the real seabed is too deep. This artificial seabed is composed of a submerged net of tensioned cables across the fjord, on both sides of the bridge, resembling the system of cables and hangers of a suspension bridge, but in the horizontal plane, improving the bridge stiffness in that plane.

Fig. A.8 – Chained floating bridge alternative, proposed in 2011.

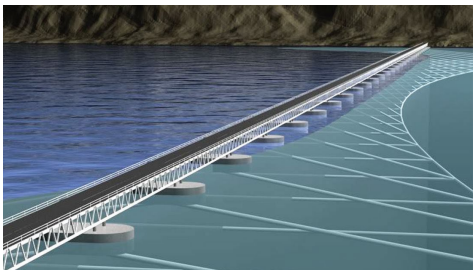

Fig. A.9 – Artificial seabed: submerged tensioned cables for horizontal support.

In 2012, an additional analysis by the NPRA and a third-party quality assessment recommended that the Bjørnafjord should be crossed by a floating bridge at the chosen location shown in Fig. A.5. The third party added that the project should be

built promptly. In December 2013, the Norwegian government decided to support these decisions and to proceed further with the project planning (Samferdselsdepartementet, 2021b). This marked the conclusion of Phase 1 of the project.

Phase 2 of the Bjørnafjord crossing project took place from 2013 to 2016. Here, the fjord crossing alternatives a), b) and d) were taken for further development studies. In this phase, the suspension bridge alternative c) and other bridge technology proposals were discarded and no longer pursued for the Bjørnafjord.

A submerged floating tube bridge was again proposed in Phase 2 of the project. The concept changed from one single tube to two independent tubes, each carrying traffic independently in one direction. This makes the bridge stiffer in the horizontal plane and provides safer emergency escape routes. The tubes can be anchored to the seabed or supported by floating pontoons at the sea surface, as in Phase 1. These solutions are illustrated in Fig. A.10 and Fig. A.11.

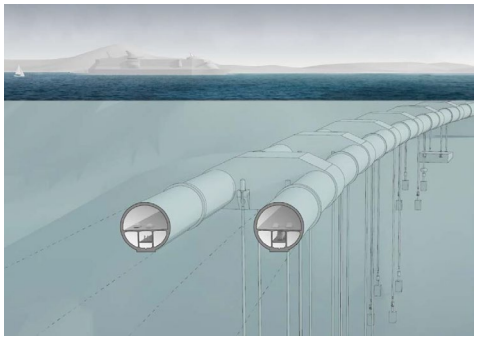

Fig. A.10 – Submerged floating tunnel, anchored to the seabed, as in 2016.

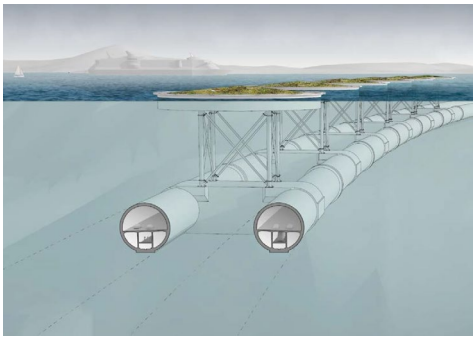

Fig. A.11 – Submerged floating tunnel, supported by pontoons, as in 2016.

The surface floating bridge alternative was at this stage divided into two sub-alternatives:

- A straight floating bridge, horizontally supported by mooring lines anchored to the seabed, with a large expansion joint at one end.
- A curved floating bridge without mooring lines or expansion joints.

The straight floating bridge was proposed with a single steel box girder. The curved floating bridge was proposed with a triple steel box girder, where each of two box girders supports the traffic in one direction, and a smaller middle girder is reserved for the pedestrian lane. Cross-beams are used to engage all three box girders similarly to a Vierendeel girder. This wider cross-section provides a much stiffer

bridge girder than in its straight bridge alternative. Technical drawings of both bridge alternatives are shown in Fig. A.12 and Fig. A.13.

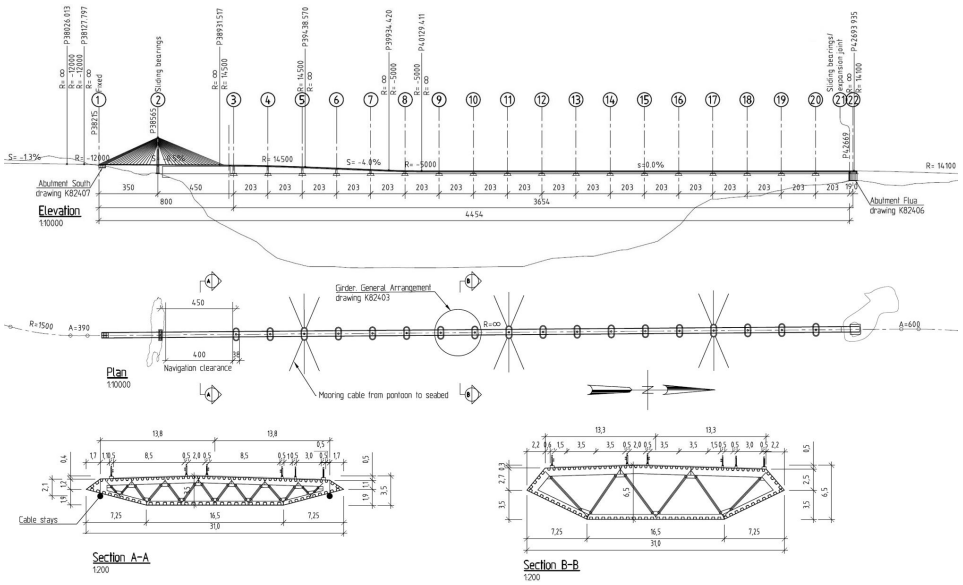

Fig. A.12 – Straight floating bridge alternative in 2016.

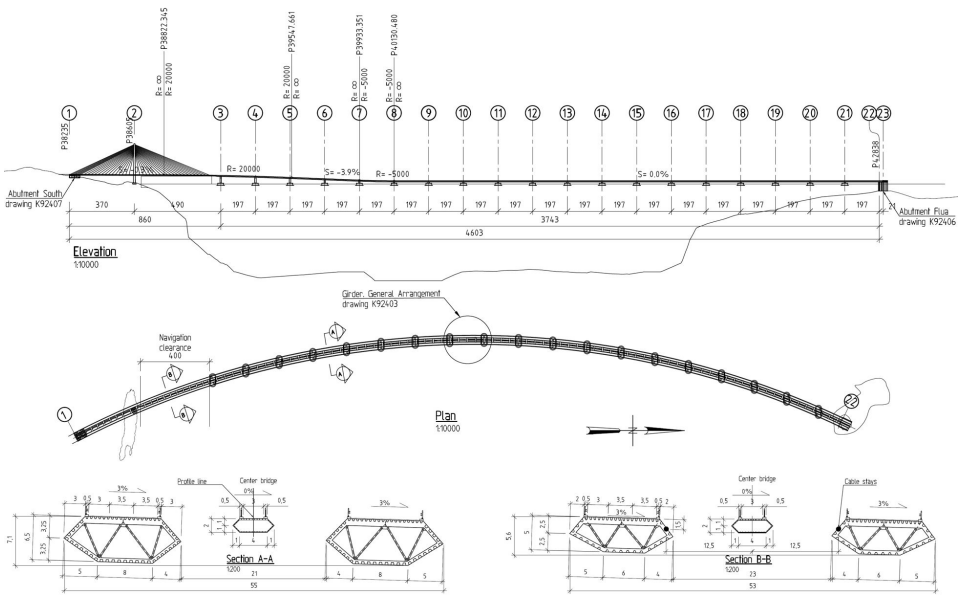

Fig. A.13 – Curved floating bridge alternative in 2016.

Regarding the TLP suspension bridge alternative, an extra span and floating tower were added to the solution. Different single-leg and four-leg floaters, in either concrete or steel, were suggested to support the towers. Excessive differential vertical displacements under uneven loads led to the introduction of a top cable connecting the tops of all towers, which improved the bridge's in-plane stiffness and stability.

At the end of Phase 2, the submerged floating tunnel solution was deemed too expensive compared to its floating and TLP bridge alternatives. Phase 3 of the Bjørnafjord crossing project was initiated to further improve these two concepts and to select one of them for further design. Phase 3 reports were delivered shortly after, in 2017.

In Phase 3, the TLP bridge solution was kept similar to that in Phase 2. A bridge model is shown in Fig. A.14. The studies of Phase 3 focused on documenting the bridge behaviour and on reducing the project uncertainties.

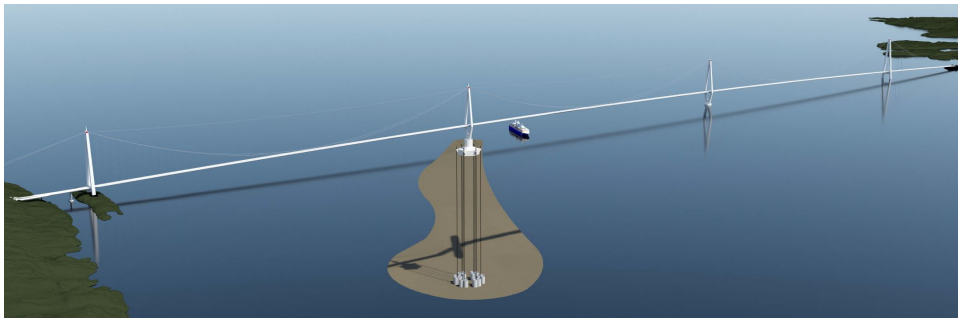

Fig. A.14 – TLP suspension bridge alternative in 2017.

Regarding the floating bridge, significant design modifications and cost reductions were achieved in Phase 3 of the project. The straight floating bridge alternative saw the number of moored pontoons increase and its cross-section height reduced. In the curved floating bridge alternative, the triple-box cross-section was changed to a more flexible and aerodynamic single-box cross-section. The concrete pontoons of both solutions were changed to lighter and smaller steel pontoons. This led to substantial reductions in material, self-weight and thus in the required pontoon size and buoyancy. The decrease in pontoon size further led to an important reduction in wave loads. This solution is illustrated in Fig. A.15.

Fig. A.15 – Curved floating bridge alternative in 2017.

At the end of Phase 3, with the help of third-party control checks and an international panel of advising experts, the floating bridge concept was chosen for the Bjørnafjord, and the TLP bridge solution was discarded.

Following Phase 3, a short Phase 4, lasting until 2018, focused exclusively on improving the support documentation for the project, including the design basis document, based on relevant research projects, both new and ongoing ones. A few examples of these research topics are: 1) further analysis of wind, waves, currents and temperature measurements; 2) study of vehicle-bridge motions and interactions under storm conditions for traffic comfort and safety; 3) analysis of fatigue load models from real traffic measurements; 4) risk and vulnerability analyses regarding ship collisions; 5) bedrock and bathymetry investigations; 6) wave model tests; 7) wind model tests, including the study of skew winds and wave-induced turbulence; 8) investigations of parametric excitations and dynamic buckling of the bridge girder.

Phase 5 took place from 2018 to 2019, with the goal of further defining the key characteristics and components of the floating bridge. Four possible floating bridge sub-alternatives were studied, as shown in Fig. A.16, and described next:

a) Single-curvature floating bridge, without mooring lines.

b) Single-curvature floating bridge, with mooring lines.

c) Straight floating bridge, with mooring lines.

d) Double-curvature floating bridge, with mooring lines.

Fig. A.16 – Floating bridge sub-alternatives in 2019: a) curved bridge (without mooring lines); b) curved bridge with mooring lines; c) straight bridge; d) double-curved bridge.

Two independent consortia of consultancy companies were assigned to the project, to study, develop and rank the four sub-alternatives. Both groups nominated the second sub-alternative b), a single-curvature floating bridge with mooring lines, to be the solution best suited for Bjørnafjorden.

The ongoing Phase 6, similarly to Phase 4, focuses once again on improving the support documentation for the project to further reduce uncertainties and to continue and expand research projects in progress, such as the present work.

Phase 7 is expected to start in 2023, where a more comprehensive design of one selected floating bridge sub-alternative will be performed.

Consortia of large and reputable consultancy companies, regular and independent third-party quality assessments, continuous cooperation with several universities, collaboration with a committee of internationally recognized experts and continuous efforts by the Norwegian Public Roads Administration contributed, together, to an increased quality of the work performed, throughout the many phases of this innovative project.

Appendix B: Inhomogeneous mean wind turbulence predictions

B.1. Preface

This appendix is reproduced from a published article (Costa et al., 2021). The formatting has been adapted to the thesis, but the content remains essentially unchanged. The full reference of the paper is:

Costa, B.M., Snæbjörnsson, J.Þ., Øiseth, O.A., Wang, J., Jakobsen, J.B., 2021. Data-driven prediction of mean wind turbulence from topographic data, IOP Conference Series: Materials Science and Engineering. IOP Publishing, p. 012005. https://doi.org/10.1088/1757-899X/1201/1/012005

B.2. Abstract

This study presents a data-driven model to predict mean turbulence intensities at desired generic locations, for all wind directions. The model, a multilayer perceptron, requires only information about the local topography and a historical dataset of wind measurements and topography at other locations. Five years of data from six different wind measurement mast locations were used. A k-fold cross-validation evaluated the model at each location, where four locations were used for the training data, another location was used for validation, and the remaining one to test the model. The model outperformed the approach given in the European standard, for both performance metrics used. The results of different hyperparameter optimizations are presented, allowing for uncertainty estimates of the model performances.

B.3. Introduction

Wind turbulence in the atmospheric boundary layer is an important phenomenon in the design of civil structures, for both static and dynamic wind loads, and for the safe operation of transport vehicles. It arises from both mechanical and thermal sources. Frictional forces between the moving air and the Earth's surface are the main drivers of atmospheric turbulence and are closely linked to the local topography. Thermal sources such as surface heating/cooling and downbursts can also cause turbulence in the atmosphere by convection.

Measuring the wind properties at some desired locations can be challenging, despite promising advances in remote sensing (Bourassa et al., 2019; Cheynet et al., 2018; Floors et al., 2016; Simma et al., 2020). Cheynet et al. (Cheynet et al., 2020) showed a high heterogeneity of wind turbulence in a fjord with the wind direction, which can significantly impact the design of wind-sensitive bridges and other man-made structures. In these situations, wind measurements, when available, are often only found at nearby locations. If there is enough diversity in the topography of the available measurement locations and sufficient wind data is available, it is, in principle, possible to use machine learning to learn the complex effects that the upstream topography has on the wind turbulence.

Artificial neural networks (ANN) (see, e.g. (Graupe, 2013; Rosenblatt, 1958)) can be of different types. Among them, multilayer perceptrons (Rosenblatt, 1961; Rumelhart et al., 1985) have been used in many problems in atmospheric sciences (Gardner and Dorling, 1998). They have been used to, e.g. predict wind speeds from ocean surface images (Krasnopolsky et al., 1995) and effectively identify topographic features such as water bodies, hills and vegetation (Venkatesh and Raja, 2003). They are thus deemed adequate for the simplified vector inputs used in this study, despite broader support for, e.g. convolutional neural networks and transformers in more challenging computer vision tasks (Dosovitskiy et al., 2020; Sharif Razavian et al., 2014).

To the authors' knowledge, this study is the first attempt to use topographic information to predict mean wind turbulence intensities at new locations, without explicitly parametrizing the topography. Parametric models representing terrain effects are inherently imperfect and are based on numerous simplifications and difficult assessments in an attempt to systematically represent a complex terrain. They were previously proposed in, e.g. the Eurocode (Norwegian Standard, 2009), Engineering Science Data Unit (ESDU, 1995) and Bitsuamlak et al. (Bitsuamlak et

al., 2007). Other studies (Brahimi, 2019; Ehsan, 2021; Velo et al., 2014) model the dependencies between wind measurements at different locations and predict wind speeds but cannot predict mean wind characteristics at new locations where no measurements were available, given only information about the local topography. Bodini et al. (Bodini et al., 2020) predict the turbulent kinetic energy dissipation rate while condensing the effects of the upstream topography into two variables, namely the standard deviation of the terrain elevation and the mean vegetation height, but also test their model at previously trained locations.

The model developed in this study is trained, validated and tested using measured along-wind turbulence intensities that are averaged within 1-degree-wide wind direction sectors, here denoted sectoral averages, and the topographic data associated with each sector, for each measurement mast location. The model hyperparameters were optimized after each iteration of a so-called k-fold cross-validation, and uncertainty estimates were provided for the model performance on each tested location.

B.4. Data description

B.4.1. Wind measurement data

Five years of wind data, between 2015 and 2020, from six measurement masts in the region around the Bjørnafjord, in Norway, are used. The locations and names of these masts are shown in Fig. B.1.

Each mast has three sonic anemometers (model: *Gill WindMaster Pro*) that measure the three components of the wind with a sampling frequency of 10 Hz. The anemometers are located at 13, 33 and 48 meters above the ground. To avoid measurements affected by smaller nearby obstacles such as trees and buildings, which are not represented in the topographic data, only the data recorded at 48 m height was used for simplicity. Thus, the turbulence intensities being predicted at the different locations also refer to a 48 m height above ground. The data is pre-processed to address faulty and missing data. Outlier detection is performed through a Z-score analysis, where the 99.99% most probable data is kept.

For each 10-minute interval in the five-year period, the mean wind speed U, the mean wind direction and the along-wind turbulence intensity I_u are recorded for each anemometer at 48 m height, when available. A threshold of 5 m/s was adopted, and observations with lower mean wind speeds were discarded. High threshold values require more data but help to remove turbulence observations that are not likely governed by friction but by, e.g. local thermal effects.

B.4.2. Topographic data

The Norwegian mapping authority provides freely accessible Digital Terrain Models of Norway (Kartverket). A 10×10 m resolution model (DTM 10) was used, consistently represented in the map projection system UTM 33. For each mast and each 1-degree-wide wind sector, a 10 km long upstream terrain profile, aligned with the wind, was obtained. It should be noted that a 10 km fetch is also suggested in NS-EN 1991-1-4:2005+NA:2009 NA.4.3.2(2) (901.1).

The heights above sea level of 45 points along the profile at the upstream distances $X = [0, 10, 30, 60, 100, 150, \dots, 9900]$ (meters) were collected into a normalized terrain profile vector Z, where for each single point, a min-max normalization is performed from that point's extreme values (for all masts and directions), as exemplified in Fig. B.2. The chosen distance between collected points is linearly increasing. This decrease in resolution assumes that, far upstream, only larger topographic features still affect turbulence (see, e.g. (Norwegian Standard, 2009), NA.4.3.2(2) (901.2)). Different sizes of X, between 15 and 60, were also tested, with roughly similar results.

To consider the effect of the different categories of terrain roughness, a vector R was added to the data used. Two categories were considered, sea and ground, normalized into a binary vector. This procedure could be expanded to include other terrain categories in the R vector.

Fig. B.1 – Locations and adopted names of the wind measurement masts used.

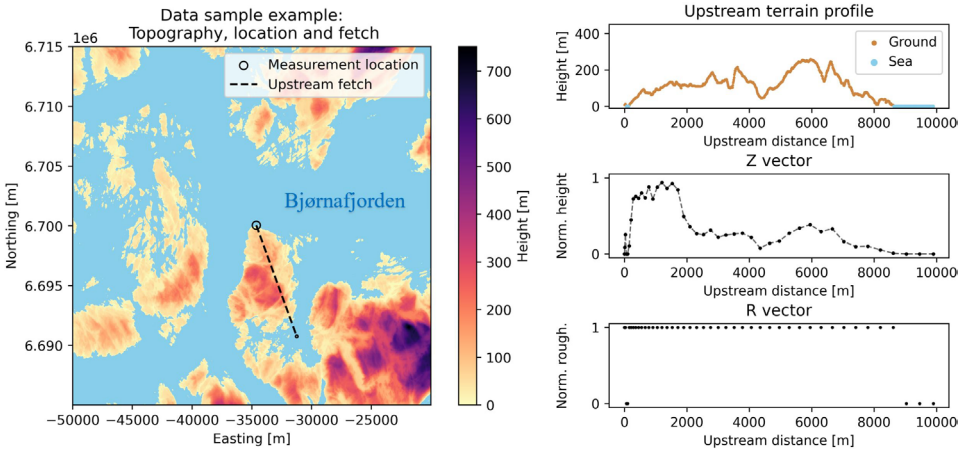

Fig. B.2 – Example of an elevation (Z) and roughness (R) data sample collection, given a location and a mean wind direction, associated with an upstream fetch and terrain profile.

B.5. Methodology

B.5.1. Artificial neural network

An artificial neural network (ANN) was established using *PyTorch* (v.1.9.0) (a *Python* library for deep learning). A multilayer perceptron arrangement was used, whose representation is shown in Fig. B.3. The ANN predicts the sectoral/directional averages of the along-wind turbulence intensities $\overline{I_u}$, i.e., the mean value of all I_u within each 1-degree-wide wind sector, at each wind mast, at 48 m above ground. A k-fold cross-validation method is used where the data is divided into six folds and where each fold corresponds to the data of one measurement mast location. This forces the model to predict turbulence intensities at locations it has never "seen" before. Each fold contains up to 360 data samples, one for each wind sector. The procedure for training, validating, optimizing and testing is further detailed in Fig. B.3. The domain of hyperparameters investigated is described in Table B.1.

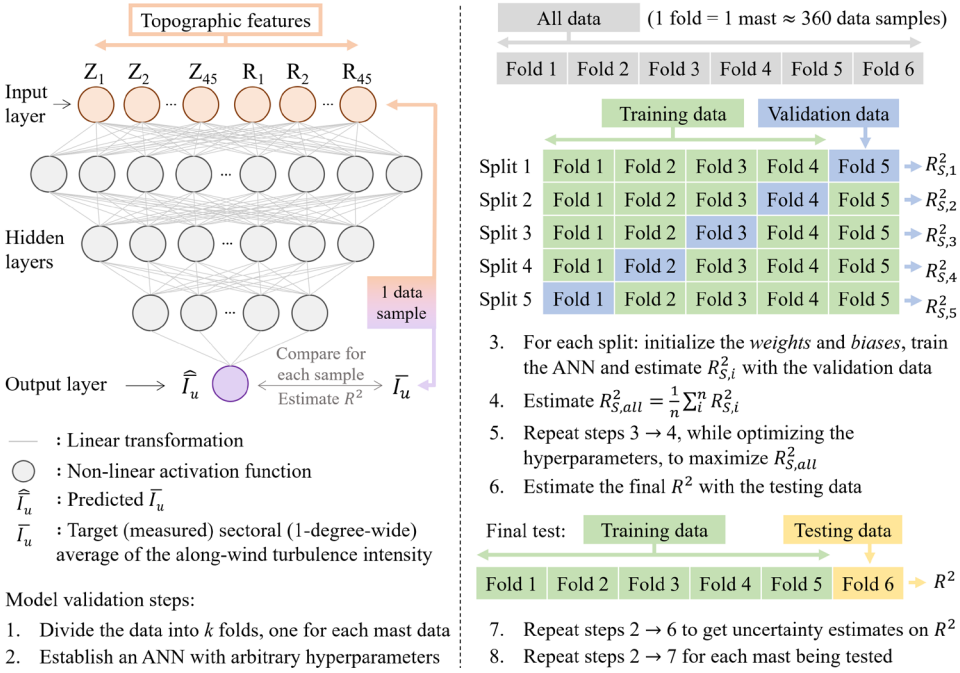

Fig. B.3 – Representation of the multilayer perceptron and the cross-validation procedure adopted.

Table B.1 – Domain of hyperparameters investigated.

Hyperparameter	Sampled intervals/categories
Num. of hidden layers	0 – 4 (each having $\approx 2/3$ of the size of the preceding one)
Activation function	ReLU / Leaky ReLU / ELU
Loss function	L1 Loss / MSE Loss / Log-Cosh Loss
Num. of epochs	20 - 2000
Learning rate	10^{-3} - 1
Weight decay	10^{-5} - 1
Momentum	0 - 0.95

A min-max normalization is applied to all inputs and target outputs to improve learning and stability. The target values $\overline{I_u}$ are compared with the predicted values $\widehat{\overline{I_u}}$ through a loss function, and learning is achieved by backpropagation. A batch gradient descent was found suitable due to the limited data size and the use of GPU-accelerated algorithms. The hyperparameters were optimized to maximize the R^2 value (coefficient of determination) of the validation data predictions, using 500 iterations with a so-called "Tree-structured Parzen Estimator Approach". This is preferable to grid and random searches and has been shown to have a good balance between performance and computer efficiency compared to other methods, such as gaussian processes and random forests (Akiba et al., 2019; Bergstra et al., 2011). Since the resultant "optimal" hyperparameters depend on the initial conditions, 20 initial sets of arbitrary hyperparameters, thus 20 different models, were used to estimate the uncertainty of the R^2 of the final testing data predictions. Lastly, when predicting the sectoral averages $\overline{I_u}$, instead of each 10-min occurrence of I_u, the topographic effects are better isolated and other time- and thermal-related effects can be disregarded.

B.5.2. Norwegian Standard - Eurocode NS-EN 1991-1-4

For comparison purposes, the along-wind turbulence intensity is also estimated following the Norwegian Standard and Eurocode NS-EN 1991-1-4 (ref. (Norwegian Standard, 2009)). The measurement masts presented in this study are in a region with strong contrasts of terrain roughness, namely sea water (terrain cat. 0) and forests in relatively small hills (terrain cat. III). This transition in the upstream terrain roughness is considered in the Eurocode NA.4.3.2(2) (901.2.2). Different orographic effects on turbulence could also be considered. Those described in NA.4.3.3 (901.2.1) and NA.4.3.3 (901.3.2) can be applicable to some of the studied locations. However, in NA.4.4, it is not clear how to combine these effects with those from the different terrain roughnesses upstream, so only the latter

ones are considered. Also, the orography factor is intended to represent isolated hills and escarpments, not undulating and mountainous regions.

To consider the upstream roughness heterogeneity, the upstream terrain is divided into two continuous patches of either terrain category 0 or III. The length of the two patches and the location of the transition between them were found iteratively for each mast and wind direction by minimizing the number of misclassifications when compared to the original R vector.

B.6. Results and discussion

The main results of the data-driven analysis are presented in Fig. B.4, Fig. B.5 and Fig. B.6. In Fig. B.4, the predictions of one ANN model, per location, are plotted. The plotted models were those that had their performance (R^2) closest to the average performance of all models for a given location (dark red dots in Fig. B.5). Displaying only the best performing ANN models would lead to bias due to a regression to the mean of future dataset test performances and is thus avoided. Contour and line plots are shown for each mast location. The contour plots show the upstream topography for each mean wind direction, with the same resolution as given in the input data for the Z and R vectors (see Section B.4.2). A blue color is superposed to represent the seawater, with lower surface roughness. The line plots show the measurements and ANN predictions of $\overline{I_u}$. The sectoral averages of the mean wind speeds, $\overline{U}$, from the data described in Section B.4.1, are also included for completeness.

Upstream hills close to the masts affect the results to a greater extent than hills further away. Long upstream fetches of water are associated with low turbulence intensities. The ANN predictions are best at Ospøya 1 and Ospøya 2, as expected due to their proximity (260 meters) and topographic similarity. Some predicted values at Ospøya 2, Landrøypynten and Nesøya seem slightly misaligned with the measurements. This can be due to local deflections of the wind direction around hills or/and discrepancies between reported and real anemometer orientations. At Svarvhelleholmen, the ANN underestimates turbulence for southern winds due to the inexistence of such high turbulence intensities in its training database. The Eurocode prediction also underestimates turbulence, but it could be argued that the alternative procedure in NA.4.3.3 (901.3.2) (“Lower lying construction site downstream of a hill or escarpment”) would lead to higher turbulence intensities for this particular site and direction. At Synnøytangen, nearby buildings and tall trees presumably affect the measurements to some extent for some directions.

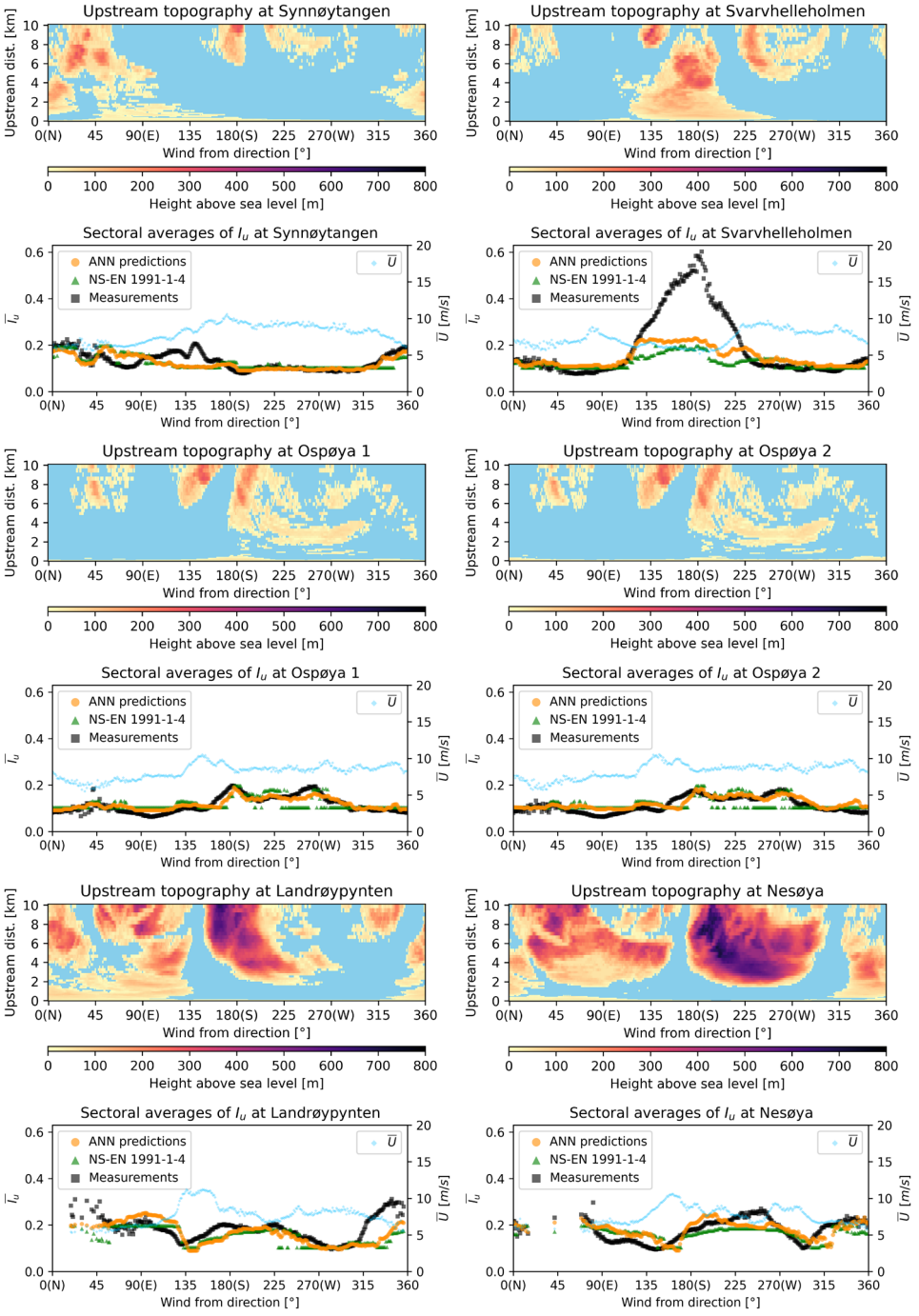

Fig. B.4 – Upstream topography for each mast and wind direction. Sectoral (1-degree-wide) averages of I_u: measurements vs predictions of an average performing ANN vs NS-EN 1991-1-4.

In Fig. B.5, the R^2 values, between the predictions of all ANN models and the tested measurements are shown as an indication of the model performances. It should be noted that the hyperparameter optimization is a chaotic process that is dependent on the initial conditions, hence the 20 models per tested location and associated R^2 uncertainty estimates. A value of $R^2 = 1$ indicates a perfect fit, whereas $R^2 = 0$ indicates a fit that is as good as a simple average of all 360 values of $\overline{I_u}$ (which is unknown a priori). Another performance metric, accuracy, is also included, taken as $100\% - MAPE$ (mean absolute percentage error).

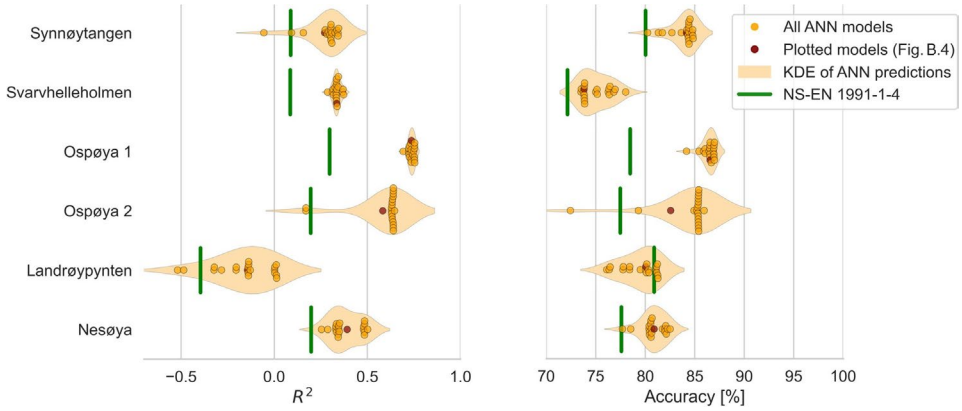

Fig. B.5 – R^2 values and accuracies of the ANN predictions of $\overline{I_u}$. Kernel density estimations (KDE) are provided to help visualize the underlying uncertainties. The Eurocode (NS-EN 1991-1-4) predictions are included for comparison.

In Fig. B.6, seven histograms show the final choices of the hyperparameters for all the different ANN models tested, after all optimization iterations were complete. It took roughly 110 hours to compute the 6 mast locations × 20 ANN models × 500 optimization iterations on a laptop PC (Intel Core i7-8850H, 64 GB 2666 MHz RAM, Nvidia Quadro P4200).

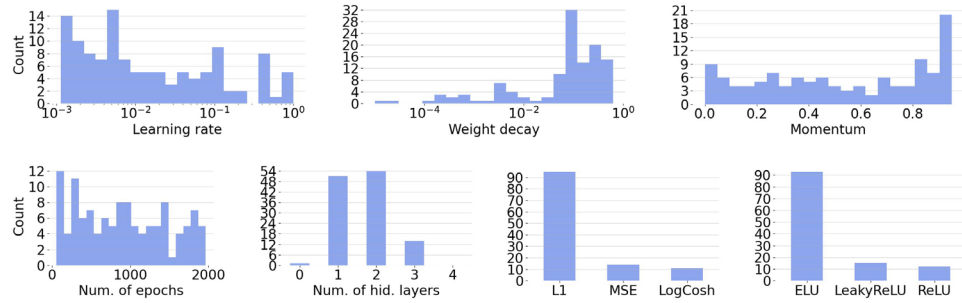

Fig. B.6 – Histograms of the optimal hyperparameters of all ANN models.

For all masts, the ANN predictions roughly captured the main trends of the mean turbulence intensities with the location and wind direction, showing overall better performances than the Eurocode predictions. Nonetheless, it remains a challenging task to accurately predict turbulence, regardless of the model adopted.

B.7. Summary

A data-driven model was developed to predict mean wind turbulence intensities for each mean wind direction in a complex terrain, where no wind measurements are available. The model consists of an artificial neural network, namely a multilayer perceptron, whose hyperparameters were systematically optimized to improve the predictions. First, a database of topographic data and measured turbulence intensities at 48 meters height above ground, at different locations, for each wind direction, was used to train the model. Each topographic data sample consisted of 45 terrain elevation points associated with a location, a wind direction and an upstream terrain profile, plus 45 binary classifications of those points' roughnesses into "ground" or "sea". Then, the model required only the topographic data at the desired new location to predict the mean turbulence intensities at the same height above ground for each mean wind direction.

For the six locations studied, prediction accuracies between 72% and 87% were obtained, despite the relatively small training databases with only four or five locations. The model outperformed the procedures given in the relevant standard (Eurocode NS-EN 1991-1-4), which inherently require numerous simplifications that are difficult to implement and systematize in complex terrain. The model is simple to establish, and the suggested framework can be easily adapted to include other input features and to predict other wind properties.

These findings can be useful when estimating the design wind loads on structures in complex terrains as a function of the wind direction. The proof-of-concept presented could also encourage other stakeholders to establish a comprehensive and global database with a larger number of measurement locations and diversified topographies, which could increase model accuracy and reliability. Such a database and model could significantly impact the design, safety and cost-effectiveness of wind-sensitive structures.

References

Akiba, T., Sano, S., Yanase, T., Ohta, T., Koyama, M., 2019. Optuna: A next-generation hyperparameter optimization framework, Proceedings of the 25th ACM SIGKDD International Conference on Knowledge Discovery & Data Mining, pp. 2623-2631.

Arena, A., Lacarbonara, W., Valentine, D.T., Marzocca, P., 2014. Aeroelastic behavior of long-span suspension bridges under arbitrary wind profiles. Journal of Fluids and Structures 50, 105-119.

Askeland, T., Dørum, C., Hjorteland, E., Alsaker, I., Roppen, T., 2022. Beregning av klimagassutslipp for fast samband kontra ferjedrift (Report). Statens vegvesen.

Bartoli, G., Contri, S., Mannini, C., Righi, M., 2009. Toward an improvement in the identification of bridge deck flutter derivatives. Journal of Engineering Mechanics 135, 771-785.

Basso, M.N., Hernas, S., Albertsen, M., Erraia, J., Fjose, S., Jakobsen, E., 2021. Eksportmeldingen 2021 - Et årlig dypdykk i Norges eksport. Menon - Publikasjon Nr. 58/2021 (Report).

Bathe, K.J., 2006. Finite element procedures. Klaus-Jurgen Bathe.

Bergstra, J., Bardenet, R., Bengio, Y., Kégl, B., 2011. Algorithms for hyper-parameter optimization. Advances in Neural Information Processing Systems 24.

Bitsuamlak, G.T., Bédard, C., Stathopoulos, T., 2007. Modeling the effect of topography on wind flow using a combined numerical–neural network approach. Journal of Computing in Civil Engineering 21, 384-392.

Bodini, N., Lundquist, J.K., Optis, M., 2020. Can machine learning improve the model representation of turbulent kinetic energy dissipation rate in the boundary layer for complex terrain? Geoscientific Model Development 13, 4271-4285.

Bourassa, M.A., Meissner, T., Cerovecki, I., Chang, P.S., Dong, X., De Chiara, G., Donlon, C., Dukhovskoy, D.S., Elya, J., Fore, A., 2019. Remotely sensed winds and wind stresses for marine forecasting and ocean modeling. Frontiers in Marine Science 6, 443.

Brahimi, T., 2019. Using artificial intelligence to predict wind speed for energy application in Saudi Arabia. Energies 12, 4669.

Bursnall, W.J., Loftin Jr, L.K., 1951. Experimental investigation of the pressure distribution about a yawed circular cylinder in the critical Reynolds number range. National Aeronautics and Space Administration Washington DC.

Castellon, D.F., Fenerci, A., Øiseth, O.A., 2021. A comparative study of wind-induced dynamic response models of long-span bridges using artificial neural networks, support vector regression and buffeting theory. Journal of Wind Engineering and Industrial Aerodynamics 209, 104484.

Chen, Z.Q., Yu, X.D., Yang, G., Spencer Jr, B.F., 2005. Wind-induced self-excited loads on bridges. Journal of Structural Engineering 131, 1783-1793.

Cheynet, E., 2020. Wind field simulation (text-based input). Zenodo. Retrieved from https://zenodo.org/record/3823864.

Cheynet, E., Jakobsen, J.B., Snæbjörnsson, J., 2016. Buffeting response of a suspension bridge in complex terrain. Engineering Structures 128, 474-487.

Cheynet, E., Jakobsen, J.B., Snæbjörnsson, J., 2019. Flow distortion recorded by sonic anemometers on a long-span bridge: towards a better modelling of the dynamic wind load in full-scale. Journal of Sound and Vibration 450, 214-230.

Cheynet, E., Jakobsen, J.B., Snæbjörnsson, J., Ágústsson, H., Harstveit, K., 2018. Complementary use of wind lidars and land-based met-masts for wind measurements in a wide fjord, Journal of Physics: Conference Series. IOP Publishing, p. 012028.

Cheynet, E., Liu, S., Ong, M.C., Jakobsen, J.B., Snæbjörnsson, J., Gatin, I., 2020. The influence of terrain on the mean wind flow characteristics in a fjord. Journal of Wind Engineering and Industrial Aerodynamics 205, 104331.

Chopra, A.K., 2007. Dynamics of structures. Pearson Education India.

Clough, R.W., Penzien, J., 2003. Dynamics of structures. Berkeley. CA: Computers and Structures.

Costa, B.M., Snæbjörnsson, J.Þ., Øiseth, O.A., Wang, J., Jakobsen, J.B., 2021. Data-driven prediction of mean wind turbulence from topographic data, IOP Conference Series: Materials Science and Engineering. IOP Publishing, p. 012005.

Costa, B.M., Wang, J., Jakobsen, J.B., Øiseth, O.A., Snæbjörnsson, J.Þ., 2022a. Bridge buffeting by skew winds: A revised theory. Journal of Wind Engineering and Industrial Aerodynamics 220, 104806.

Costa, B.M., Wang, J., Jakobsen, J.B., Øiseth, O.A., Snæbjörnsson, J.Þ., 2022b. Bridge buffeting by skew winds: A quasi-steady case study. Journal of Wind Engineering and Industrial Aerodynamics 227, 105068.

Costa, B.M., Wang, J., Jakobsen, J.B., Snæbjörnsson, J.Þ., Øiseth, O.A., 2022c. Long-term response of a floating bridge to inhomogeneous wind fields. Manuscript submitted for publication.

Daniotti, N., 2022. Bridge deck aerodynamics: A case study in full-scale. University of Stavanger.

Davenport, A.G., 1961a. The application of statistical concepts to the wind loading of structures. Proceedings of the Institution of Civil Engineers 19, 449-472.

Davenport, A.G., 1961b. The spectrum of horizontal gustiness near the ground in high winds. Quarterly Journal of the Royal Meteorological Society 87, 194-211.

Davenport, A.G., 1962. The response of slender, line-like structures to a gusty wind. Proceedings of the Institution of Civil Engineers 23, 389-408.

Dee, D.P., Uppala, S.M., Simmons, A.J., Berrisford, P., Poli, P., Kobayashi, S., Andrae, U., Balmaseda, M.A., Balsamo, G., Bauer, d.P., 2011. The ERA-Interim reanalysis: Configuration and performance of the data assimilation system. Quarterly Journal of the Royal Meteorological Society 137, 553-597.

Deodatis, G., 1996. Simulation of ergodic multivariate stochastic processes. Journal of Engineering Mechanics 122, 778-787.

Di Paola, M., 1998. Digital simulation of wind field velocity. Journal of Wind Engineering and Industrial Aerodynamics 74, 91-109.

Diana, G., Resta, F., Zasso, A., Belloli, M., Rocchi, D., 2004. Forced motion and free motion aeroelastic tests on a new concept dynamometric section model of the Messina suspension bridge. Journal of Wind Engineering and Industrial Aerodynamics 92, 441-462.

Dosovitskiy, A., Beyer, L., Kolesnikov, A., Weissenborn, D., Zhai, X., Unterthiner, T., Dehghani, M., Minderer, M., Heigold, G., Gelly, S., 2020. An image is worth 16x16 words: Transformers for image recognition at scale. arXiv preprint arXiv:2010.11929.

Dyrbye, C., Hansen, S.O., 1997. Wind loads on structures. Wiley.

Eames, M.C., 1968. Steady-state theory of towing cables. Trans. RINA 110, 185-206.

Ehsan, M.A., 2021. Predictive models for wind speed using artificial intelligence and copula, Department of Electrical and Computer Engineering. University of the District of Columbia.

Eidem, M.E., 2016. History of the Bjørnafjorden fjord crossing project, IABSE Congress: Challenges in Design and Construction of an Innovative and Sustainable Built Environment, Stockholm, Sweden, 21-23 September 2016, pp. 1943-1950.

Ersdal, S., Faltinsen, O.M., 2006. Normal forces on cylinders in near-axial flow. Journal of Fluids and Structures 22, 1057-1077.

ESDU, 1995. Computer program for wind speeds and turbulence properties: flat or hilly sites in terrain with roughness changes. ESDU International London.

Faltinsen, O., 1993. Sea loads on ships and offshore structures. Cambridge university press.

Floors, R., Peña, A., Lea, G., Vasiljević, N., Simon, E., Courtney, M., 2016. The RUNE experiment - A database of remote-sensing observations of near-shore winds. Remote Sensing 8, 884.

Forbord, E.M., Hjellvik, H., 2017. Wind-induced response of long-span suspension bridges subjected to span-wise non-uniform winds: a case study. [EM Forbord & H. Hjellvik].

Gardner, M.W., Dorling, S.R., 1998. Artificial neural networks (the multilayer perceptron) - a review of applications in the atmospheric sciences. Atmospheric Environment 32, 2627-2636.

Gramkow, C., 2001. On averaging rotations. Journal of Mathematical Imaging and Vision 15, 7-16.

Graupe, D., 2013. Principles of artificial neural networks. World Scientific.

Gu, M., Zhang, R., Xiang, H., 2000. Identification of flutter derivatives of bridge decks. Journal of Wind Engineering and Industrial Aerodynamics 84, 151-162.

Haan Jr, F.L., Wu, T., Kareem, A., 2016. Correlation structures of pressure field and integrated forces on oscillating prism in turbulent flows. Journal of Engineering Mechanics 142, 04016017.

Helgedagsrud, T.A., Bazilevs, Y., Korobenko, A., Mathisen, K.M., Øiseth, O.A., 2019. Using ALE-VMS to compute aerodynamic derivatives of bridge sections. Computers & Fluids 179, 820-832.

Hémon, P., Santi, F., 2003. Applications of biorthogonal decompositions in fluid-structure interactions. Journal of Fluids and Structures 17, 1123-1143.

Hong, S.Y., Noh, Y., Dudhia, J., 2006. A new vertical diffusion package with an explicit treatment of entrainment processes. Monthly Weather Review 134, 2318-2341.

Hu, L., Xu, Y.L., Zhu, Q., Guo, A., Kareem, A., 2017. Tropical storm-induced buffeting response of long-span bridges: enhanced nonstationary buffeting force model. Journal of Structural Engineering 143, 04017027.

Huang, M.H., Lin, Y.Y., Weng, M.X., 2012. Flutter and buffeting analysis of bridges subjected to skew wind. Journal of Applied Science and Engineering 15, 401-413.

Hutton, D.V., 2004. Fundamentals of finite element analysis. McGraw-hill.

Iwamoto, M., Fujino, Y., 1995. Identification of flutter derivatives of bridge deck from free vibration data. Journal of Wind Engineering and Industrial Aerodynamics 54, 55-63.

Jakobsen, J.B., 1995. Fluctuating wind load and response of a line-like engineering structure with emphasis on motion-induced wind forces, Department of Structural Engineering. Univ. of Trondheim.

Jakobsen, J.B., 1997. Span-wise structure of lift and overturning moment on a motionless bridge girder. Journal of Wind Engineering and Industrial Aerodynamics 69, 795-805.

Jakobsen, J.B., Hjorth-Hansen, E., 1995. Determination of the aerodynamic derivatives by a system identification method. Journal of Wind Engineering and Industrial Aerodynamics 57, 295-305.

Janić, Z.I., 2001. Nonsingular implementation of the Mellor-Yamada level 2.5 scheme in the NCEP Meso model. US Department of Commerce, National Oceanic and Atmospheric Administration.

Jermstad, O., Johansen, A., 2011. Anslag KVU E39 Aksdal - Bergen (internal report from SINTEF nr. F17687).

Jian, B., Su, Y., Li, M., 2020. Buffeting response of cable-stayed bridge during construction under skew winds and pylon interference. KSCE Journal of Civil Engineering 24, 2971-2979.

Jones, R.T., 1947. Effects of sweepback on boundary layer and separation.

Jonkman, B.J., 2009. TurbSim user's guide: Version 1.50. National Renewable Energy Lab. (NREL), Golden, CO (United States).

Kaimal, J.C., Wyngaard, J.C., Izumi, Y., Coté, O.R., 1972. Spectral characteristics of surface-layer turbulence. Quarterly Journal of the Royal Meteorological Society 98, 563-589.

Kapić, Z., Crnkić, A., Jaćimović, V., Mijajlović, N., 2021. A new dynamical model for solving rotation averaging problem, 2021 20th International Symposium INFOTEH-JAHORINA (INFOTEH). IEEE, pp. 1-6.

Karlgren, B., 1950. The book of Odes. Museum of Far Eastern Antiquities.

Kartverket, Høydedata (https://hoydedata.no/).

Kimura, K., Tanaka, H., 1992. Bridge buffeting due to wind with yaw angles. Journal of Wind Engineering and Industrial Aerodynamics 42, 1309-1320.

Kjeller Vindteknikk AS, 2016. Document: Bjørnafjorden, Hordaland, Kartlegging av vindforhold. Document no.: KVT/KH/2016/R020. Client document no.: SBJ-01-C3-KJE-01-RE-005. (limited access).

Kjeller Vindteknikk AS, 2018. Document: E39, Bjørnafjorden, Hordaland, Analysis of extreme wind at the fjord crossing. Document no.: KVT/ASH/2018/R089. Client document no.: SBJ-01-C4-KJE-01-TN-005. (limited access).

Klemp, J.B., Skamarock, W.C., Dudhia, J., 2007. Conservative split-explicit time integration methods for the compressible nonhydrostatic equations. Monthly Weather Review 135, 2897-2913.

Krasnopolsky, V.M., Breaker, L.C., Gemmill, W.H., 1995. A neural network as a nonlinear transfer function model for retrieving surface wind speeds from the special sensor microwave imager. Journal of Geophysical Research: Oceans 100, 11033-11045.

Kvåle, K.A., 2017. Dynamic behaviour of floating bridges exposed to wave excitation: A numerical and experimental investigation. Norwegian University of Science and Technology.

Lalee, M., Nocedal, J., Plantenga, T., 1998. On the implementation of an algorithm for large-scale equality constrained optimization. SIAM Journal on Optimization 8, 682-706.

Larose, G.L., 1997. The dynamic action of gusty winds on long-span bridges. Technical University of Denmark.

Larose, G.L., Mann, J., 1998. Gust loading on streamlined bridge decks. Journal of Fluids and Structures 12, 511-536.

Li, Q.C., 1995. Measuring flutter derivatives for bridge sectional models in water channel. Journal of Engineering Mechanics 121, 90-101.

Li, S., Li, M., Larose, G.L., 2018. Aerodynamic admittance of streamlined bridge decks. Journal of Fluids and Structures 78, 1-23.

Li, S., Li, M., Zhang, L., 2016. Buffeting response of cable-stayed bridge under skew wind, in: Proceedings of the Advances in Civil, Environmental and Materials Research.

Liepmann, H.W., 1952. On the application of statistical concepts to the buffeting problem. Journal of the Aeronautical Sciences 19, 793-800.

Lystad, T.M., Fenerci, A., Øiseth, O.A., 2018a. Aerodynamic effect of non-uniform wind profiles for long-span bridges, Conference of the Italian Association for Wind Engineering. Springer, pp. 427-439.

Lystad, T.M., Fenerci, A., Øiseth, O.A., 2018b. Evaluation of mast measurements and wind tunnel terrain models to describe spatially variable wind field characteristics for long-span bridge design. Journal of Wind Engineering and Industrial Aerodynamics 179, 558-573.

Mah, J., Samson, C., McKinnon, S.D., Thibodeau, D., 2013. 3D laser imaging for surface roughness analysis. International Journal of Rock Mechanics and Mining Sciences 58, 111-117.

Michalakes, J., Chen, S., Dudhia, J., Hart, L., Klemp, J., Middlecoff, J., Skamarock, W., 2001. Development of a next-generation regional weather research and forecast model, Developments in Teracomputing. World Scientific, pp. 269-276.

Midjiyawa, Z., Cheynet, E., Reuder, J., Ágústsson, H., Kvamsdal, T., 2021. Potential and challenges of wind measurements using met-masts in complex topography for bridge design: Part I - Integral flow characteristics. Journal of Wind Engineering and Industrial Aerodynamics, 104584.

Mills, G., Fotopoulos, G., 2013. On the estimation of geological surface roughness from terrestrial laser scanner point clouds. Geosphere 9, 1410-1416.

Newmark, N.M., 1959. A method of computation for structural dynamics. Journal of the Engineering Mechanics Division 85, 67-94.

Nikitas, N., Macdonald, J.H., Jakobsen, J.B., 2011. Identification of flutter derivatives from full-scale ambient vibration measurements of the Clifton Suspension Bridge. Wind and Structures 14, 221-238.

Norwegian Public Roads Administration, 2011. Konseptvalutgreiing E39 Aksdal - Bergen (report).

Norwegian Public Roads Administration, 2012. Ferjefri E39 Delprosjekt Fjordkryssing (report).

Norwegian Public Roads Administration, 2015. Handbook N400 for Bridge Design.

Norwegian Public Roads Administration, 2017a. Document: Appendix B - Global analyses rev A. Document no.: SBJ-30-C3-NOR-90-RE-102 (Version A) (limited access).

Norwegian Public Roads Administration, 2017b. Document: K7 Bjørnafjorden end-anchored floating bridge - Appendix A - Drawings binder. Document no.: SBJ-30-C3-NOR-90-RE-101. (limited access).

Norwegian Public Roads Administration, 2018. Document: MetOcean Design basis. Document no.: SBJ-01-C4-SVV-01-BA-001. https://hdl.handle.net/11250/2676915.

Norwegian Public Roads Administration, 2019a. Document: Concept evaluation - Appendix C - Architectural evaluation. Document no.: SBJ-32-C5-AMC-22-RE-103. (limited access).

Norwegian Public Roads Administration, 2019b. Document: Concepts definition and description. Document no.: SBJ-32-C5-OON-22-RE-001. (limited access).

Norwegian Public Roads Administration, 2019c. Document: Preferred solution, K12 - Appendix E - Aerodynamics. Document no.: SBJ-33-C5-AMC-20-RE-105. https://hdl.handle.net/11250/2659946.

Norwegian Public Roads Administration, 2019d. Document: Preferred solution, K12 - Appendix F - Global analyses - Modelling and assumptions. Document no.: SBJ-33-C5-AMC-90-RE-106. https://hdl.handle.net/11250/2660044.

Norwegian Public Roads Administration, 2019e. Document: Wind model-tests, floating bridge, step 1, small scale testing. Document no.: SBJ-32-C4-SOH-20-RE-001. Rev 1. (limited access).

Norwegian Standard, 2009. NS-EN 1991-1-4: 2005 + NA: 2009. Eurokode 1, 1-4.

Øiseth, O.A., 2011. Dynamic behaviour of cable supported bridges subjected to strong natural wind. Norwegian University of Science and Technology.

Øiseth, O.A., Rönnquist, A., Sigbjörnsson, R., 2013. Effects of co-spectral densities of atmospheric turbulence on the dynamic response of cable-supported bridges: a case study. Journal of Wind Engineering and Industrial Aerodynamics 116, 83-93.

Olesen, H.R., Larsen, S.E., Højstrup, J., 1984. Modelling velocity spectra in the lower part of the planetary boundary layer. Boundary-Layer Meteorology 29, 285-312.

Opgård, B., Allievi, F., 2014. Chained floating bridge, IABSE Symposium Report. International Association for Bridge and Structural Engineering, pp. 1236-1243.

Rawlinson, H.C., Wilkinson, J.G., 1861. The history of Herodotus.

Relf, E.F., Powell, C.H., 1917. Tests on smooth and stranded wires inclined to the wind direction and a comparison of the results on stranded wires in air and water. Advisory Committe for Aeronautics. Reports and Memoranda (New Series) 307, 8-14.

Rosenblatt, F., 1958. The perceptron: a probabilistic model for information storage and organization in the brain. Psychological Review 65, 386.

Rosenblatt, F., 1961. Principles of neurodynamics. Perceptrons and the theory of brain mechanisms. Cornell Aeronautical Lab Inc Buffalo NY.

Rumelhart, D.E., Hinton, G.E., Williams, R.J., 1985. Learning internal representations by error propagation. California Univ San Diego La Jolla Inst for Cognitive Science.

Ryggvik, H., 2015. A short history of the Norwegian oil industry: From protected national champions to internationally competitive multinationals. Business History Review 89, 3-41.

Samferdselsdepartementet, 1995. St. Meld. Nr. 21 (1994-95) Stamveg Kristiansand - Bergen - Trondheim.

Samferdselsdepartementet, 2021a. Nasjonal transportplan 2022-2033. Meld. St. 20.

Samferdselsdepartementet, 2021b. Prop. 228 S (2020 - 2021) Proposisjon til Stortinget (forslag til stortingsvedtak) - Utgreiing og planlegging av E39 Stord-Os, Ådland–Svegatjørn (Hordfast) i Vestland.

Scanlan, R.H., 1993. Bridge buffeting by skew winds in erection stages. Journal of Engineering Mechanics 119, 251-269.

Scanlan, R.H., 1999. Estimates of skew wind speeds for bridge flutter. Journal of Bridge Engineering 4, 95-98.

Scanlan, R.H., Tomko, J.J., 1971. Airfoil and bridge deck flutter derivatives. Journal of the Engineering Mechanics Division 97(6)1717-1737.

Sears, W.R., 1941. Some aspects of non-stationary airfoil theory and its practical application. Journal of the Aeronautical Sciences 8, 104-108.

Sears, W.R., 1948. The boundary layer of yawed cylinders. Journal of the Aeronautical Sciences 15, 49-52.

Sharif Razavian, A., Azizpour, H., Sullivan, J., Carlsson, S., 2014. CNN features off-the-shelf: an astounding baseline for recognition, Proceedings of the IEEE conference on computer vision and pattern recognition workshops, pp. 806-813.

Shen, Z., Li, J., Li, R., Gao, G., 2021. Nonuniform wind characteristics and buffeting response of a composite cable-stayed bridge in a trumpet-shaped mountain pass. Journal of Wind Engineering and Industrial Aerodynamics 217, 104730.

Shinozuka, M., 1972. Monte Carlo solution of structural dynamics. Computers & Structures 2, 855-874.

Siedziako, B., Øiseth, O.A., Rønnquist, A., 2017. An enhanced forced vibration rig for wind tunnel testing of bridge deck section models in arbitrary motion. Journal of Wind Engineering and Industrial Aerodynamics 164, 152-163.

Simma, M., Mjøen, H., Boström, T., 2020. Measuring wind speed using the internal stabilization system of a quadrotor drone. Drones 4, 23.

Skamarock, W.C., Klemp, J.B., Dudhia, J., Gill, D.O., Barker, D., Duda, M.G., Huang, X.Y., Wang, W., Powers, J.G., 2008. A description of the advanced research WRF version 3 (No. NCAR/TN-475+ STR), University Corporation for Atmospheric Research. National Center for Atmospheric Research Boulder, Colorado, USA, https://doi.org/10.5065/D68S4MVH.

Søreide, T.H., Reinertsen, A.S., Bjerkås, M., 2013. Mooring concept for deep water crossings. Reinertsen AS, Trondheim, Norway.

Statistisk Sentralbyrå, 2022. Befolkning - Tabell 11342: Areal og befolkning i kommuner, fylker og hele landet.

Strømmen, E., 2010. Theory of bridge aerodynamics. Springer Science & Business Media.

Strømmen, E., 2014. Structural dynamics. Springer.

Sumer, B.M., 2006. Hydrodynamics around cylindrical structures. World scientific.

Tanaka, H., Davenport, A.G., 1982. Response of taut strip models to turbulent wind. Journal of the Engineering Mechanics Division 108, 33-49.

Tao, T., Wang, H., Zhao, K., 2021. Efficient simulation of fully non-stationary random wind field based on reduced 2D hermite interpolation. Mechanical Systems and Signal Processing 150, 107265.

Thompson, G., Rasmussen, R.M., Manning, K., 2004. Explicit forecasts of winter precipitation using an improved bulk microphysics scheme. Part I: Description and sensitivity analysis. Monthly Weather Review 132, 519-542.

Van Atta, C.W., 1968. Experiments on vortex shedding from yawed circular cylinders. AIAA Journal 6, 931-933.

Velo, R., López, P., Maseda, F., 2014. Wind speed estimation using multilayer perceptron. Energy Conversion and Management 81, 1-9.

Venkatesh, Y.V., Raja, S.K., 2003. On the classification of multispectral satellite images using the multilayer perceptron. Pattern Recognition 36, 2161-2175.

Veritas, D.N., 2010. Recommended practice DNV-RP-C205: environmental conditions and environmental loads. DNV, Norway.

Virtanen, P., Gommers, R., Oliphant, T.E., Haberland, M., Reddy, T., Cournapeau, D., Burovski, E., Peterson, P., Weckesser, W., Bright, J., 2020. SciPy 1.0: fundamental algorithms for scientific computing in Python. Nature Methods 17, 261-272.

Viuff, T.H., 2020. Uncertainty assessment of wave-and current-induced global response of floating bridges-a numerical investigation.

Wahl, F., Espinasse, T., 2014. Polynomial regression under shape constraints.

Wang, H., Li, A.Q., Hu, R.M., 2011. Comparison of ambient vibration response of the Runyang suspension bridge under skew winds with time-domain numerical predictions. Journal of Bridge Engineering 16, 513-526.

Wang, R., Cheng, S.H., Ting, D.S.K., 2019. Effect of yaw angle on flow structure and cross-flow force around a circular cylinder. Physics of Fluids 31.

Watanabe, E., 2003. Floating bridges: past and present. Structural Engineering International 13, 128-132.

Wild, J.M., 1949. The boundary layer of yawed infinite wings. Journal of the Aeronautical Sciences 16, 41-45.

Xiang, X., Viuff, T., Leira, B., Øiseth, O.A., 2018. Impact of hydrodynamic interaction between pontoons on global responses of a long floating bridge under wind waves, International Conference on Offshore Mechanics and Arctic Engineering. American Society of Mechanical Engineers, p. V07AT06A049.

Xie, J., Tanaka, H., Wardlaw, R.L., Savage, M.G., 1991. Buffeting analysis of long span bridges to turbulent wind with yaw angle. Journal of Wind Engineering and Industrial Aerodynamics 37, 65-77.

Xu, F., Zhang, Z., 2017. Free vibration numerical simulation technique for extracting flutter derivatives of bridge decks. Journal of Wind Engineering and Industrial Aerodynamics 170, 226-237.

Xu, Y.L., 2013. Wind effects on cable-supported bridges. John Wiley & Sons.

Xu, Y.L., Zhu, L.D., 2005. Buffeting response of long-span cable-supported bridges under skew winds. Part 2: case study. Journal of Sound and Vibration 281, 675-697.

Zhang, X., 2007. Influence of some factors on the aerodynamic behavior of long-span suspension bridges. Journal of Wind Engineering and Industrial Aerodynamics 95, 149-164.

Zhou, Y., Sun, L., Xie, M., 2020. Wind characteristics at a long-span sea-crossing bridge site based on monitoring data. Journal of Low Frequency Noise, Vibration and Active Control 39, 453-469.

Zhu, L.D., 2002. Buffeting response of long span cable-supported bridges under skew winds: field measurement and analysis, Department of Civil and Structural Engineering. Pao Yue-kong Library, The Hong Kong Polytechnic University, Hong Kong.

Zhu, L.D., Xu, Y.L., 2005. Buffeting response of long-span cable-supported bridges under skew winds. Part 1: Theory. Journal of Sound and Vibration 281, 647-673.

Zhu, L.D., Xu, Y.L., Xiang, H.F., 2002a. Tsing Ma bridge deck under skew winds - Part II: flutter derivatives. Journal of Wind Engineering and Industrial Aerodynamics 90, 807-837.

Zhu, L.D., Xu, Y.L., Zhang, F., Xiang, H.F., 2002b. Tsing Ma bridge deck under skew winds - Part I: Aerodynamic coefficients. Journal of Wind Engineering and Industrial Aerodynamics 90, 781-805.

Zhu, L.D., Zhao, C., Wen, S., Ding, Q., 2009. Signature turbulence effect on buffeting responses of a long-span bridge with a centrally-slotted box deck, Computational Structural Engineering. Springer, pp. 399-409.

Zhu, L.D., Zhou, Q., Ding, Q., Xu, Z., 2018. Identification and application of six-component aerodynamic admittance functions of a closed-box bridge deck. Journal of Wind Engineering and Industrial Aerodynamics 172, 268-279.

Zhu, Q., Xu, Y.L., 2014. Characteristics of distributed aerodynamic forces on a twin-box bridge deck. Journal of Wind Engineering and Industrial Aerodynamics 131, 31-45.